THÈSE DE DOCTORAT

Simulations cinétiques du plasma de la magnétosphère de Mercure pour préparer BepiColombo

Federico Lavorenti

Laboratoire Lagrange, Observatoire de la Côte d'Azur
Dipartimento di Fisica, Università di Pisa

LAGRANGE   esa   UNIVERSITÉ FRANCO ITALIENNE | UNIVERSITÀ ITALO FRANCESE

Kinetic plasma simulations of Mercury's magnetosphere to prepare BepiColombo

Simulations cinétiques du plasma de la magnétosphère de Mercure pour préparer BepiColombo

Simulazioni cinetiche del plasma della magnetosfera di Mercurio per preparare BepiColombo

Jury

Président du jury

- Méheut Héloise, Directrice de Recherche CNRS, Lagrange OCA, Nice, France

Rapporteurs

- Hideyuki Usui, Full professor, Kobe University, Kobe, Japan
- Emma Bunce, Full professor, Leicester University, Leicester, UK

Examinateurs

- Francesco Pegoraro, Emeritus Professor, University of Pisa, Pisa, Italy
- Thomas Karlsson, Professor, KTH Royal Institute of Technology, Stockholm, Sweden
- Johannes Benkhoff, Senior Scientist, ESA/ESTEC, Noordwijk, The Netherlands

Directeurs de thèse

- Pierre Henri, Chargé de Recherche CNRS, Lagrange OCA, Nice, France
- Francesco Califano, Full Professor, University of Pisa, Pisa, Italy

Ringraziamenti

In questo gran marasma che è la vita, son felice di aver vissuto tre anni intensi. Il dottorato non è una cosa semplice, ma, al che conclusa, sento sorgere un senso di "plénitude". Questo traguardo è anche merito delle molte persone che hanno incrociato il mio cammino in questi anni, e delle molte altre che lo accompagnano già da prima. Mi è difficile spendere parole in ringraziamenti puntuali e coerenti, piuttosto preferisco spronarvi a riflettere ai bei momenti passati insieme in questi anni; per poi chiudere con un caro abbraccio a chi c'è, e soprattutto, a chi non c'è più.

Remerciements

Dans ce grand chambardement qu'est la vie, je suis heureux d'avoir vécu trois années in- tenses. Un doctorat n'est pas une chose facile, mais une fois terminé, je ressens un sentiment de pléni- tude. Cette réussite, je la dois aussi aux nombreuses personnes qui ont croisé mon chemin au cours de ces années, et aux nombreuses autres qui l'accompagnent depuis tou- jours. Il m'est difficile de consacrer des mots à des remerciements ponctuels et cohérents, mais je préfère vous encourager à réfléchir aux bons moments que nous avons passés ensem- ble au cours de ces années, et terminer en embrassant chaleureusement ceux qui sont ici et, surtout, ceux qui ne sont plus là.

Acknwowledgements

In this great welter that is life, I am happy to have lived three intense years. A PhD is not an easy task, but upon completion, a sense of "plénitude" arise. This achievement owes a lot to the many people who have crossed my path over these years, and to the many others who have accompanied me from before. It is difficult for me to spend words in punctual and coherent thanks, rather I prefer to encourage you to contemplate the good times we have spent together over these years; and then I would like to close with a dear embrace to those who are here, and above all, to those who are no longer here.

Abstract

Space plasmas permeate the Solar System, from the solar corona to the upper layers of planetary environments (e.g. magnetosphere and ionosphere). In the Solar System, only two telluric planets possess an intrinsic magnetic field, and therefore a magnetosphere, those are the Earth and Mercury. Differently from the Earth, Mercury has been rarely visited by exploratory space missions. Therefore, many of the properties of Mercury's environment, and of its magnetosphere in particular, remain poorly investigated at present. This work contributes to the global understanding of Mercury's plasma and planetary environment, in light of ongoing exploratory space missions. The ongoing ESA/JAXA BepiColombo mission provides in situ observations at Mercury with an advanced payload, able to observe the plasma dynamics – for the first time– down to electron kinetic scales. To interpret such observations, numerical models resolving electron kinetic scales are needed. In this work, I use two fully-kinetic models to study electron-scale processes in Mercury's magnetosphere, both at local and global scales. I focus on the plasma processes at the origin of (i) electron acceleration by wave-particle interaction at the magnetopause, (ii) electron acceleration by magnetic reconnection in the magnetotail, and (iii) electron precipitation onto the surface of Mercury. The impact of these processes on Mercury's magnetosphere-exosphere-surface coupling is also extensively studied. For this purpose, I develop and validate the first ab initio fully-kinetic global model of Mercury's magnetosphere.

In this PhD, I characterize the main processes that accelerate electrons in the magnetosphere of Mercury. First, electrons are accelerated by resonant wave-particle interaction with drift waves (generated by the lower-hybrid-drift instability) at the magnetopause. This process increases the parallel electron temperature up to a factor two, if the magnetopause width is of the order of the ion gyroradius. Second, electrons are accelerated by magnetic reconnection in the magnetotail. This process generates a flow of electrons with an energy of few keV directed towards the planet from the X-line in the tail. Such electrons populate the inner shells of the magnetosphere to form Mercury's "partial ring current". Third, a large fraction of the electrons in this "partial ring current" precipitates onto the surface of Mercury, thus driving plasma-exosphere and plasma-surface interactions. Magnetic reconnection in the tail is the main process accelerating electrons (up to few keV) in the magnetosphere of Mercury. These electrons, while being partially trapped in the nightside, precipitate onto the surface to drive (i) efficient ionization of exospheric H, He, O and Mn, (ii) a pattern of X-ray emissions more prominent at dawn consistent with MESSENGER/XRS observations, and (iii) differential space weathering of Mercury's regolith. Finally, the findings of this work will be used to advance global models of Mercury's coupled magnetosphere-exosphere-surface system and to interpret (ongoing) and to plan (future) observations by BepiColombo mission. The global model developed in this work for Mercury will also find applications to other bodies (such as the Moon, asteroids, Mars, and the Galilean Moons of Jupiter) in future works.

Keywords: Mercury – plasma – simulation – space – BepiColombo – astrophysics

Resumé

Les plasmas spatiaux se répandent dans le système solaire, depuis la couronne solaire jusqu'aux couches supérieures des environnements planétaires (comme la magnétosphère et l'ionosphère). Dans le système solaire, seules deux planètes telluriques possèdent un champ magnétique intrinsèque, et donc une magnétosphère : la Terre et Mercure. Contrairement à la Terre, Mercure a été rarement visitée par des missions d'exploration spatiale. Par conséquent, de nombreuses propriétés de l'environnement de Mercure, et de sa magnétosphère en particulier, restent peu étudiées à l'heure actuelle. Ce travail contribue à la compréhension globale du plasma et de l'environnement planétaire de Mercure, à la lumière des missions spatiales exploratoires en cours. La mission ESA/JAXA BepiColombo fournit des observations in situ de l'environnement de Mercure avec des instruments avancés, capables d'observer la dynamique du plasma – pour la première fois – jusqu'aux échelles cinétiques des électrons. Pour interpréter de telles observations, des modèles numériques résolvant les échelles cinétiques des électrons sont nécessaires. Dans ce travail, j'utilise deux modèles cinétiques pour étudier les processus à l'échelle des électrons dans la magnétosphère de Mercure, à la fois à l'échelle locale et à l'échelle globale. Je me concentre sur les processus à l'origine (i) de l'accélération des électrons par interaction onde-particule à la magnétopause, (ii) de l'accélération des électrons par reconnexion magnétique dans la queue de la magnétosphère, et (iii) de la précipitation des électrons à la surface de Mercure. L'impact de ces processus sur le couplage magnétosphère-exosphère-surface de Mercure est également étudié de manière approfondie. À cette fin, je développe et valide le premier modèle cinétique global ab initio de la magnétosphère de Mercure.

Dans cette thèse, je caractérise les principaux processus qui accélèrent les électrons dans la magnétosphère de Mercure. Premièrement, les électrons sont accélérés par l'interaction onde-particule résonante avec les ondes de dérive, générées par l'instabilité de dérive à la fréquence hybride basse, à la magnétopause. Ce processus augmente la température parallèle des électrons jusqu'à un facteur deux, si la largeur de la magnétopause est de l'ordre du rayon de gyration des ions. Deuxièmement, les électrons sont accélérés par la reconnexion magnétique dans la queue de la magnétosphère. Ce processus génère un flux d'électrons d'une énergie de quelques keV dirigés depuis la queue vers la planète. Ces électrons peuplent les enveloppes internes de la magnétosphère pour former un anneau de courant partiel. Troisièmement, une grande partie des électrons dans ce courant annulaire précipite à la surface de Mercure, ce qui entraîne des interactions plasma-exosphère et plasma-surface. La reconnexion magnétique dans la queue est le principal processus d'accélération des électrons (jusqu'à quelques keV) dans la magnétosphère de Mercure. Ces électrons, tout en étant partiellement piégés du côté nuit, précipitent sur la surface de la planète pour entraîner (i) une ionisation efficace de H, He, O et Mn dans l'exosphère, (ii) des émissions de rayons X avec une prédominance pour le côté aube, conformément aux observations de MESSENGER/XRS, et (iii) de l'érosion spatiale du régolithe de Mercure. Enfin, les résultats de ce travail seront utilisés pour progresser dans la modélisation globale du système couplé magnétosphère-exosphère-surface de Mercure et pour interpréter et planifier les observations, en cours et future, de la mission BepiColombo. Le modèle global développé ici pour Mercure pourrait être appliqué, dans le futur, à d'autres corps célestes tels que les astéroïdes, Mars, la Lune terrestre et les lunes de Jupiter.

Mots-clés : Mercure – plasma – simulation – espace – BepiColombo – astrophysique

Sommario

I plasmi spaziali permeano il Sistema solare, dalla corona solare agli strati superiori degli ambienti planetari (ad esempio, magnetosfera e ionosfera). Nel Sistema solare, solo due pianeti tellurici possiedono un campo magnetico intrinseco, e quindi una magnetosfera: si tratta della Terra e di Mercurio. A differenza della Terra, Mercurio è stato raramente visitato da missioni di esplorazione spaziale. Pertanto, molte delle proprietà dell'ambiente di Mercurio, e della sua magnetosfera in particolare, rimangono attualmente poco studiate. Questo lavoro contribuisce alla comprensione globale del plasma e dell'ambiente planetario di Mercurio, alla luce delle missioni di explorazione spaziale in corso. La missione ESA/JAXA BepiColombo, attualmente in corso, fornisce osservazioni in situ di Mercurio con un payload avanzato, in grado di osservare la dinamica del plasma - per la prima volta - fino alle scale cinetiche degli elettroni. Per interpretare tali osservazioni, sono necessari modelli numerici che risolvano le scale cinetiche degli elettroni. In questo lavoro, utilizzo due modelli "fully-kinetic" per studiare i processi a scala elettronica nella magnetosfera di Mercurio, sia localmente che globalmente. In particolare, mi concentro sui processi che danno origine (i) all'accelerazione degli elettroni per interazione onda-particella alla magnetopausa, (ii) all'accelerazione degli elettroni per riconnessione magnetica nella coda della magnetsfera e (iii) alla precipitazione degli elettroni sulla superficie di Mercurio. L'impatto di questi processi sull'accoppiamento magnetosfera-esosfera-superficie di Mercurio è anche ampiamente studiato. A questo scopo, ho sviluppato e validato il primo modello globale ab initio "fully-kinetic" della magnetosfera di Mercurio.

In questo dottorato, caratterizzo i principali processi che accelerano gli elettroni nella magnetosfera di Mercurio. In primo luogo, gli elettroni sono accelerati dall'interazione risonante onda-particella con onde di deriva (generate dall'instabilità "lower-hybrid-drift") alla magnetopausa. Questo processo aumenta la temperatura parallela degli elettroni fino a un fattore due, se la larghezza della magnetopausa è dell'ordine del raggio di girazione degli ioni. In secondo luogo, gli elettroni sono accelerati dalla riconnessione magnetica nella coda. Questo processo genera un flusso di elettroni con un'energia dell'ordine del keV diretti verso il pianeta dalla "X-line" nella coda. Questi elettroni popolano gli strati interni della magnetosfera e formano la "partial ring current" di Mercurio. In terzo luogo, una grande frazione degli elettroni di questa "partial ring current" precipita alla superficie del pianeta, provocando così interazioni plasma-esosfera e plasma-superficie. La riconnessione magnetica nella coda è il processo principale che accelera gli elettroni (fino a qualche keV) nella magnetosfera di Mercurio. Questi elettroni, pur essendo parzialmente intrappolati nel lato notturno del pianeta, precipitano sulla superficie per provocare (i) un'efficiente ionizzazione di H, He, O e Mn esosferici, (ii) un emissione di raggi X dalla superficie più prominente all'alba, coerentemente con le osservazioni di MESSENGER/XRS, e (iii) "space weathering" del regolite di Mercurio. Infine, i risultati di questo lavoro saranno utilizzati per far progredire i modelli globali del sistema accoppiato magnetosfera-esosfera-superficie di Mercurio e per interpretare e pianificare le osservazioni, in corso e future, della missione BepiColombo. Il modello globale sviluppato in questo lavoro per Mercurio potrà, inoltre, essere applicato allo studio di altri corpi celesti come gli asteroidi, Marte, la Luna terrestre e le lune di Giove.

Parole chiave : Mercurio – plasma – simulazione – spazio – BepiColombo – astrofisica

Contents

Contents

1 INTRODUCTION

Any body in the Solar System (planet, comet, asteroid etc.) is exposed to the flux of plasma emitted from the Sun, the so-called solar wind[1]. If one of these bodies possess a large intrinsic magnetic field (such as Mercury, the Earth, and Jupiter), or small localized crustal magnetic fields (such as the Moon and Mars), or an ionosphere (such as Venus), then the interaction between the solar wind and the body is governed by complex phenomena rooted in plasma physics theory. For this reason, plasma physics is of the uttermost importance to study Solar System bodies.

A plasma is obtained when a "sufficiently large" fraction of the atoms in a gas is ionized[2]. At this point, the electric forces between ions and electrons (typical of a plasma) dominate over the atom-atom collisions (typical of a gas) On Earth, plasmas are artificially produced in a large number of laboratories (Braams and Stott, 2002; Bonizzoni and Vassallo, 2002), where they are used for low-temperature industrial applications (such as microelectronics and satellite propulsion), as well as high-temperature nuclear experiments (such as laser-plasma and nuclear fusion). In space, plasmas are found everywhere, from the upper layers of Earth's atmosphere (thunders, sprites, ionosphere etc.), out into the Solar System (solar wind, planetary magnetospheres, solar corona etc.), and further out in many astrophysical objects (stars, supernova, accretion disks etc.). Plasmas permeate the Universe, and more importantly for this work, they permeate the the Solar System. For this reason, plasmas play a key role in the interaction between the gaseous, liquid and solid matter composing any Solar System body and the surrounding ionized environment.

Any body in the Solar System forms an interface plasma-gas (such as at Venus, the Earth and Mars) or plasma-surface (such as at Mercury, the Moon and asteroids) when interacting with the solar wind. At this interface, important processes that alter the atmospheric, optical, chemical, and biological properties of the body can take place. On Earth, this interaction is at the origin of the beautiful auroras, but it also leads to sporadic hazardous events affecting

---

[1] Analogously to the Solar System, any stellar system is expected to have bodies (exoplanets, exocomets etc.) that interact with the stellar wind. This is a topic of great relevance for exoplanet studies, nevertheless it remains out of the scope of this work.

[2] There exists a blurry transition region between gas and plasma, where partially-ionized plasma, such as the one in Earth's ionosphere, exists.

the electrical grid (Boteler, 2001) as well as low-Earth-orbit satellites (Miteva et al., 2023). At Venus, the solar wind is thought to be, at least partially, responsible for the lack of water in the present-day atmosphere; a consequence of H_2O atmospheric loss operated by the solar wind over billions of years (Lammer et al., 2006). On airless bodies such as Mercury, the interaction with the solar wind alters the surface optical and spectral properties, contributing to the so-called space weathering of the surface (Pieters and Noble, 2016). It follows that a good understanding of the plasma-atmosphere and/or plasma-surface interaction is a key element in the global understanding of any Solar System body, to infer its present state as well as its evolution.

This work focuses on the planet Mercury, the closest planet to the Sun and the least explored in the inner Solar System. Mercury presents a "weak" intrinsic magnetic field able to sustain a "small" Earth-like magnetosphere, strongly affected by the interaction with the solar wind. This represents a perfect natural plasma laboratory to study magnetospheric plasma processes with parameters and conditions different from the ones typically observed at Earth. At Mercury, as the solar wind affects the magnetosphere, the magnetosphere in turn affects the inner layers of the planet (exosphere and surface), creating a globally coupled system formed by ionized (solar wind and magnetosphere) and non-ionized (exosphere and surface) parts. Moreover, Mercury remains largely unexplored, with only three missions visiting it in the history of space exploration: NASA Mariner 10 mission in the 1970s (Dunne, 1974), NASA MESSENGER mission in the 2000s (Solomon et al., 2007), and ESA/JAXA BepiColombo mission in the 2020s (ongoing; Benkhoff et al. 2021). As a consequence, the properties of Mercury's environment, and especially of its magnetosphere, remains poorly investigated by in situ observations. A thorough study of the properties of Mercury is extremely important, at the present times, in light of the ongoing exploration efforts by the ESA/JAXA BepiColombo mission. The mission, now in cruise phase, will arrive at Mercury in December 2025 to start its science phase in early 2026.

The results of this work contribute to advance in the general understanding of the interaction between the Sun and the bodies in the Solar System, by applying plasma physics to the study of planetary environments. This broad objective –summarized by the formula "*Space plasma for planetology*"– is tackled more specifically in this work by focusing on the interaction between the solar wind plasma and the planet Mercury. A topic of particular interest for planetology and for the investigation of plasma physics in space. The two main questions addressed in this work are the following:

(Q1) What is the most relevant mechanism for electron acceleration in the magnetosphere of Mercury?

(Q2) What is the role of electrons in the coupling between the solar wind, magnetosphere, exosphere and surface at Mercury?

In the rest of this introduction, I introduce the tasks undertaken in this work to answer these two questions.

The Earth and Mercury are the only telluric planets in the Solar System with an intrinsic, dipole-like magnetic field. These magnetic fields, by deflecting a substantial fraction of the impinging solar wind, generate the magnetospheres of these two planets, as sketched in Fig. 1.1. The magnetosphere envelops the planet in a pear-shaped, anti-sunward-elongated region, where the dynamics is governed by the strong magnetic field of the planet.

Earth's magnetosphere presents various analogies with the one of Mercury, nonetheless, the two systems are also profoundly different for the following reasons:

- Mercury's magnetosphere is internally bounded to the surface and not to the ionosphere, as on Earth. This is due to the lack of a dense, Earth-like atmosphere at Mercury, which only presents an exosphere (R. Killen et al., 2007).

- Mercury's magnetosphere is about 20 times smaller than the one of the Earth. This is due to the weak magnetic field of Mercury (about $0.2\ \mu$T at the surface) as compared to the one of the Earth (about $35\ \mu$T at the surface) (Ness et al., 1974).

- The solar wind at $0.3 - 0.5$ AU[3] (interacting with Mercury) has different plasma parameters as compared to the one at 1 AU (interacting with the Earth). At Mercury, the solar wind has a higher ram pressure, a lower Mach number and a lower Parker spiral angle as compared to the one at the Earth (Milillo et al., 2020, Sect. 2.1 therein).

- Mercury's magnetosphere presents a more important fraction of kinetic-scale plasma dynamics as compared to Earth. This is due to the smaller size of Mercury's magnetosphere that, in turn, results in a higher ratio between proton kinetic scales and the typical scales of the system (Kallio and Janhunen, 2003).

Consequently, Mercury's magnetosphere is not to be considered as a simple scaled-down version of Earth's magnetosphere, but rather both (i) a unique space environment, and (ii) a rich natural laboratory presenting both similarities and profound differences with its terrestrial analog, as shown in Fig. 1.1. A detailed description of Mercury's environment in light of the ongoing exploration by the ESA/JAXA BepiColombo mission is presented in Chap. 3.

By the end of the 1960s, multiple missions by the Soviet space program and by US NASA observed the plasma environment surrounding the Earth, with both plasma and magnetic

---

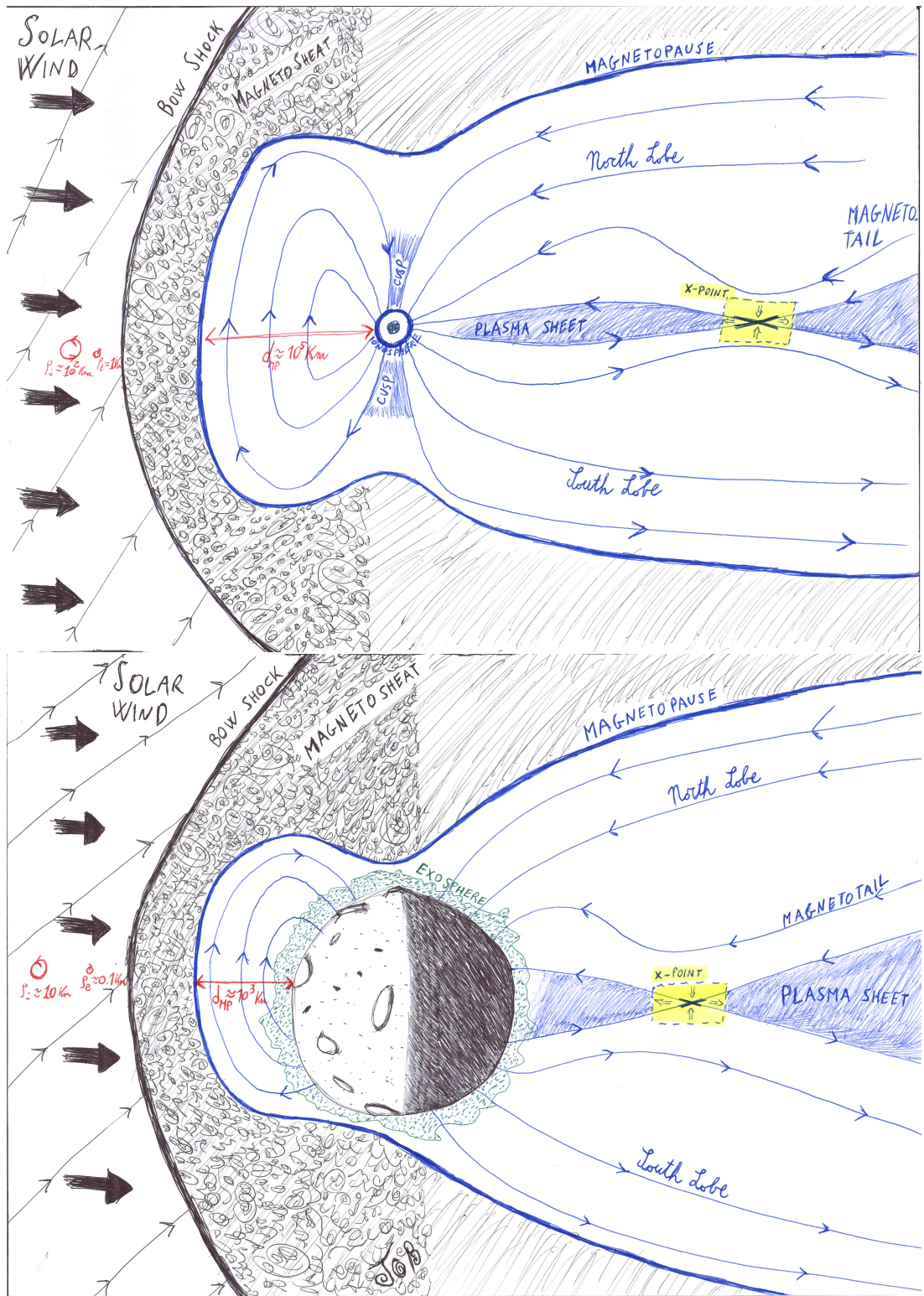[3]Acronyms are specified at the end of this document in Acronyms.

3

Figure 1.1: Sketch (not to scale) of the solar wind interaction with the magnetospheres of the Earth (top panel) and of Mercury (bottom panel).

field instruments (Ness, 1967; Ness, 1970). These observations proved the existence of the solar wind, of the Earth's bow shock and of many of the regions composing Earth's magnetosphere. These first pioneering observations showed that space above our ionosphere (from roughly 500 km altitude) is filled with plasma, and that the dynamics of this environment obeys the rules of plasma physics. Nowadays, space missions observe the plasma dynamics in situ with unprecedented resolution and effectiveness. State-of-the-art exploratory space missions are characterized by (i) multiple spacecraft, (ii) a large number of complementary instruments or experiments (usually more than ten), and (iii) high-resolution scientific instruments able to resolve small temporal and spatial scales. Typically, such missions carry instruments able to resolve the electron kinetic scales (namely the electron gyroradius and gyroperiod, of the order of 1 km and 10 ms in the solar wind at 1 AU). Therefore, in situ observations of the ion and electron kinetic physics in space are now possible. At these small scales, the plasma dynamics deviates from the large-scale fluid behaviour, described by MHD equations, and it is strongly affected by kinetic effects (e.g. non-maxwellian particle distributions and wave-particle interactions). A thorough discussion of plasma models, from kinetic to fluid, can be found in Chap. 2 to better illustrate how I have, first, chosen and, second, made use of such plasma models to identify and quantify the most relevant mechanisms for electron acceleration in the magnetosphere of Mercury.

Recent in situ observations are starting to scratch the surface of the wide variety of kinetic processes at play at electron scales. These observations mostly target the plasma in Earth's magnetosphere. As an example, electron-scale observations by the NASA MMS mission pointed out the fundamental role of electrons in the onset and relaxation of collisionless magnetic reconnection (Burch et al., 2016; Torbert et al., 2018; Cozzani et al., 2021). These studies suggest that electrons play an important role in the global dynamics of the Earth's magnetosphere-ionosphere system. However, to obtain a good understanding of the underlying physics, observations of the same process under different plasma conditions are needed. For this scope, electron-scale observations in different environments, such as Mercury's magnetosphere, are on track. This work aims at contributing to the ongoing exploration of electron-scale plasma processes in space, by using a numerical approach.

Numerical models are a fundamental tool for the analysis and interpretation of in situ plasma observations. Spacecraft in situ observations are intrinsically limited in two ways. First, in situ observations are local. Spacecraft measure the plasma in their vicinity and they are not able to infer the global property of the magnetosphere at the time of the measurement. Second, the plasma moves relative to the spacecraft. For this reason, spacecraft are not able to separate spatial from temporal variations in the detected signal. One utopistic solution is to fill the

system, e.g. the magnetosphere, with a myriad of identical satellites all measuring the state of the magnetosphere at each instant of time at every point[4]! Of course, this is not doable.

To mitigate the limits of in situ observations, numerical plasma models are used in conjunction with observations. Numerical models can be either global or local. This distinction is not related to the type of plasma model used, but only to the size of the system under study. Global models include all the magnetosphere in the computational domain while local models include only a sub-region, such as a subpart of the magnetotail or magnetopause. First, global numerical models are used to disentangle the local properties of the plasma (observed by the spacecraft) from the global state of the system (accessible to global models). Second, global and/or local models are used to disentangle spatial and temporal scales, because in these models the plasma properties are computed point-by-point in space and time. Moreover, numerical models allow more freedom in the choice of the parameters of the "numerical experiment", as compared to situ observations where the parameters of a given "event" cannot be chosen. All in all, numerical plasma models –when coupled to in situ observations– are a powerful tool to understand the complex dynamics of space plasma environments.

Numerical plasma models come in different "sizes" and "shapes". In general, the scientific objectives together with a trade-off between model's accuracy and complexity define the choice of the model. This work focuses on electron kinetic processes in the magnetosphere of Mercury, as a consequence, a kinetic plasma model resolving the electron physics is needed. Given its high computational cost, this model is used both to study local processes with a high resolution (e.g. wave particle interaction) and global processes with a coarse resolution (e.g electron circulation in the magnetosphere). These two types of local and global simulations target complementary objectives, and both are employed in this work. A detailed description of the simulation codes and setup can be found in Chap. 4.

Kinetic simulations have been widely used, since the advent of sufficiently powerful computing machines in the 1970s, to interpret in situ space plasma observations (Cuperman et al., 1973; Hubbard and Joyce, 1979) as well as to study the dynamics of laboratory plasma experiments (Winske and Hewett, 1975; Winske and Liewer, 1978). Over the past decades, kinetic plasma simulations strongly helped to increase our understanding of the plasma processes in Earth's magnetosphere, as well as in many other plasma environments (fusion, laboratory, space and astrophysical plasmas). However, most of the past studies were limited to local simulations, modeling a small region of space embedded into the global system. Just recently, the improvement of computational technologies is enabling to run global kinetic simulations of a given plasma environment. Global kinetic simulations of Earth's magnetosphere remain computationally challenging nowadays, but the magnetosphere of Mercury (roughly 20 times smaller

---

[4]Multi-satellite missions (such as NASA MMS and HelioSwarm missions, with four and nine satellites, respectively) are a first step towards such a solution. Nevertheless, a satisfactory global coverage of the whole magnetosphere remains impossible in the foreseeable future.

than the one of the Earth) is now attainable using global kinetic models: this work demonstrates this statement and shows how much they can bring to our understanding of multi-scale, global magnetospheric physics, as well as planetary space exploration. For this purpose, the main scientific results of this work are summarized in Chap. 5, while ongoing works and future perspective are discussed in conclusive Chap. 6. The peer-reviewed works published during the PhD are reported integrally in Sect. 5.2-5.5 and listed in Appendix C.

The document is organized as follows. The basic concepts of plasma physics theory of interest for this work are presented in Chap. 2. A description of the plasma environment around Mercury and its coupling to the planetary environment is presented in Chap. 3. The numerical models used in this work are described in Chap. 4. The results of this work are presented in Chap. 5. Conclusions and perspectives are discussed in Chap. 6.

2 INTRODUCTION TO PLASMA PHYSICS OF INTEREST FOR SPACE ENVIRONMENTS

This chapter introduces the theoretical concepts of plasma physics useful to interpret the results of this work in a broader plasma physics context. In Sect. 2.1, the basic theoretical concepts of plasma physics (typical scales, plasma models, and energy equations) are introduced. In this first section, I present a brief detour on two-fluid, single-fluid MHD and ion kinetic models (Sect. 2.1.2), as well as reduced quasi-linear models for wave-particle interactions (Sect. 2.1.3). In Sect. 2.2, few important dynamical processes at play in plasmas (instabilities, magnetic reconnection, and adiabatic motion) and few basic concepts of plasma-atoms interaction are introduced. These processes represent the building blocks of the complex interactions driven by space plasmas in Mercury's environment.

2.1 HOW TO MODEL A PLASMA?

Plasma physics is intrinsically nonlinear and multi-scale. Therefore to tackle the inherent complexity of plasma physics, a large set of models is typically used. These models are presented in this section, focusing specifically on those of interest for space plasma environments.

2.1.1 TYPICAL SCALES IN A PLASMA

Plasma physics focuses on the collective behaviour of a globally neutral, large ensemble of charged particles. Collisions between particles are infrequent, and for this reason the thermodynamical state of a plasma is typically far from local thermodynamic equilibrium. In a plasma, and particularly in space plasmas, the temperature T (defined as the mean kinetic energy of the particles) is not an equilibrium quantity but a dynamical quantity. This quantity can be different for ions and electrons.

The dominant force acting on a plasma particle is the electromagnetic force self-consistently generated by the plasma, plus any (possible) external field. To have a plasma, the thermal energy of the charged particles must be much higher than the electric potential energy between them. The ratio between the two energies is called the "plasma parameter" $g = T/e^2 n^{1/3} \gg 1$[1]. The condition $g \gg 1$ also means that a large number of particles must be found inside a sphere of radius λ_D (the Debye length). This is the smallest length scale at which the system can be defined as a plasma. At scales smaller than λ_D, the collective behaviour is lost, and the individual behaviour of the charged particles becomes more and more dominant. A sketch of different plasma physics regimes and applications is shown in Fig. 2.1, where the green box highlights the applications of direct interest for this work (planetary magnetospheres, such as the one of Mercury, and the solar wind, indicated with SW in the figure.
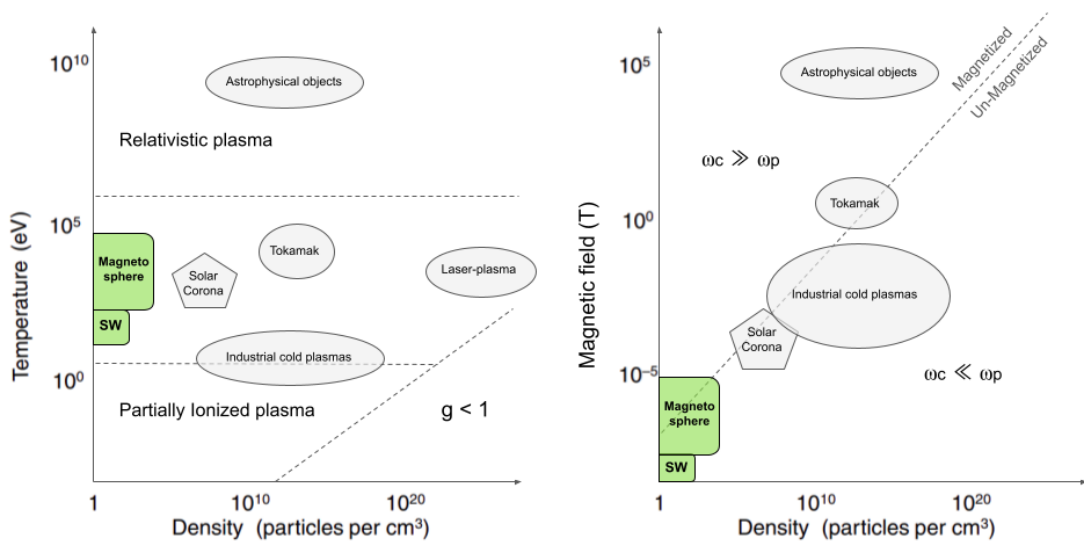
Figure 2.1: Sketch of plasma physics regimes and applications showing both typical temperatures (left panel) and magnetic fields (right panel) as a function of the plasma density. Figure adapted from Council (2007, Fig. 1.2 therein) and Chien et al. (2023, Tab. 1 therein).

In a plasma, small-scale collective oscillations define typical length and time scales for the system. In space, the Debye length λ_D represents the typical distance at which the electric potential of one free charge is screened by the rest of the particles. In time, the plasma frequency $\omega_{p,e}$ represent the typical frequency of oscillations of electrons around the heavier and oppositely charged ions. These are called "plasma" or "Langmuir" waves, and they are typically used to measure the plasma density n in situ by making use the resonance around the plasma fre-

---

[1]Symbols are specified at the end of this document in Glossary.

quency, this type of measure is further discussed in Sect. 5.6.4. In summary, the characteristic electrostatic scales of a plasma are:

$$\lambda_{D,e} = \sqrt{\frac{T_e}{4\pi n e^2}} \quad , \quad \omega_{p,e} = \sqrt{\frac{4\pi n e^2}{m_e}} \tag{2.1}$$

The product of the two is the electron thermal $v_{th,e} = \sqrt{T_e/m_e}$.

Considering the interaction between an electromagnetic light wave and a non-magnetized plasma, the electron skin depth d_e is the typical distance characterizing this interaction:

$$d_e = \frac{c}{\omega_{p,e}} = \sqrt{\frac{m_e c^2}{4\pi n e^2}} \tag{2.2}$$

In the case of a magnetized plasma embedded in an external magnetic field B, the typical spatial and temporal scales are given by the gyroradius and gyrofrequency of electrons (or ions analogously):

$$\varrho_e = \frac{c\sqrt{T_e m_e}}{eB} \quad , \quad \omega_{c,e} = \frac{eB}{m_e c} \tag{2.3}$$

Other typical quantities of interest in a magnetized plasma are the plasma beta (ratio between thermal and magnetic pressures):

$$\beta = \frac{8\pi n T}{B^2} \tag{2.4}$$

The Alfvén and ion sound speeds (characteristic speeds in MHD):

$$V_{A,i} = \frac{B}{\sqrt{4\pi m_i n}} \quad , \quad V_S = \sqrt{\frac{\gamma T_e}{m_i}} \tag{2.5}$$

where γ is the adiabatic index. The plasma-to-cyclotron frequency ratio (parameter of magnetization of the plasma):

$$\frac{\omega_{p,e}}{\omega_{c,e}} = \frac{\sqrt{4\pi n c^2 m_e}}{B} \tag{2.6}$$

The diagonal line in the right panel in Fig. 2.1 corresponds to the threshold $\omega_{p,e} = \omega_{c,e}$, the boundary between "magnetized" and "non-magnetized" plasma regimes.

A plasma is a complex, multi-scale system characterized by the nonlinear transfer of energy across scales. Given the huge range of scales covered in a plasma (e.g. λ_D is separated from ϱ_i by roughly five orders of magnitude in space plasmas such as the solar wind and the magneto-

sphere of Mercury), a plasma model accounting for all the phenomena at all scales is practically impossible to build. Therefore, two possible strategies are foreseen to reduce the complexity of the problem. The first strategy is to use a reduced model with many assumptions (such as ideal MHD) but able to run with realistic plasma parameters. The second strategy is to use a more complex model with little or no assumptions (such as the kinetic Vlasov-Maxwell equations) but that needs to run with rescaled plasma parameters. This second strategy is the one that is mostly used throughout this work (see Sect. 4.2.2), although the best approach is to use both strategies in a complementary way. Such a complementary approach using multiple models is used in Sect. 5.2 to study wave-particle interactions at the magnetopause of Mercury, and it is also discussed in Chap. 6 for future applications of the global numerical model at the core of this work. In the next section 2.1.2, I introduce the large spectrum of plasma models commonly used to study space plasmas (in order of decreasing complexity, from kinetic Vlasov-Maxwell to ideal MHD). The full analytical derivation of the equations is not reported in this document and it can be found in plasma physics monographs such as the classic Krall and Trivelpiece (1973) or the more recent Belmont et al. (2013).

2.1.2 HIERARCHY OF PLASMA MODELS: FROM KINETIC TO FLUID

The Vlasov-Maxwell (VM) system of equations is the fundamental model for a collisionless plasma:

$$\frac{\partial f_s}{\partial t} + \mathbf{v} \cdot \nabla f_s + \frac{q_s}{m_s}\left(\mathbf{E} + \frac{\mathbf{v} \times \mathbf{B}}{c}\right) \cdot \nabla_v f_s = 0 \qquad s = i, e \tag{2.7}$$

$$\nabla \cdot \mathbf{E} = 4\pi \left[\sum_{s=i,e} q_s \int f_s d^3 v \right] \tag{2.8}$$

$$\nabla \times \mathbf{B} = \frac{4\pi}{c}\left[\sum_{s=i,e} q_s \int f_s \mathbf{v} d^3 v \right] + \frac{1}{c}\frac{\partial \mathbf{E}}{\partial t} \tag{2.9}$$

$$\frac{\partial \mathbf{B}}{\partial t} = -c\nabla \times \mathbf{E} \tag{2.10}$$

where $f_s(\mathbf{x}, \mathbf{v}, t)$ is the distribution function of the particles of species s, with charge q_s and mass m_s[2]. The VM model includes self-consistently the kinetic physics of both ions and electrons. So, this model must be used when kinetic scale fluctuations are involved in the dynamics, i.e. when the plasma is in the so-called *fully-kinetic* regime. In this regime, the gradient scales of the system $\left(\frac{\partial}{\partial t}\right)^{-1}$ and $\left(\frac{\partial}{\partial x}\right)^{-1}$ are of the order or smaller than the kinetic scales of the system $\omega_{c,e}^{-1}$ (or $\omega_{p,e}^{-1}$) in time and ϱ_e (or d_e, $\lambda_{D,e}$) in space.

---

[2] Albeit not explicitly reported in this section, the condition $\nabla \cdot \mathbf{B} = 0$ must be always verified as well.

The VM model in Eqs. (2.7)-(2.10) is a system of nonlinear coupled integro-differential equations, a complicated beast to solve from a mathematical and numerical point of view. Due to the difficulties in solving the VM model, it is common to derive reduced fluid models by taking the moments of the Vlasov equation (2.7) in velocity space. A self-consistent solution of the VM model can be obtained, a priori, by considering the infinite chain of coupled equations for the moments (n_s, $\mathbf{u}_s$, $\mathbf{P}_s$, ...). In practice, such an infinite chain is of no use. One must cut the chain of equations at some level using a closure equation. Considering a generic closure Φ_s on the second-order moment $\mathbf{P}_s$, the reduced system of equations reads:

$$\frac{\partial n_s}{\partial t} + (\mathbf{u}_s \cdot \nabla)n_s = -n_s(\nabla \cdot \mathbf{u}_s) \qquad\qquad s = i, e \qquad (2.11)$$

$$\frac{\partial \mathbf{u}_s}{\partial t} + (\mathbf{u}_s \cdot \nabla)\mathbf{u}_s = -\frac{1}{m_s}\nabla \cdot \mathbf{P}_s + \frac{q_s}{m_s}\left(\mathbf{E} + \frac{\mathbf{u}_s \times \mathbf{B}}{c}\right) \qquad (2.12)$$

$$\Phi_s(n_s, \mathbf{u}_s, \mathbf{P}_s) = 0 \qquad (2.13)$$

$$\nabla \cdot \mathbf{E} = 4\pi \left[\sum_{s=i,e} q_s n_s\right] \qquad (2.14)$$

$$\nabla \times \mathbf{B} = \frac{4\pi}{c}\left[\sum_{s=i,e} q_s n_s \mathbf{u}_s\right] + \frac{1}{c}\frac{\partial \mathbf{E}}{\partial t} \qquad (2.15)$$

plus Faraday's law (2.10). The zero-th, first, and second order central moments of the distribution function f_s correspond to the density n_s, momentum flux $n_s\mathbf{u}_s$, and pressure tensor $\mathbf{P}_s$[3]. The model in Eqs. (2.11)-(2.15) is the two-fluid or multi-fluid model.

The choice of the closure Φ_s in Eq. (2.13) is of paramount importance to well-represent the plasma dynamics in reduced fluid models. Many closures have been proposed in the past, such as the double-adiabatic Chew-Goldberger-Low (CGL) closure (Chew et al., 1956; Chust and Belmont, 2006) accounting for anisotropic effects induced by the presence of a magnetic field, or the Landau-fluid closure (Hammett and Perkins, 1990; Sulem and Passot, 2008) including kinetic effects in a multi-fluid model. Each one of these closures is suitable to reproduce a given class of plasma process but less suitable to reproduce others. A detailed discussion on the closure equation remains, however, out of the scope of this work. All in all, two-fluid models leverage a lower complexity as compared to VM model, with the need for *ad hoc* approximations in the form of a closure equation (Eq. 2.13). Two-fluid models can be used to study effectively large scale systems, such the magnetosphere of Mercury (Dong et al., 2019), while neglecting the ion and electron kinetic processes. To account for electron kinetic processes such as wave-particle interaction, VM fully-kinetic models must be used, as done in this work.

---

[3]Definitions of the moments are given in Glossary.

From the two-fluid model (2.11)-(2.15), one can derive the single-fluid MHD model using three main assumptions. First, the plasma is locally neutral, $n = n_i = n_e$. Second, the characteristic velocity at fluid scales is much lower than the light speed, $\ell/\tau \ll c$, where the characteristic fluid length and time scales are the gradient scale lengths $\ell^{-1} = \frac{\partial}{\partial x}$ and $\tau^{-1} = \frac{\partial}{\partial t}$. This means that sharp boundaries and fast time variations, such as the growth of a kinetic plasma instability, are neglected in MHD models. Third, zero electron mass limit, $m_e/m_i \to 0$. Using these assumptions, the single-fluid mass density ρ, charge density ρ_c, mean velocity $\mathbf{u}$, and current density $\mathbf{J}$ are as follows:

$$\rho = \sum_s n_s m_s \approx n(m_i + m_e) \qquad \rho_c = \sum_s n_s q_s \approx 0 \qquad (2.16)$$

$$\mathbf{u} = \frac{\sum_s n_s m_s \mathbf{u}_s}{\sum_s n_s m_s} \approx \mathbf{u}_i + \frac{m_e}{m_i}\mathbf{u}_e \qquad \mathbf{J} = \sum_s n_s q_s \mathbf{u}_s \approx en(\mathbf{u}_i - \mathbf{u}_e) \qquad (2.17)$$

Using these definitions (2.16)-(2.17) in the multi-fluid model (2.11)-(2.15), one obtains the following single-fluid MHD equations:

$$\frac{\partial n}{\partial t} + (\mathbf{u} \cdot \nabla)n = -n(\nabla \cdot \mathbf{u}) \qquad (2.18)$$

$$m_i n \left[\frac{\partial \mathbf{u}}{\partial t} + (\mathbf{u} \cdot \nabla)\mathbf{u} \right] = -\nabla \cdot (\mathbf{P}_i + \mathbf{P}_e) + \frac{(\nabla \times \mathbf{B}) \times \mathbf{B}}{4\pi} \qquad (2.19)$$

$$\frac{\partial \mathbf{B}}{\partial t} = -c\nabla \times \mathbf{E} \quad \text{where} \quad \mathbf{E} + \frac{\mathbf{u} \times \mathbf{B}}{c} = \left[\frac{(\nabla \times \mathbf{B}) \times \mathbf{B}}{4\pi en} \right] - \left[\frac{(\nabla \cdot \mathbf{P}_e)}{en} \right] \qquad (2.20)$$

$$\Phi_s(n, \mathbf{u}, \mathbf{B}, \mathbf{P}_s) = 0 \qquad s = i, e \qquad (2.21)$$

In the MHD model (2.18)-(2.21) the electric field is computed explicitly from the so-called Ohm's law (2.20) and not from the Poisson equation (2.14), as in multi-fluid models. This greatly simplifies the system of equations. The generalized Ohm's law in Eq. (2.20) includes two "non-ideal" terms in the RHS of the equation: the so-called "Hall" and "electron pressure" terms[4] (Vasyliunas, 1975). The two terms in the RHS of Eq. (2.20) have an important role in MHD since they can demagnetize the ions (Hall term) and break the magnetic topology (electron pressure term) when considering the plasma dynamics at small spatial scales. This is particularly relevant for magnetic reconnection, a fundamental plasma processes discussed in Sect. 2.2.2.

In the limit of ideal MHD, the terms in the RHS of Ohm's law (2.20) are neglected. Moreover, using vectorial identities[5], one obtains the ideal MHD equations as follows:

---

[4]The Eq. (2.20) does not include the collisional, and electron inertia terms because we consider a collisionless plasma in the strict limit $m_e/m_i \to 0$.

[5]$(\nabla \times \mathbf{B}) \times \mathbf{B} = (\mathbf{B} \cdot \nabla)\mathbf{B} - (\nabla\mathbf{B}) \cdot \mathbf{B} = (\mathbf{B} \cdot \nabla)\mathbf{B} - \frac{1}{2}\nabla(\mathbf{B}^2)$

$$\frac{\partial n}{\partial t} + (\mathbf{u} \cdot \nabla)n = -n(\nabla \cdot \mathbf{u}) \tag{2.22}$$

$$m_i n \left[\frac{\partial \mathbf{u}}{\partial t} + (\mathbf{u} \cdot \nabla)\mathbf{u} \right] = -\nabla \cdot \left(\mathbf{P}_i + \mathbf{P}_e + \frac{\mathbf{B}^2}{8\pi} \right) + \frac{(\mathbf{B} \cdot \nabla)\mathbf{B}}{4\pi} \tag{2.23}$$

$$\frac{\partial \mathbf{B}}{\partial t} = -c\nabla \times \mathbf{E} \quad \text{where} \quad \mathbf{E} = -(\mathbf{u} \times \mathbf{B}) \tag{2.24}$$

$$\Phi_s(n, \mathbf{u}, \mathbf{B}, \mathbf{P}_s) = 0 \qquad s = i, e \tag{2.25}$$

This is the simplest and most approximated plasma model, valid only at large, fluid scales. Numerical simulations of Mercury's magnetosphere using MHD models have been extensively performed in the past (e.g., Gombosi et al. 2000; Yagi et al. 2010) to study the large-scale structure of the magnetosphere (magnetopause position, bow shock etc.). However, given the relatively small size of Mercury's magnetosphere, subsequent works showed that ion kinetic processes (not inluded in MHD models) play an important role at Mercury (e.g., Trávníček et al. 2010; Herčík et al. 2013; Herčík et al. 2016). Ion kinetic processes are commonly studied using an hybrid approach that treats ions kinetically and electrons as a massless, charge-neutralizing fluid. This approach leads to the so-called hybrid ion-kinetic model, of interest to study ion kinetic processes while neglecting the electron kinetic physics.

The hybrid ion-kinetic model is given by the following equations:

$$\frac{\partial f_i}{\partial t} + \mathbf{v} \cdot \nabla f_i + \frac{e}{m_i} \left(\mathbf{E} + \frac{\mathbf{v} \times \mathbf{B}}{c} \right) \cdot \nabla_v f_i = 0 \tag{2.26}$$

$$\mathbf{u}_e = \frac{\mathbf{u}_i}{n} - \frac{4\pi}{c} \frac{\nabla \times \mathbf{B}}{ne} \tag{2.27}$$

$$\frac{\partial \mathbf{B}}{\partial t} = -c\nabla \times \mathbf{E} \quad \text{where} \quad \mathbf{E} + \frac{\mathbf{u}_i \times \mathbf{B}}{c} = \left[\frac{(\nabla \times \mathbf{B}) \times \mathbf{B}}{4\pi en} \right] - \left[\frac{(\nabla \cdot \mathbf{P}_e)}{en} \right] \tag{2.28}$$

$$\Phi_e(n, \mathbf{u}_e, \mathbf{P}_e) = 0 \tag{2.29}$$

In this model, the Vlasov equation for the ions (Eq. 2.26) is coupled to the approximated Ampère's law (Eq. 2.27), to the generalized Ohm's law (Eq. 2.28), and to the closure equation for the electron fluid (Eq. 2.29). This model is designed to study the plasma dynamics from large fluid scales down to ion kinetic scales, without including the small-scale electron kinetic physics.

This picture of the plasma dynamics as composed of three different, well-separated regimes can, however, be misleading. Indeed, there is no *neat* separation between fully-kinetic, ion-kinetic and fluid regimes in plasmas because these regimes are coupled by the nonlinear plasma dynamics. Plasma dynamics is typically fed by energy injection at large scales. This energy then

non-linearly transfers to smaller and smaller scales, reducing the initially-prescribed gradient scales of the system $\left(\frac{\partial}{\partial t}\right)^{-1}$ and $\left(\frac{\partial}{\partial x}\right)^{-1}$. Eventually, the plasma dynamics falls in the fully-kinetic regime. For this reason, kinetic plasma processes around and below the electron kinetic scale naturally occur in plasmas. At the same time, small-scale plasma processes are known to have an important feedback on the large-scale dynamics. This loop of energy transfer from large to small scale and viceversa is of great relevance for the results of this work. In particular, in Sect. 5.1 I discuss how this loop of energy transfer affects Mercury's environment.

Now that the hierarchy of most common plasma models is introduced, I present a reduced model derived from the VM model to address wave-particle interactions specifically. This reduced model is used in this work to study the interaction between lower-hybrid waves and electrons in the direction parallel to the local magnetic field at the magnetopause of Mercury. The results of this study are presented in Sect. 5.2.

2.1.3 Quasilinear models for wave-particle interaction

A common approximation of the VM system of equations suitable to study wave-particle interactions is the so-called quasilinear (QL hereafter) approximation. The QL model is an extension of the linearized VM model. Considering a perturbative expansion of the distribution function $f_s = f_{0,s} + f_{1,s} + \dots$ with $f_{0,s} \gg f_{1,s} \gg \dots$, if only the first order approximation f_1 is retained, one obtains the *linear* plasma response, i.e. the spectrum of waves that exists in a plasma, without describing any feedback on the distribution function itself. Instead, if the feedback of the linear perturbation $f_{1,s}$ on the equilibrium function $f_{0,s}$ on long time scales is retained, one obtains the *quasilinear* plasma response. By doing so, the QL model conserves the description of the feedback of the waves onto the distribution functions. Below, I present a quick derivation of the QL model for a one-dimensional, electrostatic, non-magnetized plasma, adapted from Alexandrov et al. (1984, Chap. 11 therein).

Considering the VM model (2.7)-(2.10) in 1D-1V, without magnetic field, one obtains the following system of equations:

$$\frac{\partial f_s}{\partial t} + v\frac{\partial f_s}{\partial x} + \frac{q_s}{m_s}E\frac{\partial f_s}{\partial v} = 0 \tag{2.30}$$

$$\frac{\partial E}{\partial t} + 4\pi \sum_s q_s \int v f_s(v)dv = 0 \tag{2.31}$$

Then using a perturbative expansion, one splits Eq. (2.30) into two equations, a first one evolving on a slow time scale (Eq. 2.32) and a second one evolving on a fast time scale (Eq. 2.33).

$$\frac{\partial f_{0,s}}{\partial \mu t} + \frac{q_s}{m_s}\left\langle E_1 \frac{\partial f_{1,s}}{\partial v} \right\rangle = 0 \tag{2.32}$$

$$\frac{\partial f_{1,s}}{\partial t} + v\frac{\partial f_{1,s}}{\partial x} + \frac{q_s}{m_s}E_1\frac{\partial f_{0,s}}{\partial v} = 0 \tag{2.33}$$

where $\mu \ll 1$, and $\langle ... \rangle$ is an operator of time average over a time interval much larger than the wave period. The zero-order electric field is assumed to be null $E_0 = 0$. By expressing the first-order quantities in Fourier space, one readily obtains the solution of Eq. (2.33) as follows:

$$f_{1,s,k} = -i\frac{q_s}{m_s}\frac{E_{1,k}}{(\omega - kv)}\frac{\partial f_{0,s}}{\partial v} \tag{2.34}$$

and, substituting this solution into Eq. (2.32), one obtains the following diffusion equations for f_0 in velocity space:

$$\frac{\partial f_{0,s}}{\partial t} = \frac{\partial}{\partial v}D_s\frac{\partial f_{0,s}}{\partial v} \tag{2.35}$$

$$D_s = \frac{\pi q_s^2}{m_s^2}\int S_k\delta(\omega - kv)dk \tag{2.36}$$

where, the electric field energy $S_k = E_{1,k}^2/8\pi$ is used. The evolution equation for S_k is obtained self-consistently in the QL model using Eq. (2.31) as follows:

$$\frac{\partial S_k}{\partial t} = \gamma_k S_k \tag{2.37}$$

$$\gamma_k = \sum_s \frac{4\pi^2 q_s^2\omega}{k^2}\partial_v f_{0,s}(v = \omega/k, t) \tag{2.38}$$

The equations (2.35)-(2.38) define the quasilinear model for wave-particle interaction in a simplified 1D geometry without magnetic field. From these equations, the QL model for the interaction between lower-hybrid-drift waves and electrons is derived (see Sect. 5.2).

The main advantage of a QL model is its relative simplicity, as compared to a fully-kinetic model. Indeed, a QL model is able to reproduce, using few assumptions, the basic kinetic physics of wave-particle interactions in a plasma. The QL model is typically solved numerically with the aid of a simple numerical integrator (such as a Runge-Kutta integrator). On the one hand, the solution of a QL model with realistic plasma parameters is typically achieved in few minutes on a standard laptop machine. On the other hand, fully-kinetic ab initio models require large machines with thousands of cores to run a simulation using rescaled plasma

parameters. The simplicity of the QL model is counterbalanced by its limits. A QL model is intrinsically limited by its perturbative approach; when the first-order perturbation f_1 becomes larger than the zero-order distribution function f_0, the ordering used to derive the QL model breaks down. At this point, the solution of the QL model is no longer valid and more advanced models able to describe strong non-linearities must be used. This is exactly the goal of my first work, presented in Sect. 5.2, to build an extended QL model that overcomes the limits of standard QL theory.

The QL model enables to describe the energy exchange between the electromagnetic and the thermal energies stored in a plasma, in the specific case of quasilinear wave-particle interactions. A more general approach to describe the evolution of the energy of a plasma is discussed in the next section 2.1.4. This energy is divided into different forms (thermal, kinetic, and electromagnetic) all playing a key role in the energy transfer across scales typical of the nonlinear plasma dynamics.

2.1.4 The different forms of energy in a plasma

Space plasmas are typically far from local thermodynamics equilibrium. Nonetheless, in analogy to thermodynamics, we can define the internal and kinetic energy of a plasma as follows:

$$U_s = \mathbf{P}_s \cdot \mathbf{I}/2 \quad , \quad K_s = \frac{1}{2}n_s m_s |\mathbf{u}_s|^2 \tag{2.39}$$

where $\mathbf{I}$ is the unitary tensor, and $|...|$ indicates the magnitude of a vector. The internal energy U_s is a measure of the energy stored in the random thermal motion of the particles, while the kinetic energy K_s is a measure of the energy stored in the ordered motion of the plasma.

The evolution equations for these two energies U_s, K_s are obtained from the equation of motion for a fluid element (Eq. 2.12) and from the evolution equation for the pressure tensor (second-order moment of Vlasov equation, see, e.g. Yang et al. 2017). Similarly to what was done in Yang et al. (2017) and Fadanelli et al. (2021), one obtains:

$$\frac{\partial U_s}{\partial t} + \nabla \cdot (U_s \mathbf{u}_s) = -\mathbf{P}_s \cdot (\nabla \mathbf{u}_s) - \frac{1}{2}\nabla \cdot (\mathbf{Q}_s \cdot \mathbf{I}) \tag{2.40}$$

$$\frac{\partial K_s}{\partial t} + \nabla \cdot (K_s \mathbf{u}_s) = -\mathbf{u}_s \cdot \nabla \cdot \mathbf{P}_s + q_s n_s \mathbf{u}_s \cdot \mathbf{E} \tag{2.41}$$

where $\mathbf{Q}_s$ is the heat flux tensor (third-order moment of the distribution function, see Glossary).

The evolution equation for the total energy of the particles $\mathcal{U}_s = U_s + K_s$ is obtained by summing together the two equations above (2.40)-(2.41), therefore one obtains:

$$\frac{\partial \mathcal{U}_s}{\partial t} + \nabla \cdot \left(\mathcal{U}_s \mathbf{u}_s + \mathbf{u}_s \cdot \mathbf{P}_s + \frac{\mathbf{Q}_s \cdot \mathbf{I}}{2} \right) = q_s n_s \mathbf{u}_s \cdot \mathbf{E} \qquad (2.42)$$

The divergence terms on the LHS of Eq. (2.42) operates a redistribution in space of the available particle energy $\mathcal{U}_s$. On the contrary, the power density $q_s n_s \mathbf{u}_s \cdot \mathbf{E} = \mathbf{J}_s \cdot \mathbf{E}$ on the RHS of Eq. (2.42) modifies the total amount of particle energy $\mathcal{U}_s$. This term $\mathbf{J}_s \cdot \mathbf{E}$ accounts for all the forms of particle acceleration (increase of K_s) and heating (increase of U_s) in a collisionless plasma.

The other reservoir of energy in a plasma is the electromagnetic field. From Maxwell equations, one derives the evolution equation for the electromagnetic energy $W = \frac{1}{8\pi}(|\mathbf{E}|^2 + |\mathbf{B}|^2)$, as follows:

$$\frac{\partial W}{\partial t} + \frac{c}{4\pi} \nabla \cdot (\mathbf{E} \times \mathbf{B}) = -\mathbf{J} \cdot \mathbf{E} \qquad (2.43)$$

The source term on the RHS of this equation is equal in magnitude and opposite to the one in Eq. (2.42) summed over the species index $_s$. This ensures that the total energy in a plasma is conserved. A net increase in the particle energy $\sum_s \mathcal{U}_s$ is equal to a net decrease in the electromagnetic energy W.

Continuous energy exchanges between particles (characterized by U_s) and fields (characterized by W) and viceversa, are at the origin of most of the plasma dynamics in planetary magnetospheres. In particular, plasma instabilities (presented in Sect. 2.2.1) and magnetic reconnection (presented in Sect. 2.2.2) are examples of such an energy conversion. Magnetic reconnection, at play at the nose and in the tail of the magnetosphere, drives the global plasma convection pattern called the Dungey cycle (Dungey, 1961). This is one of the most important process of magnetospheric physics, and it derives directly from the energy conversion terms in the RHS of Eqs. (2.42)-(2.43).

2.2 THE BUILDING BLOCKS OF PLASMA DYNAMICS

In this section, I introduce fundamental plasma phenomena useful to interpret the results of the simulations at the core of this work. First, I introduce the theory of plasma instabilities driven by a relative ion-electron drift (Sect. 2.2.1), focusing on the lower-hybrid-drift instability. Second, I introduce the main properties of collisionless magnetic reconnection (Sect. 2.2.2), a fundamental plasma physics process with application from nuclear fusion to space and astrophysical plasmas. Third, I introduce the theory of adiabatic particle motion in

an inhomogeneous magnetic field (Sect. 2.2.3), such as the dipolar magnetic field of Mercury. Fourth, I introduce the basic concepts of plasma-atoms interaction (Sect. 2.2.4) of interest to study plasma-exosphere and plasma-surface interactions at Mercury.

2.2.1 Plasma instabilities: unstable ion-electron drifts

An unstable plasma configuration is characterized by eigenfrequencies with a positive imaginary part $\Im\{\omega\} = \gamma > 0$. As a consequence, the unstable plasma eigenmodes grow according to:

$$f(x,t) \sim \cos(kx)\cos(\omega_r t)e^{\gamma t} \tag{2.44}$$

where $\omega(k) = \omega_r + i\gamma$ is the dispersion relation of the plasma. It expresses the eigenfrequencies ω as a function of the wavevector k. Unstable modes have an important role in plasma physics because they tend to re-arrange the plasma from an initially unstable configuration to a different more stable and isotropic one, thus modifying the large-scale plasma configuration. Therefore, plasma instabilities are one main driver of mass, momentum and energy transport in a collisionless plasma, leveraging –in a way– the absence of collisional transport. Plasma instabilities are one important source of transport across the magnetopause of planetary magnetospheres, enabling the "anomalous" diffusion of solar wind particles inside the magnetosphere. In the rest of this section, I focus on a precise class of plasma instabilities, those driven by a relative ion-electron drift.

In multi-fluid or fully-kinetic models, an ion-electron drift corresponds to a current and to a peculiar, non-symmetric shape of the distribution functions f_i and f_e (or to their moments). For instance, two plasmas with the same current may be described by two substantially different distribution functions, and therefore drive different instabilities. Such a difference cannot be captured using single-fluid models, but only using multi-fluid or fully-kinetic ones. Fully-kinetic models, such as the ones used in this work, present a broad zoology of drift-driven instabilities Gary (1993, Chap. 4 therein). Drift-driven instabilities such as the universal, the ion cyclotron, the temperature gradient, the drift-kink, and the lower-hybrid-drift instabilities are of great importance for both laboratory and space plasma applications[6] (Gary, 1993). In particular, the lower-hybrid-drift instability (hereafter LHDI) is one major driver of anomalous transport and heating both in space and laboratory plasmas (Carter et al., 2002).

---

[6]Here, we differentiate drift-driven from beam-driven instabilities. The former are the main topic of this section, while the latter, such as the two-stream or the bump-on-tail instabilities, are out of the scope of this work.

The LHDI is an electrostatic instability driven by the diamagnetic drift:

$$\mathbf{u}_{D,s} = -\frac{c}{q_s B^2} \frac{\nabla \cdot \mathbf{P}_s}{n_s} \times \mathbf{B} \tag{2.45}$$

Assuming that the magnetic field is directed along the z-axis, the gradient along the x-axis, and that the plasma is isothermal with a diagonal and isotropic pressure tensor $\mathbf{P}_s = nT_s \mathbf{I}$ with equal ion and electron temperatures $T_i = T_e$, then, the diamagnetic drift for ions and electrons reads:

$$\mathbf{u}_{D,i} = -\mathbf{u}_{D,e} = v_{th,i} \left(\frac{\nabla n}{n} \varrho_i \right) \hat{\mathbf{y}} = v_{th,i} (\epsilon_n \varrho_i) \hat{\mathbf{y}} \tag{2.46}$$

where we have introduced the inverse density gradient scale ϵ_n. Typically, to drive unstable the LHDI, the gradient scale must be of the order of the ion gyroradius $\epsilon_n \varrho_i \approx 1$, or analogously, the drift speed must be of the order of the ion thermal speed $u_{D,e}/v_{th,i} \approx 1$. In this case, the LHDI is driven unstable in the range of frequencies where ions are demagnetized ($\omega_r > \omega_{c,i}$) and electrons are magnetized ($\omega_r < \omega_{c,e}$). In this frequency range, and considering purely perpendicular propagation $\mathbf{k} = k\hat{\mathbf{y}}$, the LHDI dispersion relation reads (Krall and Liewer, 1971; Graham et al., 2017; André et al., 2017):

$$\varepsilon(\omega, k) = 1 - k^2 \left(\frac{1}{\omega^2} - \frac{\omega_{c,e}^2}{\omega_{p,e}^2} \right) - e^{-k^2} I_0(k^2) \left(1 + u_{D,e} \frac{k}{\omega} \right) = 0 \tag{2.47}$$

where I_0 is the modified Bessel function of the first kind, and all quantities are normalized using the electron gyroradius ϱ_e, the lower-hybrid frequency $\omega_{LH} = \sqrt{\omega_{c,i}\omega_{c,e}}$, and the ion thermal speed $v_{th,i} = \sqrt{T_i/m_i}$. In the limit of slow growth rate $\gamma \ll \omega_r$, one can solve the dielectric function in Eq. (2.47) as follows (Huba et al., 1978):

$$\omega_r(k) = \left[\frac{e^{-k^2} I_0(k^2)}{2 - e^{-k^2} I_0(k^2)} \right] k u_{D,e} \tag{2.48}$$

$$\gamma(k) = \sqrt{\frac{\pi}{2}} \left[\frac{e^{-k^2} I_0(k^2)}{(2 - e^{-k^2} I_0(k^2))^2} \right] (\omega_r u_{D,e} + k u_{D,e}^2) \tag{2.49}$$

The dispersion relation for the LHDI derived from the Eqs. (2.48)-(2.49) is shown in Fig. 2.2 for various values of the drift speed $u_{D,e}/v_{th,i}$. Here, the important message is that the fastest growing mode of the LHDI is always found at $k\varrho_e \approx 1/2$ with real frequency $\omega \approx (\epsilon_n \varrho_i)\omega_{LH}$ and growth rate $\gamma \approx (\epsilon_n \varrho_i)^2 \omega_{LH}$ (Huba et al., 1978). Moreover, the LHDI is unstable in a narrow cone centered around $k_z = 0$ with the following limit angle (Gary and Sanderson, 1978):

$$\tan \theta = \frac{k_z}{k_y} \lesssim \sqrt{\frac{m_e}{m_i}} (\epsilon_n \varrho_i) \tag{2.50}$$
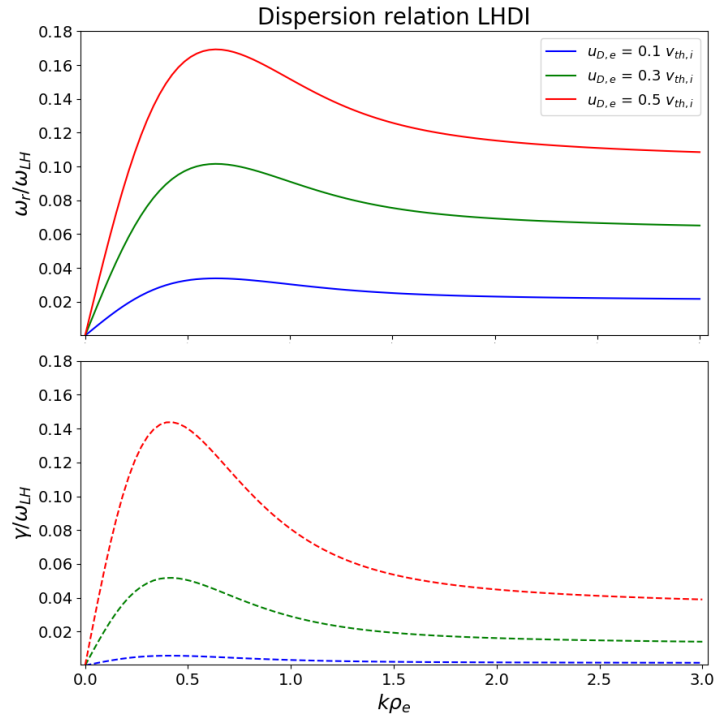
Figure 2.2: Dispersion relation LHDI for different drift speed values, showing the real frequency in Eq. (2.48) (top panel) and the growth rate in Eq. (2.49) (bottom panel). Note that the fastest growing mode is always around $k\varrho_e \approx 0.5$.

On top of the LHDI, other type of instabilities can be driven in inhomogeneous plasmas with an analogous mechanism: the free energy stored in the current "pumps" electromagnetic oscillations. For instance, at the boundary between two plasmas with anti-parallel magnetic fields a fundamental instability exists, that disrupts the magnetic field configuration by "reconnecting" the anti-parallel magnetic field lines in proximity of the boundary. This process is called magnetic reconnection and it is the topic of the following section 2.2.2.

2.2.2 COLLISIONLESS MAGNETIC RECONNECTION

Magnetic reconnection (MR) is a fundamental plasma process that enables oppositely directed magnetic field lines to reconnect. In its simplest 2D configuration, MR is driven at

the interface between two slabs of oppositely directed magnetic fields[7]. In this case, the "reconnecting" magnetic field in the slabs, and the corresponding current can be written as:

$$\mathbf{B}_r = B_r(z)\hat{\mathbf{x}} \tag{2.51}$$

$$\mathbf{J} = \frac{c}{4\pi} \nabla \times \mathbf{B}_r = \frac{c}{4\pi} \frac{B_r}{L} \hat{\mathbf{y}} \tag{2.52}$$

where L is the characteristic scale length of the varying magnetic field between the two slabs. This typical configuration for MR is sketched in Fig. 2.3.
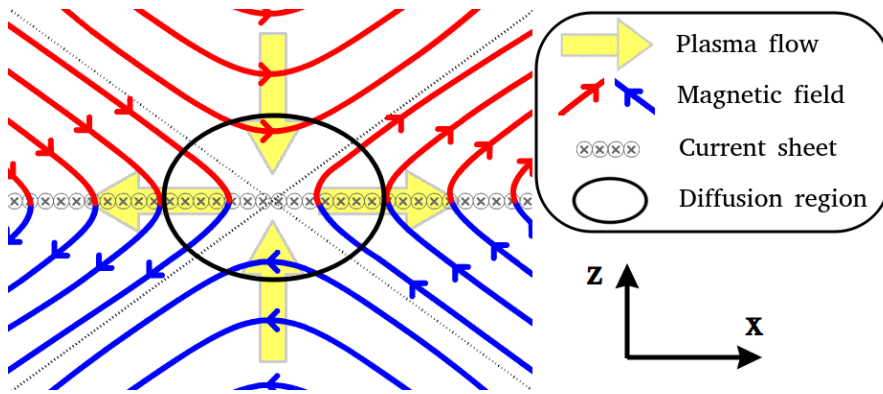

Figure 2.3: Sketch of 2D magnetic reconnection. Figure taken from Finelli (2022, Fig. 2.1 therein).

MR is characterized by the amount of magnetic flux advected-into or escaping from the reconnection site. This flux is commonly termed "reconnection rate" $\mathcal{R}$. According to Faraday's law, the rate $\mathcal{R}$ is proportional to the out of plane electric field E_y found in the region of reconnecting field lines. In normalized units, the reconnection rate is:

$$\mathcal{R} = \frac{E_y}{B_r} \frac{c}{V_{A,r}} \tag{2.53}$$

In many natural space plasmas, as well as in laboratory plasmas, the rate $\mathcal{R}$ is found to be of the order of 0.1 (Cassak et al., 2017). This means that in a broad variety of plasma physics context, MR evolves in a way such that the out of plane electric field E_y balances the reconnecting field and Alfvén speed $B_r V_{A,r}$. The electric field E_y is one main actor in MR since it induces the perturbations of $\mathbf{B}$ (see Faraday's law 2.10) that enable magnetic field lines to reconnect. This "reconnection" happens in the so-called "diffusion region", shown in Fig. 2.3, defined as the region where non-ideal terms in Ohm's law (2.20) become important. Outside the diffusion region, the plasma is frozen-in the magnetic field lines because the ideal Ohm's law (2.24) is

---

[7]More complicated effects such as 3D magnetic reconnection, asymmetric reconnection, and guide field reconnection are not addressed in this section.

fulfilled. The ratio between non-ideal and ideal terms in Ohm's law suggests the typical scale of the diffusion region:

$$\frac{\text{Hall term}}{\text{Ideal}} = \frac{\frac{1}{4\pi e n}(\nabla \times \mathbf{B} \times \mathbf{B})}{\frac{1}{c}(\mathbf{u} \times \mathbf{B})} \sim \frac{V_{A,i}}{u} \frac{d_i}{(\partial_x)^{-1}} \sim \frac{1}{M_{A,i}} \frac{d_i}{(\partial_x)^{-1}} \tag{2.54}$$

$$\frac{\text{Pressure grad.}}{\text{Ideal}} = \frac{\frac{1}{e n}\nabla \cdot \mathbf{P}_e}{\frac{1}{c}(\mathbf{u} \times \mathbf{B})} \sim \frac{v_{th,e}}{u} \frac{\varrho_e}{(\partial_x)^{-1}} \sim \frac{1}{M_{th,e}} \frac{\varrho_e}{(\partial_x)^{-1}} \tag{2.55}$$

where $M_{A,i} = u/V_{A,i}$ is the Alfvén Mach number typically of order one, and $M_{th,e} = u/v_{th,e}$ the electron thermal Mach number typically much smaller than one. The Hall term becomes important at scales of the order of the ion skin depth d_i, while the pressure term becomes important at scales larger than ϱ_e that might be comparable to ion kinetic scales. The Hall term decouples the motion of the ions from the one of electrons in the ion diffusion region (IDR), defined as $d_e \lesssim (\partial_x)^{-1} \lesssim d_i \sim \varrho_i$. In the IDR the ions are demagnetized while the electron are still magnetized. The pressure term becomes important in the electron diffusion region (EDR), found at scales $(\partial_x)^{-1} \lesssim d_e \sim \varrho_e$. In this region, both ions and electrons are demagnetized.

MR converts the energy stored in the electromagnetic fields into particle energy (from W into $\mathcal{U}_s$, as discussed in Sect. 2.1.4). From the energy equations (2.42)-(2.43), the transfer of energy between fields and particles is operated by the term $\mathbf{J} \cdot \mathbf{E}$. Using the current density in Eq. (2.52) and the reconnection rate in Eq. (2.53) one can find that:

$$\mathbf{J} \cdot \mathbf{E} = 4\left(\frac{B_r^2}{8\pi}\right)\left(\frac{V_{A,r}}{L}\right)\mathcal{R} \tag{2.56}$$

So, the energy conversion term $\mathbf{J} \cdot \mathbf{E}$ is proportional to the reconnection rate $\mathcal{R}$ (typically of the order of 0.1), to the upstream magnetic field energy $B_r^2/8\pi$, and to the timescale $V_{A,r}/L$ corresponding to the Alfvén time scale (the typical fluid scale of the system). This dependence of the energy conversion term $\mathbf{J} \cdot \mathbf{E}$ on the plasma parameters is key to interpret the energy of the MR outflow in the global magnetosphere simulations at the core of this work (see, for instance, Sect. 5.3).

To conclude, MR plays a major role in planetary magnetospheres (such as the one of Mercury and of the Earth) by shaping the particles trajectories and by increasing their energy. The fully-kinetic global model developed in this work is built to study self-consistently both MR and the particle motion in the magnetosphere. This unique property of the model comes with a lot of analytical and computational complexity. To interpret the results of such a complex model, the particle motion in the magnetosphere is also studied using a relatively simple, analytical theory called single-particle adiabatic theory. This theory is discussed in the following section 2.2.3.

2.2.3 SINGLE-PARTICLE ADIABATIC MOTION

Consider the motion of a charged particle with charge q, mass m, position $\mathbf{r}$ and velocity $\mathbf{v}$ in a region with uniform magnetic field $\mathbf{B} = B\hat{b}$ and uniform force field $\mathbf{F} = F\hat{f}$. The equation of motion for the particle reads:

$$m\frac{d\mathbf{v}}{dt} = \frac{q}{c}(\mathbf{v} \times \mathbf{B}) + \mathbf{F} \tag{2.57}$$

Introducing the guiding center $\mathbf{r_c} = \mathbf{r} + \varrho$, we decompose the gyromotion of the particle from the motion of the center of gyration, to obtain:

$$\varrho = \frac{mc}{qB^2}(\mathbf{v} \times \mathbf{B}) \quad \text{gyromotion} \tag{2.58}$$

$$\frac{d\mathbf{r_c}}{dt} = \mathbf{u}_\perp \quad \text{motion of the gyrocenter} \tag{2.59}$$

By merging the three equations above together (Eqs. 2.57-2.59), the drift motion of a particle in a generic force field $\mathbf{F}$ is obtained as follows:

$$\mathbf{u}_\perp = \frac{c}{qB^2}\mathbf{F} \times \mathbf{B} \tag{2.60}$$

The force field $\mathbf{F}$ can have different origins, such as a gravitational field $m\mathbf{g}$, an electric field $q\mathbf{E}$, or a fictitious force induced by spatial variations of the magnetic field on scales much larger than the gyroradius and gyroperiod. In the latter case, the motion of the particle is solved in the "adiabatic" approximation. This approximation states that the gyromotion of the particle happens on spatial and temporal scales much smaller than variations in the magnetic field:

$$\varrho \ll \left(\frac{1}{B}\nabla B\right)^{-1} \quad ; \quad \frac{2\pi}{\omega_c} \ll \left(v_\parallel \frac{1}{B}\nabla B\right)^{-1} \tag{2.61}$$

In the rest of this section, I present the adiabatic motions of a particle in three different inhomogeneous magnetic field configurations. These three configurations are of interest to discuss the motion of particles in planetary magnetospheres, as sketched in Fig. 2.4. For example, the motion of electrons in the inner magnetosphere of Mercury obtained from global fully-kinetic simulations is analyzed in Sect. 5.3 by means of adiabatic theory.

Gradient of magnetic field parallel to $\mathbf{B}$

The adiabatic motion of a particle in a inhomogeneous magnetic field preserves to first order the magnetic moment $\mu = mv_\perp^2/2B$ and the kinetic energy $E = \frac{1}{2}m\left(v_\perp^2 + v_\parallel^2\right)$.

Where, using the parallel coordinate "s" relative to the local magnetic field, one defines the speed $v_\parallel = ds/dt$. Substituting the perpendicular kinetic energy with the magnetic moment, the total kinetic energy of the particle reads:

$$E = \frac{1}{2}mv_\parallel^2 + \mu B(s) \tag{2.62}$$

Therefore, the magnetic field acts on the parallel motion of the particle as an "effective" potential $U(s) = \mu B(s)$, or equivalently in the form of a force $-dU/ds = -\mu dB/ds$. This force is opposite to the magnetic field gradient and it does not depend on the particle charge.

If the magnetic field $B(s)$ presents a local minimum, then, periodic motions are possible around such minimum. For periodic solutions to exist, the total energy must be higher than the potential minimum $E > \min(\mu B(s))$ and there must exist two solutions s_1 and s_2 to the equation $E = \mu B(s)$; these are the inversion points. In general, if the profile of $B(s)$ is not specified, one can derive the period of the bounce motion as follows:

$$T_{bounce} = \sqrt{2m} \int_{s_1}^{s_2} \frac{ds}{\sqrt{E - \mu B(s)}} \tag{2.63}$$

However, it is easier to get a rough idea of this motion by approximating the magnetic field with a parabolic profile. This reads:

$$B(s) = \frac{(B_{surf} - B_{eq})}{L^2}s^2 + B_{eq} \tag{2.64}$$

where, in analogy with the magnetosphere, the minimum magnetic field is B_{eq} (at the equator), the maximum is B_{surf} (at the surface of the planet), and L is the half-length of the field line, from the equator to the surface. In this case $s_1 = -s_2$ because the profile is symmetric.

Using the expression for $B(s)$ in Eq. (2.64), we find the period and the inversion point as follows:

$$T_{bounce} = \pi L \sqrt{\frac{2m}{\mu(B_{surf} - B_{eq})}} = 2\pi \frac{s_2}{v_{\parallel,eq}} \tag{2.65}$$

$$s_2 = L\sqrt{\frac{E - \mu B_{eq}}{\mu(B_{surf} - B_{eq})}} > 0 \tag{2.66}$$

Introducing the pitch angle $\tan\theta = v_\perp/v_\parallel$, Eq. (2.66) simplifies to:

$$s_2 = L\left[\tan(\theta_{eq})\left(\frac{B_{surf}}{B_{eq}} - 1\right)\right]^{-1/2} > 0 \tag{2.67}$$

This is the so-called adiabatic "bounce motion", at play in the inner regions of planetary magnetospheres (as sketched in Fig. 2.4). To have an idea, consider an electron with a parallel kinetic energy of 50 keV (velocity of 10^5 km/s) and pitch angle $\pi/4$ at the equator, moving along a field line at Mercury and at Earth[8]. In this situation, the electron bounces back and forth between the two hemispheres following a periodic motion with amplitude $s_2 \sim 1.4\, R_E$ (at Earth) and $s_2 \sim 1.4\, R_M$ (at Mercury) and period $T_{bounce} \sim 0.5$ s (at Earth) and $T_{bounce} \sim 0.2$ s (at Mercury).

Gradient of magnetic field perpendicular to B

Assuming that the particle gyrates in a region with a perpendicular magnetic field gradient, then the particle experience an "effective" force due to the spatial inhomogeneity of B according to Eq. (2.62). This grad-B force equal to $-\mu \nabla_\perp B$ induces a drift of the guiding center, according to Eq. (2.60). This "grad-B drift" reads:

$$\mathbf{u}_{grad} = -\frac{c\mu}{qB^2}(\nabla_\perp B) \times \mathbf{B} \tag{2.68}$$

The grad-B drift depends on the charge sign, and it is proportional to the perpendicular kinetic energy, and to the inverse gradient length $\ell_\perp^{-1} = (\nabla_\perp B)/B$.

Curvature of magnetic field

When a particle moves along a curved magnetic field with non-zero parallel speed, it experiences the following centrifugal force:

$$\mathbf{F}_{curv} = -\frac{mv_\parallel^2}{R_C}\hat{n} = -\frac{mv_\parallel^2}{B^2}(\mathbf{B}\cdot\nabla)\mathbf{B} \tag{2.69}$$

where R_C is the radius of curvature, and $\hat{n}$ is the direction towards the center of curvature. This force is by definition perpendicular to the magnetic field. As a consequence, it induces a drift in the guiding center of the particle according to Eq. (2.60). This is the so-called "curvature drift":

$$\mathbf{u}_{curv} = -\frac{mcv_\parallel^2}{qB^2 R_C}\hat{n} \times \mathbf{B} \tag{2.70}$$

This drift is oppositely directed for ions and electrons, and it is proportional to the parallel kinetic energy, and to the inverse curvature radius $R_C^{-1} = |(\mathbf{B}\cdot\nabla)\mathbf{B}|/B^2$. In the inner shells of planetary magnetospheres, the curvature drift drives the longitudinal circulation of electrons and ions (in opposite direction) that forms the radiation belts (Koskinen and Kilpua,

---

[8]The parameters for the Earth are $B_{eq} \sim 1\,\mu$T, $B_{surf} \sim 50\,\mu$T, and $L \sim 10\,R_E$; while, for Mercury $B_{eq} \sim 0.1\,\mu$T, $B_{surf} \sim 0.3\,\mu$T, and $L \sim 2\,R_M$.
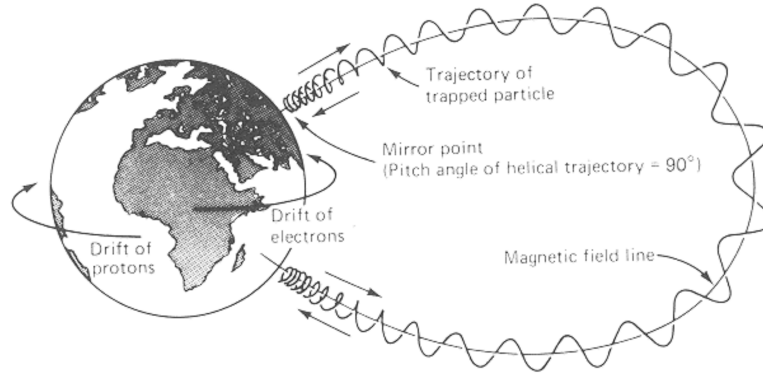
Figure 2.4: Sketch of the adiabatic motion of charged particles in Earth's magnetosphere. Analogous drifts are also observed on other magnetized planets, such as Mercury and Jupiter. Figure taken from unh.edu (n.d.).

2022). Considering this motion at a distance r from the center of the planet, and assuming that the curvature does not depend on the longitude, the period of rotation of the particles is:

$$T_{curv} = \frac{2\pi r}{|\mathbf{u}_{curv}|} = \frac{2\pi r R_C \omega_c}{v_\parallel^2} \tag{2.71}$$

For instance, a particle (ion or electron is the same) with a parallel energy of 50 keV completes one full orbit in $T_{curv} \sim 9$ hours with a speed of $|\mathbf{u}_{curv}| \sim 4$ km/s, in the ring current of the Earth. At Mercury, the same particle complete one full orbit in $T_{curv} \sim 15$ seconds with a speed of $|\mathbf{u}_{curv}| \sim 800$ km/s[9].

To understand the motion of the particles in the inner magnetosphere in the adiabatic approximation, it is useful to write down the most important drifts encountered in the system in physical units. Considering a particle with perpendicular and parallel kinetic energies $E_\perp = \frac{1}{2}mv_\perp^2$ and $E_\parallel = \frac{1}{2}mv_\parallel^2$, respectively. The E-cross-B, Grad-B and curvature drifts are given by:

$$\mathbf{u}_{E \times B} \approx \frac{E \text{ [V/km]}}{B \text{ [}\mu\text{T]}} \frac{\text{km}}{\text{s}} \tag{2.72}$$

$$\mathbf{u}_{grad} \approx \frac{E_\perp \text{ [eV]}}{\ell_\perp \text{ [km]} \, B \text{ [}\mu\text{T]}} \frac{\text{km}}{\text{s}} \tag{2.73}$$

$$\mathbf{u}_{curv} \approx \frac{2E_\parallel \text{ [eV]}}{R_C \text{ [km]} \, B \text{ [}\mu\text{T]}} \frac{\text{km}}{\text{s}} \tag{2.74}$$

---

[9]The parameters for the Earth are $r \sim 3\,R_E$, $R_C \sim 4\,R_E$, and $B \sim 1\,\mu$T; while, for Mercury $r \sim 1.2\,R_M$, $R_C \sim 0.5\,R_M$, and $B \sim 0.1\,\mu$T.

2.2.4 Interaction plasma-atoms

The interaction between a plasma (ionized matter) and an atom (non-ionized matter) can lead to a great variety of processes that transfer energy and momentum from the plasma to the non-ionized matter (gas, solid etc.). An example of such a process is the one at play at Mercury when plasma from the magnetosphere precipitates onto the surface and drives the emission of photons via X-ray fluorescence (XRF), see Sect. 3.3. The electrons in the plasma interact with the atoms in the regolith and excite them. Then, the de-excitation of these atoms leads to the emission of X-ray photons. XRF is further discussed in Sect. 3.2.2 in connection to MESSENGER X-ray observations at Mercury. In this section, I discuss the interaction plasma-atoms from a general perspective that does not make any assumption on the specific process at play in the interaction.

Let's suppose that one species of the plasma (say electrons) interact with a given atomic species (say Oxygen) via a generic process indicated by X and characterized by a given cross section (in this case $\sigma_{e,O,X}(E)$, where E is the energy of the electrons[10]). Therefore, using the energy distribution function of the plasma species (electrons) at one point in space, one obtains the rate of interaction as follows:

$$\nu_{e,O,X} = \int_0^\infty f_e(E)\sigma_{e,O,X}(E)\sqrt{\frac{2E}{m_e}}dE \tag{2.75}$$

This quantity $\nu_{e,O,X}$ is a measure of the typical time of interaction between one atom and a flow of plasma particles (in this case, electrons). As a consequence, one obtains the number of reaction products N_{pr} in a given time interval δT as follows:

$$N_{pr} = N_O \nu_{e,O,XRF} \delta T \tag{2.76}$$

where N_O is the number of interacting Oxygen atoms.

In this work, we focus specifically on two processes driven by the interactions between electrons and atoms: electron impact ionization (EII) and X-ray fluorescence (XRF). Both processes are extensively discussed in Sect. 3.3, here I just show the cross sections of these two processes for the typical atomic species encountered in Mercury's exosphere (for EII) and surface (for XRF), as shown in Fig. 2.5. The cross sections are taken from Kim, Y.-K. et al. (2005), Zatsarinny et al. (2019), and Golyatina and Maiorov (2021) for EII, and from Llovet et al. (2014) for XRF. The peak of EII is typically around $10 - 100$ eV for the species considered, while XRF typically peaks around $1 - 10$ keV.

---

[10]Here, I neglect the contribution of the target atom to the relative energy E. This is typically a very good approximation for space plasma where electrons have an energy of the order, or even higher, than $10 - 100$ eV.
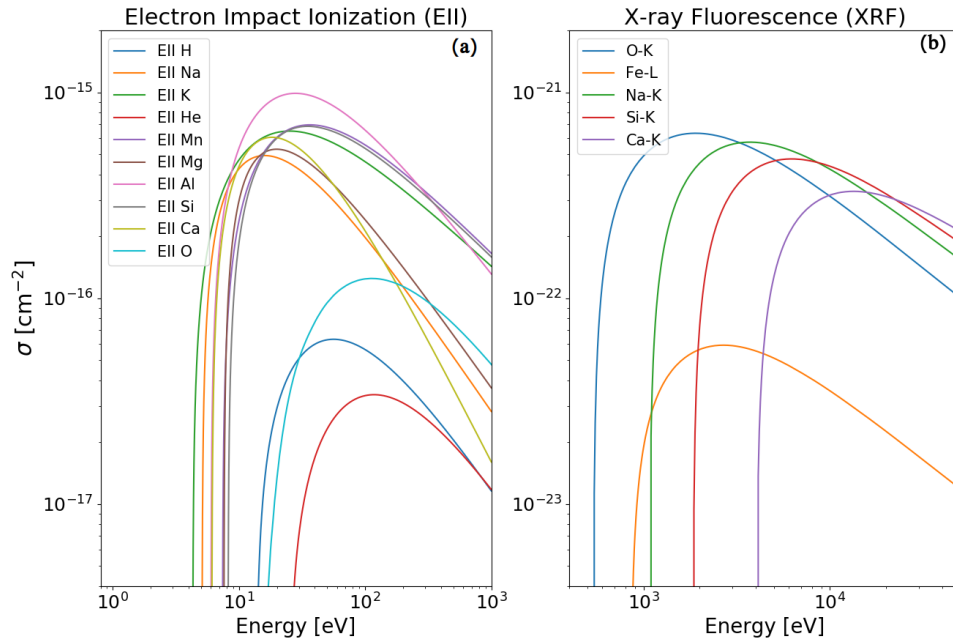
Figure 2.5: Cross sections of electron impact ionization (left panel) and electron-induced X-ray fluorescence (right panel). Note that vertical and horizontal axes are different in the two panels.

The plasma physics concept introduced in this chapter are used in Chap. 3 to describe the ionized environment surrounding Mercury, and in Chap. 5 to present the results of this work. All in all, this work addresses electron kinetic processes at Mercury's environment using the fully-kinetic model in equations (2.7)-(2.10) and the quasilinear model described in Sect. 2.1.3. The fundamental plasma dynamics introduced in Sect. 2.2 is key to interpret the results of this work both in local simulations of the magnetopause (where drift plasma instabilities develop, see Sect. 2.2.1) and in global simulations of the magnetosphere (where electrons gets accelerated by MR, see Sect. 2.2.2, and move adiabatically in the inner magnetosphere, see Sect. 2.2.3). In the end, electrons precipitate from the magnetosphere onto the surface, there plasma-atoms interactions become important (see Sect. 2.2.4).

3 Mercury's plasma, neutral and solid environments as targets of the BepiColombo mission

Mercury has been considered for a long time a far and "boring" target for exploratory space missions: basically a huge piece of rock in the vicinity of the Sun. It was not until 1974 that the NASA mission Mariner10 performed the first flyby of Mercury. Mariner10 observed many unexpected features such as an intrinsic magnetic field, an energetic plasma environment, and a planet density incompatible with Solar System formation models. These findings sparked the interest for further exploration of Mercury. However, due to the strong gravitational field of the Sun, missions to Mercury are expensive in fuel and require complex trajectories involving multiple flybys and long cruise periods. For this reason, Mercury remained unexplored for about 30 years. The NASA MESSENGER mission launched in 2004 was the first mission to orbit Mercury, and it provided a wealth of in situ data over four years of science operations (from 2011 to 2015). Now, the joint ESA/JAXA BepiColombo mission is cruising towards Mercury with orbit insertion planned for December 2025. After insertion, BepiColombo will revolutionize our understanding of Mercury, but at present, only partial observations from three Mercury flybys are available.

3.1 Mercury's magnetosphere: a closer look

The magnetosphere of Mercury presents unique properties among the large spectrum of Solar System bodies. The strong solar wind forcing, the weak magnetic field of the planet, and the lack of a dense atmosphere are the most remarkable properties of this system. In this section, I discuss the typical solar wind plasma parameters at Mercury (Sect. 3.1.1), past in situ observations of the magnetosphere (Sect. 3.1.2), and past global numerical models of the magnetosphere in support to such observations (Sect. 3.1.3).

3.1.1 SOLAR WIND PLASMA PARAMETERS

The great majority of solar wind observations are collected around Earth at 1 AU. At 1 AU, the solar wind has a density $n_{sw} = 6 \pm 3$ cm^{-3}, a magnetic field magnitude $B_{sw} = 6 \pm 3$ nT, a velocity $V_{sw} = 440 \pm 100$ km/s, a proton temperature $T_{i,sw} = 10 \pm 4$ eV (Venzmer and Bothmer, 2018, Tab. 1 and Fig.1 therein)[1], and an electron temperature $T_{e,sw} = 12 \pm 4$ eV (Newbury, 1996; Maksimovic et al., 2005). Here, I do not discuss separately the substructures of the solar wind (e.g. fast and slow solar winds), its periodic time variations (e.g. modulation of the parameters with the solar cycle), and higher-order effects that require extra parameters to define the solar wind plasma (e.g. proton temperature anisotropy, electron halo and strahl). These three sources of variability are hidden in the variability range of the solar wind plasma parameters listed above.

To study the interaction between the solar wind and other Solar System bodies (such as Mercury), one must extrapolate the mean solar wind parameters from 1 AU to a generic heliocentric distances R. From decades of in situ observations of the heliosphere, we now know that –to a good degree of approximation– the solar wind density decreases as R^{-2}, the magnetic field magnitude decreases roughly as $R^{-3/2}$, and the plasma velocity remains roughly constant (Mariani et al., 1978; Slavin and Holzer, 1981; Bougeret et al., 1984; Venzmer and Bothmer, 2018). Moreover, the proton temperature decreases roughly as $R^{-2/3\pm\delta}$ (Gazis and Lazarus, 1982; Marsch et al., 1982; Hellinger et al., 2011; Hellinger et al., 2013; Venzmer and Bothmer, 2018), and the electron temperature as $R^{-2/5\pm\delta}$ (Sittler and Scudder, 1980; Marsch et al., 1989; Maksimovic et al., 2005), with an uncertainty on the exponent $\delta \approx 0.2$ resulting from the different values published in the literature. As a result, the solar wind Mach number, plasma beta, ion gyroradius, and ion gyroperiod gets smaller when approaching the Sun. The mean solar wind parameters extrapolated from 1 AU to different heliocentric distances are shown in Tab. 3.1[2]. The parameters in Tab. 3.1 for Mercury are in agreement with in situ observations by Helios at $0.3 - 0.5$ AU (Sarantos et al., 2007) and MESSENGER (James et al., 2017).

At Mercury, the solar wind parameters change substantially as compared to Earth, as shown in Tab. 3.1. The solar wind at Mercury has a plasma beta lower than one (which means that the magnetic pressure dominates the thermal pressure), a higher Alfvén speed (which means a lower alfvénic Mach number, occasionally of the order or below one), and a higher solar wind ram pressure $P_{ram} = n_{sw}V_{sw}^2 \sim R^{-2}$ (which means a more compressed magnetosphere). Moreover, solar wind parameters change significantly between Mercury's perihelion and aphelion (e.g. n_{sw} is a factor 2 smaller at aphelion). This, in turn, drives seasonal vari-

---

[1] In Venzmer and Bothmer (2018), the authors extensively characterized the solar wind at 1 AU using the OMNI 2 dataset (King and Papitashvili, 2005), which combines magnetic field and plasma data from multiple satellites since 1963.

[2] In Tab. 3.1, I do not considered the uncertainty δ on the temperature scaling index because it affects minimally the extrapolated temperatures.

Parameter	Var [%]	Scaling [R^α]	Mercury Perihel.	Aphel.	Venus	**Earth**	Mars	Jupiter
R [AU]	—	1	0.31	0.47	0.72	**1.00**	1.52	5.20
n_{SW} [cm^{-3}]	50	-2	62	27	12	**6**	2.6	0.2
B_{SW} [nT]	50	-3/2	35	19	10	**6**	3.2	0.5
$T_{i,SW}$ [eV]	40	-2/3	22	16	12	**10**	8	4
$T_{e,SW}$ [eV]	33	-2/5	19	15	14	**12**	10	6
β_i	190	1/3	0.3	0.5	0.8	**1.3**	2.4	13
$V_{A,i}$ [km/s]	75	-1/2	172	113	75	**53**	35	10
ϱ_i [km]	70	7/6	8	15	30	**54**	100	900
$\omega_{c,i}^{-1}$ [s]	50	2	0.2	0.4	0.9	**1.7**	4.0	47.3

Table 3.1: Mean solar wind plasma parameters at different heliocentric distances. Values extrapolated from 1 AU using the scaling indexes listed in the third column "Scaling". The entry "Var" in the second column shows the range of variability of the parameter in percentage.

ations in the magnetosphere size and shape (Zhong et al., 2015b; Zhong et al., 2020), as well as variations in the induced component of the dipolar magnetic field of the planet (Johnson et al., 2016). This magnetospheric seasonal variability is a unique characteristic of Mercury among all planets in the Solar System.

The solar wind presents strong fluctuations around the mean values listed in Tab. 3.1, usually of the order of $50\% - 100\%$ (column "Var" in Tab. 3.1). These fluctuations occur on different timescales depending on the process that originates them. For instance, very long fluctuations on the order of years are driven by the solar cycle (period of 11 years), long fluctuations of the order of days are driven by the Sun's rotation (period of 27 days), and short fluctuations of the order of hours or less are driven by plasma turbulence. These turbulent fluctuations are responsible for the high variability of the solar wind on time scales of the order of $\sim 10 - 20$ minutes at Mercury and $\sim 1 - 2$ hours at Earth (Cuesta et al., 2022)[3]. In particular, small fluctuations (e.g. $\Delta B/B \lesssim 0.2$) are observed more frequently than large fluctuations (e.g. $\Delta B/B \gtrsim 0.7$), with a typical timescale of $\lesssim 20$ minutes and $\gtrsim 1$ hour at Mercury, respectively (James et al., 2017). These fluctuations are one important source of variability for Mercury's environment. This point is discussed extensively in the next section 3.1.2, when introducing the properties and variabiliy of the magnetosphere. Here, I only focus on the characterization of the solar wind parameters.

Solar wind parameters not only change in magnitude, but also in direction. For instance, rotations of the IMF are commonly observed at Mercury's heliocentric distances. In James

---

[3]The time scales listed here are derived from the correlation lengths in Cuesta et al. (2022), divided by a solar wind speed of 400 km/s.

et al. (2017), using MESSENGER magnetic field observations, the authors showed that the IMF at Mercury has a bimodal clock angle[4] distribution centered around $+90°$ and $−90°$ (corresponding to a dawnward and a duskward direction, respectively), and a bimodal cone angle[5] distribution centered around $35°$ and $150°$ (corresponding to a quasi-planetward and a quasi-sunward direction, respectively). From these clock and cone angles, one derives a typical Parker spiral angle[6] of the order of $\pm 35°$ at Mercury. As expected, the Parker spiral angle is smaller at Mercury as compared to the Earth (roughly $45°$ at the Earth, see, for instance, Milillo et al. 2020, Tab. 2 therein). Bimodal distributions in these angles originate from the double polarity of the Solar magnetic field. Indeed, when crossing the heliospheric current sheet, the magnetic field direction changes by roughly $180°$.

Under extreme solar wind conditions, the plasma impinging on Mercury deviates from the nominal parameters described above. Extreme events include Coronal Mass Ejections (CMEs), Co-rotating Interaction Regions (CIRs), and Solar Energetic Particle (SEP) events, and they can alter significantly the average structure of Mercury's magnetosphere. In particular, CMEs with an high ram pressure (up to a factor $10−20$ higher than nominal solar wind) are thought to be responsible for the so-called disappearing dayside magnetopause (DDM) events (Slavin et al., 2019). In such events, the dayside magnetopause is totally eroded and the surface is directly exposed to the solar wind. Nonetheless, these DDM events remain rare, with a mean occurring frequency of one event per year, as identified during MESSENGER science campaign. For this reason, in this work, I focus on the study of Mercury's magnetosphere under nominal solar wind conditions.

3.1.2 MAGNETIC FIELD STRUCTURE AND DYNAMICS: IN SITU OBSERVATIONS

Mariner10 discovered that Mercury has an intrinsic magnetic field with a southward magnetic moment (Ness et al., 1974). Magnetic field observations during the first and third Mercury flyby showed the existence of an intrinsic magnetic dipole with a strength of $280 − 360$ nT at the equator (Ness et al., 1976). MESSENGER observations refined this crude estimate, yielding a dipole field of $190 − 200$ nT at the magnetic equator, shifted northward by 480 km with respect to the geographic equator, and quasi-aligned with the spin axis (Anderson et al., 2011; Anderson et al., 2012).

---

[4]Clock angle defined as $\arctan(−B_y/B_z)$ in MSO coordinates. In the MSO reference frame, the x-axis points from Mercury's center to the Sun, the z-axis is anti-parallel to Mercury's magnetic dipole, and the y-axis points from dawn to dusk.

[5]Cone angle defined as $\arccos(−B_x/|\mathbf{B}|)$ in MSO coordinates.

[6]Parker spiral angle defined as $\arctan(−B_y/B_x)$ in MSO coordinates.

Mercury's intrinsic magnetic field, although being roughly two orders of magnitude weaker than the one of the Earth, is able to standoff the impinging solar wind and to create a small magnetosphere. Mercury's magnetosphere, to a first order approximation, is a scaled-down version of Earth's one, as shown schematically in Fig. 1.1, with a scaling factor of roughly 7 (i.e. a distance of 1 R_M in Mercury's magnetosphere corresponds to 7 R_E in Earth's one; Siscoe et al. 1975). Using the large dataset of MESSENGER magnetic field observations, Winslow et al. (2013) was able to fit the average position of the bow shock and of the magnetopause using the conic model of Slavin et al. (2009) and the magnetopause model of Shue et al. (1997), respectively. There, the authors found that the bow shock and magnetopause standoff distance from the center of the planet are $1.9 - 2.3\,R_M$ (increasing with decreasing solar wind alfvénic Mach number) and $1.35 - 1.55\,R_M$ (increasing with decreasing solar wind ram pressure), respectively.

Analogously to the Earth's magnetosphere, at Mercury the circulation of plasma in the magnetosphere is driven by magnetic reconnection at the "nose" of the magnetopause and in the tail, that drives the Dungey cycle (Dungey, 1961). Due to the smaller size of Mercury's magnetosphere, the period of the Dungey cycle is very short, roughly $1 - 2$ minutes, as compared to the one of the Earth, of roughly 1 hour (Baumjohann et al., 2006, Tab. 1 therein). Therefore, Mercury's magnetosphere is able to respond quickly (on the order of minutes) to variations in the upstream plasma parameters. Since variations in the IMF magnitude and direction are typically observed on time scales of the order of tens of minutes (Sect. 3.1.1) at Mercury, one can expect to have a succession of quasi-steady-state magnetosphere configurations with a steady IMF lasting $\sim$ 10 minutes, separated by transient reconfiguration periods lasting roughly $\sim$ $1 - 2$ minutes. In this work, I neglect transient reconfiguration periods, by focusing only on the quasi-steady-state global modeling of the magnetosphere[7]. Since in situ observations (Slavin, 2004; Slavin et al., 2012) and global numerical simulations (Ip and Kopp, 2002; Kallio and Janhunen, 2003; Kallio and Janhunen, 2004; Exner, 2021) have shown that the IMF direction is the dominant parameter in determining the topology and convection pattern of Mercury's magnetosphere, I focus on three different solar wind configuration with nominal *fixed* solar wind parameters and different IMF directions (purely southward, purely northward, and oblique), as discussed in Sect. 4.3.2. This choice enable to sample different regions of the variability range of the Hermean[8] system. In particular, the different IMF directions chosen here drive a substantially different magnetic reconnection in the nose and in the tail of the magnetosphere.

Magnetic reconnection at Mercury's magnetosphere has been addressed by several authors using MESSENGER in situ magnetic field and ion observations. The lack of instruments

---

[7]To study the transient periods, one would need a more refined implementation of the boundary conditions allowing for unsteady solar wind conditions in the model. This task resides out of the scope of this PhD thesis.

[8]Meaning:"of or relating to Hermes". Hermes here is used as a synonym to Mercury.

targeting electron energy distribution and electron-scale plasma waves onboard MESSENGER limited the observational capabilities of the spacecraft. For this reason, MESSENGER provided a first-order picture of magnetic reconnection at Mercury, to be refined by future observations by the BepiColombo mission (discussed in Sect. 3.2). Magnetopause reconnection is driven at Mercury with a high reconnection rate, weakly-dependent on the magnetic shear angle (Dibraccio et al., 2013; Gershman et al., 2013). In contrast with these results, Leyser et al. (2017) found that the formation of flux transfer events at the magnetopause –a proxy for magnetic reconnection– depends on the direction of the magnetic field, and it is depleted for a more northward IMF, as at Earth. In Dibraccio et al. (2013), the authors found a reconnection rate (defined in this document in Sect. 2.2.2) of about $0.2 - 0.3$. This value is about $2 - 3$ times larger than the one found at Earth. This is a consequence of the low plasma-beta environment found at the magnetopause of Mercury. Indeed, in situ observations both at Mercury (Dibraccio et al., 2013, Fig. 11 therein) and at Earth (Scurry et al., 1994) suggest that the reconnection rate increases with decreasing plasma beta. Magnetotail reconnection is also strongly driven at Mercury (Slavin et al., 2009; Slavin et al., 2012; Zhong et al., 2023). In the tail, symmetric reconnection between the lobes magnetic field takes place at the near Mercury neutral line (hereafter NMNL) usually found $\sim 2 - 4$ R_M downstream of the planet (Poh et al., 2017). The position of the NMNL depends upon the upstream IMF direction and it also presents considerable dawn-dusk asymmetries (Zhong et al., 2023). In Zhong et al. (2023), the authors found that on average the NMNL current sheet is thinner on the duskside (i.e. premidnight sector in local time) and that it is closer to the planet on the dawnside (i.e. post-midnight sector).

Dibraccio et al. (2013) also estimated that Mercury's magnetopause thickness is ~ 100 km; a much smaller value than that of the other magnetized planets in the Solar System. For instance, the magnetopause thickness is ~ 500 km at Earth (Berchem and Russell, 1982), $\sim 3500 - 5200$ km at Jupiter (Sonnerup et al., 1981), and ~ 5000 km at Saturn (Lepping et al., 1981). This supports the idea that drift instabilities such as the LHDI (introduced in Sect. 2.2.1) are driven efficiently at the magnetopause of Mercury. The nonlinear evolution of this instability is addressed in this document using local plasma simulations in Sect. 5.2. In the next section 3.1.3, I present an overview of past numerical models addressing the magnetosphere of Mercury to set the context for the numerical simulations performed in this work.

3.1.3 Past global numerical studies of the magnetosphere

Numerical models for Mercury's magnetosphere work in synergy with in situ observations for a comprehensive understanding of the plasma environment around Mercury. Numerical models to study the magnetosphere can be classified on a scale of increasing computational complexity. On this scale one finds (in order) "Tsyganenko-like" magnetic field models,

test-particle models, MHD single fluid models, multi-fluid models, hybrid models, and fully-kinetic models. This scale is based on the hierarchy of plasma models presented in Sect. 2.1.2.

After the discovery of Mercury's intrinsic magnetic field by Mariner10, researchers started to model Mercury's magnetic field by re-adapting existing models for the Earth (Luhmann et al., 1998; Korth et al., 2004), or by developing new models accounting for Mercury's large conductive iron core (Grosser et al., 2004). In particular, "Tsyganenko-like" models are widely used to describe Mercury's magnetic field as a sum of different independent sources (planet interior, magnetopause current sheet, plasma sheet current etc.) (Johnson et al., 2012; Korth et al., 2015; Korth et al., 2017). The advantage of these magnetic field models is that they are computationally light and therefore, fast. But this type of model is limited since (i) it uses a steady-state approach that does not allow to study the plasma dynamics, (ii) it parameterizes plasma currents such as the magnetopause and plasma sheet currents using a simplified shape, and (iii) it contains free parameters that have to be tuned by fitting in situ observations.

Test-particle simulations use Mercury's steady-state magnetic field models to compute a posteriori the plasma dynamics in the magnetosphere (Delcourt et al., 2003; Massetti et al., 2003; Delcourt et al., 2005a; Delcourt et al., 2005b; Mura et al., 2005; Schriver et al., 2011a; Walsh et al., 2013). In this approach, test particles (ions and/or electrons) are injected in some part of the magnetosphere with a prescribed initial velocity. Their trajectories are then computed from the Lorentz force in the prescribed electromagnetic fields. This type of simulation can be computationally inexpensive (it depends on the number of particles used) and it gives a useful hint on the type of plasma dynamics expected in the system. However, the predictive character of this type of models is strongly limited by (i) the lack of a self-consistent approach including the dynamics of the electromagnetic fields, and (ii) the dependence of the output on specific parameters set as input (e.g. initial position and velocity of the particle).

From the beginning of the 21st century, the increase in computational power has enabled researchers to run "ab initio" models of the interaction between the solar wind and the magnetosphere of Mercury (Gombosi et al., 2000; Kabin et al., 2000; Ip and Kopp, 2002; Kallio and Janhunen, 2003). Ab initio models overcome the limitations of steady-state magnetic field and test-particle models since (i) they include the time evolution of the system, (ii) they include in the computation both electromagnetic fields and the plasma self-consistently, and (iii) they do not make use of free parameters to be tuned on observations or by the user, except for the magnetic field of the planet and the solar wind parameters that are the boundary conditions of this type of models. This type of models are then discriminated by the plasma model used (see Sect. 2.1.2). The simplest, less computationally-demanding simulations use a fluid approach. Fluid models include ideal MHD models with numerical resistivity (Kabin et al., 2000; Kabin et al., 2008; Pantellini et al., 2015; Varela et al., 2016), resistive MHD models (Yagi et al., 2010; Jia et al., 2015; Jia et al., 2019), multi-fluid models with massless electrons (Kidder et al., 2008; Benna et al., 2010), and multi-fluid models with electron mass (Dong et al., 2019). A good

compromise between model complexity and computational resources is achieved using ion-kinetic models implemented in hybrid codes. These plasma models treat ions kinetically and assume electrons as a massless charge-neutralizing fluid (Kallio and Janhunen, 2003; Kallio and Janhunen, 2004; Trávníček et al., 2007; Trávníček et al., 2009; Trávníček et al., 2010; Schriver et al., 2011b; Richer et al., 2012; Müller et al., 2012; Herčík et al., 2013; Herčík et al., 2016; Exner et al., 2018; Fatemi et al., 2018; Fatemi et al., 2020). By comparing the results of four hybrid and fluid models for Mercury's magnetosphere, Aizawa et al. (2020) showed that the models produce a similar global structure in the dayside consistent with the nominal bow shock and magnetopause observed by MESSENGER (Winslow et al., 2013); however, the results differ in the nightside and close to the surface. Fully-kinetic models have not yet been applied "ab initio" to the study of Mercury's magnetosphere, due to their huge computational cost. Recently, and in parallel to this work, Lapenta et al. (2022) published a short (simulation time equal to 3.8 s in real time) global fully-kinetic simulations of Mercury's magnetosphere that started from the output of a global ion-kinetic one. Also, Chen et al. (2019) used a fully-kinetic plasma model to simulate the dynamics of a sub-region of the global system, at the same time as the global Hall-MHD model was running. This is a sort of mixed approach, coupling local fully-kinetic simulations to global fluid ones. Nonetheless, to my knowledge, no fully-kinetic global ab initio simulations of Mercury's magnetosphere have been published in the literature.

One of the goals of this work is to produce the first ab initio global simulations of Mercury's magnetosphere using a fully-kinetic plasma model. These simulations are conceived to support ongoing and future observations by the BepiColombo mission, discussed in the next section 3.2, thus helping to achieve the scientific goals of the mission. BepiColombo will observe for the first time electron kinetic processes at Mercury, and therefore fully-kinetic models are needed to first plan and later interpret such observations.

3.2 The BepiColombo mission

This work, albeit using a numerical approach, presents strong links with the observational community focusing on Mercury. To understand the links between the numerical results of this work and observations, I present a quick overview of the ongoing BepiColombo mission (Sect. 3.2.1) and the first plasma observations of this mission in comparison to past results by Mariner10 and MESSENGER (Sect. 3.2.2).

3.2.1 OVERVIEW OF THE MISSION

BepiColombo[9] is a planetary Cornerstone mission of ESA's Cosmic Vision Programme, and it is devoted to the thorough exploration of Mercury and its environment (Benkhoff et al., 2021). BepiColombo is the first space mission that benefits from the cooperation between the European and the Japanese space agencies. Each agency supports one of the spacecraft that are part of the mission: the ESA Mercury Planetary Orbiter (MPO) and the JAXA Mercury Magnetospheric Orbiter (MMO, renamed Mio after launch), both shown in Fig. 3.1.

First, MPO is mainly devoted to the exploration of Mercury's exosphere, surface, and interior (Benkhoff et al., 2021). With a polar orbit with periapsis $1.02\,R_M$ and apoapsis $1.62\,R_M$, MPO will be able to observe the dynamical processes coupling the surface of Mercury with the outer environment (e.g. neutrals release from the surface, plasma precipitation, ion sputtering). MPO payload includes a magnetometer to characterize Mercury's intrinsic magnetic field (MPO-MAG; Heyner et al. 2021), an infrared spectrometer to characterize the surface spectra in the range $7 - 40\,\mu m$ (MERTIS; Hiesinger et al. 2020), an X-ray spectrometer to measure the light emitted from the surface in the range $0.5 - 10$ keV (MIXS; Bunce et al. 2020), an UV spectrometer to characterize the exosphere (PHEBUS; Quémerais et al. 2020), a particle sensor to measure both neutrals and ions (SERENA; Orsini et al. 2021), and an X-ray spectrometer to measure both solar X-rays and high-energy charged particles (SIXS; Huovelin et al. 2020). The orbit of MPO is shown in the left panel of Fig. 3.2 (red line).

Second, Mio is mainly devoted to the exploration of Mercury's magnetosphere (Murakami et al., 2020). With a polar orbit with periapsis $1.02\,R_M$ and apoapsis $5.85\,R_M$, Mio will be able to observe unexplored regions of Mercury's magnetosphere with a novel set of plasma instruments never flown to Mercury before. Mio payload includes a magnetometer (MGF; Baumjohann et al. 2020), a suite of particle instruments to measure ions, electrons and neutrals in different energy ranges (MPPE; Saito et al. 2021), a suite of plasma wave instruments to measure electromagnetic waves in different frequency bands (PWI; Kasaba et al. 2020), and a spectral imager to observe the distribution of sodium atoms around the planet (MSASI; Yoshikawa et al. 2010). The orbit of Mio is shown in the left panel of Fig. 3.2 (blue line).

At present, BepiColombo is cruising to Mercury with limited observational capabilities. The spacecraft is flying to Mercury in a "stacked" configuration, where MPO, Mio and the transfer module (MTM) fly together as a mechanically and electrically coupled stack (see Fig. 3.1 left panel). To protect Mio from the solar radiation, a conical shield (called MOSIF) envelops the Japaneses spacecraft, leaving just a small opening angle of about $16°$ to perform parti-

---

[9]Giuseppe (Bepi) Colombo (1920–1984): Italian mathematician who made many contributions to planetary research, celestial mechanics, including the development of new space flight concepts. His contributions include the explanation of Mercury's 3:2 spin-orbit resonance, and the definition of Mariner10 trajectory allowing for multiple Mercury flybys.
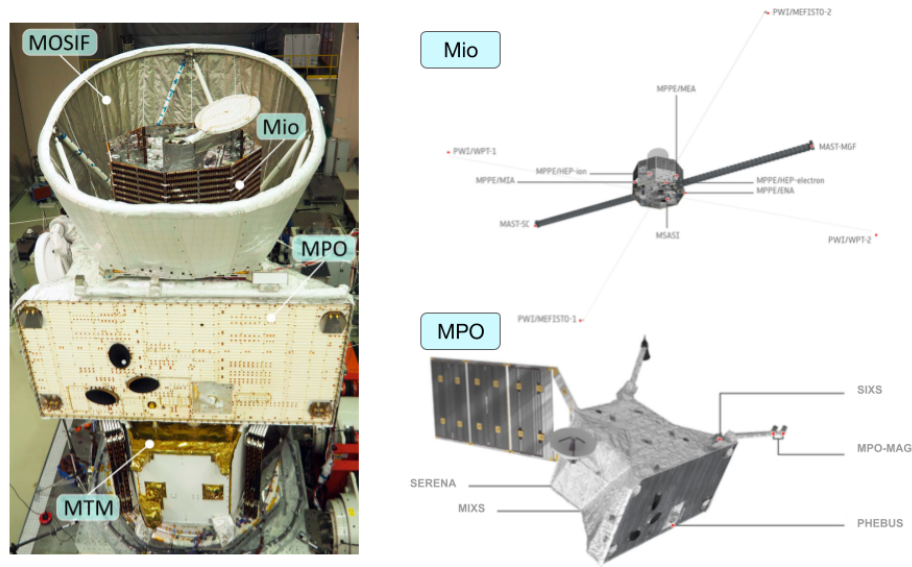
Figure 3.1: BepiColombo spacecraft stacked configuration during cruise (left panel), and fully deployed configuration for science operations (right panel). Only the instruments of interest for this work are listed (list non exhaustive). Figure adapted from Murakami et al. (2020, Fig. 7 therein) and Benkhoff et al. (2021, Fig. 4-5 therein).
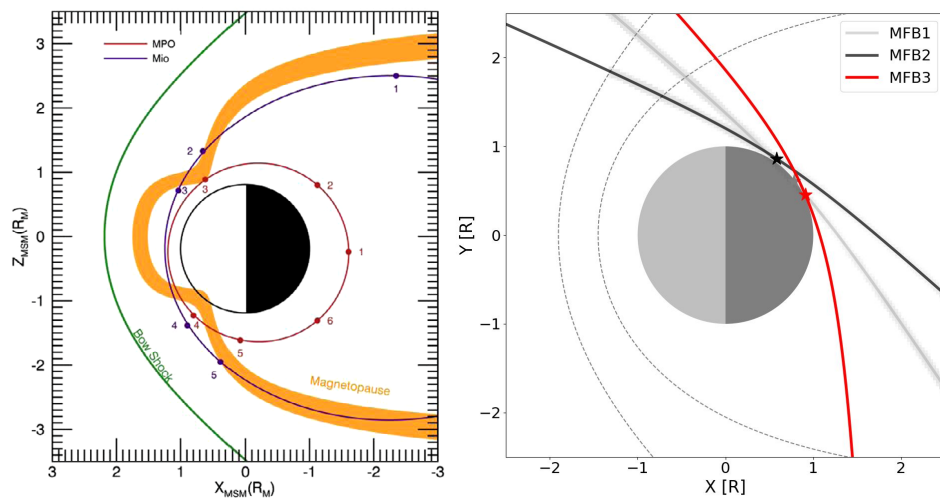

Figure 3.2: BepiColombo trajectory around Mercury during the science phase (left panel) and during flybys (right panel). Left panel: orbits configuration at Mercury's aphelion, MPO orbit in red, Mio orbit in blue, magnetopause model from Zhong et al. (2015a) in orange and bow shock model from Winslow et al. (2013) in green. Figure adapted from Milillo et al. (2020, Fig. 14 therein). Right panel: trajectories of the first three Mercury flybys projected onto the equatorial plane. The bow shock and magnetopause model of Winslow et al. (2013) are shown using dashed gray lines.

cle observations with MPPE instruments. In this configuration, BepiColombo already performed three Mercury flybys (1st Oct. 2021, 23rd Jun. 2022, and 20th Jun. 2023) as shown in right panel of Fig. 3.2, and it will perform other three Mercury flybys before orbit insertion. With these flybys, BepiColombo probed –and will probe– various parts of the exosphere and magnetosphere of Mercury, providing important (albeit limited) observations of Mercury's environment prior to orbit insertion. For instance, electron observations from the MPPE instrument during the first Mercury flyby published in Aizawa et al. (2023) are discussed in the next section 3.2.2. BepiColombo orbit insertion is planned for December 2025 (in about two years from the time of the writing).

After orbit insertion, BepiColombo will revolutionize our understanding of the Hermean system for three reasons. First, BepiColombo will provide complementary multi-point observations of the Hermean environment with MPO and Mio satellites. This aspect is particularly important given the short temporal and spatial scales of the system. Second, the polar orbit of both spacecraft (see left panel Fig. 3.2) will allow to observe in-depth the southern hemisphere of Mercury's environment. This region was poorly explored by MESSENGER due to orbital constraints. Third, MPO and Mio will carry instruments not included in the MESSENGER payload, such as an infrared spectrometer (MPO-MERTIS), a full set of plasma particle instruments (MPO-SERENA and Mio-MPPE), and a suite of plasma wave instruments (Mio-PWI). These new instruments will open new windows on our understanding of the Hermean environment, in particular concerning the interaction between the plasma and the other non-ionized parts of the system. In Tab. 3.2, Icompare BepiColombo plasma instruments with the ones onboard MESSENGER. The numerical works described in this thesis aims at addressing ongoing (in a limited configuration) and future (during the science phase) BepiColombo observations by the MPPE, PWI, and MIXS, SIXS instruments.

Once in orbit, BepiColombo will provide a wealth of in situ observations of Mercury's magnetosphere, exosphere and surface, providing new insights on the coupling between these three sub-parts of the system. However, as with any exploratory mission carrying new payload, BepiColombo observations will probably come with lots of surprises. The complexity of BepiColombo orbital observations is such that only through numerical models, including the electron dynamics, can the true potential of these observations be unveiled. The goal of this work, in the context of the BepiColombo mission, is to help the planning and interpretation of plasma measurements using a novel class of fully-kinetic plasma models including the nonlinear electron physics self-consistently. At present, the constrained observational windows during Mercury flybys do not allow to fully exploit the capabilities of the instruments. Nonetheless, flyby plasma observations represent an interesting opportunity to test the results of our numerical models against in situ BepiColombo observations –albeit constrained. In the next section 3.2.2, I quickly present BepiColombo's first Mercury flyby electron observations (Aizawa et al., 2023) and their interpretation in light of past observations by Mariner10 and MESSENGER.

Target	BepiColombo			MESSENGER	
B-field	MPO-MAG	$DC - 128\,Hz$	Lim	MAG	$DC - 20\,Hz$
	Mio-MGF	$DC - 64\,Hz$	Lim		
	Mio-PWI	$0.1\,Hz - 640\,kHz$	No		
E-field	Mio-PWI	$DC - 10\,MHz$	No	None	
Ions	Mio-PWI	Density	No	None	
	Mio-MPPE	$1\,eV - 1.5\,MeV$	Lim	EPPS	$50\,eV - 3\,MeV$
		$m/\Delta m \sim 10 - 40$			$m/\Delta m \sim 2 - 10$
	MPO-SERENA	$10\,eV - 15\,keV$	Yes		
		$m/\Delta m \sim 50$			
	MPO-SIXS	$1 - 10\,MeV$	Yes		
Electrons	Mio-PWI	Density, Temperature	No	None	
	Mio-MPPE	$3\,eV - 700\,keV$	Lim	EPPS	$25\,keV - 1\,MeV$
	MPO-SIXS	$50\,keV - 1\,MeV$	Yes		

Table 3.2: Plasma instruments onboard the mission BepiColombo (2018-ongoing) as compared to the ones onboard MESSENGER (2004-2015). The entry in the fourth column describes the status of the BepiColombo instrument during cruise (Yes=nominal, Lim=limited performances, No=not usable). Table adapted from Murakami et al. (2020, Tab. 3 therein).

3.2.2 EVOLUTION OF ELECTRON OBSERVATIONS FROM MARINER10 TO BEPICOLOMBO

Past space missions to Mercury (Mariner10 and MESSENGER) explored the magnetosphere of Mercury with a limited plasma payload. Those missions relied on the exploration of the magnetosphere mainly through magnetic field observations, and therefore little observations of the complex plasma environment at Mercury are available at present. Mariner10 was able to observe low-energy electrons (below roughly 700 eV) with the Plasma Science Experiment, and high-energy electrons (above roughly 100 keV) with the Energetic particle detector[10]. But no ion observations were performed by Mariner10 due to a technical failure. On the other hand, MESSENGER was able to observe ions (with the FIPS instrument) but not low-energy electrons (Andrews et al., 2007). Moreover, MESSENGER/EPS instrument was able to observe sporadically electrons above $\sim 30\,keV$ (Ho et al., 2011; Ho et al., 2012), in agreement with indirect observations of electrons in the range $1 - 10\,keV$ reported by the GRNS and XRS instruments (Lawrence et al., 2015; Ho et al., 2016; Dewey et al., 2018). For instance, MESSENGER/XRS instrument was able to detect, among other processes, the X-ray fluorescence induced by electrons precipitating onto the surface of Mercury (shown in bottom right panel

---

[10]This detector had some extra sensitivity to low-energy electrons of energy greater > 35 keV due to pulse pile-up in the detector. A spurious phenomenon discovered years after the flybys using a spare model of the instrument on ground (Wurz and Blomberg, 2001, and references therein).

of Fig. 3.3). All in all, past missions to Mercury showed the existence of high-energy electron populations at Mercury, but they weakly characterized their origin and spatial/temporal distribution. These goals will be fulfilled by the BepiColombo mission.

The BepiColombo mission carries an extensive plasma payload onboard the Mio spacecraft, as discussed in the previous section 3.2.1. Concerning electrons, the MPPE/MEA and MPPE/HEP instruments allow to measure directly in situ low-to-high energy electrons from few eV to hundreds of keV. Observations from MPPE/MEA instrument during the first Mercury flyby, published in Aizawa et al. (2023), are reported in the bottom panel of Fig. 3.3. These observations can be used to study electrons in the magnetosphere of Mercury, in synergy with (i) Mariner10 electron observations, and (ii) MESSENGER/XRS observations of electron-induced X-ray fluorescence from the surface. Such a multi-mission, multi-instrument approach help to compensate for the weak points of each set of observations.

Fig. 3.3 shows a comprehensive picture of electron observations at Mercury over five decades of space exploration, from the Mariner10 Energetic particle detector (top panels) to Bepi-Colombo/MEA observations (bottom panels) passing by MESSENGER/XRS observations (bottom right panel). Mariner10 observations pointed out the presence of high-energy electrons (typically above tens of keV) in the dawn-side of the magnetosphere. The shaded counts along the trajectory in the top panels of Fig. 3.3 indicate electrons above 35 keV, found in the region indicated as "hot". More recently, BepiColombo showed a similar high-energy population in the dawn-side of the magnetosphere (bottom panels in Fig. 3.3). This observation is strongly correlated with the electron-induced X-ray emissions from the surface observed by MESSENGER/XRS instrument (shaded regions onto the surface in bottom right panel of Fig. 3.3). These observations show the potential of BepiColombo instruments to address the fundamental scientific questions at the core of this PhD work dealing with the coupling between the plasma and the planetary environment (see Q1 and Q2 in Chap. 1). In the next section 3.3, I discuss in more details this coupling encompassing magnetosphere, exosphere and surface.

3.3 THE COUPLING BETWEEN MAGNETOSPHERE, EXOSPHERE AND SURFACE

The Hermean system is composed of (i) the outer plasma environment connected to Mercury's magnetic field (i.e. the magnetosphere; Korth et al. 2018; Slavin et al. 2018), (ii) the neutral atoms surrounding the planet as a very tenuous atmosphere (i.e. the exosphere; McClintock et al. 2018; R. M. Killen et al. 2018), and (iii) the rocky crust of the planet covered in regolith and exposed to space (i.e. the surface; Nittler et al. 2018; McCoy et al. 2018; Murchie et al. 2018). These
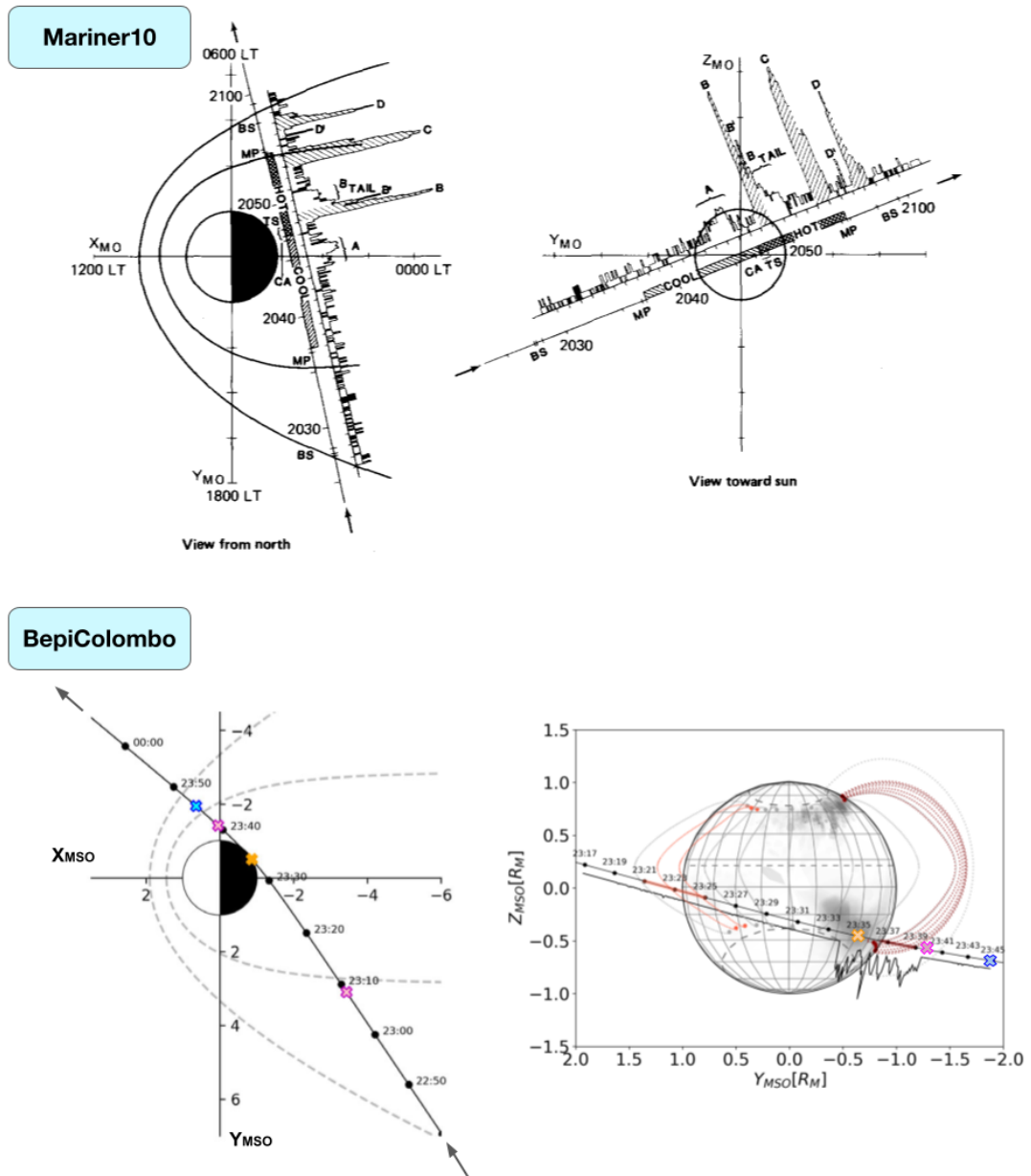
Figure 3.3: Electron observations at Mercury during Mariner10 (top panel) and BepiColombo (bottom panel) first Mercury flybys. *Top panel*: Mariner10 trajectory 29th Mar. 1974. The hatched and cross-hatched areas indicate cool and hot plasma regions, respectively. Offset from the trajectory curve is the ID1 counting rate in log scale. The shaded portion of the ID1 counting rate identifies electron fluxes with energies > 35 keV (due to pulse pile-up), otherwise energies are > 170 keV. Figure adapted from Christon (1987, Fig. 1 therein). *Bottom panel*: BepiColombo trajectory 1st Oct. 2021. The pink, blue and orange crosses indicate the magnetopause crossings, the bow shock crossing, and the closest approach, respectively. In the right panel, the trajectory is shown from the nightside looking towards the Sun. X-ray observations by MESSSENGER/XRS (Lindsay et al., 2016) are shown onto the surface of the planet. Magnetic field lines from the KT17 model (Korth et al., 2017) connecting the trajectory to the surface are also shown. Offset from the trajectory curve is the MPPE/MEA2 count in the energy range $1 - 4$ keV. Figure adapted from Aizawa et al. (2023, Fig.1 and 5 therein).
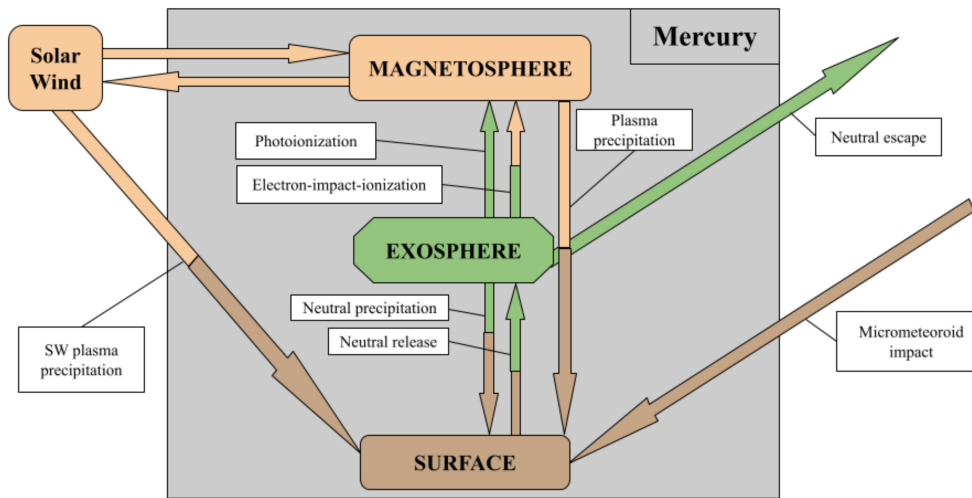
Figure 3.4: Schematic representation of the different parts of Mercury's environment and the interactions between them (list not exhaustive). Different colors indicate different state of the matter (orange is plasma, green is neutral atoms, and brown is solid rocks). Figure adapted from Milillo et al. (2005, Fig. 1 therein).

three environments have completely different physical properties and interact in a complex fashion to generate the bizarre Hermean system. Fig. 3.4 shows a schematic representation of this interaction.

The exosphere of Mercury has a density of $\sim 10^5$ atoms/cm^3 (for comparison, Earth's atmosphere has a density of $\sim 10^{19}$ atoms/cm^3) with a scale height ranging from ~ 10 km (for Sodium) to ~ 1000 km (for Hydrogen). Given this very low density, atom-atom collisions are rare, and the atoms in the exosphere follow ballistic trajectories without mutual collisions. For this reason, the exosphere is never at equilibrium; its dynamics results from the sum of production from the surface and loss into space. The neutral atoms are produced from the surface through various processes, e.g. ion sputtering, micro-meteoroid impact vaporization, thermal desorption, and photon- or electron-stimulated desorption (Gamborino et al., 2019; Exner et al., 2020). All these processes are of interest in the discussion of the results of this work concerning plasma precipitation Sect. 5.4-5.5. The released atoms are then lost into space when their velocity reaches the escape velocity of Mercury (roughly 4 km/s). From in situ and ground-based observations, we know that Mercury's exosphere is composed of hydrogen (H) and helium (He) (Broadfoot et al., 1976), sodium (Na) (A. Potter and T. Morgan, 1985), potassium (K) (A. E. Potter and T. H. Morgan, 1986), calcium (Ca) (Bida et al., 2000), magnesium (Mg) (McClintock et al., 2009), manganese (Mn) (Vervack et al., 2016), and aluminium (Al) (Bida and R. M. Killen, 2017). The aforementioned eight elements, plus Oxygen (O) and

Properties		O	Na	Mg	Al	Si	S	Ca	Fe
Mass [amu]		16	23	24	27	28	32	40	56
Density [wt%]		40	4	15	7	27	2	4	1
Density [10^{20} cm^{-3}]		450	65	250	130	500	23	46	5

Table 3.3: Surface composition derived from McCoy et al. (2018, Tab. 1 therein), assuming a mean surface mass density of 3 g/cm^3.

Silicon (Si)[11], are used to study electron impact ionization of exospheric atoms in Sect. 5.4 (the cross sections for this process are given in Sect. 2.2.4). The exosphere of Mercury is not able to shield the surface against particles or radiation coming from space (as it does Earth's atmosphere), but the neutral exosphere is a useful proxy to monitor the state of the Hermean system using both in situ instruments (McClintock and Lankton, 2007) and ground-based telescopes (Leblanc et al., 2008; Mangano et al., 2015; Orsini et al., 2018). Unique among the Solar System planets, the surface-bounded exosphere of Mercury presents many similarities with the exosphere of the Moon and of the Galilean satellites of Jupiter (Io, Callisto, Europa and Ganymede).

Mercury's surface is enriched in magnesium (Mg) and sulfur (S), and depleted in aluminium (Al), calcium (Ca), and iron (Fe), as compared to the other terrestrial planets (McCoy et al., 2018; Nittler et al., 2018; Nittler and Weider, 2019). The mean surface composition of Mercury, shown in Tab. 3.3, is be used in Sect. 5.4 to compute the flux of emitted X-rays from the surface via XRF (see Sect. 2.2.4). The composition in Tab. 3.3 indicates that Mercury formed under more chemically reducing conditions as compared to the other planets, but a comprehensive understanding of Mercury's formation history is still lacking at present. Mercury's surface is the window onto the planet's origin and evolution. For this reason understanding the surface mineralogical and chemical composition, as well as its geological and geophysical structure is of paramount importance. However, the remotely-sensed properties of the surface can be hidden by plasma and micro-meteoroid precipitation. For instance, a piece of rock exposed to strong ion or micro-meteoroid fluxes becomes darker (lower albedo), acquires a more red color (higher reflectivity at higher wavelengths in the visible range), and show less prominent absorption bands (lower band depths) (Zeller and Ronca, 1967; Noble and Pieters, 2003; Vernazza et al., 2009; Gaffey, 2010; Domingue et al., 2014). The sum of these processes is typically referred to as "space weathering" (Pieters and Noble, 2016). Mercury is a laboratory for space weathering processes with unique properties among the Solar System bodies. Observations of Mercury's surface allow us to test our current knowledge of space weathering processes, adding to comparisons with other airless bodies in the Solar System (such as the Moon or the main belt Asteroids). Such comparative space weathering studies allow to grasp

---

[11]We decided to add O and Si since, albeit not directly detected in the exosphere, these elements are very abundant onto the surface and they can be released in the exosphere at some point.

the more profound nature of this process by exploring a wider range of the parameter space. A discussion on the difference between space weathering induced by plasma irradiation at Mercury, the Moon and Asteroids is given in Sect. 5.5.

All in all, Mercury's ionized, neutral and solid environments are affected by a complex mix of interacting physical processes. Here below, I list the most important interactions between the plasma environment and the other parts of the Hermean system[12].

- **Magnetosphere-Exosphere**: neutral atoms in the exosphere become ionized, and therefore part of the magnetosphere, via *photoionization* and *electron-impact ionization*. Moreover, *charge-exchange* (not considered in this study) between ions and neutrals is an important process at Mercury responsible for the formation of energetic neutral atoms (e.g, Szabo et al. 2023). In the formulas below, exospheric neutrals are indicated as N_a, and photons as ν.

$$N_a + \nu \rightarrow N_a^+ + e^- \qquad \text{Photoionization} \qquad (3.1)$$
$$N_a + e^- \rightarrow N_a^+ + e^- + e^- \qquad \text{Electron-impact ionization} \qquad (3.2)$$
$$N_a + H^+ \rightarrow N_a^+ + H \qquad \text{Charge-exchange (not considered)} \qquad (3.3)$$
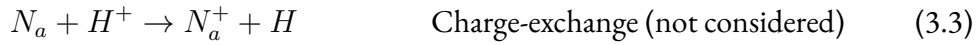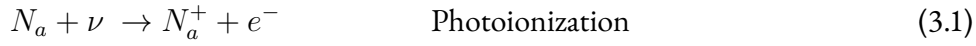
- **Magnetosphere-Surface**: plasma precipitation onto the surface is responsible for the emission of neutral atoms in the exosphere and ions in the magnetosphere via *ion sputtering* and *electron-stimulated desorption (ESD)*. Moreover, at Mercury, ion precipitation alters the spectral properties of the surface contributing to *space weathering*. Also, high-energy electrons precipitating from the magnetosphere onto the surface drive the emission of X-rays via *X-ray fluorescence*. In the formulas below, the surface is indicated as "surf.".

$$H^+ + \text{surf.} \rightarrow N_a + N_a^+ + \text{surf.} \qquad \text{Ion sputtering} \qquad (3.4)$$
$$e^- + \text{surf.} \rightarrow N_a + N_a^+ + \text{surf.} \qquad \text{ESD} \qquad (3.5)$$
$$H^+ + \text{surf.} \rightarrow \text{surf.} \qquad \text{Space weathering} \qquad (3.6)$$
$$e^- + \text{surf.} \rightarrow \nu + \text{surf.} \qquad \text{X-ray fluorescence} \qquad (3.7)$$

---

[12]I do not include here the interactions between the neutral exosphere and the surface because this is out of the scope of this work.

4 Methods: fully-kinetic numerical simulations

In situ observations of space plasmas at electron kinetic scales are now attainable with state-of-the-art plasma instruments. For this reason, numerical simulations including the electron kinetic physics are needed to interpret such observations and to understand their feedback on the larger scales. Fully-kinetic simulations include the electron kinetic physics self-consistently by solving the Vlasov-Maxwell system of equations (2.7)-(2.10). In this work, I use two fully-kinetic numerical codes to run both local and global simulations of the planet Mercury. Local simulations zoom on a small region of the magnetosphere (of the order of 100 km) centered around a plasma boundary (e.g. the magnetopause). Global simulations include the dynamics of the whole system (of the order of 3000 km), from the solar wind to the surface of the planet. In this chapter, I present the simulation codes (Sect. 4.1), the caveats of these codes (Sect. 4.2), and the simulation setup (Sect. 4.3). This last section includes an extensive presentation of my contributions to the code iPIC3D that enabled me to build the first global fully-kinetic model of Mercury's magnetosphere (Sect. 4.3.3).

4.1 The Particle-In-Cell numerical scheme

The Vlasov-Maxwell system of equations (2.7)-(2.10) is solved numerically using the Particle-In-Cell, namely PIC, numerical scheme (Hockney and Eastwood, 1988; Birdsall and Langdon, 1991). In the PIC scheme, the distribution function of each species $f_s(\mathbf{x}, \mathbf{v}, t)$ is split into N_s "macro-particles", each one of those corresponding to a Dirac delta in velocity space and a diffuse cloud in real space:

$$f_s = \sum_{p=1}^{N_s} w_p S(\mathbf{x} - \mathbf{x}_p(t))\delta(\mathbf{v} - \mathbf{v}_p(t)) \tag{4.1}$$

Here, each macro-particle has weight w_p, position $\mathbf{x}_p$ and velocity $\mathbf{v}_p$. The shape function $S(\mathbf{x})$ is symmetric, with compact support, and with normalization $\int S(\mathbf{x})d\mathbf{x} = 1$[1]. From Eq. (4.1) and the Vlasov equation (2.7), it can be shown that each macro-particle obeys the following equations of motion:

$$\frac{d\mathbf{x}_p}{dt} = \mathbf{v}_p \tag{4.2}$$

$$\frac{d\mathbf{v}_p}{dt} = \frac{q_s}{m_s}(\mathbf{E}_p + \mathbf{v}_p \times \mathbf{B}_p) \tag{4.3}$$

where $\mathbf{E}_p$ and $\mathbf{B}_p$ are the electric and magnetic fields interpolated onto the position of the macro-particle. These are given by:

$$\mathbf{E}_p = \int \mathbf{E}(\mathbf{x})S(\mathbf{x} - \mathbf{x}_p(t))d\mathbf{x} \tag{4.4}$$

$$\mathbf{B}_p = \int \mathbf{B}(\mathbf{x})S(\mathbf{x} - \mathbf{x}_p(t))d\mathbf{x} \tag{4.5}$$

In the PIC approach, the solution of Eqs. (4.2)-(4.3) corresponds to a Lagrangian approach, in which the "chunks" of the distribution functions, i.e. the macro-particles, move in real space. On the contrary, the solution of Maxwell equations (2.8)-(2.10) correspond to an Eulerian approach, in which the fields are solved on a fixed grid (typically a three-dimensional Cartesian grid). Therefore, to couple the motion of the macro-particles (Lagrangian) to Maxwell equations (Eulerian), an interpolation from the macro-particle position in phase space to the fixed cartesian grid has to be performed. This interpolation is used to compute the charge and current densities ρ and $\mathbf{J}$ from the macro-particle positions and velocities, as follows:

$$\rho(\mathbf{x}, t) = \sum_s \rho_s = \sum_s q_s \int f_s d\mathbf{v} = \sum_s q_s \sum_{p=1}^{N_s} w_p S(\mathbf{x} - \mathbf{x}_p(t)) \tag{4.6}$$

$$\mathbf{J}(\mathbf{x}, t) = \sum_s \mathbf{J}_s = \sum_s q_s \int f_s \mathbf{v} d\mathbf{v} = \sum_s q_s \sum_{p=1}^{N_s} w_p S(\mathbf{x} - \mathbf{x}_p(t)) \mathbf{v}_p(t) \tag{4.7}$$

All in all, the system of equations (4.2)-(4.7) plus (2.8)-(2.10) summarizes the PIC scheme to solve the Vlasov-Maxwell system. These equations are solved via an iterative scheme, shown in Fig. 4.1, called the PIC loop. The algorithms adopted in the PIC loop can be either *explicit* or *implicit*. This means that the solution at a new time $(t + dt)$ can be calculated either

---

[1] The detailed implementation of the profile of S differs between different codes. A common choice are b-spline functions of order l (de Boor, 1978).

from the solution at the current time (t) (explicit algorithm) or from both the solution at the current time (t) and at the new time $(t + dt)$ (implicit algorithm). In the following, I briefly present the two numerical algorithms used in this work (SMILEI in Sect. 4.1.1 and iPIC3D in Sect. 4.1.2) characterized by different implementations of the same PIC scheme (explicit and implicit, respectively).
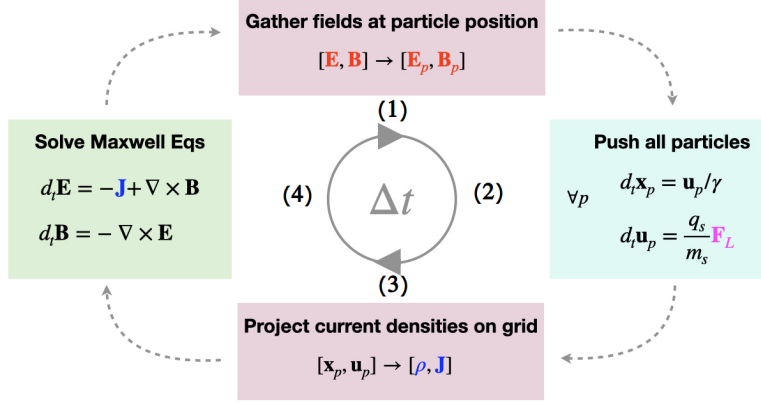

Figure 4.1: Iterative scheme, also called PIC loop, to solve the Vlasov-Maxwell system using the Particle-In-Cell numerical scheme. Figure adapted from Kleij (2023, Fig. 3.2 therein)

4.1.1 THE EXPLICIT PIC CODE SMILEI

The code SMILEI (Derouillat et al., 2018) is a PIC code written in C++ with an explicit electromagnetic algorithm. This open-source code is optimized for massively parallel HPC machines, since it is efficiently parallelized using MPI[2], OpenMP[3], and dynamic load balancing[4]. This code solves the system of equations (4.2)-(4.7) plus (2.8)-(2.10) numerically via the iterative scheme reported in Fig. 4.1 (in the figure, F_L si the Lorentz force and γ is the relativistic Lorentz factor). The code SMILEI is intended as a multi-purpose and collaborative code, and therefore, it allows the user to choose between different algorithms (for example, either the Boris (1970) or the Vay (2008) pusher for the macro-particles). In this section and in Appendix A, I describe only the algorithms that I used in my simulations. Also, SMILEI is build to study relativistic plasmas where the velocity of the particles is of the order of c; since this is not the case for my simulations, the relativistic corrections –although being present in the

---

[2]MPI (Message Passing Interface) is a distributed-memory parallelization standard that allows to run one code on multiple CPU cores that do not share the same memory.

[3]OpenMP (Open Multi-Processing) is an API (application programming interface) that allows to run one code on multiple CPU cores sharing the same memory.

[4]Dynamic load balancing is a technique that distributes the computational load of the whole simulation homogeneously among different processing units (i.e. groups of CPU cores).

code– have a negligible impact on the simulation results (i.e. $\gamma \approx 1$ in Fig. 4.1). Below, I briefly present the algorithms used by SMILEI to perform these four steps (a more detailed description of each step is given in Appendix A).

Step (1): projection of the field at the macro-particle positions. In this step, the integral in Eq. (4.4)-(4.5) is computed numerically using as shape function $S(\mathbf{x})$ a b-spline function of order 2.

Step (2): particle pushing. The macro-particles are pushed using a second order leap-frog integrator (the so-called Boris pusher; Boris 1970).

Step (3): computation of the particle moments on the grid. The current density $\mathbf{J}$ is computed from the macro-particle velocities and positions using the charge-conserving algorithm of Esirkepov (2001).

Step (4): time evolution of the fields on the grid. Using a discrete Yee mesh (Yee, 1966), the electric field is computed from Ampère's law (2.9) and the magnetic field is computed from Faraday's law (2.10).

The Courant-Friedrich-Lewy (CFL) condition that applies to the numerical scheme used in SMILEI is the following:

$$\Delta t_{CFL} \sqrt{\frac{1}{\Delta x^2} + \frac{1}{\Delta y^2} + \frac{1}{\Delta z^2}} = \frac{1}{c} \tag{4.8}$$

This condition implies, from a physical point of view, to resolve the propagation of light waves in the simulation. The Eq. (4.8) sets an upper limit on the timestep for a given grid spacing that severely constraints the numerical efficiency of the code, this point is addressed in details in Sect. 4.2.1.

4.1.2 THE IMPLICIT PIC CODE IPIC3D

The code iPIC3D (Markidis et al., 2010) is a PIC code written in C++ with an implicit electromagnetic algorithm. This code, parallelized using MPI, is also built to run on state-of-the-art HPC machines. iPIC3D is a non-relativistic code and it does not associate a weight to the macro-particles (i.e. $w_p = 1 \,\forall\, p$). The numerical implementation of iPIC3D remains structurally similar to the one of an explicit code, such as the one of SMILEI discussed in the previous section 4.1.1. Nevertheless, the two codes differ substantially in the implementation of the particle pusher (Step 2) and of the solver of Maxwell equations (Step 4). In the following, I discuss briefly the four steps performed in the PIC loop of iPIC3D with a particular

focus on Step (2) and Step (4). More details on the numerical steps of the code are given in Appendix A.

Step (1): projection of the field at the macro-particle positions. Same as SMILEI, but using as shape function $S(\mathbf{x})$ a b-spline function of order zero (this choice leads to the so-called "cloud-in-cell" scheme; Hockney and Eastwood 1988).

Step (2): particle pushing. The macro-particles are pushed from the old to the new timestep using the implicit solver developed by Vu and Brackbill (1992) and Vu and Brackbill (1995).

Step (3): computation of the particle moments on the grid.

Step (4): time evolution of the fields on the grid. The solution of Maxwell equations from the old to the new timestep is found using an implicit, approximated scheme that constitutes the core of the whole code (Mason, 1981; Brackbill and Forslund, 1982; Lapenta et al., 2006; Markidis et al., 2010).

4.2 CAVEATS

Explicit and implicit PIC codes, such as SMILEI and iPIC3D, represent two different numerical approaches to solve the same model: the Vlasov-Maxwell system. On the one hand, while explicit codes are fairly easy to write, they have strong computational constraints that require to resolve small temporal and spatial scales (Sect. 4.2.1), even when not necessarily of interest for the physical process under study. On the other hand, while implicit codes require significantly more complicated implementations and generate more computations, they have much softer numerical constraints relaxing many of the limitations of explicit codes (Sect. 4.2.1). For these two reasons, explicit (implicit) codes are better suited for local (global) simulations. The computational complexity of PIC codes limits the range applicability of the simulations (both local and global). One main limitation is the use of scaled-down parameters (Sect. 4.2.2), and other limitations related to particle noise and spurious numerical effects are also present (Sect. 4.2.3).

4.2.1 NUMERICAL CONSTRAINTS FOR EXPLICIT AND IMPLICIT PIC CODES

In explicit PIC codes, such as SMILEI, the grid resolution dx and timestep dt must be small enough to resolve the smallest physical scales of the system. These scales are the electron kinetic scales: the electron plasma time $\omega_{p,e}^{-1}$ and the Debye length $\lambda_{D,e}$. Moreover, the CFL

condition (Eq. 4.8) requires to resolve the propagation of the fastest waves in the system: the light waves (since the code SMILEI is electromagnetic). These numerical constraints for an explicit electromagnetic PIC code, such as SMILEI, are summarized as follows (Hockney and Eastwood, 1988; Birdsall and Langdon, 1991):

$$\frac{dt}{dx}c < \sqrt{3} \sim 1.7 \tag{4.9}$$

$$dt < \omega_{p,e}^{-1} \tag{4.10}$$

$$dx \lesssim 3\lambda_{D,e} \tag{4.11}$$

considering a three-dimensional simulation with $dx = dy = dz$. These constraints are shown in Fig. 4.2 in green for SMILEI.

Instead, in implicit PIC codes, such as iPIC3D, the numerical constraints of explicit codes are relaxed and the grid resolution and timestep can be larger than the smallest physical scales of the system (e.g. $\omega_{p,e}^{-1}$, $\lambda_{D,e}$), as shown in Fig. 4.2. In such a case, the sub-grid physics (at scales smaller than dx and dt) is artificially altered in the simulation. In particular, implicit PIC algorithms introduce "spectral compression" and "selective damping". When waves have a frequency higher than the Nyquist frequency $2/dt$, their frequency is artificially lowered to the Nyquist frequency (spectral compression), and when the wave period is not resolved by the simulation time step, then the wave is damped (selective damping). The numerical constraints imposed on an implicit PIC code, such as iPIC3D, are the following (Brackbill and Forslund, 1982):

$$0.1 \lesssim \frac{dt}{dx}v_{th,e} < 1 \tag{4.12}$$

$$dt \lesssim 2\pi\omega_{c,e}^{-1} \tag{4.13}$$

The equations (4.12)-(4.13) show the power of an implicit PIC algorithm, as compared to an explicit one (see also Fig. 4.2), assuming that the sub-dx and sub-dt physics does not have an important feedback on the large scale dynamics. To satisfy the numerical constraints imposed by the implicit algorithm, simulations using iPIC3D can employ a fairly coarse grid spacing and large timestep. Two conditions that enable to run three-dimensional (3D) global simulations of a mini-magnetosphere representative of the one of Mercury (described in Sect. 4.3.2).
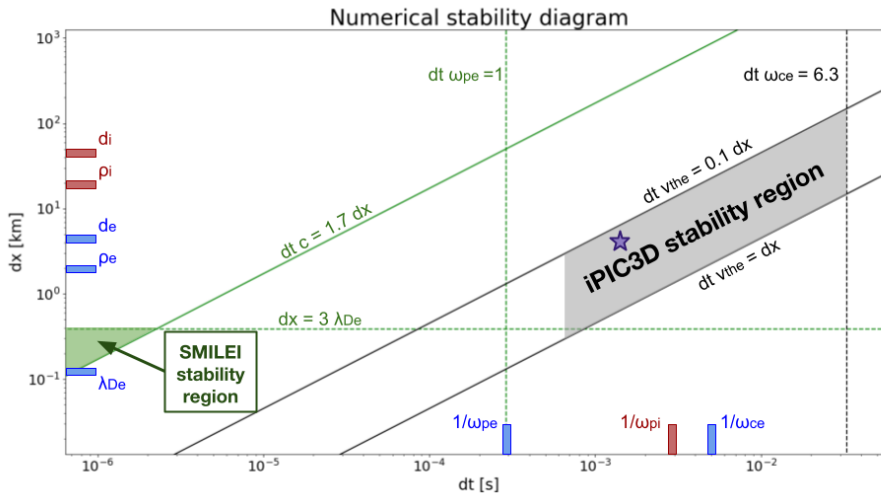
Figure 4.2: Sketch of the region of numerical stability for explicit PIC codes (e.g. SMILEI, in green) and implicit PIC codes (e.g. iPIC3D, in black). Numerical values are taken from the solar wind initialization for the iPIC3D simulations, see Tab. 4.1. The purple star shows the dt and dx values used in the iPIC3D global simulations in this work.

4.2.2 "Scaling-down" as the the strategy to run large-scale PIC simulations

Fully-kinetic simulations of a realistic proton-electron plasma remain computationally challenging, even using an implicit PIC code such as iPIC3D, due to the large scale separation between protons and electrons (i.e. $\varrho_i \approx 40\varrho_e$ and $\omega_{c,i}^{-1} \approx 2000\omega_{c,e}^{-1}$). On top of that, in global simulations the scale separation between global and proton scale (i.e. $L \approx 100\varrho_i$ for Mercury's magnetosphere) makes the situation even worse. For this reason, I operate both a scaling-down of "universal parameters" (in global and local simulations) and of "system parameters" (only in global simulations). In the following, I discuss these two rescaling techniques separately. This discussion is adapted from Lavorenti et al. (2023a, Appendix A therein).

Rescaling universal parameters: rescaling the ion-to-electron mass ratio m_i/m_e and the plasma-to-cyclotron frequency ratio $\omega_{p,i}/\omega_{c,i}$ reduces the separation between ion and electron scales. Kinetic simulations of space plasmas are commonly performed using (i) a reduced mass ratio m_i/m_e of the order of $25 - 400$ (Deca et al., 2017; Deca et al., 2018; Pucci et al., 2018; Parashar et al., 2018; Olshevsky et al., 2018; Deca et al., 2019; Lapenta et al., 2020; Vega et al., 2020; Pezzi et al., 2021; Bacchini et al., 2022; Arró et al., 2022; Lavorenti et al., 2022) instead of the real hydrogen proton-to-electron mass ratio of 1836, and (ii) a reduced $\omega_{p,i}/\omega_{c,i}$ ratio of the order of $10 - 500$ (Parashar et al., 2015b; Parashar et al., 2015a; Deca et al., 2017; Deca et al., 2018; Grošelj

et al., 2018; Parashar and Gary, 2019; Roytershteyn et al., 2019; Arró et al., 2022; Lavorenti et al., 2022) instead of more realistic values of the order of $10^3 - 10^4$ found typically in the solar wind. These two choices reduce drastically the computational time T_{comp} since[5]:

$$T_{comp} \sim \left(\frac{\omega_{p,i}}{\omega_{c,i}}\right)\left(\frac{m_i}{m_e}\right)^{\frac{D+1}{2}} \tag{4.14}$$

where D is the number of spatial dimensions of the system ($D = 3$ in this work). Multiple studies addressed the impact of such rescaled parameters on the plasma dynamics, for instance focusing on magnetic reconnection (Shay and Drake, 1998; Hesse et al., 1999; Le et al., 2013; Haggerty et al., 2015), linear wave theory (Verscharen et al., 2020), and linear beam-plasma instabilities (Bret and Dieckmann, 2010). These studies showed that rescaled parameters only affect the microphysics of the system while leaving unchanged large-scale quantities (e.g. the reconnection rate, the properties of the reconnection outflow, and the wave spectra at scales $\gtrsim 0.2 d_i$). All in all, a "moderate" rescaling of the universal parameters keeping $m_i/m_e \gtrsim 100$ and $\omega_{p,i}/\omega_{c,i} \gtrsim 10$ is expected to weakly affect the simulation results while strongly reducing the computational time required to run the simulation, thus making the simulation feasible. In my simulations, I employ a mass ratio $m_i/m_e = 100$ and a frequency ratio $\omega_{p,i}/\omega_{c,i} = 40$ (in local simulations with SMILEI) and $\omega_{p,i}/\omega_{c,i} = 180$ (in global simulations with iPIC3D). A detailed list of the simulation parameters is given in Tab. 4.1.

Rescaling system parameters: rescaling the size of the system under study reduces the scale separation between global and ion scales. In global simulations of planetary magnetospheres, the planetary radius R (being proportional to the system size) is reduced by a factor ε. At the same time, the magnetic moment of the planet is reduced by a factor ε^3 to preserve the relative shape of the magnetosphere with respect to the planet. This choice strongly reduces the computational time T_{comp} since[6]:

$$T_{comp} \sim \left(\frac{R}{d_i}\right)^{D+1} \tag{4.15}$$

This rescaling technique has been extensively used over the past two decades to study Mercury's magnetosphere using global, 3D hybrid simulations with a scaling parameter $\varepsilon \approx 1/5$ (Trávníček et al., 2007; Trávníček et al., 2009; Trávníček et al., 2010; Schriver et al., 2011b; Herčík et al., 2013; Herčík et al., 2016). Now, the increased computational power of HPC machines (as compared to the ones of $10 - 15$ years ago) enables researchers to run global, 3D hybrid simulations of Mercury using a real-sized planet (Fatemi et al., 2018; Exner et al., 2018; Exner et

---

[5]The scaling in Eq. (4.14) is obtained considering a fully-kinetic simulation with fixed system size L, grid resolution $dx \sim d_e$, time step $dt \sim \omega_{pe}^{-1}$ and total time $T \sim \omega_{ci}^{-1}$.

[6]The scaling in Eq. (4.15) is obtained considering a global fully-kinetic simulation with fixed grid resolution, fixed time step, system size L and total time $T \sim L/V_{SW}$.

al., 2020; Aizawa et al., 2020). Nonetheless, kinetic simulations using a real-sized planet remain extremely challenging at present. For this reason, in my simulations, I use a scaling factor $\varepsilon = 1/10$ to gain four orders of magnitude in computational time while keeping a sufficient separation between global scales ($R \approx 250$ km) and ion scales ($\varrho_i \approx 20$ km in the solar wind).

The implications of these two rescalings (of the universal and system parameters) on the results of the simulations are briefly outlined in the following section 4.2.3, and they are also furtherly discussed in Chap. 5.

4.2.3 OTHER LIMITATIONS OF THE PIC APPROACH AND WAYS TO OVERCOME THEM

Fully-kinetic PIC simulations require large amounts of computational resources. As a consequence, a trade-off between simulation's accuracy and required computational power typically constraints the simulation setup to use. This setup is then subject to few major limitations.

First, rescaled parameters. As stated in the previous section 4.2.2, kinetic simulations require to scale-down both universal parameters (e.g. m_i/m_e, and $\omega_{p,i}/\omega_{c,i}$) as well as system parameters (e.g. R/d_i); these rescalings have an impact on the plasma dynamics. For example, the spectral properties of the lower-hybrid drift instability (LHDI) depend on m_i/m_e (Gary, 1993, Chap.4 therein). The fastest growing mode of the LHDI corresponds to the wavevector $k_{FGM}d_i \approx \sqrt{m_i/m_e}$ and to a frequency $\omega_{FGM}/\omega_{c,i} \approx \sqrt{m_i/m_e}$ (see Sect. 2.2.1). In global simulations, the rescaled parameters affect (i) the maximum energy attainable by an electron in a given acceleration process since the electron mass is a factor ~ 20 higher than the correct one, (ii) the interaction between solar wind electrons and the magnetosphere since the electron thermal Mach number in the solar wind[7] is only ~ 1.2 instead of the correct value ~ 5, and (iii) the adiabatic motion of the ions in the magnetosphere since their gyroradius is unchanged and the system is a factor ~ 10 smaller. Therefore, it is key to fully understand, and control, the effects of these rescaled parameters on the simulation results. A possible strategy to understand such effects is presented in Chap. 6.

Second, macro-particle noise. Noise is much higher in (particle-based) Lagrangian codes, such as PIC codes, than in (grid based) Eulerian codes, such as Vlasov codes (Mangeney et al., 2002). In PIC codes, the discretization of the distribution function introduces a poissonian noise that scales as $1/\sqrt{N_s}$ (Birdsall and Langdon, 1991). Particle noise affects the resolution of the tails of the distribution function in velocity space, and therefore it hides possible wave-particle interactions. Particle noise also generates a stochastic electric field in the simulation. In global

---

[7]The electron thermal Mach number is equal to $v_{th,e}/V_{SW}$.

PIC simulations, low-density regions in the magnetosphere (such as the lobes in the magnetosphere) are populated with a very low number of particles per cell, therefore spurious effects related to particle noise can be important there. To mitigate these problems, I have used 100 (64) particles per cell per species in local SMILEI (global iPIC3D) simulations.

Third, numerical particle heating. In PIC codes, the so-called "finite grid instability" (Birdsall and Langdon, 1991; Markidis et al., 2010) is a numerical instability that appears when the Debye length is not sufficiently resolved by the numerical grid. In such a case, electrons are numerically heated in the simulation, thus hiding possible physical electron heating processes. This effect is more prominent in explicit codes as compared to implicit ones (Brackbill and Forslund, 1982). To avoid this instability, the constraint in Eq. (4.11) for SMILEI and the one on the LHS of Eq. (4.12) for iPIC3D must be fulfilled. Also, higher-order particle interpolations (such as the second-order spline interpolation in SMILEI) suppress the growth rate of this numerical instability (McMillan, 2020).

4.3 Simulations setup

The constraints of explicit and implicit PIC codes discussed in the previous section 4.2 implies that explicit codes are generally better tools to study the high-resolution plasma dynamics using local simulations (described in Sect. 4.3.1), while implicit codes are generally better tools –as they enable to use a coarser resolution– to study the large-scale plasma dynamics using global simulations (described in Sect. 4.3.2). At the end of this section, I present the new boundary conditions developed in the code iPIC3D (see Sect. 4.3.3) that enabled to run global 3D simulations of Mercury's magnetosphere.

4.3.1 Local plasma boundary simulations with SMILEI

The local simulations performed with the code SMILEI model the kinetic plasma dynamics at inhomogeneous layers in space. Differently from past numerical works that addressed this problem using a 2D numerical box (e.g., Hoshino et al. 2001; Nakamura et al. 2017; Dargent et al. 2019), my simulations employ a 3D numerical box to focus on electron acceleration parallel to the local out-of-plane magnetic field (i.e. along the z-axis). The plasmas on the two sides are characterized by different densities, different parallel magnetic fields, and uniform temperature at $t = 0$. The plasma is initialized with zero electric field, zero bulk flow velocity and zero magnetic field shear. These boundaries are representative of typical boundaries in space, such as the magnetopause, with strong density asymmetries between the high-density "magnetosheath" side (hereafter side I) and the low-density "magnetosphere" side (hereafter
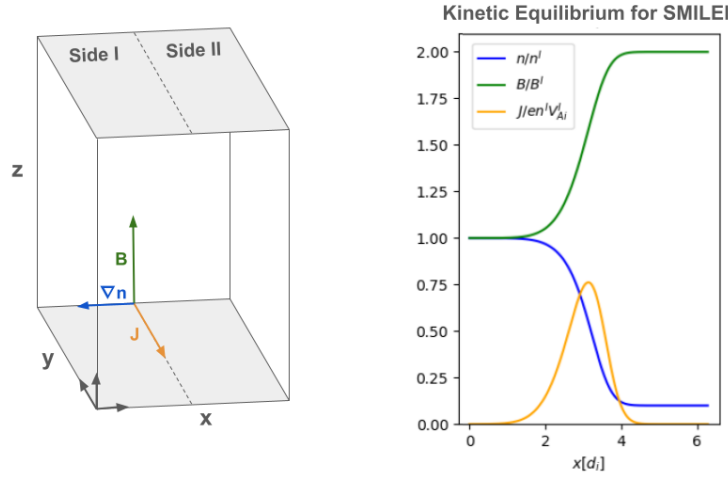
Figure 4.3: Simulation setup SMILEI local simulations of a boundary layer. Left panel: sketch of the numerical box. Right panel: initial profiles along the x-axis of the plasma density (in blue), magnetic field (in green), and plasma current (in orange) for the "strong gradient" simulation.

side II). Magnetic reconnection is suppressed in these simulations because the magnetic fields are parallel on the two sides of the layer.

I initialize the simulations ensuring pressure balance and using the Vlasov equilibrium proposed in Alpers (1969), and subsequently used in Pu et al. (1981). In this equilibrium, the distribution function, for each species, is given by:

$$f_s(x, \mathbf{v}) = \frac{e^{-\mathbf{v}^2/v_{th,s}^2}}{\pi^{3/2} v_{th,s}^3} \left[n^I + \frac{n^{II} - n^I}{2} \left[1 + \mathrm{erf}\left(\frac{w \, q_s/e}{\sqrt{\frac{m_i}{m_s} - w^2}} \frac{p_y}{m_s v_{th,s}} \right) \right] \right] \tag{4.16}$$

where $p_y = m_s v_y + q_s A_y(x)$ is the generalized momentum, and $w < 1$ is an adimensional parameter defining the layer's width. The density, computed as the zero-order moment of the distribution function in Eq. (4.16), reads:

$$n[A_y(x)] = n^I + \frac{n^{II} - n^I}{2} \left[1 + \mathrm{erf}\left(w \frac{e A_y(x)}{m_i v_{thi}} \right) \right] \tag{4.17}$$

The expression for the vector potential $A_y(x)$ is obtained by solving numerically the following ordinary differential equation:

$$B_z(x) = \frac{dA_y(x)}{dx} = \sqrt{8\pi}(PBC - n[A_y(x)]T)^{1/2} \quad \text{with} \quad A_y(L_x/2) = 0 \tag{4.18}$$
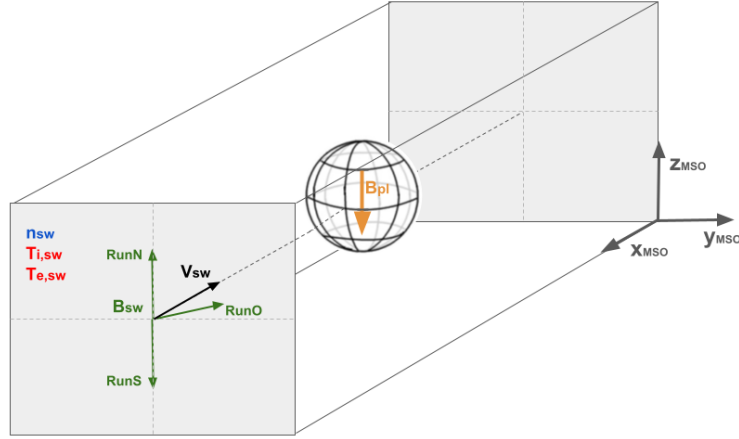
Figure 4.4: Simulation setup for global simulations with the code iPIC3D. RunN, RunS, and RunO indicates three different simulations with purely northward, purely southward and oblique IMF, respectively.

where, $T = T_i + T_e$ is the uniform initial temperature, and PBC is the total initial pressure (homogeneous in the simulation). The numerical parameters are set to have a density asymmetry $n^I/n^{II} = 10$, counterbalanced by a magnetic field asymmetry $B^I/B^{II} = 0.5$. A detailed list of the simulation parameters is shown in Tab. 4.1.

With this setup, two different simulations have been performed using two different layer widths: (i) a steeper boundary case (with $w = 0.98$), hereafter called "strong gradient" simulation, and (ii) a smoother boundary case (with $w = 0.5$) hereafter called "weak gradient" simulation. These parameters are chosen, first, to ensure that the layer's steepness is large enough to drive kinetic instabilities above the PIC noise level, and, second, to drive different saturation mechanisms of the instability. The strong-gradient setup is shown in the right panel of Fig. 4.3.

The boundary conditions are periodic along the y- and z-axis. Along the x-axis, due to the presence of the inhomogeneity, I use the absorbing Silver-Müller conditions for the electromagnetic fields (Barucq and Hanouzet, 1997) and reflective conditions for the particles, both already implemented in the code.

4.3.2 GLOBAL MAGNETOSPHERE SIMULATIONS WITH IPIC3D

The global kinetic simulations performed with the implicit code iPIC3D model the interaction between a laminar flow of plasma (i.e. the solar wind) and a magnetized obstacle (i.e. a

scaled-down version of Mercury). The setup for such an "ab initio" simulation requires to initialize the solar wind plasma with density n_{sw}, velocity V_{sw} along the x-axis, magnetic field $\mathbf{B}_{sw}$, and ion and electron temperatures $T_{i,sw}, T_{e,sw}$ (typical solar wind parameters at Mercury's orbit are discussed extensively in Sect. 3.1.1). The magnetized obstacle is characterized by a radius R, a dipole magnetic field pointing from the north to the south pole with a magnitude B_{surf} at the surface at the equator, and a dipole shift d_{off} along the z-axis. A sketch of this setup is shown in Fig. 4.4. Hereafter to discuss global simulations, I employ the Mercury-centered Solar Orbital (MSO) reference frame, where the x-axis points from the planet center to the sun, the z-axis is anti-parallel to Mercury's magnetic dipole, and the y-axis points from dawn to dusk (see Fig. 4.4). In this reference frame, the origin of the axis is the center of the planet.

At $t = 0$, solar wind particles are homogeneously loaded in a region defined by $r > 3R$ (where $r = \sqrt{x^2 + y^2 + z^2}$). Inside the sphere $r < 3R$ the plasma density is set to zero. The electromagnetic fields are initialized as follows:

$$\mathbf{E}(\mathbf{x}, t = 0) = -\mathbf{V}_{sw} \times \mathbf{B}_{sw} = V_{sw}(\hat{\mathbf{x}} B_{sw,z} - \hat{\mathbf{z}} B_{sw,y}) \tag{4.19}$$

$$\mathbf{B}(\mathbf{x}, t = 0) = \mathbf{B}_{sw} + \mathbf{B}_{pl} \tag{4.20}$$

$$\mathbf{B}_{pl}(\mathbf{x}, t = 0) = -\frac{B_{surf}}{(r/R)^3}\left[\frac{3x\tilde{z}}{r^2}\hat{\mathbf{x}} + \frac{3y\tilde{z}}{r^2}\hat{\mathbf{y}} + \frac{(2\tilde{z}^2 - x^2 - y^2)}{r^2}\hat{\mathbf{z}}\right] \tag{4.21}$$

where $\tilde{z} = (z - d_{off})$ is the shifted z-axis coordinate. The electric field in Eq. (4.19) is initialized according to the ideal Ohm's law (see discussion of ideal MHD model in Sect. 2.1.2) valid in the laminar solar wind flow. For $t > 0$, the solar wind plasma interacts with the magnetic field of the planet $\mathbf{B}_{pl}$ to form a magnetosphere around the obstacle. The simulation is stopped at $t = T$ when the interaction reaches a quasi steady-state. The simulation timescale T corresponds approximately to the solar-wind ballistic time taken to cross the simulation box, $T \approx L_x/V_{sw}$.

With this setup, three different simulations have been performed using the same solar wind parameters but changing *only* the direction of the solar wind magnetic field $\mathbf{B}_{sw}$. These three simulations called RunN, RunS, and RunO are initialized with a purely northward, a purely southward and an oblique IMF, respectively (see Fig. 4.4). On the one hand, RunN and RunS have been extensively investigated during this PhD to obtain the results in Sect. 5.3-5.5. On the other hand, the output of RunO still needs to be fully investigated and the results of this run (presented in Sect. 5.6) should be considered as preliminary. For this reason, RunO does not include a dipole shift (i.e. $d_{off} = 0$). A detailed list of the simulation parameters is given in Tab. 4.1.

The boundary conditions (BC) in global simulations must be set both at the boundaries of the numerical box (external BC) and at the surface of the obstacle/planet (internal BC). Exter-

nal BC are open-absorbing for the electromagnetic fields and open (re-injecting thermalized) for the particles. While, internal BC employ a novel charge-conserving scheme for the particles (see Sect.4.3.3). This set of boundary conditions –that I implemented in iPIC3D to run global simulations– are extensively discussed in the next section 4.3.3.

4.3.3 NEW BOUNDARY CONDITIONS FOR iPIC3D

Global fully-kinetic simulations require a particular care in the implementation of the external and internal boundary conditions (BC). At the boundaries of the numerical box, external BC must be chosen adequately in order to avoid spurious numerical effects while using a numerical box as small as possible. Spurious numerical effects at the box boundaries include, among others, (i) the net accumulation of charge due to the different velocities of ions and electrons, and (ii) the reflection of waves (such as the bow shock wave) impinging on the box boundaries. At the surface of the planet, the internal BC must be chosen adequately to allow a smooth, realistic transition between the ionized and non-ionized parts of the system. At Mercury, the magnetospheric plasma interacts directly with the surface, and therefore the internal BC are of great importance. For these reasons, I worked on the implementation of new boundary conditions in the code iPIC3D for running global simulations. These new BC are described below.

External BC employ a linear simple absorption layer (LSAL) method (Berendeev et al., 2018) to smooth the electromagnetic fields. This smoothing is performed at each timestep on the outermost N_{SAL} cells of the simulation domain, e.g. in the cells $i = 0, 1, 2, ..., N_{SAL}$. A few test runs are typically needed to assess the most suitable value of N_{SAL}, typically in the range $5 - 10$. The LSAL method is build to avoid wave reflection at the boundaries, notably bow shock reflection, while ensuring that the code remains numerically stable. In this method, the magnetic and electric field values in the outermost boundary cells (e.g. $i = 0$) are imposed to be equal to their solar wind values, $\mathbf{B_{sw}}$ and $\mathbf{E_{sw}}$ (defined in Sect. 4.3.2). Then, the magnetic and electric fields in the absorption layer are smoothed as follows:

$$\mathbf{B}_i^{(new)} = \frac{i}{N_{SAL}}\mathbf{B}_i + \mathbf{B}_{SW}\left(1 - \frac{i}{N_{SAL}}\right) \qquad i = 0, 1, 2, ..., N_{SAL} \tag{4.22}$$

$$\mathbf{E}_i^{(new)} = \frac{i}{N_{SAL}}\mathbf{E}_i + \mathbf{E}_{SW}\left(1 - \frac{i}{N_{SAL}}\right) \tag{4.23}$$

After the smoothing, a divergence cleaning routine, see Eqs. (A.35)-(A.36) in Appendix A, is applied onto the magnetic field to ensure that $\text{div}(\mathbf{B}) = 0$ in the absorbing layer. The LSAL smoothing in Eqs. (4.22)-(4.23) is applied to five sides of the box ($x = 0$, $y = 0$, $z = 0$, $y = L_y$, and $z = L_z$), while the anti-sunward side ($x = L_x$) requires a different treatment, as

shown in Fig. 4.5a. On this side, the plasma flows out of the numerical box and therefore, the magnetic and electric fields do not need to be smoothed to their solar wind values. Instead, on that side the fields are set as follows:

$$\mathbf{B}_i^{(new)} = \mathbf{B}_{N_x - n_p - 1} \qquad i = N_x - n_p, N_x - n_p + 1, ..., N_x \qquad (4.24)$$

$$\mathbf{E}_i^{(new)} = \mathbf{E}_{N_x - n_p - 1} \qquad (4.25)$$

where $n_p < N_{SAL}$ is the width of the particle repopulation layer, typically of the order of $2 - 3$ cells (layer shown in Fig. 4.5a in orange)
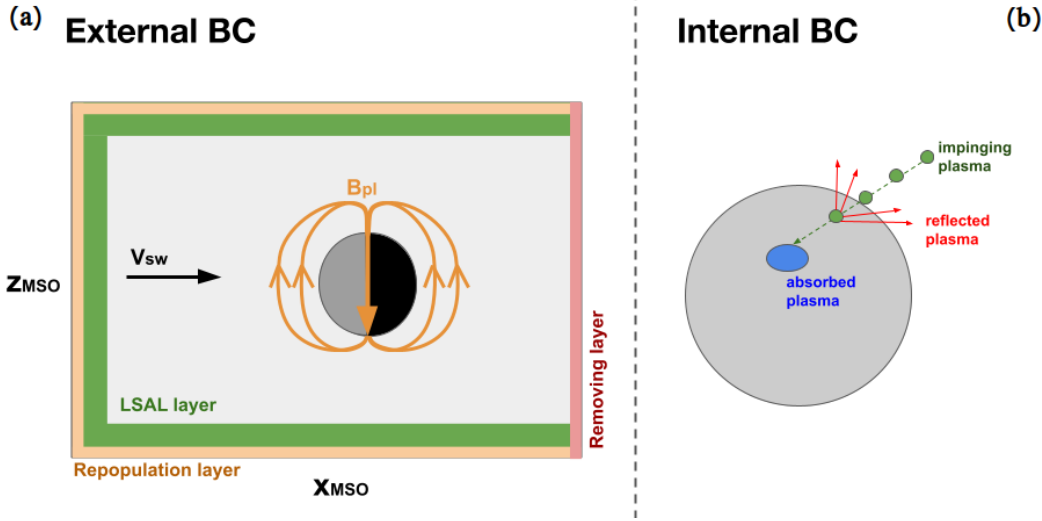
Figure 4.5: Sketch of the new boundary conditions (BC) implemented for global simulations with iPIC3D.

The external BC for the particles are implemented in a layer of width n_p (called repopulation layer) on all sides of the box. Particles in the repopulation layer are removed from the simulation and replaced with "solar wind particles". Solar wind particles mean 64 particles per cell equispaced in the three spatial directions and with a speed issued randomly from a maxwellian distribution with temperature $T_{s,SW}$ and mean speed V_{SW}. An exception is made for the anti-sunward side of the box $x = L_x$ from which particles are removed but not injected (red layer in Fig. 4.5a). Analogously to the fields, the particles on this side require a special treatment because the plasma at this boundary is not solar wind plasma but the one in the lobes/magnetotail. This open BC for the particles ensure a smooth transition from the plasma interacting with the planet (green and grey regions in Fig. 4.5a) to the solar wind plasma (orange region in Fig. 4.5a). After multiple test runs, I verified that the external BC ensure a smooth transition as long as the magnetopause is sufficiently far (of the order of $3 - 4 \, R$) from the external boundaries. For Mercury, this implies a simulation box of the

order of $L \approx 10\,R$. If a too small box is used in the simulations, then the external BC become unstable. The open BC for the particle and the LSAL method for the fields work in tandem to ensure that the injected particles in the repopulation layer (orange in Fig. 4.5a) are consistent with the smoothed fields that tend asymptotically to $\mathbf{E}_{SW}$ and $\mathbf{B}_{SW}$ in the LSAL layer (green in Fig. 4.5a).

Internal BC handle the plasma interacting with the planet, as shown in Fig. 4.5b. Since fully-kinetic models do not impose quasi-neutrality but they treat the two species (ions and electrons) independently, it is important to avoid the generation of a spurious net charge on the planet surface. In this work, I developed a charge-balanced scheme for the particles falling into the planet (assuming ions and electrons with charges q and $-q$). This method is divided into three main steps: (i) each MPI task computes the net charge precipitated onto the surface $\Delta Q = Q_i - Q_e$ (green particles in Fig. 4.5), (ii) a number of particles $\Delta Q/q$ that balances the precipitated charge is selected randomly among the ensemble of precipitated particles, (iii) these selected particles are reflected from the planet surface back into the simulation domain (red particles in Fig. 4.5). The reflected particles are ejected back from the surface by re-sampling the angle $\theta = \cos^{-1}(\mathbf{v}_p \cdot \hat{\mathbf{r}})$ from a random distribution, therefore the reflected particles conserve their kinetic energy. This method ensures that the same amount of positively and negatively charged particles is removed from the simulation box at the internal boundary. Moreover, the excess of electron flux impinging onto the planetary surface is reflected in a way that actually mimics the sub-grid plasma-surface interaction happening on length scales of the order of the Debye length. Indeed, the strength of implicit PIC codes resides in the possibility of not resolving such small scales, so that the associated physical processes (e.g. surface charging and the associated plasma sheath) are usually deliberately chosen not to be resolved. Instead, such processes are typically addressed using explicit PIC codes for surface-plasma interactions, e.g. Usui et al. (2017) and Nakazono and Miyake (2023). The results of such explicit PIC simulations can help to improve the internal BC of our model, an interesting topic to be addressed by future works.

The original iPIC3D code is available at github.com/KTH-HPC (n.d.), while the modified version of the code is available at github.com/flavorenti (n.d.). To fully exploit the capabilities of these codes, they typically run on large HPC machines (as the machine TGCC-Irene in this work). To be able to access HPC machines, applications to national grants for computational time in France were send regularly during my PhD. I actively participated to the drafting and editing of these proposals, where I was formally identified as "technical manager".

Physical parameters	Formula	Local simu		Global simu	
		Natural units	SI units	Natural units	SI units
Density	n	$1.0 \mid 0.1\, n^I$	$100 \mid 10\,\text{cm}^{-3}$	$1.0\, n_{sw}$	$30\,\text{cm}^{-3}$
Magnetic field	B	$1.0 \mid 2.0\, B^I$	$50 \mid 100\,\text{nT}$	$1.0\, B_{sw}$	$20\,\text{nT}$
Flow velocity	V_x	0.0	0.0	5.0	$400\,\text{km/s}$
Ion temperature	T_i	0.8	$105\,\text{eV}$	0.3	$21.5\,\text{eV}$
Electron temperature	T_e	0.8	$105\,\text{eV}$	0.3	$21.5\,\text{eV}$
Gradient width	w	0.98 (strong)		–	–
		0.50 (weak)		–	–
Planet radius	R	–		5.5	$230\,\text{km}$
Dipole offset	d_{off}	–		1.1	$46\,\text{km (RuN-RunS)}$
				0	0 (RunO)
Planet dipole field	B_{surf}	–		10.0	$200\,\text{nT}$
Magnetic field versor	$(B_x, B_y, B_z)/B$	$(0,0,+1)$		$(0,0,+1)$ (RunN)	
				$(0,0,-1)$ (RunS)	
				$(-0.8,+0.6,+0.1)$ (RunO)	
Derived parameters					
Alfvén speed	$V_{A,i} = B/\sqrt{m_i n}$	$1.0 \mid 6.3$	$110 \mid 690\,\text{km/s}$	1.0	$80\,\text{km/s}$
Ion sound speed ($\gamma = 1$)	$V_s = \sqrt{\gamma T_e/m_i}$	0.9	$100\,\text{km/s}$	0.6	$50\,\text{km/s}$
Total pressure	PBC	2.2	$4.4\,\text{nPa}$	1.1	$0.4\,\text{nPa}$
Plasma beta	$\beta = 2n(T_i + T_e)/B^2$	$3.3 \mid 0.1$		1.3	
Solar-wind ram pressure	$m_i n V_x^2$	–		25.0	$8.2\,\text{nPa}$
Solar-wind number flux	$\mathcal{F}_{sw} = n V_x$	–		5.0	$1.2 \cdot 10^9\,\text{cm}^{-2}\text{s}^{-1}$
Solar-wind energy flux	$\mathcal{E}_{sw} = n V_x T_e$	–		1.5	$2.4 \cdot 10^{10}\,\text{cm}^{-2}\text{s}^{-1}\text{eV}$
Cone angle	$\arccos(-B_x/B)$	–		$+36°$ (RunO)	
Clock angle	$\arctan(-B_y/B_z)$	–		$-84°$ (RunO)	
Parker angle	$\arctan(-B_y/B_x)$	–		$+36°$ (RunO)	
Numerical parameters					
Box dimensions	$L_x = (x_{min}, x_{max})$	$(0, 2\pi)$	$(0, 145)\,\text{km}$	$(-49.5, +33.0)$	$(-2080, +1400)\,\text{km}$
	$L_y = (y_{min}, y_{max})$	$(0, 2\pi)$	$(0, 145)\,\text{km}$	$(-33.0, +33.0)$	$(-1400, +1400)\,\text{km}$
	$L_z = (z_{min}, z_{max})$	$(0, 20\pi)$	$(0, 1450)\,\text{km}$	$(-33.0, +33.0)$	$(-1400, +1400)\,\text{km}$
Number of cells	(N_x, N_y, N_z)	$(288, 288, 1472)$		$(960, 768, 768)$	
Spatial resolution	$\max\{dx, dy, dz\}$	0.04	$0.9\,\text{km}$	0.08	$3.4\,\text{km}$
Time resolution	dt	$3.4 \cdot 10^{-4}$	$0.07\,\text{ms}$	$28 \cdot 10^{-4}$	$1.5\,\text{ms}$
Particles/cell/species	PPC	100		64	
Rescaled parameters					
Ion-to-electron mass ratio	m_i/m_e	$1836 \rightarrow 100$		$1836 \rightarrow 100$	
Plasma-to-cyclotron ratio	$\omega_{p,i}/\omega_{c,i}$	$2740 \mid 430 \rightarrow 40 \mid 6.3$		$3750 \rightarrow 178$	
Planet-to-gyro radius ratio	R/ϱ_i	–		$100 \rightarrow 10$	

Table 4.1: Parameters used to run the simulations discussed in this document. With the entry "Natural units", I mean the ion plasma units ($\omega_{c,i}$, d_i, and $V_{A,i}$, see Sect. 2.1.1) derived from the density and magnetic field in the first two rows. For local simulations, I show the asymptotic values on both sides of the layer separated by the symbol $\mid$ (meaning $sideI - value \mid sideII - value$). At the bottom of the table, I show both real and rescaled values of the parameters separated by the symbol $\rightarrow$ (meaning $real - value \rightarrow rescaled - value$). For the definition of clock, cone, and parker angles see Sect. 3.1.1.

5 RESULTS

In this chapter, I present the results of this PhD work to provide a new picture of the kinetic processes accelerating electrons in a "small" magnetosphere, such as the one of Mercury. First, a summary of the published results is presented in Sect. 5.1. Second, the entire body of the papers published during the PhD is reported in Sect. 5.2-5.5 following the chronological order of publication. Third, other results that complement the published results of this work are presented in Sect. 5.6; in this last section, I present both (i) unpublished results supporting the conclusions of this PhD (Sect. 5.6.1-5.6.3), and (ii) a short summary of my contributions to other works not directly part of this PhD topic (Sect. 5.6.4).

5.1 SUMMARY OF THE PUBLISHED RESULTS, OR THE FATE OF SOLAR WIND ELECTRONS ENCOUNTERING A MAGNETOSPHERE

In this section, I summarize the results published in Lavorenti et al. (2021), Lavorenti et al. (2022), Lavorenti et al. (2023a), and Lavorenti et al. (2023b) to present a new picture of the interaction between the solar wind and a magnetosphere, notably the one of Mercury, obtained using fully-kinetic self-consistent plasma models. This section focuses on the kinetic dynamics of electrons as they travel from the solar wind into the magnetosphere, and eventually onto the planet's surface. The presentation of the results below follows a sequential approach focusing, in order, on the (i) bow shock, (ii) magnetopause, (iii) magnetotail reconnection, and (iv) precipitation onto the surface.

A bow shock forms in front of all planets in the Solar System because the solar wind speed (of the order of 400 km/s) is higher than the Alfvén $V_{A,i}$ and sound V_S speed (see values in Tab. 3.1). At the bow shock, the solar wind plasma slows down to reach a velocity of the order of the downstream magnetosonic speed $V_M = \sqrt{V_{A,i}^2 + V_S^2}$ (Belmont et al., 2019), of the order of 100 km/s at Mercury. Therefore, the ion and electron kinetic energies K_i and K_e (defined in Sect. 2.1.4) are reduced by roughly one order of magnitude when crossing

the shock. On the contrary, the thermal energy of ions and electrons mildly increases downstream of the bow shock, roughly by a factor x2 (see, for example, Fig.3 in Sect. 5.3). All in all, the plasma downstream of the bow shock is characterized by (i) ions with a kinetic energy ~ 100 eV and a thermal energy ~ 50 eV, and (ii) electrons with a negligible kinetic energy (due to their smaller mass) and a thermal energy ~ 50 eV. These results are published in Lavorenti et al. (2022) (Sect. 5.3 in this document) focusing on the global distribution of electrons in the magnetosphere, and in Lavorenti et al. (2023b) (Sect. 5.5 in this document) focusing on the distribution of ions and electrons at the surface. This result for ions brings an important contribution to plasma-surface interaction studies by showing that there exist a significant ion population inside the magnetosphere with an energy of roughly 100 eV. This low-energy ion population precipitates onto the surface at high latitudes and it is expected to reduce the overall yield of ion sputtering (a release process for the exosphere of Mercury, see Sect. 3.3). The existence of this ion population, albeit not representing a discovery from a plasma physics perspective, is discussed for the first time in Lavorenti et al. (2023b) (Sect. 5.5 in this document) in the context of plasma-surface interactions at Mercury, thus pointing out the need to account for such low-energy ions in future exospheric models that, insofar, have modelled ions with a fixed energy of 1 keV. Moreover, this result for electrons is useful to interpret in situ observations by the electron sensor MEA onboard BepiColombo/Mio satellite. Virtual BepiColombo observations along the first Mercury flyby trajectory –published in Lavorenti et al. (2022, Sect. 5 therein)– will be compared to the recently-obtained and fully-calibrated data of MEA in Sect. 5.6.1 of this document. The decelerated plasma downstream of the bow shock, then encounters a "steep" plasma boundary characterized by strong plasma dynamics and instabilities, this is the magnetopause.

The magnetopause is the boundary between the shocked solar wind plasma (forming the magnetosheath) and the inner magnetosphere, as shown in Fig. 1.1. This boundary is characterized by a strongly asymmetric plasma configuration that drives different instabilities such as magnetic reconnection (see Sect. 2.2.2), and the lower-hybrid-drift instability (hereafter LHDI, see Sect. 2.2.1). First, magnetic reconnection at the magnetopause increases the thermal energy of electrons in the outflow. In the case of southward IMF, reconnection at the nose of the magnetopause leads to an increase of roughly 100 eV; instead, in the case of northward IMF, reconnection in the lobes leads to an increase of roughly 1 keV (Lavorenti et al., 2022) (Sect. 5.3 in this document). The electron acceleration at the magnetopause (and in the magnetosphere in general) is studied in Lavorenti et al. (2022) using global fully-kinetic simulations. Such new simulations are validated in Lavorenti et al. (2022) using the mean bow shock and magnetopause boundaries obtained by MESSENGER data (Winslow et al., 2013). In Sect. 5.6, I present a new validation of the simulation results using the state-of-the-art steady-state magnetic field KT17 model (Korth et al., 2017). Second, the LHDI resonates with electrons at the magnetopause to increase their energy (thermal plus kinetic) by a factor x2 at maximum (Lavorenti et al., 2021) (Sect. 5.2 in this document). Such maximum acceleration is obtained in a "steep" boundary configuration, i.e. with a magnetopause width of the order or shorter

than the ion gyroradius. In such a case, electrons are efficiently accelerated parallel to the local magnetic field, thus generating an anisotropy with $T_{\parallel,e} > T_{\perp,e}$. The nonlinear acceleration of electrons by the LHDI is studied in Lavorenti et al. (2021) using both a particle-in-cell (PIC) local plasma model and an extended quasilinear (eQL) semi-analytical model. While, the first model is constrained to use reduced parameters (e.g. mass ratio $m_i/m_e = 100$), the second model can use realistic plasma parameters. This two-model approach enabled me, in a first step, to validate the eQL model onto the PIC results using rescaled parameters, and then, in a second step, to extrapolate the eQL model to realistic plasma parameters (e.g. $m_i/m_e = 1836$). A similar semi-analytical approach is also envisaged to study global magnetospheric processes, such as plasma precipitation, as discussed in Chap. 6. A fraction of the plasma interacting with the magnetopause gets advected to the nightside of the magnetosphere, in the lobes, and eventually in the magnetotail. This region is characterized by symmetric magnetic reconnection in the plasma sheet (sketched in Fig. 1.1), and a substantial energization of the plasma.

Magnetic reconnection (see Sect. 2.2.2) in the tail of the magnetosphere is the main source of energetic electrons in the inner magnetosphere of Mercury, under southward IMF conditions. From the X-line in the tail (positioned at around $X \approx -2\ R_M$), electrons with an energy of the order of 1 keV are ejected planetward (Lavorenti et al., 2022) (Sect. 5.3 in this document). The trajectories of these high-energy electrons follow an adiabatic motion inside the magnetosphere, characterized by a bounce motion parallel to the magnetic field and a curvature drift perpendicular to it (see Sect. 2.2.3). Electrons with a sufficiently large pitch angle bounce back and forth along magnetic field lines, as they drift dawnward under the effect of the curvature drift. Electrons with a "small" pitch angle are doomed to precipitate onto the surface. For instance, electrons with a pitch angle smaller than 45° (in the nightside) and 75° (in the dayside) precipitate onto the surface (Lavorenti et al., 2022, Fig.5 therein). This kind of precipitation hinders the formation of a stable ring current (such as Earth's one) around Mercury. Instead, I argue that Mercury presents a "partial ring current" limited to the nightside and strongly dependent on the solar wind conditions. The $\sim$ 1 keV electrons ejected from the X-line in the tail populate this partial ring current (PRC). In Lavorenti et al. (2022), I show evidence that those electrons were observed by Mariner10/PLS and Mio/MEA instruments during their respective first Mercury flybys (see also the new results in Sect. 5.6.1). Further indirect evidence of these electrons, precipitating from the PRC onto the surface, can be found by observing plasma-exosphere and plasma-surface interaction processes.

Precipitation of plasma onto the surface of Mercury is an important process that couples the magnetosphere with the exosphere and surface (see Sect. 3.3). I present the first maps of electron precipitation onto the surface of Mercury using both local-time coordinates (Lavorenti et al., 2023a) (Sect. 5.4 in this document) and geographical coordinates (Lavorenti et al., 2023b) (Sect. 5.5 in this document). In these papers, I show that electrons precipitate inhomogeneously onto the surface with a flux comparable to the solar wind flux $n_{sw}V_{sw} \approx$

10^9 cm^{-2} s^{-1} and with energies up to a few keVs. Electron precipitation maps are shown in Lavorenti et al. (2023a, Fig. 1 therein), and electron distribution functions at the surface are shown in Lavorenti et al. (2023b, Fig. 7 therein). All in all, the magnetosphere acts as a filter and as an accelerator for electrons –dependent on the IMF direction. First, the magnetosphere is a filter that reduces the integrated flux onto the surface by roughly one order of magnitude (as compared to an unmagnetized planet). Second, the magnetosphere is an accelerator that generates a high-energy tail in the distribution function of electrons when passing from the solar wind down to the surface (a consequence of magnetic reconnection at the magnetoapuse and/or in the tail). In Lavorenti et al. (2023a) and Lavorenti et al. (2023b), I use electron (and ion) precipitation maps to study *three* different processes relevant for the Hermean environment:

1. **Electron Impact Ionization**

   Precipitating electrons interact with the deepest layers of the exosphere of Mercury to ionize the atoms. Electron impact ionization (hereafter EII, see Sect. 2.2.4) is usually considered a negligible process in models for Mercury's exosphere, where photoionization is considered the main ionization process. However in Lavorenti et al. (2023a), I show that EII is not to be considered negligible for H, He, O and Mn; since those species have a relatively high cross section for EII and a low photoionization rate. In particular for these species, EII is (i) locally as important as photoionization on the dayside, and (ii) the main ionization process on the nightside. Differently from photoionization, EII is localized in the regions of highest electron flux, thus EII is inhomogeneously distributed onto the surface and variable in time, in association to the upstream IMF conditions. My results show the need for global models of Mercury's exosphere to include EII of H, He, O and Mn, while safely neglecting EII for Na, Mg, Al, Si, K, and Ca.

2. **Electron-induced X-ray fluorescence**

   When hitting the surface of Mercury, electrons with an energy higher than ~ 500 eV induce the emission of photons from the regolith via X-ray fluorescence (hereafter XRF, see Sect. 2.2.4). In Lavorenti et al. (2023a), I show that electron-induced XRF emissions are driven at Mercury with flux of the order of 10^7 photons cm^{-2} s^{-1}, mostly coming from the Oxygen line. This photon flux is positively correlated with the energy flux of precipitating electrons, and therefore it is also strongly dependent on the upstream solar wind conditions, notably the IMF direction. This result corroborates and provides the physical origin of the X-ray "aurora-like" emissions observed by MESSENGER/XRS instrument; while at the same time, paving the way for future observations by the BepiColombo/MIXS instrument (Bunce et al., 2020).

3. **Space weathering**

Irradiation of a rock sample by an energetic plasma beam contributes to the space weathering of the sample (see Sect. 3.3). In Lavorenti et al. (2023b), I show plasma precipitation maps integrated in time over one Mercury year (two full orbits) to assess the typical fluence and energy spectrum of solar wind particles onto the surface of Mercury. These maps show that the magnetic field of Mercury screens the surface from a large fraction of the impinging plasma (roughly 90%), and it affects the precipitation in an inhomogeneous way. For instance, the magnetic field forces high (low) energy particles to precipitate at low (high) latitudes. I found that, on average, the surface of Mercury is exposed to $\sim 2 \times 10^{14}$ protons cm^{-2} and $\sim 4 \times 10^{14}$ electrons cm^{-2} per Mercury year. This result is of great importance for studies of comparative space weathering, addressing the regolith properties at the Moon, asteroids and Mercury. In Lavorenti et al. (2023b), I show that Mercury is bombarded by roughly $3-5$ times less protons as compared to the Moon, and roughly by the same amount of protons as compared to main belt asteroids. This means that the magnetic field screening at Mercury dominates over the increase in solar wind flux, as compared to the Moon. Therefore, signatures of "stronger-than-the-Moon" space weathering at Mercury can not be simply explained by the higher solar wind density; other explanations shall be conceived by looking comparatively at (i) the energy flux of precipitating ions and electrons, (ii) the surface composition, and (iii) the micrometeoroid flux.

5.2 Lavorenti et al. (2021) *A&A*, 652, A20

Astronomy & Astrophysics

Electron acceleration driven by the lower-hybrid-drift instability

An extended quasilinear model

Federico Lavorenti[1,2] , Pierre Henri[1,3], Francesco Califano[2], Sae Aizawa[4], and Nicolas André[4]

[1] Laboratoire Lagrange, Observatoire de la Côte d'Azur, Université Côte d'Azur, CNRS, Nice, France
  e-mail: federico.lavorenti@oca.eu
[2] Dipartimento di Fisica "E. Fermi", Università di Pisa, Pisa, Italy
[3] LPC2E, CNRS, Univ. d'Orléans, OSUC, CNES, Orléans, France
[4] IRAP, CNRS-CNES-UPS, Toulouse, France

ABSTRACT

Context. Density inhomogeneities are ubiquitous in space and astrophysical plasmas, particularly at contact boundaries between different media. They often correspond to regions that exhibit strong dynamics across a wide range of spatial and temporal scales. Indeed, density inhomogeneities are a source of free energy that can drive various instabilities such as the lower-hybrid-drift instability, which, in turn, transfers energy to the particles through wave-particle interactions and eventually heats the plasma.
Aims. Our study is aimed at quantifying the efficiency of the lower-hybrid-drift instability to accelerate or heat electrons parallel to the ambient magnetic field.
Methods. We combine two complementary methods: full-kinetic and quasilinear models.
Results. We report self-consistent evidence of electron acceleration driven by the development of the lower-hybrid-drift instability using 3D-3V full-kinetic numerical simulations. The efficiency of the observed acceleration cannot be explained by standard quasilinear theory. For this reason, we have developed an extended quasilinear model that is able to quantitatively predict the interaction between lower-hybrid fluctuations and electrons on long time scales, which is now in agreement with full-kinetic simulations results. Finally, we apply this new, extended quasilinear model to a specific inhomogeneous space plasma boundary, namely, the magnetopause of Mercury. Furthermore, we discuss our quantitative predictions of electron acceleration to support future BepiColombo observations.

Key words. plasmas – methods: numerical – instabilities – waves – methods: observational

1. Introduction

Inhomogeneities in the magnetic field, velocity, density, temperature, etc. from fluid down to kinetic scales are commonly encountered in space and astrophysical plasmas (Amatucci 1999). The gradient associated with such inhomogeneous plasma regions is a source of "free" energy that can drive various kind of plasma instabilities. For instance, in the case of density gradient on scale close to the ion gyroradius, a situation that is commonly encountered in many plasma environments, the plasma is unstable against the so-called drift instabilities. These instabilities arise from the relative motion between ions and electrons, and turn out to be of paramount importance in shaping plasma boundaries found in space, allowing for strong anomalous mass and energy transport not achievable by standard collision-like diffusion.

In situ measurements show that lower-hybrid waves (LHW) with a frequency close to the lower-hybrid frequency $f_{LH} \approx \sqrt{\omega_{ci}\omega_{ce}}/2\pi$, are ubiquitous in magnetized space plasma environments. Such waves are commonly observed at Earth's magnetotail (Huba et al. 1978; Retinó et al. 2008; Zhou et al. 2009, 2014; Khotyaintsev et al. 2011; Norgren et al. 2012; Le Contel et al. 2017) and Earth's magnetopause (André et al. 2001; Bale et al. 2002; Vaivads et al. 2004; Graham et al. 2017, 2019; Tang et al. 2020). In these two regions, LHW are commonly observed in the vicinity of magnetic reconnection sites where strong

density gradients do form. Their role on the onset (or relaxation) of magnetic reconnection has been addressed in the past and still represents a key point in the context of reconnection research (Daughton 2003; Lapenta et al. 2003, 2018; Yoo et al. 2020).

Moreover, LHW are also observed at plasma shock fronts such as the terrestrial bow shock (Walker et al. 2008), interplanetary shocks in the solar wind (Krasnoselskikh et al. 1985; Zhang & Matsumoto 1998; Wilson et al. 2013), and supernova remnants (Laming 2001). Finally, LHW have been observed in induced ionosphere of comet 67P (André et al. 2017; Karlsson et al. 2017; Goldstein et al. 2019), of the planets Venus (Scarf et al. 1980; Shapiro et al. 1995) and Mars (Sagdeev et al. 1990), as well as at Earth's ionosphere (Reiniusson et al. 2006). In this context, space observations of supra-thermal electron populations in conjunction with LHW represents one of the basic points motivating the interest in the study of the interaction of these waves with electrons (Norgren et al. 2012; Zhou et al. 2014; Le Contel et al. 2017; Broiles et al. 2016; Goldstein et al. 2019).

As more than just a mechanism at work in space plasma environments, electron acceleration by LHW is a mechanism commonly used in tokamak experiments to heat electrons and hence the plasma along the toroidal magnetic field lines (Bécoulet et al. 2011; Pericoli-Ridolfini et al. 1999). This naturally suggests that LHW generated in space are an efficient driver for electron

acceleration in space plasma environments (Broiles et al. 2016). However, the mechanism for the generation of LHW in laboratory differs strongly from the one that is at play in space plasmas. In plasma fusion experiments, the LHW are commonly excited by an external pump enabling to sustain the waves and so the electron acceleration process on long time scales, with the parameters controlled by the experimenter himself. In inhomogeneous space plasma, LHW are instead generated by the development of plasma instabilities, in which nonlinear saturation might reduce the efficiency of the acceleration process when compared to plasma fusion experiments.

In a natural plasma environment, the two instabilities that can be responsible for the generation of LHW are: (i) the modified-two-stream instability (MTSI) driven by a supra-thermal ion beam (Ott et al. 1972; McBride et al. 1972; McBride & Ott 1972); and (ii) the lower-hybrid-drift instability (LHDI) driven by the relative drift between ions and electrons (Krall & Liewer 1971; Krall & Trivelpiece 1973; Gary 1993). The electron acceleration driven by LHW generated by the MTSI has been widely addressed in the literature using quasilinear theory (McBride et al. 1972; Shapiro et al. 1999), full-kinetic simulations (McClements et al. 1993; Bingham et al. 2002), and experiments (Rigby et al. 2018). The MTSI is considered the typical source for the above-mentioned LHW observations at plasma shock fronts (Krasnoselskikh et al. 1985; Shapiro et al. 1995, 1999) due to the reflection of a large fraction of solar wind ions by the shock front; however, LHW are routinely observed also in the absence of such beams of reflected ions, a condition that stands in the way of invoking the MTSI as the underlying mechanism. In such cases, the LHW are instead generated by the LHDI. The driver for the development of the LHDI has to be found in the "strong" density gradients that reach length scales on the order of, or even shorter than, the ion gyroradius. This is the case, for instance, for the above-mentioned observations at Earth's magnetosphere and in cometary plasmas. Henceforth in this work, we focus on LHW generated by the LHDI and their interaction with the electron population.

The fastest growing modes of the LHDI propagate perpendicular to both the density gradient, say the x-direction, and the ambient magnetic field direction, the z-direction. The phase velocity is of the order of the ion thermal speed (Gary 1993). However, the LHDI modes are unstable over a narrow cone angle around this direction (in this case, the y-direction) proportional to the square root of the ion-to-electron mass ratio $k_z/k_y \approx \sqrt{m_e/m_i}$ (Gary & Sanderson 1978). This means that the oblique LHDI modes have a component of the phase velocity parallel (resp. perpendicular) to the ambient magnetic field of the order of the electron (resp. ion) thermal speed. As a result, electrons can be resonantly accelerated by LHDI fluctuations in the direction parallel to the ambient magnetic field through wave-particle interactions; hereafter, we refer to this mechanism as LHDI electron acceleration.

The goal of this paper is to investigate the efficiency of the LHDI electron acceleration. As of today, the state-of-the-art theoretical model of this mechanism is provided by the analytical quasilinear model proposed by Cairns & McMillan (2005), hereafter, called the QL model. The QL model is well suited to the study of the early stage of the electron acceleration, but eventually it breaks down when the nonlinear feedback from the particle distribution to the wave becomes important. More precisely, the QL model breaks down as soon as nonlinear effects locally modify the distribution function shape (i.e. around the resonant velocity); hereafter referred to as nonlinear LD-like

effects because they are analogous to the well-known nonlinear Landau damping effects (see Brunetti et al. 2000 and references therein).

Other past works have addressed the problem of the interaction between pump-generated LHW and electrons, including such nonlinear LD-like effects (Singh et al. 1996, 1998; Zacharegkas et al. 2016). However, the configuration adopted in these works is not well suited for space plasma configurations where LHW are typically driven by a plasma instability, such as the LHDI, and not by an external pump. To the best of our knowledge, the LHDI electron acceleration mechanism has not yet been studied using a self-consistent full-kinetic model.

In the past, the efficiency of LHDI electron acceleration has been addressed by means of reduced analytical models similar to the QL model, mostly because of the limitations on computational resources. Indeed, the computational power required to solve the Vlasov equation for LHDI electron acceleration is challenging because (i) ion and electron kinetic physics must be included self-consistently in the model, meaning that a full-kinetic numerical simulation is required; and (ii) the wave propagation occurs over an angle, in the $y-z$ plane, perpendicular to the inhomogenity direction, the x-direction, meaning that three-dimensional (3D) numerical simulations are required. All in all, investigating the electron acceleration generated by the LHDI requires full-kinetic 3D-3V simulations. This is one of the methods used in this work.

In this paper we investigate the electron acceleration associated with the LHDI through a comparison of complementary numerical simulations. We use the quasilinear approach and direct full-kinetic 3D-3V simulations. This enables us to assess the intrinsic limits of the QL model and to investigate the consequences of nonlinear LD-like effects on the LHDI electron acceleration. We present the first direct numerical evidence of LHDI electron acceleration from full-kinetic 3D-3V simulations, and we build up an extended quasilinear (eQL) model that takes into account the effect of such nonlinear saturation to quantitatively estimate electron acceleration under realistic space plasma parameters.

The paper is organized as follows: Section 2 describes the QL model and the full-kinetic 3D-3V simulation model we use here. Section 3 presents the results of both models using two common sets of plasma parameters ("strong" and "weak" gradient configurations). Section 4 compares the results of the two models, shows the limitations of the QL model as compared to the full-kinetic one, and presents a novel eQL model. Finally, we apply this new eQL model to the magnetopause of Mercury in view of the future observations of the BepiColombo space mission. Section 5 summarizes our findings and presents our conclusions.

2. Models and methods

In this study, we use two different models of plasma evolution. First, a QL model of LHDI electron interaction based on the work of Cairns & McMillan (2005). Second, a full-kinetic 3D-3V plasma simulations of a plasma boundary initially unstable to the LHDI. The former is a simplified model of the plasma dynamics that does not account for the full response of the plasma itself to nonlinear interactions, and is therefore considered a reduced model. The latter instead is fully self-consistent, even if constrained by a specific parameter choice, and it is therefore considered an ab initio model. The full-kinetic model, being more general than the QL one, is used to assess the limits of

the latter and eventually, to build an extended description that properly models the LHDI electron acceleration still within a quasilinear framework.

2.1. Quasilinear analytical model

The wave-particle interaction between LHW (generated from LHDI) and electrons can be modeled using a powerful analytical tool: quasilinear theory (Bernstein & Engelmann 1966; Alexandrov et al. 1984). Quasilinear theory is based on a second order perturbative expansion of the Vlasov equation averaged over the spatial variables. The system of quasilinear equations describes: (i) the diffusion in velocity space of the electron distribution function through a diffusion coefficient proportional to the electric field energy (Eqs. (1) and (2)); and (ii) the time evolution of the electric field energy (Eqs. (3) and (4)). The state-of-the-art QL model for LHDI electron interaction is the one developed in Cairns & McMillan (2005) and summarized here:

$$\partial_t f_e(v_\parallel, t) = \partial_{v_\parallel} D_e(v_\parallel, t) \partial_{v_\parallel} f_e, \tag{1}$$

$$D_e(v_\parallel, t) = \frac{e^2}{4\epsilon_0 m_e^2} \int S_k(k_\perp, k_\parallel, t) \frac{k_\parallel^2}{k_\perp^2} \delta(\omega - k_\parallel v_\parallel) d^3\mathbf{k}, \tag{2}$$

$$\partial_t S_k(k_\perp, k_\parallel, t) = \left[\gamma_{\mathrm{LHDI}} \left(1 - \frac{S_k}{S_{k,\max}}\right) + \gamma_e(k_\perp, k_\parallel, t)\right] S_k, \tag{3}$$

$$\gamma_e(k_\perp, k_\parallel, t) = \frac{\pi \omega_{\mathrm{LH}}^2 \omega(k_\perp, k_\parallel)}{2n_0 k_\perp^2} \frac{m_i}{m_e} \partial_{v_\parallel} f_e(v_\parallel = \omega/k_\parallel, t). \tag{4}$$

Here, $f_e(v_\parallel, t)$ is the electron distribution function, $k_\perp$ (resp. $k_\parallel$) is the wavevector perpendicular (resp. parallel) to the ambient magnetic field, $S_k = E_k^2/8\pi$ is the electric field energy density in wavevector-space, $S_{k,\max}$ is the maximum value of S_k attained at saturation, n_0 is the plasma density, ω_{LH}, ω_{ci} are the lower-hybrid and ion cyclotron frequencies, $\omega(k_\perp, k_\parallel)$ is the spectrum of the wave, γ_{LHDI} is twice the linear growth rate of the LHDI, and $\delta(x)$ is the Dirac delta function. In the following, ρ_i is the ion gyroradius, and $v_{\mathrm{thi}} = \rho_i \omega_{ci}$ is the ion thermal speed.

After normalization, this nonlinear system of coupled partial differential equations (Eqs. (1)–(4)) is solved by numerical integration using a time staggered leapfrog scheme. In k-space, we limit the computation to the region of LHDI fastest growing modes, that is, $0.7 < k_\perp \rho_e < 1$ and $0 < k_\parallel \rho_i < 1$, as done in Cairns & McMillan (2005). Since the wavevectors are limited to this region, the wave spectrum turns out to be more or less flat with a corresponding frequency for the fastest growing mode given by the lower-hybrid frequency, $\omega(k_\perp, k_\parallel) \simeq \omega_{\mathrm{LH}}$. The grid in velocity space is chosen by testing the convergence of the solution.

The QL model, Eqs. (1)–(4), depends on four parameters: m_i/m_e, ω_{pe}/ω_{ce}, γ_{LHDI}, and $S_{k,\max}$. The first two parameters, m_i/m_e, ω_{pe}/ω_{ce}, define the plasma itself. The last two parameters γ_{LHDI} and $S_{k,\max}$ (or analogously $S_{\max} = \int d^3k S_{k,\max}$) define the linear growth and saturation level of the instability, and they only depend on the initial plasma configuration. The analytical expressions for these two quantities are given by:

$$\gamma_{\mathrm{LHDI}} = \frac{\sqrt{2\pi}}{4} \frac{1}{\sqrt{1 + \beta_i/2}} (\epsilon_n \rho_i)^2 \omega_{\mathrm{LH}}, \tag{5}$$

$$S_{\max} = \begin{cases} 2\frac{m_e}{m_i}\frac{(\epsilon_n\rho_i)^2}{(1+\omega_{pe}^2/\omega_{ce}^2)}n_0 T_i & \text{current relaxation} \\ \frac{2}{45\sqrt{\pi}}\frac{(\epsilon_n\rho_i)^5}{(1+\omega_{pe}^2/\omega_{ce}^2)}n_0 T_i & \text{ion trapping,} \end{cases} \tag{6}$$

where β_i is the ion plasma beta, and the inverse gradient scale length ϵ_n is defined as

$$\epsilon_n = \max\left\{\frac{1}{n(x)}\frac{dn(x)}{dx}\right\}. \tag{7}$$

The growth rate γ_{LHDI} in Eq. (5) has been obtained using a linearized kinetic model by Davidson et al. (1977). The electric energy at saturation $S_{\max}$ in Eq. (6) has been obtained using an analytic quasilinear approach by Davidson (1978), and it was later tested numerically by Brackbill et al. (1984) using 2D full-kinetic simulations. The LHDI can saturate through two different processes depending on the initial value of the density gradient: ion trapping (resp. current relaxation) for high (resp. low) values of the density gradient (Brackbill et al. 1984).

The derivation of Eqs. (5) and (6) is based on the assumption that the only source of drift in the plasma is the density gradient. Thus, all particle drifts, apart from the diamagnetic drift v_{Di}, are considered negligible. As a consequence, $v_{\mathrm{Di}}/v_{\mathrm{thi}} = \epsilon_n \rho_i$. In the full-kinetic simulations, presented in the next section (Sect. 2.2), this assumption is essentially verified.

Quasilinear models are inherently limited because they do not include the nonlinear feedback from the modified plasma dispersion function on the electromagnetic fields. To overcome this limitation, we present in the next section (Sect. 2.2) a full-kinetic 3D-3V numerical plasma model.

2.2. Setup for full-kinetic 3D-3V simulations

The full-kinetic model of the plasma is based on a direct solution of the Vlasov-Maxwell system of equations using a Lagrangian PIC (particle-in-cell) approach.

To run the simulations of a plasma boundary unstable to the LHDI, we used the explicit, electromagnetic, relativistic, PIC code SMILEI (Derouillat et al. 2018). The ambient magnetic field is directed along the z-axis and the density gradient along the x-axis. In order to model both wave propagation (predominantly along the y-axis, perpendicular to both the magnetic field and the density gradient direction) and the electron wave-particle interaction (predominantly along the z-axis, parallel to the magnetic field), we considered a 3D numerical box. Compared to previous numerical investigations of the LHDI (Brackbill et al. 1984; Gary & Sgro 1990; Hoshino et al. 2001; Shinohara & Hoshino 1999; Lapenta & Brackbill 2002), which focused on the wave generation mechanism only through 2D-3V simulations in the equivalent of our (x, y) plane, we also include in this study the out-of-plane direction that hosts the electron acceleration resonant processes. An overview of the numerical setup is shown in Fig. 1, with the right panel showing the 3D numerical box used here and highlighting: (i) a slice of the ion density field in the (x, y) plane; and (ii) the plane (y, z) that is most unstable to the LHDI in yellow.

The initialization of the simulations ensures pressure balance by means of the Vlasov equilibrium proposed in Alpers (1969), Pu et al. (1981), which shapes a plasma boundary with density and magnetic field asymmetries, uniform temperature, with no electric field and no velocity nor magnetic field shear. Hereafter, we refer to the side I (resp. side II) of this boundary as the high (resp. low) density side. The expressions for the initialization profiles are:

$$n(x) = n^I + \frac{n^{II} - n^I}{2}\left(1 + \mathrm{erf}\left(w\frac{eA_y(x)}{m_i v_{\mathrm{thi}}}\right)\right), \tag{8}$$
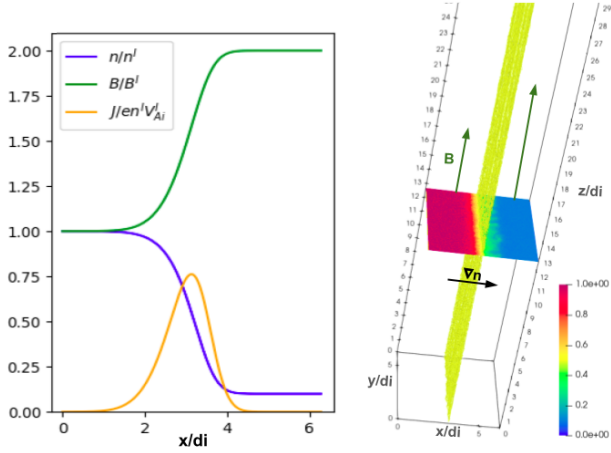
$$B_z(x) = \sqrt{8\pi}\,(PBC - n(x)T)^{1/2}, \tag{9}$$

Fig. 1. Schematic view of the setup of the full-kinetic 3D-3V simulations presented in this study. *Left panel:* Density, magnetic field, and current profiles at $t = 0$ along the direction of the inhomogeneity (*x*-axis) in the "strong gradient" simulation. *Right panel:* 3D visualization of the ion density in the "strong gradient" simulation at $t\omega_{ci}^I = 12$, the LHDI fluctuations are highlighted in the unstable plane (yellow) and in a cut that is perpendicular to the ambient magnetic field.

$$B_z(x) = \frac{\mathrm{d}A_y(x)}{\mathrm{d}x} \quad \text{with } A_y(L_x/2) = 0. \tag{10}$$

Here, $T = T_i + T_e$ is the uniform temperature, *PBC* is the constant of pressure balance (set to have the plasma beta $\beta^I = 10/3$ and $\beta^{II} = 1/12$), and w is a constant that defines the width of the layer – set to 0.98 (resp. 0.5) in the "strong" (resp. "weak") gradient case. We use a density and magnetic field asymmetry of $n^I/n^{II} = 10$ and $B^I/B^{II} = 0.5$. The shape of these initialization profiles is shown in the left panel of Fig. 1. In the following, all quantities are normalized to ion quantities in side *I*: the ion gyrofrequency, $\omega_{ci}^I = eB^I/m_ic$; the ion skin depth, $d_i^I = c\sqrt{m_i/4\pi n^I e^2}$; and the Alfvén speed $V_A^I = B^I/\sqrt{4\pi m_i n^I}$. The numerical box dimensions are: $L_x = L_y = 2\pi$ and $L_z = 20\pi$, with a number of cells, namely, $N_x = N_y = 288$ and $N_z = 1472$. The box is elongated (by a factor of $\sqrt{m_i/m_e} = 10$) in the magnetic field direction in order to reliably include the narrow cone angle over which unstable LHDI modes grow. The timestep used in the simulations is $\mathrm{d}t = 3.4 \times 10^{-4}$ to satisfy the CFL stability condition. The simulations are ran for several tens of the ion gyroperiods until electron acceleration saturates. We use 100 macro-particles per cell and a second order spline interpolation for the macro-particles. We use a reduced ion-to-electron mass ratio $m_i/m_e = 100$ to make simulations computationally feasible while maintaining a sufficient scale separation between ions and electrons. The implications of using such a reduced mass ratio are discussed in Sect. 4. We use an ion-to-electron temperature ratio $T_i/T_e = 1$, and a plasma-to-cyclotron frequency ratio of $\omega_{pe}^I/\omega_{ce}^I = 4$. The magnitude of the density asymmetry used in these simulations encompasses the typical parameters observed in small planetary magnetospheres such as Mercury (Gershman et al. 2015).

Two different simulations are investigated using two different layer widths: (i) a steeper boundary case (with the inverse gradient scale length $\epsilon_n = 1$, defined in Eq. (7)), hereafter called a "strong gradient" simulation; and (ii) a smoother boundary case (with $\epsilon_n = 0.5$), hereafter called the "weak gradient" simulation. These parameters are chosen to ensure that the amplitude of the LHDI fluctuations is well above the PIC noise level and also

to saturate through the two different mechanisms introduced in Sect. 2.1: ion trapping or current relaxation.

3. Evolution of LHDI and associated electron acceleration: Simulations results

First, we show the results of the full-kinetic model. Then we show those obtained with the QL model using the same parameters as for the full-kinetic simulations. Finally, we compare the results of the two models showing the range of validity and the limitations of the QL model.

3.1. Results from the full-kinetic 3D-3V simulations

In both the "strong gradient" and "weak gradient" full-kinetic simulations, the layer is unstable to the LHDI due to the presence of a density gradient on ion kinetic scales. The LHDI fluctuations grow exponentially in the layer for times $t < t_{sat}$ as predicted by kinetic linear theory. The fastest growing mode (FGM) is electrostatic and directed along the *y*-axis with wavevector of $k_y\rho_e \approx 1$, frequency of $\omega \lessgtr \omega_{LH}$ and a growth rate of $\gamma \lessgtr \omega_{LH}$, which are in agreement with the linear estimation (Eq. (5)) for both simulations. The growth of the electric field energy – normalized to the ion thermal energy and integrated over the unstable layer – is shown in Fig. 3 with green curves for both simulations. At $t \approx t_{sat}$ (corresponding to the first vertical dashed lines in each panel of Fig. 3), the electric field fluctuation's growth saturates. Using the growth rate and the saturation level from Eqs. (5) and (6), we compute the saturation time analytically as

$$t_{sat} = \frac{\ln[S_{max}/S(t=0)]}{\gamma_{LHDI}}. \tag{11}$$

We note that the initial amplitude of the electric field energy, $S(t = 0) \approx 10^{-4}nT_i$ in both simulations, is due to the particle noise intrinsic to the full-PIC algorithm that we use.

The saturation mechanism of the LHDI has been extensively addressed in the past, see, e.g., (Winske & Liewer 1978; Davidson 1978; Chen & Birdsall 1983; Brackbill et al. 1984), with results demonstrating that LHDI saturates because of ion trapping (resp. current relaxation) in the case of strong (resp. weak) density gradients. The saturation mechanisms at play in our simulations are shown in Fig. 2. First, in the strong gradient simulation, we give evidence for ion trapping (top left panel) in the potential well of the LH waves (bottom left panel). These phase space vortices are not observed in the weak gradient simulation. Second, we show a significantly stronger decrease of the total charge current in the layer in the weak gradient simulation (orange) compared to that in the strong gradient one (blue) (right panel). This is consistent with saturation taking place via current relaxation in the weak gradient simulation, that is, the LHDI fluctuations inhibit its source of free energy by reducing the electron drift in the layer. We conclude that in the strong gradient simulation the LHDI saturates due to ion trapping, while in the weak gradient simulation, the LHDI saturates due to current relaxation, as is expected based on past studies. This is further confirmed by the fact that in both cases, the saturation levels are comparable with the ones obtained by Eq. (6). Subsequently, in the strong gradient simulation, we observe for $t > t_{sat}$ a rapid decrease of the electric fluctuations amplitude, characteristic of an overshoot pattern, which is shown in the electric-to-thermal energy ratio in Fig. 3 (left panel, green curve) at a time $t = t_{sat}$. Such an overshoot of the electric field fluctuations is not observed in the weak gradient simulation. An important point to
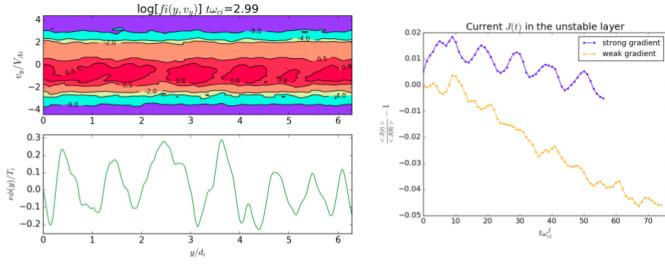
Fig. 2. Saturation mechanisms at play in the two simulations: ion trapping (*left panels*) and current relaxation (*right panel*). *Left panels*: iso-contour of the ion phase space density (*top panel*) together with the electric potential of the LHDI waves (*bottom panel*) on the same spatial axis, both quantities being computed in the unstable layer. *Right panel*: evolution of the difference between the average charged current in the unstable layer ($2 < x < 4$) and its value at $t = 0$, for both simulations.

note is that in both simulations, the electric field energy always remains much smaller than the thermal energy of the particles (it never exceeds 1%).

We also note that a common issue with PIC simulations is the possible occurrence of spurious numerical heating of the macroparticles population during the simulation. This effect, due to the so-called "finite grid instability" (Birdsall & Langdon 1991; Markidis & Lapenta 2010; McMillan 2020), appears when the Debye length is not sufficiently resolved by the numerical grid. In such a case, the electrons would be numerically heated, which would hide the wave-particle interaction we are looking for. We carefully checked that our PIC simulations are free from such numerical spurious heating, by comparing the evolution of the supra-thermal electron density in the unstable layer to the one outside the layer on both sides, where the plasma is stable, to check that the numerical heating of the electrons is negligible compared to the one arising from wave-particle interaction in the layer.

To quantify the efficiency of the LHDI in accelerating electrons parallel to the ambient magnetic field, we define a supra-thermal electrons density as follows:

$$N_{e,\mathrm{sup}}(t) = \int_{-\infty}^{2v_{\mathrm{the}}} f_e(v_z, t)\mathrm{d}v_z + \int_{2v_{\mathrm{the}}}^{\infty} f_e(v_z, t)\mathrm{d}v_z. \quad (12)$$

Here, the supra-thermal electrons density $N_{e,\mathrm{sup}}$ is used as a quantitative tracer of the LHDI electron acceleration. The growth and saturation of $N_{e,\mathrm{sup}}$ is shown for both simulations in Fig. 3, with red curves.

In both simulations, the efficiency of the LHDI electron acceleration process can be described through a three-phase evolution: (i) the linear phase, $0 < t < t_{\mathrm{sat}}$; (ii) the quasilinear phase, $t_{\mathrm{sat}} < t < \tau_{\mathrm{NL}}$; and (iii) the strongly nonlinear phase, $t > \tau_{\mathrm{NL}}$. The characteristic time scales, t_{sat} and τ_{NL}, computed from Eqs. (11) and (16), respectively, are marked in Fig. 3 by vertical dashed lines. The latter time scale constitutes the fundamental outcome of the full-kinetic model and an extensive discussion is provided in Sect. 4.2.

In the linear phase (phase I in Fig. 3), the electric field grows exponentially, as predicted by linear theory. In the weak gradient case, in phase I, the electron acceleration remains weak compared to the overall electron acceleration observed at saturation. This is understandable since the resonant electric field fluctuations themselves remain weak compared to their steady-state value at saturation. On the contrary, in the strong gradient case, in phase I, around t_{sat}, the electric field of the LHDI waves reaches values even higher than the saturation value. As a result,
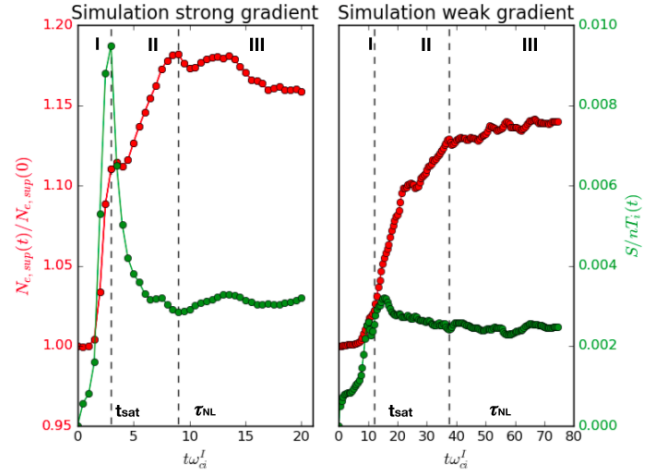
Fig. 3. Full-kinetic simulations: evolution of the electron supra-thermal density $N_{e,\mathrm{sup}}(t)/N_{e,\mathrm{sup}}(0)$ (red curves) and of the electric field energy normalized to the ion thermal energy $S/nT_i(t)$ (green curves), both curves are integrated over the unstable layer ($3.5 < x < 4$ for strong gradient and $3.5 < x < 4.5$ for weak gradient). We note that time axes are different for the two simulations.

we observe a non-negligible increase of the supra-thermal electron density in a very short time scale around t_{sat}, this process is discussed in detail in Sect. 4.

In the quasilinear phase (phase II in Fig. 3), electron acceleration starts to take place as observed in both simulations. In this phase, the efficiency of the acceleration is directly related to the driver intensity (i.e., the stronger the electric field the stronger the acceleration), as expected from the QL diffusion equations (Eqs. (1) and (2)).

Finally, in the strongly nonlinear phase (phase III in Fig. 3), while the electric field amplitude remains constant and finite, the acceleration stops due to the onset of nonlinear LD-like effects.

Such a multi-phase evolution is observed in both strong and weak gradient simulations (see Fig. 3). One main difference between the two simulations is the presence – in the strong gradient simulation – of an overshoot in the electric energy, which is not observed in the weak gradient simulation. Such an overshoot corresponds to a sharp peak in the electric-to-thermal energy ratio at $t \approx t_{\mathrm{sat}}$, which subsequently leads to a strong electron acceleration for the overshoot duration (see Fig. 3, left panel around t_{sat}). However, the overall contribution of this phenomenon to the total amount of accelerated electrons is shown not to be significant in Sect. 4. In the end, for both simulations, the supra-thermal electron density in the inhomogeneous layer is increased by around 15%−20%. However, in the two cases, this same final value is attained through a different evolution: in the strong gradient simulation, the acceleration is faster but stops sooner (at $\tau_{\mathrm{NL}} \approx 10$), while in the weak gradient simulation the acceleration occurs at a slower rate but remains efficient on longer time scales (up to $\tau_{\mathrm{NL}} \approx 40$). Interestingly, these two effects seems to compensate each other.

The nonlinear LD-like time scale τ_{NL}, which is not accessible to quasilinear models, represents the original result of our full-kinetic simulations. An extensive discussion of this is given in Sect. 4.

3.2. Results of the standard quasilinear model

To enable a quantitative comparison between the QL model described in Sect. 2.1 and the full-kinetic one, the former is

solved using the same plasma parameters as for the unstable layer of the full-kinetic simulations. More precisely, the input parameters of the QL model are obtained by averaging the plasma density, and the magnetic field in the layer $3.5 < x < 4$ (resp. $3.5 < x < 4.5$) for the strong (resp. weak) gradient full-kinetic simulation.

Numerical integration of the QL model (Eqs. (1)–(4)) provides the time evolution of the electron distribution function $f_e(v_z)$ shown in Fig. 4 at different time instants. We observe a diffusion in velocity space for both "strong" and "weak" gradient cases, corresponding to electron acceleration by LHW. The characteristic timescale for such acceleration turns out to be of the order of hundreds of ion cyclotron periods. As expected, this time scale is longer in the weak gradient case than in the strong gradient one.

Eventually, electron acceleration described by QL theory slows down after long times. Indeed, as already explained in Cairns & McMillan (2005), the characteristic time scale to accelerate an electron of velocity $v_\parallel$ by an amount $\delta v_\parallel$ scales as $\sim v_\parallel^5$ for $\delta v_\parallel \sim v_\parallel$. With the parameters used in our two simulations, the electron acceleration obtained from the QL model becomes negligible after time $\tau_{\rm Diff} \gtrsim 150$ (resp. $\tau_{\rm Diff} \gtrsim 400$) in the strong (resp. weak) gradient case, as shown in Fig. 4.

Such LHDI electron acceleration appears much weaker than those presented in the work of Cairns & McMillan (2005). This discrepancy is directly associated with the choice of the parameter $S_{\rm max}/nT_i$, the electric-to-thermal energy at the saturation of the LHDI, which is proportional to the quasilinear diffusion coefficient (Eq. (2)). In this study, we use $S_{\rm max}/nT_i = 0.01$ (resp. 0.002) for the strong (resp. weak) gradient case to obtain the results shown in Fig. 4. These values are obtained from Eq. (6) and are consistent with those observed in our full-kinetic simulations. Differently, in the seminal paper of Cairns & McMillan (2005) the authors have used a value $S_{\rm max}/nT_i = 0.5$ that is two orders of magnitude larger than what is expected from the theory of saturation of the LHDI in Davidson (1978) using the configuration considered in that study. Such a choice for an overestimated value of the parameter $S_{\rm max}/nT_i$ unavoidably leads to an overestimation of the quasilinear diffusion coefficient and, therefore, of a higher electron acceleration efficiency. This indicates that a consistent choice of the electric-to-thermal energy ratio at saturation is crucial in quasilinear models in order to accurately assess a reliable value of the quasilinear diffusion coefficient.

Despite the different choice of the parameter $S_{\rm max}/nT_i$, the time evolution of the electron distribution function obtained with the QL model agrees qualitatively with the one presented in Cairns & McMillan (2005). The comparison with the evolution obtained from the full-kinetic model is given in the next section (Sect. 4.1).

4. Discussion: Toward an extended quasilinear model and beyond

In this section, we first compare the full-kinetic and standard quasilinear results, then we show the discrepancies between the two models, and we highlight the physical processes that give rise to such discrepancies. Next, in order to overcome the intrinsic limits of the standard quasilinear theory, we build an extended quasilinear model (eQL) that includes the consequences of nonlinear LD-like effects. Finally, we validate such eQL and extrapolate how it scales with the plasma parameters of interest (e.g., ion-to-electron mass ratio, gradient length) in order to enable its
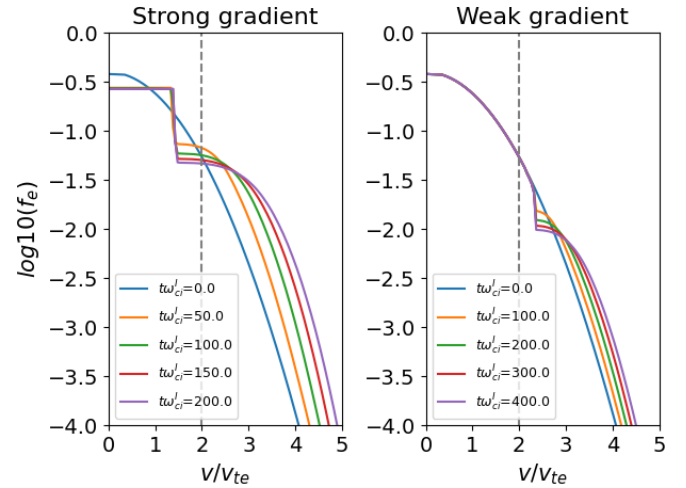
Fig. 4. Results of the QL model for the strong and weak gradient parameter case, shown in the *left and right panel*, respectively. Both panels show the electron distribution function at different time instants in the direction parallel to the magnetic field. Grey vertical dashed lines at $v = 2v_{\rm the} \approx v_{\rm phz}$ correspond to the point from where the supra-thermal electron density (Eq. (12)) is computed.

use beyond the two specific set of parameters of our full-kinetic simulations.

4.1. Comparison between the full-kinetic and the QL models

To quantitatively compare the results of the full-kinetic and QL models on LHDI electron acceleration, we focus on the evolution of the supra-thermal electron density (defined in Eq. (12)), shown for both strong and weak gradient cases in Fig. 5, where the two characteristic times, $t_{\rm sat}$ and $\tau_{\rm NL}$, (previously identified from the full-kinetic simulations) are recalled for sake of clarity (vertical dashed lines). The three-phase evolution of LHDI electron acceleration observed in the full-kinetic simulations (red lines in Fig. 5) is not explicable in terms of the QL model (blue lines in Fig. 5). Two main discrepancies are identified.

First, we observe a minor discrepancy between the two models around $t = t_{\rm sat}$ in the strong gradient case, see Fig. 5 left panel. At this time, the supra-thermal electron density obtained from the full-kinetic simulation (red curve) is higher than that obtained from the QL model (blue curve). This enhanced electron acceleration is due to the overshoot of the electric field in the full-kinetic simulation, an effect that is not included in the QL model and not observed in the weak gradient case. However, this short and sharply peaked phenomenon brings a negligible contribution to the total amount of supra-thermal electrons at the end of the simulation.

Second, we observe a strong discrepancy between the two models for times $t > \tau_{\rm NL}$ (phase III in Fig. 5). Indeed, on the one hand, the electron acceleration stops at time $t \approx \tau_{\rm NL}$ in full-kinetic simulations (red curve) due to the onset of nonlinear LD-like effects, while on the other hand, the electron acceleration goes on in the QL model (blue curve) up to time $t \approx \tau_{\rm Diff}$. The fact that the value of $\tau_{\rm NL}$ (obtained from full-kinetic simulations) is about one order of magnitude lower than $\tau_{\rm Diff}$ (obtained from QL simulations) is the main reason for the strong discrepancy between the two models. Such discrepancy is due to the fact that the QL model does not include the nonlinear LD-like effects that are responsible for the abrupt stop of electron acceleration observed at $t = \tau_{\rm NL}$ in the full-kinetic simulations. Therefore,
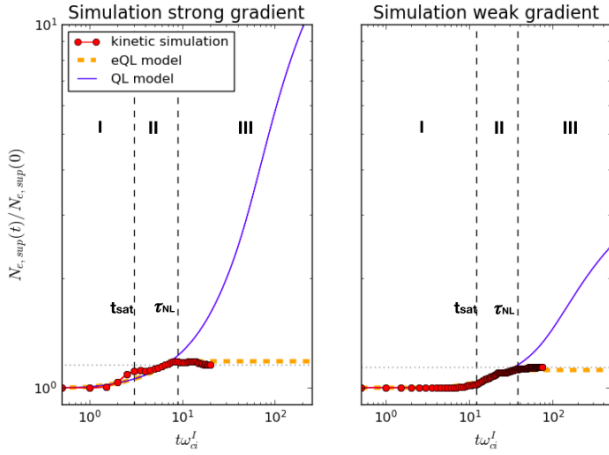
Fig. 5. Comparison of the evolution of supra-thermal electron density (tracer of LHDI electron acceleration) computed from full-kinetic simulations (red curve), QL model (blue curve), extended QL model (orange curve). Vertical dashed lines indicate the saturation time t_{sat}, and nonlinear time τ_{NL}. Horizontal dotted gray lines indicate the results of Eq. (20). We note that time axes are different for the two simulations.

even though the two models are in good agreement in the linear and quasilinear phases (phases I and II in Fig. 5), the final value of the supra-thermal electron density is strongly overestimated by the QL model. In the following, we use the increase in the supra-thermal electron density, defined as:

$$\Delta N_{e,\text{sup}} = N_{e,\text{sup}}(t \to +\infty) - N_{e,\text{sup}}(0) \qquad (13)$$

to quantify the discrepancy between the models. In particular, the value of $\Delta N_{e,\text{sup}}$ is 50 (resp. 20) times higher in the strong (resp. weak) gradient case for the QL model as compared to the full-kinetic model.

4.2. Need for an extended quasilinear model

Quasilinear theory is a powerful tool to study wave-particle interaction in an analytical framework due to its relative simplicity. Therefore, it represents an ideal way to provide quantitative predictions on LHDI electron acceleration or heating.

However, due to its derivation via a perturbative approach, QL theory does not include "strong" nonlinear effects (i.e., those effects, arising at sufficiently long times, that alter the wave fluctuations due to the feedback from the modified distribution function to the fields), also called nonlinear LD-like effects. Although they are not included in the QL model, these effects are well self-consistently reproduced by the full-kinetic simulations. The comparison between both models (Sect. 4.1) highlights the need to build an extended QL model (hereafter called eQL) that overcomes the intrinsic limitations of standard QL model and provide a dynamics consistent with that observed in full-kinetic models. For this purpose, we argue that such eQL model: (1) does not require us to include the possible overshoot of the electric field, as we have shown it is not a dominant process in energizing electrons; (2) does require us to include the eventual inhibition of LHDI electron acceleration by nonlinear LD-like effects through the parameter τ_{NL}.

The nonlinear time τ_{NL} is the parameter used in the eQL to define when nonlinear LD-like effects become dominant in the layer, inhibiting efficient wave-particle interactions. From such time, the QL diffusion coefficient (Eq. (2)) becomes negligible even though the amplitude of the electric field remains constant,
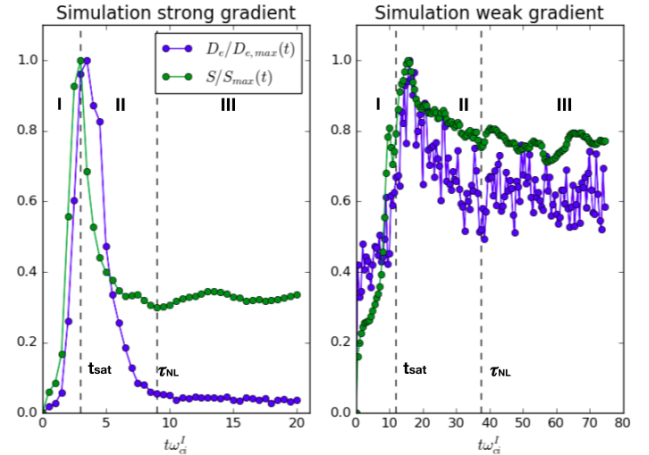
Fig. 6. Evolution of the electric field energy $S(t)/S_{\text{max}}$ (green curve), and of the QL diffusion coefficient $D_e(t, v_z = 2v_{\text{the}})/D_{e,\text{max}}$ in Eq. (2) (blue curve), computed for both full-kinetic simulations. We note that time axes are different for the two simulations.

as shown in Fig. 6 for both full-kinetic simulations. This is due to its integral dependence on $k_\parallel^2/k_\perp^2$. The underlying physical process is the energy transfer, in k-space, from resonant, oblique modes to out-of-resonance, more perpendicular modes, which physical mechanism is discussed below. Therefore, we explicitly switch off the QL diffusion coefficient for $t > \tau_{\text{NL}}$ in the eQL model (Eqs. (14) and (15)).

We now focus on the estimation of this new parameter τ_{NL}. Previous works on the LHDI addressing its nonlinear evolution using 2D full-kinetic simulations suggest a connection between LHDI modes and drift-kink-instability (fvDKI) modes (Pritchett et al. 1996; Shinohara & Hoshino 1999; Lapenta & Brackbill 2002). The DKI is driven unstable in the presence of a current sheet on a scale length on the order of (or smaller than) the ion gyroradius, as in our full-kinetic simulations setup (see Fig. 1, left panel). The main characteristics of the LHDI are as follows: (i) While the LHDI is an electrostatic instability, the DKI is electromagnetic; (ii) The growth rate of the DKI is much smaller than that of the LHDI: indeed, the DKI frequency and growth rate γ_{DKI} are both smaller than the ion gyrofrequency; (iii) The DKI wavevectors are smaller than the inverse of the ion gyroradius; (iv) The DKI modes propagate perpendicular to the magnetic field (Daughton 1998, 1999). In our simulations, the LHDI saturates and start to behave nonlinearly when the DKI is still in its linear stage. As a consequence of the nonlinear dynamics of the LHDI, we observe a coupling between the two instabilities that allows energy to flow from oblique LHDI modes (in their nonlinear stage) to perpendicular DKI modes (in their linear stage). Such a coupling mechanism between LHDI and DKI has been reported and studied in past numerical studies (Pritchett et al. 1996; Shinohara & Hoshino 1999; Lapenta & Brackbill 2002). Therefore, we assume that the mechanism underlying the energy transfer from oblique to strictly perpendicular modes at $t > \tau_{\text{NL}}$, observed in our full-kinetic simulations, is a LHDI-DKI coupling. Consequently, we estimate that the time of onset of LHDI nonlinear LD-like effects scales as the inverse linear growth rate of the DKI, that is, $\tau_{\text{NL}} \propto 1/\gamma_{\text{DKI}}$. The DKI linear growth rate, γ_{DKI}, scaling with plasma physical parameters has been addressed in Daughton (1998) using kinetic theory, and validated in Daughton (1999) using a two-fluid theory. In our work, we use such results to build our eQL model (Eq. (16)).

Taking all those considerations into account, the eQL model is defined as follows:

$$\partial_t f_e(v_\parallel, t) = \partial_{v_\parallel} \mathcal{D}_{NL} \partial_{v_\parallel} f_e, \tag{14}$$

$$\mathcal{D}_{NL}(v_\parallel, t) = \begin{cases} D_e(v_\parallel, t) & t < \tau_{NL} \\ 0 & t \geq \tau_{NL}, \end{cases} \tag{15}$$

$$\tau_{NL} = \tau_0 \left(\frac{m_i}{m_e}\right)^{1/2} (\epsilon_n \rho_i)^{-2} \left(1 + \frac{T_e}{T_i}\right)^{-1}, \tag{16}$$

where $\tau_0 = 1.5$ is a constant obtained from our two full-kinetic simulations. This value is obtained by fitting the evolution of the supra-thermal electron density of the full-kinetic simulations with the one of the eQL model.

4.3. Validation of the extended quasilinear model

The eQL model presented in Sect. 4.2 (Eqs. (14)–(16)) retains all the advantages of the standard QL model (namely being analytical and easily integrable using a numerical solver) while extending its range of validity to asymptotically long time scales. This now enables us to provide quantitative predictions of LHDI electron acceleration. Indeed, as shown by the time evolution of the supra-thermal electron density in Fig. 5, unlike the standard QL predictions (blue), the eQL model (orange) is able to reproduce the predictions of the nonlinear Vlasov-Maxwell theory (red). The relative discrepancy between the two curves does never exceed 5% in both simulations. This validation of the eQL model is of particular interest with regard to quantifying the LHDI electron acceleration over a long time scale.

The results of the eQL model strongly depend on the estimation of the nonlinear time τ_{NL}, identified as the inverse linear growth rate of the DKI $1/\gamma_{DKI}$. This choice is justified both (i) a priori via previous numerical works that have shown evidence that the long time evolution of a LHDI-unstable layer gets coupled to a DKI (Pritchett et al. 1996; Shinohara & Hoshino 1999); and (ii) a posteriori by validating that the scaling $\gamma_{DKI} \propto (\epsilon_n \rho_i)^2$ in Eq. (16) is consistent with the outputs of our two full-kinetic simulations.

In our two full-kinetic simulations – which have enabled us to both define and validate the eQL model – we used a reduced ion-to-electron mass ratio $m_i/m_e = 100$. Using such a reduced mass ratio is standard procedure in PIC plasma simulations since it allows us to reduce the scale separation among the two species in order to run the numerical simulation on reasonable amount of CPU time (still about one million computational hours per simulation, in our case), while maintaining the necessary temporal and spatial scales separations between both species dynamics. However, the properties of the LHDI actually depend on the ion-to-electron mass ratio because of the hybrid character of the instability. Therefore, the quantitative predictions of our full-kinetic simulations are not directly applicable to a realistic plasma configuration (with a physical proton-to-electron mass ratio of 1836). This is exactly where an eQL model becomes extremely useful.

4.4. Using the extended quasilinear model to assess LHDI electron acceleration at physical mass ratio

The eQL model does not suffer from the strong computational constraints of full-PIC simulations and enables us to address, in this section, the question of LHDI electron acceleration using a realistic proton-to-electron mass ratio. The results of the eQL models are summarized in Fig. 7, showing both the electron
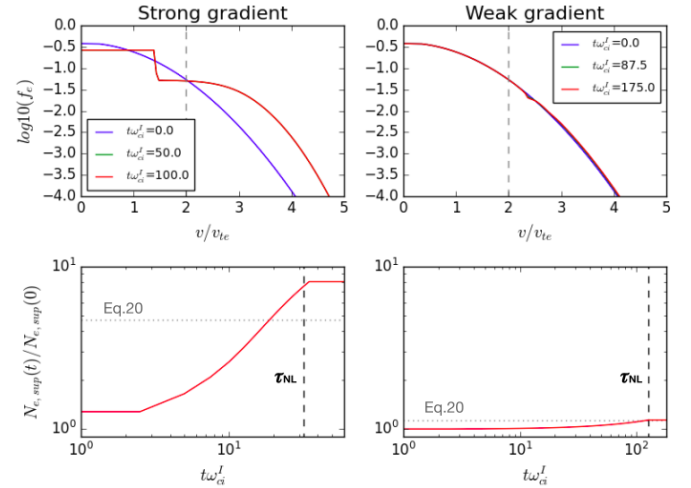
Fig. 7. Output of the eQL model using the strong (*left panels*) and weak (*right panels*) set of plasma parameters with realistic proton-to-electron mass ratio. *Top panels*: electron distribution function at different time instants in the direction parallel to the magnetic field. Grey vertical dashed lines correspond to $v = 2v_{the} \approx v_{phz}$. *Bottom panels*: evolution supra-thermal electron density in Eq. (12). Vertical dashed line indicate the nonlinear time τ_{NL} in Eq. (16). Horizontal dotted gray lines indicate the results of Eq. (20). We note that time axes are different for the two simulations.

distribution function evolution averaged in the inhomogeneous layer (top panels) and the resulting supra-thermal electron density (bottom panels), for both strong and weak gradient setups. Here, we use the two setups described in Sect. 2, where only the mass ratio is modified to address the case $m_i/m_e = 1836$. We emphasize that full kinetic simulations using such a physical mass ratio would have been extremely challenging computationally, so that we consider the eQL model as a way to extrapolate the results of our full-kinetic simulations (done using a reduced mass-ratio) to a physical plasma environment.

Compared to results shown in Sect. 4.3 for a reduced mass ratio, using a physical mass ratio the nonlinear time increases following Eq. (16). This means that the LHW-particle interaction occurs over longer times, thus more electrons are accelerated. However, on the one hand, this effect can be compensated by the reduction of the electric field energy of order $\sim m_e/m_i$ (Eq. (6)) if the LHDI saturates through current relaxation, namely, in the weak gradient case, see Fig. 7 right panel. On the other hand, if the LHDI saturates through ion trapping the saturation level does not depend on the mass-ratio (Eq. (6)); therefore, the LHDI electron acceleration is more efficient by a factor $\sim m_i/m_e$ due to the increase in the nonlinear time.

All in all, the mass ratio does not affect the weak gradient case, while it increases the fraction of LHDI accelerated electrons by a factor $\sim 1836/100$ in the strong gradient case. These predictions – solely based on scaling arguments – are well reproduced by the numerical solution of the eQL using a realistic proton-to-electron mass-ratio, as shown in Fig. 7, and are also confirmed by the analytical estimates developed below in this section.

Now, we focus on the value of the supra-thermal electron density at asymptotically long times, since, all in all, this is the quantity relevant for space plasma observations of LHDI accelerated electrons. Under some simplifying assumptions, we derive an analytical expression for this quantity in the framework of the eQL model.

Table 1. Values of $\Delta N_{e,\text{sup}}/N_{e,\text{sup}}^0$ for the different plasma configurations considered in this study, computed using the eQL model outlined in Sect. 4.2 and the approximated analytical expression in Eq. (20).

Gradient $\epsilon_n\rho_i$	m_i/m_e	eQL model	Eq. (20)	Error [%]
1	100	0.18	0.16	12
0.5	100	0.12	0.14	15
1	1836	7.62	3.67	70
0.5	1836	0.14	0.15	7

Notes. The last column shows the relative discrepancy between these two results.

First, we approximate the evolution of the supra-thermal electron density by a linear interpolation in the time interval $t_{\text{sat}} < t < \tau_{\text{NL}}$ to get

$$\Delta N_{e,\text{sup}} = N_{e,\text{sup}}(\tau_{\text{NL}}) - N_{e,\text{sup}}(0) = (\tau_{\text{NL}} - t_{\text{sat}})\frac{d}{dt}N_{e,\text{sup}}(t), \quad (17)$$

then, we integrate Eq. (1) in $v_\parallel$-space to get

$$\frac{d}{dt}N_{e,\text{sup}}(t) = [D_e\partial_v f_e]_{v_\parallel=2v_{\text{the}}}, \quad (18)$$

which is constant in the interval $t_{\text{sat}} < t < \tau_{\text{NL}}$ since we assume that (i) the distribution function is weakly modified by the interaction with the wave, that is, $f_e(t, v_\parallel) \approx f_e(0, v_\parallel)$, and (ii) the amplitude of the resonant electric field wave $|E(k_\perp, k_\parallel)|$ remains constant after the saturation of the LHDI for $t > t_{\text{sat}}$. Finally, under the previous assumptions, using the expression for the QL diffusion coefficient (Eq. (2)) and assuming a Maxwellian distribution function for the electrons, Eqs. (17) and (18) lead us to:

$$\frac{\Delta N_{e,\text{sup}}}{N_{e,\text{sup}}^0} = 0.1\left(\frac{\tau_{\text{NL}} - t_{\text{sat}}}{\omega_{ci}^{-1}}\right)\left(\frac{\omega_{pe}^2}{\omega_{ce}^2}\frac{S_{\max}}{n_0 T_i}\sqrt{\frac{m_i}{m_e}}\left(\frac{T_i}{T_e}\right)^{3/2}\right), \quad (19)$$

Before going on, we stress here that the increase in supra-thermal density $\Delta N_{e,\text{sup}}$ is proportional to the amplitude of the electric field at saturation, $S_{\max}$. This emphasizes how the input parameter $S_{\max}/nT_i$ impacts the output of QL theory and further supports the discussion regarding the difference between our results and the ones by Cairns & McMillan (2005) in Sect. 3.2.

Finally, expressing the electric field at saturation $S_{\max}$ using Eq. (6), the nonlinear time, τ_{NL}, using Eq. (16), the saturation time, t_{sat}, using Eq. (11), and the LHDI growth rate, γ_{LHDI}, using Eq. (5), and under the assumption $\omega_{pe} > \omega_{ce}$, the supra-thermal density increase in Eq. (19) becomes:

$$\frac{\Delta N_{e,\text{sup}}}{N_{e,\text{sup}}^0} = \begin{cases} 0.3\left(1 + \frac{T_e}{T_i}\right)^{-1}(1 - \chi\frac{m_e}{m_i}) & \text{current relaxation} \\ 0.004\left(1 + \frac{T_e}{T_i}\right)^{-1}(1 - \chi\frac{m_e}{m_i})\frac{m_i}{m_e}(\epsilon_n\rho_i)^3 & \text{ion trapping,} \end{cases} \quad (20)$$

where χ reads:

$$\chi = \frac{1.6}{\tau_0}\left(1 + \frac{T_e}{T_i}\right)\sqrt{1 + \beta_i/2}\ln[S_{\max}/S(t=0)]. \quad (21)$$

With the parameters considered in this study, and typically encountered in space plasmas, $\chi\frac{m_e}{m_i} \ll 1$. As a consequence, the supra-thermal electron density increase at long times is well approximated analytically by:

$$\frac{\Delta N_{e,\text{sup}}}{N_{e,\text{sup}}^0} = \begin{cases} 0.3\left(1 + \frac{T_e}{T_i}\right)^{-1} & \text{current relaxation} \\ 0.004\left(1 + \frac{T_e}{T_i}\right)^{-1}\frac{m_i}{m_e}(\epsilon_n\rho_i)^3 & \text{ion trapping,} \end{cases} \quad (22)$$

depending on the LHDI saturation mechanism at play.

This estimation leads to a total increase in the supra-thermal electron density summarized in Table 1 for the different sets of parameters used throughout this work. These values are also shown as horizontal gray dotted lines in both panels of Fig. 5 – for reduced mass ratio – and Fig. 7 for a physical mass ratio.

From the values in Table 1, we infer that our analytical approximation (Eq. (20)) is valid (error of the order of 10%) in the limit of "weak" LHDI electron acceleration (i.e., $\Delta N_{e,\text{sup}}/N_{e,\text{sup}}^0 \lesssim 1$). Stronger discrepancies arise for stronger electron acceleration (see third row in Table 1), as expected.

4.5. Application to Mercury's magnetopause

Mercury's magnetopause represents an excellent "textbook" example of a plasma boundary with an ion kinetic scale density gradient potentially LHDI-unstable. Previous space missions at Mercury – Mariner 10 (Russell et al. 1988) and MESSENGER (Solomon et al. 2007) – did not bring an instrumental payload capable of providing simultaneous measurements of electric field in the lower-hybrid frequency range and of the electron distribution function. Therefore, the expected LHW physics at Mercury cannot yet be tackled from past observations. However, the physics at these scales is exactly one of the main scientific objectives of the ongoing ESA/JAXA space mission BepiColombo (Benkhoff et al. 2010). Different plasma instruments onboard the Mio spacecraft will provide measurements of: (i) the plasma density profile along the spacecraft trajectory, using different complementary experiments, namely, Langmuir probe measurements (Karlsson et al. 2020), quasi-thermal noise measurements (Moncuquet et al. 2006), and mutual impedance measurements (Gilet et al. 2019), all within the Plasma Wave Investigation (PWI) consortium (Kasaba et al. 2020), (ii) the electric field in the lower-hybrid frequency range (PWI), and (iii) the electron distribution function (MPPE/MEA, Mercury Plasma Particle Experiment and Mercury Electron Analyzer (Saito et al. 2010)). This will enable us to directly address the physics of Mercury's strongly inhomogeneous magnetopause. In this section, we quantify the expected efficiency of LHDI electron acceleration at Mercury's magnetopause using the eQL model developed in our work in support for future BepiColombo observations.

As previously pointed out in Sect. 2.2, the parameters used in our strong and weak gradient cases are taken in the range expected at Mercury's magnetopause (Slavin et al. 2008; Gershman et al. 2015). Therefore, we make use of the results of our eQL model with physical mass ratio in Sect. 4.4 to assess the importance of electron acceleration driven by the LHDI at Mercury's magnetopause.

First, we discuss the features of the LHW that are expected to be generated by the development of the LHDI at Mercury's magnetopause. These waves have a frequency of $f \approx f_{\text{LH}} \approx 5-20$ Hz (in the frame of the drifting ions) and wavelength $\lambda \approx 2\pi\rho_e \approx 5-15$ km (hereafter using typical magnetic field values at Mercury's magnetopause of $10-30$ nT, ion temperature $30-70$ eV, and density $10-30$ cm^{-3}; see Milillo et al. 2020). In the reference frame of the spacecraft, given that those waves are advected by the shocked solar wind flow, estimated to have a speed $V_{\text{sw}} \approx 100$ km s^{-1}, and with an ion drift speed $v_{\text{Di}} \approx v_{\text{thi}} \approx 50-80$ km s^{-1}, the Doppler-shifted frequency of the LHW, expected to be observed in the spacecraft frame, lies in the range $f' = f \pm k(v_{\text{Di}} + V_{\text{sw}}) \approx 50-200$ Hz. We note that the Doppler-shifted component is expected to be much higher that the intrinsic frequency, so that the Taylor's hypothesis is valid for these
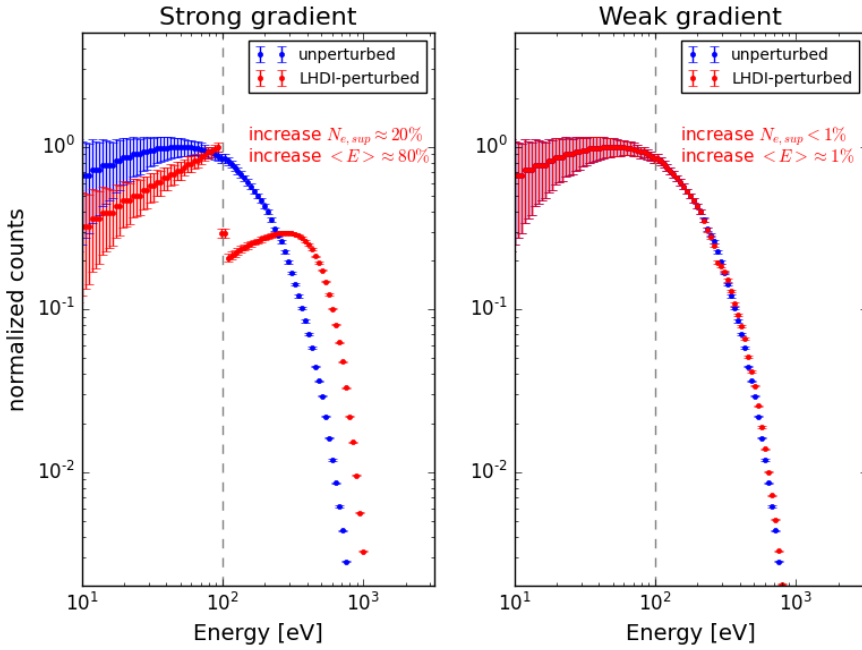
Fig. 8. Instrumental response of the instrument MPPE/MEA simulated using our extended QL model for both strong $\epsilon_n \rho_i = 1$ and weak $\epsilon_n \rho_i = 0.5$ gradient cases (*left and right panels*), in the direction parallel to the magnetic field. Unperturbed electron distribution function using temperature $T_e = 50$ eV in blue, and results of eQL model at time $t = \tau_{NL}$ in red. The dashed vertical line indicates the energy from which the supra-thermal electron density $N_{e,\text{sup}}$ is computed.

waves at Mercury's magnetopause. Moreover, the electric field amplitude of these LHW at saturation is $E \approx 10{-}100$ mV m^{-1}, as obtained from Eq. (6). These typical frequency and energy range of LHW at Mercury suggests the use of electric field instruments onboard Mio spacecraft to address the LHW physics at Mercury's magnetopause. In particular, the sensors MEFISTO and WPT that are part of the PWI consortium (Kasaba et al. 2020) will provide electric field observations in this frequency range with a sensitivity on the order of 10^{-3} mV m^{-1}, which is well below the expected amplitude of these waves.

Second, we discuss the features of electron distribution functions possibly modified by resonant interaction with the previously discussed LHW. This resonant wave-particle interaction accelerates sub-thermal electrons (with speed $v_z \lesssim v_{\text{the}}$) to supra-thermal energies (with speed $v_z \gtrsim 2v_{\text{the}}$) in the direction parallel to the ambient magnetic field, as shown in Fig. 7 top panels. In the following we assume an unperturbed electron temperature of 50 eV (typical values at Mercury's magnetopause being $\sim$20$-$100 eV (Ogilvie et al. 1974; Uritsky et al. 2011)). This acceleration process is well in the range of observations of the electron instrument MPPE/MEA onboard the Mio spacecraft of the BepiColombo mission (Saito et al. 2010), since this instrument includes two electron analyzers that can measure the three-dimensional energy distribution of electrons in the range 3–3000 eV (in solar wind mode) or 3–25 500 eV (in magnetospheric mode), with a time resolution of 1 second (Milillo et al. 2020). Here, we simulate the instrumental response of MPPE/MEA when encountering electrons accelerated by a LHDI at Mercury's magnetopause, as shown in Fig. 8, with the unperturbed electron distribution function in blue, and the one resulting from interaction with LHDI at long times in red. In Fig. 8, the uncertainties on the simulated response of the sensor MEA are obtained using the uncertainty on the G-factor of the instrument reported in Saito et al. (2010) (of the order of 10%). So, on the one hand we predict that the modifications in the electron distribution function above 100 eV are observable by MPPE/MEA in the case of a strongly inhomogeneous magnetopause (width around one ion gyroradius, or less), as shown in the left panel of Fig. 8. On the other hand, since

this process is very sensitive to the width of the magnetopause layer, we expect negligible modifications in the electron distribution function for less inhomogeneous magnetopause conditions (width around two ion gyroradii or more), as shown in the right panel of Fig. 8. With typical magnetic field and temperature values at Mercury's magnetopause the ion gyroradius is around 20$-$80 km.

We also assess that the interaction between LHDI and electrons increases both (i) the density of supra-thermal electrons $N_{e,\text{sup}}$ (i.e., electrons with energy higher than 100 eV; see Eq. (12)) and (ii) the electron temperature. In the simulated responses with a strong (resp. weak) density gradient, the former increases by 20% (resp. 0.3%), due to the interaction with the LHW, and the latter increases by 80% (resp. 1.5%). We stress here how these two scalar quantities could be used as tracers of LHDI-electron interaction events in MPPE/MEA data, and how this response is limited to the direction parallel (anti-parallel) to the ambient magnetic field (i.e., around $\theta = 0°$ and $180°$ in the electron pitch-angle distributions).

Third, we present electron observations made by the NASA spacecraft Mariner 10 during its first Mercury flyby on 29 March 1974 (Ogilvie et al. 1974). In Fig. 9, we show the data for the magnetic field (upper panels) and electrons (bottom panels) for the inbound (left) and outbound (right) magnetopause crossings. In particular, we observe a bimodal character of the electron energy distribution during the crossing (bottom panels), with one ambient electron population around 10–30 eV and a second energized population around 100–300 eV. This is consistent with the signatures expected for LHDI-accelerated electrons. Although these observations suggest that the LHDI might play a role in the electron energization at Mercury's Magnetopause, the Mariner 10 data cannot unambiguously confirm this hypothesis because of the lack of electric field observations. Moreover, the low time resolution of Mariner 10 electron measurements (1/6 s^{-1}), along with the narrow energy range (13.4–687 eV) and the lack of a statistically significant number of crossings mean that the Mariner 10 observations stand in the way of establishing conclusive evidence of LHDI-accelerated electrons at Mercury's magnetopause.
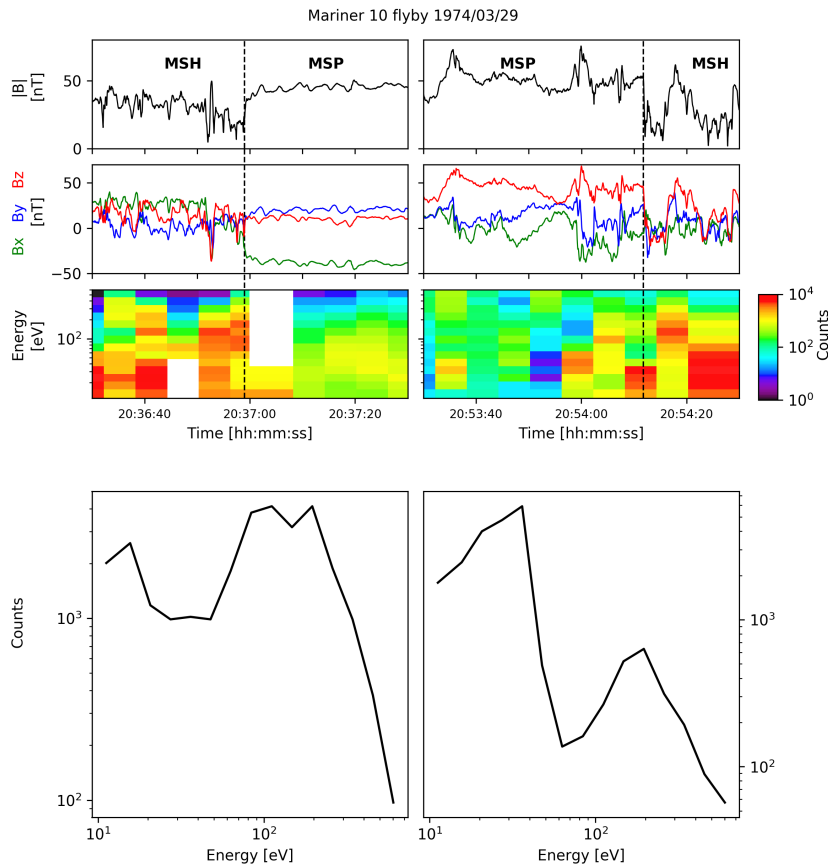
Fig. 9. Mariner 10 observations during its first Mercury flyby on the 29 March 1974, inbound (*left panels*) and outbound (*right panels*) magnetopause crossings are shown, the associated time intervals are 20:36:30–20:37:30 and 20:53:30–20:54:30, respectively. Magnetosphere (MSP) and magnetosheat (MSH) plasma measurements are shown. From top to bottom, we show the magnetic field module (first row) and its components in MSEQ coordinate (second row) obtained from the magnetometer onboard Mariner 10. Moreover, we show the electron energy spectra as a function of time (third row) and the electron energy spectrum at the time of the crossings (fourth row), obtained from the PLS instrument onboard Mariner 10. The time of the crossings is highlighted by black vertical dashed lines in the first three panels.

The limits of such Mariner 10 measurements will be overcome by the more advanced and complete payload of the ESA-JAXA BepiColombo space mission, especially the joint electric field observations of LHW (with PWI/MEFISTO and PWI/WPT) and electrons (with MPPE/MEA). We are therefore confident that the Mio plasma and electric field instrumental suites of BepiColombo will soon enable us to shed some light on the statistical relevance of LHDI and associated electron heating in the global dynamics of Mercury's magnetosphere frontier with the solar wind.

5. Conclusions

In this work, we address the question of electron acceleration efficiency by lower-hybrid waves generated by the lower-hybrid-drift instability.

For this purpose, we have performed 3D, full-kinetic numerical simulations to provide numerical evidence of electrons acceleration parallel to the ambient magnetic field by resonant wave-particle interaction with LHDI waves. Our self-consistent nonlinear model has also enabled us to address the consequences of the saturation of the instability on the eventual stoppage of the electron acceleration. To our the best of our knowledge, this is the first time that this process is self-consistently observed in full-kinetic simulations. This represents the first original contribution of this work.

Moreover, we have provided quantitative estimates of the efficiency of this resonant acceleration process. To model this process, we have (i) used a standard QL model based on the work of Cairns & McMillan (2005), and (ii) developed an extended QL model that includes the consequences of nonlinear LD-like effects on long time scales evolution of the electron distribution function. We compared the results of these two quasilinear models and the full-kinetic model. Such comparison highlighted the limitations at long time scales of the standard quasilinear theory that paved the way for an extended one, designed to overcome such limitations. Such a comparison also enabled us to validate the eQL model. This new extended quasilinear (eQL) model successfully captures the electron acceleration properties found on full-kinetic simulation results and represents the second original contribution of this work.

Thanks to its simplicity, the eQL model has enabled us to explore a range of parameter space that is not accessible to full-kinetic simulations due to computational constraints. In particular, we have addressed the efficiency of LHDI electron acceleration at Mercury's magnetopause, using a realistic proton-to-electron mass ratio. In this context, we estimate that LHDI electron acceleration is an efficient mechanism for energizing electrons during periods of strong magnetospheric compression (when the magnetopause boundary steepens on scales of the order or lower than the ion gyroradius). This efficiency strongly depends on the density gradient at the magnetopause. Under such conditions of a "steep" magnetopause at Mercury, we expect strong signatures of LHDI electron acceleration in the BepiColombo instrumental suite response (PWI and MPPE/MEA).

We are confident that our extended quasilinear model will enable quantitative studies of the efficiency of electron acceleration in inhomogeneous space plasmas in support of past and future space plasma observations. More importantly, this work also provides a validated framework for extending the range of the validity and applicability of quasilinear modeling, not only associated with the lower-hybrid-drift instability – as in this study – but also to a broader variety of waves and instabilities in space plasmas.

References

Alexandrov, A. F., Bogdankevich, L. S., & Rukhadze, A. A. 1984, Principles of Plasma Electrodynamics, Series in Electrophysics (Springer)

Alpers, W. 1969, Ap&SS, 5, 425

Amatucci, W. E. 1999, J. Geophys. Res., 104, 14481

André, M., Behlke, R., Wahlund, J. E., et al. 2001, Ann. Geophys., 19, 1471

André, M., Odelstad, E., Graham, D., et al. 2017, MNRAS, 469

Bale, S. D., Mozer, F. S., & Phan, T. 2002, Geophys. Res. Lett., 29, 33

Bécoulet, A., Hoang, G., Artaud, J., et al. 2011, Fusion Eng. Des., 86, 490

Benkhoff, J., van Casteren, J., Hayakawa, H., et al. 2010, Planet. Space Sci., 58, 2

Bernstein, I. B., & Engelmann, F. 1966, Phys. Fluids, 9, 937

Bingham, R., Dawson, J. M., & Shapiro, V. D. 2002, J. Plasma Phys., 68, 161

Birdsall, C. K., & Langdon, A. B. 1991, Plasma Physics via Computer Simulation (Adam Hilger IOP Publishing)

Brackbill, J. U., Forslund, D. W., Quest, K. B., & Winske, D. 1984, Phys. Fluids, 27, 2682

Broiles, T. W., Burch, J. L., Chae, K., et al. 2016, MNRAS, 462, S312

Brunetti, M., Califano, F., & Pegoraro, F. 2000, Phys. Rev. E, 62, 4109

Cairns, I. H., & McMillan, B. F. 2005, Phys. Plasmas, 12

Chen, Y., & Birdsall, C. K. 1983, Phys. Fluids, 26, 180

Daughton, W. 1998, J. Geophys. Res., 103, 29429

Daughton, W. 1999, J. Geophys. Res., 104, 28701

Daughton, W. 2003, Phys. Plasmas, 10, 3103

Davidson, R. C. 1978, Phys. Fluids, 21, 1375

Davidson, R. C., Gladd, N. T., Wu, C. S., & Huba, J. D. 1977, Phys. Fluids, 20, 301

Derouillat, J., Beck, A., Pérez, F., et al. 2018, Comput. Phys. Commun., 222, 351

Gary, S. P. 1993, Theory of Space Plasma Microinstabilities, Cambridge Atmospheric and Space Science Series (Cambridge University Press)

Gary, S. P., & Sanderson, J. J. 1978, Phys. Fluids, 21, 1181

Gary, S. P., & Sgro, A. G. 1990, Geophys. Res. Lett., 17, 909

Gershman, D. J., Raines, J. M., Slavin, J. A., et al. 2015, J. Geophys. Res.: Space Phys., 120, 4354

Gilet, N., Henri, P., Wattieaux, G., et al. 2019, Front. Astron. Space Sci., 6, 16

Goldstein, R., Burch, J. L., Llera, K., et al. 2019, A&A, 630, A40

Graham, D. B., Khotyaintsev, Y. V., Norgren, C., et al. 2019, J. Geophys. Res.: Space Phys., 124, 8727

Graham, D. B., Khotyaintsev, Y. V., Norgren, C., et al. 2017, J. Geophys. Res.: Space Phys., 122, 517

Hoshino, M., Mukai, T., Terasawa, T., & Shinohara, I. 2001, J. Geophys. Res., 106, 25979

Huba, J., Gladd, T., & Papadopoulos, K. 1978, J. Geophys. Res., 83

Karlsson, T., Eriksson, A. I., Odelstad, E., et al. 2017, Geophys. Res. Lett., 44, 1641

Karlsson, T., Kasaba, Y., Wahlund, J.-E., et al. 2020, Space Sci. Rev., 216

Kasaba, Y., Kojima, H., Moncuquet, M., et al. 2020, Space Sci. Rev., 216, 65

Khotyaintsev, Y. V., Cully, C. M., Vaivads, A., André, M., & Owen, C. J. 2011, Phys. Rev. Lett., 106, 165001

Krall, N. A., & Liewer, P. C. 1971, Phys. Rev. A, 4, 2094

Krall, N. A., & Trivelpiece, A. W. 1973, Principles of Plasma Physics (McGraw-Hill)

Krasnoselskikh, V. V., Kruchina, E. N., Volokitin, A. S., & Thejappa, G. 1985, A&A, 149, 323

Laming, J. M. 2001, ApJ, 563, 828

Lapenta, G., & Brackbill, J. U. 2002, Phys. Plasmas, 9, 1544

Lapenta, G., Brackbill, J. U., & Daughton, W. S. 2003, Phys. Plasmas, 10, 1577

Lapenta, G., Pucci, F., Olshevsky, V., et al. 2018, J. Plasma Phys., 84, 715840103

Le Contel, O., Nakamura, R., Breuillard, H., et al. 2017, J. Geophys. Res.: Space Phys., 122, 12,236

Markidis, S., Lapenta, G., & Rizwan-uddin 2010, Math. Comput. Simul., 80, 1509

McBride, J., & Ott, E. 1972, Phys. Lett. A, 39, 363

McBride, J. B., Ott, E., Boris, J. P., & Orens, J. H. 1972, Phys. Fluids, 15, 2367

McClements, K. G., Bingham, R., Su, J. J., Dawson, J. M., & Spicer, D. S. 1993, ApJ, 409, 465

McMillan, B. F. 2020, Phys. Plasmas, 27, 052106

Milillo, A., Fujimoto, M., Murakami, G., et al. 2020, Space Sci. Rev., 216, 93

Moncuquet, M., Matsumoto, H., Bougeret, J. L., et al. 2006, Adv. Space Res., 38, 680

Norgren, C., Vaivads, A., Khotyaintsev, Y. V., & André, M. 2012, Phys. Rev. Lett., 109, 055001

Ogilvie, K. W., Scudder, J. D., Hartle, R. E., et al. 1974, Science, 185, 145

Ott, E., McBride, J. B., Orens, J. H., & Boris, J. P. 1972, Phys. Rev. Lett., 28, 88

Pericoli-Ridolfini, V., Barbato, E., Cirant, S., et al. 1999, Phys. Rev. Lett., 82, 93

Pritchett, P. L., Coroniti, F. V., & Decyk, V. K. 1996, J. Geophysical. Res.: Space Phys., 101, 27413

Pu, Z.-Y., Quest, K. B., Kivelson, M. G., & Tu, C.-Y. 1981, J. Geophys. Res.: Space Phys., 86, 8919

Reiniusson, A., Stenberg, G., Norqvist, P., Eriksson, A. I., & Rönnmark, K. 2006, Ann. Geophys., 24, 367

Retinó, A., Nakamura, R., Vaivads, A., et al. 2008, J. Geophys. Res.: Space Phys., 113

Rigby, A., Cruz, F., Albertazzi, B., et al. 2018, Nat. Phys., 14, 475

Russell, C. T., Baker, D. N., & Slavin, J. A. 1988, The Magnetosphere of Mercury (NTRS), 514

Sagdeev, R. Z., Shapiro, V. D., Shevchenko, V. I., et al. 1990, Geophys. Res. Lett., 17, 893

Saito, Y., Sauvaud, J. A., Hirahara, M., et al. 2010, Planet. Space Sci., 58, 182

Scarf, F. L., Taylor, W. W. L., Russell, C. T., & Elphic, R. C. 1980, J. Geophys. Res.: Space Phys., 85, 7599

Shapiro, V. D., Szegö, K., Ride, S. K., Nagy, A. F., & Shevchenko, V. I. 1995, J. Geophys. Res., 100, 21289

Shapiro, V. D., Bingham, R., Dawson, J. M., et al. 1999, J. Geophys. Res.: Space Phys., 104, 2537

Shinohara, I., & Hoshino, M. 1999, Adv. Space Res., 24, 43

Singh, N., Al-Sharaeh, S., Abdelrazek, A., Leung, W. C., & Wells, B. E. 1996, Geophys. Res. Lett., 23, 3663

Singh, N., Wells, B. E., Abdelrazek, A., Al-Sharaeh, S., & Leung, W. C. 1998, J. Geophys. Res., 103, 9333

Slavin, J. A., Acuña, M. H., Anderson, B. J., et al. 2008, Science, 321, 85

Solomon, S. C., McNutt, R. L., Gold, R. E., & Domingue, D. L. 2007, Space Sci. Rev., 131, 3

Tang, B., Li, W. Y., Graham, D. B., et al. 2020, Geophys. Res. Lett., 47, e89880

Uritsky, V. M., Slavin, J. A., Khazanov, G. V., et al. 2011, J. Geophys. Res.: Space Phys., 116

Vaivads, A., André, M., Buchert, S. C., et al. 2004, Geophys. Res. Lett., 31, L03804

Walker, S. N., Balikhin, M. A., Alleyne, H. S. C. K., et al. 2008, Ann. Geophys., 26, 699

Wilson, L. B., Koval, A., Szabo, A., et al. 2013, J. Geophys. Res. (Space Phys.), 118, 5

Winske, D., & Liewer, P. C. 1978, Phys. Fluids, 21, 1017

Yoo, J., Ji, J.-Y., Ambat, M. V., et al. 2020, Geophys. Res. Lett., 47

Zacharegkas, G., Isliker, H., & Vlahos, L. 2016, Phys. Plasmas, 23, 112119

Zhang, Y., & Matsumoto, H. 1998, J. Geophys. Res.: Space Phys., 103, 20561

Zhou, M., Deng, X. H., Li, S. Y., et al. 2009, J. Geophys. Res.: Space Phys., 114

Zhou, M., Li, H., Deng, X., et al. 2014, J. Geophys. Res.: Space Phys., 119, 8228

5.3 Lavorenti et al. (2022) *A&A*, 664, A133

Astronomy & Astrophysics

Electron dynamics in small magnetospheres

Insights from global, fully kinetic plasma simulations of the planet Mercury

Federico Lavorenti[1,2], Pierre Henri[1,3], Francesco Califano[2], Jan Deca[4,5,6], Sae Aizawa[7],
Nicolas André[7], and Johannes Benkhoff[8]

[1] Laboratoire Lagrange, Observatoire de la Côte d'Azur, Université Côte d'Azur, CNRS, Nice, France
   e-mail: federico.lavorenti@oca.eu
[2] Dipartimento di Fisica "E. Fermi", Università di Pisa, Pisa, Italy
[3] LPC2E, CNRS, Univ. d'Orléans, OSUC, CNES, Orléans, France
[4] LASP, University of Colorado Boulder, Boulder, CO, USA
[5] Institute for Modeling Plasma, Atmospheres and Cosmic Dust, NASA/SSERVI, Silicon Valley, CA, USA
[6] LATMOS, Université de Versailles à Saint Quentin, Guyancourt, France
[7] IRAP, CNRS-CNES-UPS, Toulouse, France
[8] ESA/ESTEC, Keplerlaan 1, 2200 AG Noordwijk, The Netherlands

ABSTRACT

Context. The planet Mercury possesses a small but highly dynamic magnetosphere in which the role and dynamics of electrons are still largely unknown.
Aims. We aim to model the global dynamics of solar-wind electrons impinging on Mercury's magnetosphere. Particular relevance is given to local acceleration processes and the global circulation patterns.
Methods. The goals of this work are pursued by means of three-dimensional, fully kinetic particle-in-cell simulations modeling the interaction of the solar wind with the Hermean magnetosphere. This method allows a self-consistent representation of the plasma dynamics from the large planetary scale down to the electron kinetic scale. We carried out numerical simulations using two different solar-wind conditions: purely northward or purely southward interplanetary magnetic field direction.
Results. We find a high plasma current (of the order of few $\mu A\,m^{-2}$) flowing at the magnetospheric boundaries (bow shock and magnetopause) dominated by electrons. This current is driven by the small-scale electron physics resolved in our model. Furthermore, we observe strong electron acceleration up to tens of keV as a consequence of magnetic reconnection when the interplanetary magnetic field is directed southward. Such energetic electrons are partially trapped in the dipolar magnetic field of the planet mainly at nightside. Finally, by studying the distribution of electrons in our simulations along Mariner10 and BepiColombo first-Mercury-flyby trajectories, we propose that both spacecraft observed this energetic quasi-trapped electron population around closest approach.

Key words. magnetic reconnection – plasmas – methods: numerical – planet-star interactions – planets and satellites: magnetic fields

1. Introduction

Mercury is one of the least explored planets of the Solar System. Over decades of space exploration, only two missions have been devoted to the innermost planet of the Solar System.

The NASA Mariner10 mission in the 1970s provided a snapshot of the Hermean environment with its three flybys (Russell et al. 1988). These observations showed the presence of a planetary magnetic field (Ness et al. 1974) and of a structured plasma environment (Ogilvie et al. 1977). In particular, Mariner10 was able to perform measurements of the core of the electron distribution function (in the range 13.4–687 eV) during most of its orbit inside the Hermean magnetosphere (Christon 1987). However, Mariner10 was not able to observe ions due to a technical failure (Ogilvie et al. 1974).

Three decades later, the NASA MESSENGER mission deeply extended our knowledge of the Hermean environment during its four years of orbital observations (Solomon & Anderson 2018). This wealth of in situ observations enabled the first systematic studies of the interaction between the solar-wind plasma and Mercury's magnetized

environment (Raines et al. 2015 and references therein). These studies evidence the highly dynamical character of Mercury's plasma environment and shed light on the tight coupling between the solar-wind, magnetosphere, exosphere and surface of Mercury. The mission addressed several plasma processes occurring at the global planetary scale (of the order of 2400 km) and down to the ion kinetic scale (of the order of 100 km) (Boardsen et al. 2012; Raines et al. 2014; Gershman et al. 2014, 2015; Schmid et al. 2021). However, given the instrumental constraints of the mission, MESSENGER did not address the plasma processes ongoing at the electron scale. The instrumental suite onboard MESSENGER provided observations of electrons above ∼10 keV, thus missing the core of the distribution function, and it could not provide plasma wave observations below the typical ion frequency range (of the order of a few Hz).

The ESA/JAXA BepiColombo mission has been designed to continue building upon the legacy left by MESSENGER (Benkhoff et al. 2021). BepiColombo is now cruising to Mercury (arrival expected in 2025) and performed its first Mercury flyby on 1 October 2021. The novelty of this mission resides in (i) its two-spacecraft nature (BepiColombo is composed of one

Mercury Planetary Orbiter, MPO, and of one magnetospheric orbiter, nicknamed Mio) and in (ii) its advanced instrumental suite for environmental studies enabling observations down to the electron scale (Milillo et al. 2020). BepiColombo is the first mission able to provide a simultaneous multi-point picture of the Hermean environment from the global planetary scale down to the electron scale (of the order of 1 km). In order to both analyze and optimally plan such novel observations, global numerical models of the Hermean environment with resolutions down to the electron scale are needed.

To date, global numerical models of Mercury's plasma environment have been mostly limited to magnetohydrodynamic (MHD; Kabin et al. 2000; Ip & Kopp 2002; Yagi et al. 2010; Pantellini et al. 2015; Jia et al. 2015, 2019), multifluid (Kidder et al. 2008; Benna et al. 2010; Dong et al. 2019), and hybrid (meaning kinetic ions and fluid massless electrons) (Kallio & Janhunen 2003; Trávníček et al. 2007, 2009, 2010; Richer et al. 2012; Müller et al. 2012; Herčík et al. 2013; Herčík & Trávníček 2016; Fatemi et al. 2018, 2020; Exner et al. 2018, 2020) models. These models appropriately reproduce the plasma dynamics down to the ion kinetic scale and have been extensively and successfully used in support of the Mariner10 and MESSENGER missions. However, to interpret the forthcoming new observations of the BepiColombo mission, more refined models able to self-consistently include electron kinetic physics are required.

Recently, a first attempt to locally embed electron kinetic physics in a global MHD simulation was carried out by Chen et al. (2019). Their model can be used to study the role of electrons in a precise subset of the global magnetosphere (for instance, the magnetotail); on the other hand, it cannot reproduce dynamical processes encompassing the global magnetosphere system such as, for example, the global electron circulation around the planet (Walsh et al. 2013). In order to overcome this limitation and to self-consistently include both ion and electron physics, in this work, we study the interaction between the solar wind and the Hermean plasma environment using a global fully-kinetic model. A similar approach was presented by Lapenta et al. (2022) using the results of a global hybrid simulation to initialize a fully-kinetic one. In that work, the authors found that the feedback of kinetic electrons does not affect the large-scale structure of the magnetosphere. Nonetheless, on the small scale, they found (i) thinner magnetospheric boundaries with higher currents and (ii) more efficient energization processes in the magnetosphere. The results of Lapenta et al. (2022) point out the importance of a kinetic model for electrons in global simulations of planetary magnetospheres, a goal that is today attainable thanks to the increasing computational power of current High Performance Computing (HPC) facilities.

Although only a few in situ electron observations are available at Mercury, some hints on their global dynamics have been discussed in past works using Mariner10 (Christon 1987) and MESSENGER data (Ho et al. 2012, 2016; Baker et al. 2016; Dewey et al. 2018). One of the most significant outcomes of these observations is the presence of a quasi-stable, high-energy (up to tens of keV) electron population inside the Hermean magnetosphere, mainly observed in the night post-midnight sector (local time 0–6 h). According to those observations, the Hermean environment is significantly populated by electrons with energies up to tens of keV. In this work, we investigate the origin of these energetic electrons and their loss mechanism inside the Hermean magnetosphere by means of global, fully kinetic simulations.

The paper is organized as follows. In Sect. 2, we present our fully kinetic model, and in Sect. 3 we analyze the large-

scale structure obtained from our simulations and validate our model against nominal bow shock and magnetopause shapes and positions at Mercury. In Sect. 4, we focus on our simulations results regarding electron energization and circulation in the Hermean magnetosphere, and in Sect. 5 we build and discuss synthetic electron energy spectra obtained from our simulations along Mariner10 and BepiColombo trajectories during their first Mercury flybys. Finally, in Sect. 6, we discuss the results and conclude the paper.

2. The model: Fully kinetic global simulations

The simulations are done using the semi-implicit, fully kinetic particle-in-cell (PIC) code iPIC3D (Markidis & Lapenta 2010). It solves the Vlasov-Maxwell system of equations for both ions and electrons by discretizing the distribution function of both species using macro-particles. We present two different simulations, namely RunN and RunS, characterized by a purely northward or southward interplanetary magnetic field (IMF), respectively. In the following, we use the Mercury-centered Solar Orbital (MSO) reference frame, where the x-axis points from the planet center to the sun, the z-axis is anti-parallel to Mercury's magnetic dipole, and the y-axis points from dawn to dusk.

The simulations use a three-dimensional cartesian geometry, a simulation domain $(L_x, L_y, L_z) = (-9 : +6, \pm 6, \pm 6) R$ (here, R is the planet radius) in MSO coordinates, divided into $(N_x, N_y, N_z) = (960, 768, 768)$ grid cells. The simulations are initialized with 64 macro-particles per cell per species. The time step is $dt = 1.4$ ms, much smaller than the electron gyro-period ($\tau_{ce} \equiv 2\pi/\omega_{ce} \equiv 2\pi m_e c/eB_{SW} = 31.5$ ms). The grid spacing is $dx = dy = dz = 0.015 R = 1.5 \rho_e$, where $\rho_e \equiv c\sqrt{T_{e,SW} m_e}/eB_{SW}$ is the electron gyro-radius. One important feature of implicit PIC codes is that, even if the grid spacing is of the order of the electron gyro-radius $\rho_e \lesssim dx < \rho_i$, the code correctly captures the sub-grid electron kinetic physics as long as the condition $0.1 < v_{the}dt/dx < 1$ is fulfilled (Brackbill & Forslund 1982). In our case, $v_{the}dt/dx = 0.18$. However, since sub-grid oscillations on the electron scale tend to accumulate energy at the grid scale, a smoothing technique is required to avoid numerical instabilities at the grid scale (see Tóth et al. 2017 for details on the filter used; in our case, the filter is applied two times per cycle with a factor of $\alpha = 0.5$).

The simulation setup includes (i) the solar-wind plasma (uniform density, magnetic field, and temperature), (ii) the spherical planet centered at $x, y, z = (0, 0, 0)$ with radius R, and (iii) the dipolar magnetic field centered in $x, y, z = (0, 0, 0.2) R$ with intensity 200 nT$/R^3$.

Given that we simulate an infinite system using a finite numerical box, particular care must be taken when imposing the external boundary conditions. Because the planet interaction region is sufficiently far (on the order of 5 planet radii) from the external boundaries of the box, we populate the last cells of the boundaries with solar-wind plasma (an exception is made for the antisunward boundary from which plasma is only allowed to exit the box). To smooth out the electromagnetic fields fluctuations close to the boundaries, we employ a linear simple absorption layer (LSAL) method (Berendeev et al. 2018) on the ten outermost cells of the simulation domain. As discussed in Berendeev et al. (2018), this method avoids wave reflection and ensures numerical stability at the boundaries. With this method, the magnetic and electric field values in the outermost boundary cells are equal to their corresponding solar-wind values, $\mathbf{B}_{SW}$ and $\mathbf{E}_{SW}$. Since in the solar wind the plasma

frozen-in condition holds, the electric field is given by $\mathbf{E}_{SW} = -\mathbf{V}_{SW} \times \mathbf{B}_{SW}$. A divergence cleaning routine for the magnetic field ensures that $\text{div}(\mathbf{B}) = 0$ in the absorbing layer.

Particular care must also be taken in handling the plasma interacting directly with the planet. This is especially true for models, such as fully kinetic ones, that do not impose quasi-neutrality. In order to avoid the generation of spurious net charge density on the planet surface, the macro-particles falling into the planet are removed from the simulation using a charge-balanced method. This method ensures that (i) the same amount of positive and negative charged macro-particles is removed from the simulation box at the planet surface boundary and that (ii) the excess of electron flux at the planetary surface is expelled back radially. This inner boundary condition mimics the sub-grid interaction between precipitating plasma and the planet surface ongoing on length scales of few Debye lengths.

In both simulations, the solar-wind plasma is initialized with a density of $n_{SW} = 30\,\text{cm}^{-3}$, velocity of $\mathbf{V}_{SW} = (-400,0,0)\,\text{km s}^{-1}$, magnetic field of $\mathbf{B}_{SW} = (0,0,\pm20)\,\text{nT}$, and temperature of $T_{i,SW} = T_{e,SW} = 21.5\,\text{eV}$. The ram pressure is $P_{ram} \equiv n_{SW}V_{SW}^2 = 8.2\,\text{nPa}$, and the plasma beta is $\beta \equiv 8\pi n_{SW}T_{SW}/B_{SW}^2 = 1.3$. The only parameter that is different between the two runs (RunN and RunS) is the direction of the magnetic field $\mathbf{B}_{SW}$. These parameters are representative of those expected in the proximity of Mercury at aphelion (James et al. 2017; Sarantos et al. 2007) and similar to those used in Aizawa et al. (2021).

Once the interaction between the solar-wind flow and the planetary magnetic field reached a quasi steady-state, we stopped the simulation. Such a timescale corresponds approximately to the solar-wind ballistic time taken to cross the simulation box, $T \approx L_x/V_{x,SW} \approx 10\,\text{s}$ (corresponding to approximately 7000 numerical cycles).

In order to keep computational resources manageable, we chose to reduce (i) the ion-to-electron mass ratio $m_i/m_e = 100$ (from its real value of 1836), (ii) the electron plasma-to-cyclotron frequency ratio $\omega_{pe}/\omega_{ce} = 17.8$ (from its real value of 83), and (iii) the planet radius $R = 230\,\text{km}$ (from its real value of 2440 km). With these values, we obtain a hierarchy of scale lengths $R = 10\rho_i = 100\rho_e$ that – although compressed – maintains a sufficiently large separation between planetary, ion, and electron kinetic scales. The first and second rescalings represent a standard procedure in plasma fully kinetic simulations (see, e.g., Bret & Dieckmann 2010). The third rescaling is analogous to what was proposed and validated in Tóth et al. (2017) for the case of the Earth and also discussed extensively in Markidis et al. (2021). Moreover, this planet rescaling approach was already adopted in past works using global hybrid models in support of MESSENGER observations (Trávníček et al. 2007, 2009, 2010) and recently in a global fully-kinetic model (Lapenta et al. 2022).

In the next section, we validate our scaled-down model against the nominal shapes and positions of the magnetosphere boundaries. A broader discussion on the impact of these rescalings on our results is given in Sect. 6.

3. Overview of the large-scale structure: Magnetosphere boundary identification

3.1. Validation of the global, fully kinetic model

We start by validating our model by showing that the large-scale structure of the system typically obtained by fluid and hybrid models is correctly reproduced, as shown in Fig. 1. Indeed, both

simulations show the formation of a bow shock standing in front of the planet, the magnetosheath with increased density and magnetic field amplitude, the magnetopause with its strong current, J_y, and the magnetosphere cavity with very low density and high magnetic field. Such a large-scale configuration is shown in Fig. 1 for both simulations using the ion density n_i [cm^{-3}] (left panels), the magnetic field amplitude $|\mathbf{B}|$ [nT] (central panels), and the plasma current J_y [nA m^{-2}] (right panels). In Fig. 2, we show a cut along the subsolar line, $Y_{MSO} = Z_{MSO} = 0$.

The observed bow shock and magnetopause are compared to their nominal shape and position obtained from MESSENGER data (Winslow et al. 2013). The authors modeled the bow shock using a paraboloid model (with parameters $X_0 = 0.5\,R$, $e = 1.04$, $p = 2.75\,R$; Slavin et al. 2009) and the magnetopause using the Shue et al. (1997) model (with parameters $R_{ss} = 1.45\,R$, $\alpha = 0.5$). The resulting bow shock and magnetopause profiles are shown in Fig. 1 using dashed and solid black lines, respectively. Overall, the bow shock and magnetopause found in our simulations are in good agreement with their nominal shapes. As expected, a better agreement is observed in the equatorial plane (see Fig. 1), whereas some discrepancy is found in the dipolar plane due to the broken assumption of cylindrical symmetry assumed in these relatively simple analytical models (the magnetic field along the z-axis breaks the symmetry).

We compute the bow shock and magnetopause stand-off distances as the maximum of the current density, $|\mathbf{J}(x)|$, and the point where the magnetic pressure equals the solar-wind ram pressure, respectively. The stand-off positions of the bow shock and magnetopause obtained from our simulations are in agreement with the nominal values reported by Winslow et al. (2013), as shown in Fig. 2. The relative discrepancy for the bow shock and the magnetopause is on the order of 1% and 10%, respectively. Interestingly, the discrepancy for the magnetopause is larger in both runs when compared to the one for the bow shock. Nonetheless, similar discrepancies of the order of 10% have been found by Aizawa et al. (2021) using global hybrid and fluid models. We conclude that our fully-kinetic model satisfactorily reproduces the large-scale structures of the Hermean magnetosphere. This validates our model at large scales and paves the way for further analysis of the small-scale electron physics in the next sections.

3.2. Impact of electron physics at large scales: Boosting the charge current at the boundaries

Past works using hybrid or fluid models found a total current density at the bow shock and magnetopause on the order of 100 nA m^{-2} (Janhunen & Kallio 2004; Benna et al. 2010; Exner et al. 2020; Aizawa et al. 2021). From our fully kinetic simulations, we instead find significantly higher values of the current density on the order of 1000 nA m^{-2}, as shown in Figs. 2e,f. Such higher values are due to the presence of a dominant electron current at the magnetic field boundaries, as shown in Figs. 2e,f.

Past global fluid (Benna et al. 2010; Aizawa et al. 2021) and hybrid (Janhunen & Kallio 2004; Exner et al. 2020; Aizawa et al. 2021) simulations treated electrons as a massless neutralizing fluid. Under such assumptions, the electron current was computed from Ampère's equation using the curl of the magnetic field and the proton current. Differently from those works, in our model the electron current is computed self-consistently from their distribution function evolving under the Vlasov-Maxwell system of equations. Since the magnetic field amplitude on both sides of the magnetospheric layers
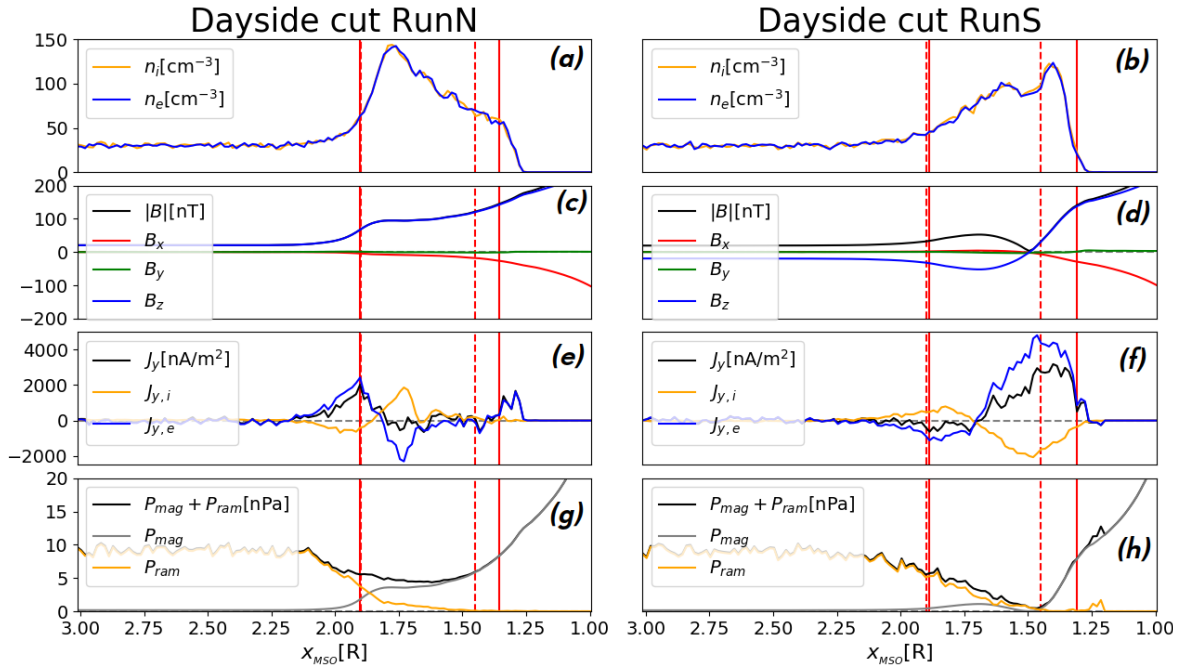
North IMF (RunN)

South IMF (RunS)

Fig. 1. Overview of large-scale structure and magnetosphere boundaries in our simulations. *Panels a–f* show the results of RunN. *Panels a–c* show dipolar $Y_{MSO} = 0$ cuts of the ion density n_i (*a*), magnetic field amplitude $|\mathbf{B}|$ (*b*), and plasma current density along the *y*-axis J_y (*c*). *Panels d–f* show equatorial $Z_{MSO} = 0$ cuts of the same quantities for RunN. *Panels g–l* show the results of RunS in the same format as those of RunN. All plots represent a time of $t = 15.9 \, R/V_x$. The average bow shock (dashed black line) and magnetopause (solid black line) profiles found by Winslow et al. (2013) using MESSENGER observations are added. The white region around the planet corresponds to grid cells with zero macro-particles.

Fig. 2. Cut of results of our two simulations RunN (*left panels*) and RunS (*right panels*) along the subsolar line (*x*-axis). *Panels a–b*: proton and electron densities. *Panels c–d*: magnetic field components and amplitude. *Panels e–f*: current density along Y_{MSO} of protons, electrons, and total. *Panels g–h*: magnetic $P_{mag} \equiv B^2/2\mu_0$, ram $P_{ram} \equiv m_i n_i V_{x,i}^2 + m_e n_e V_{x,e}^2$, and total pressures. These cuts were performed at the same time as Fig. 1 ($t = 15.9 \, R/V_x$). We highlight the bow shock and magnetopause stand-off distances obtained from our model (solid red vertical lines) and the ones obtained using the average model of Winslow et al. (2013) constrained by MESSENGER observations (dashed red vertical lines).

in our work is consistent with past simulations, we conclude that the width of these layers (bow shock and magnetopause) tends to be overestimated in global fluid and hybrid models with massless electrons. This result highlights the key role of electrons as current carriers in the magnetic boundaries of the Hermean magnetosphere, and the importance of an appropriate modeling of this species even in global simulations to satisfactorily address large-scale planetary boundaries. In other words, even if the location of the magnetospheric boundaries is well-reproduced with models using fluid massless electrons, a more physically correct treatment of the electrons is required to draw conclusions on the physics at the magnetopause at and below the ion scale.

3.3. IMF configuration and magnetic reconnection: Feedback from small to large scales

By changing the direction of the IMF, a strong reconfiguration of the global structure of the magnetosphere is observed, as shown in Figs. 1 and 2 where we show the results of the two different IMF configurations. Such global reconfiguration is primarily driven by magnetic reconnection at the nose (around $X_{MSO} \approx 1.5 \, R$) and in the tail (around $X_{MSO} \approx -2 \, R$) of the magnetosphere. It is much more active in RunS (run with southward IMF) as compared to RunN (run with northward IMF). These regions are highlighted in Figs. 1i and 2f for RunS by the plot of the current J_y. The position of the neutral line in the tail in RunS is in good agreement with MESSENGER observations (Poh et al. 2017).

Magnetic reconnection has a strong impact on the global dynamics of the magnetosphere since it rapidly changes the large-scale magnetic field topology, thus allowing for an efficient plasma injection in the magnetosphere and fast conversion of magnetic to particle energy (Vasyliunas 1975; Yamada et al.

2010; Treumann & Baumjohann 2013). Magnetic reconnection is intrinsically a multi-scale phenomenon strongly coupling the ion and sub-ion kinetic scale dynamics. Therefore, a precise description of the physics at the electron scale is important to correctly capture the features observed in laboratory and space plasmas. This is usually achieved by means of fluid or hybrid models with inertial electron closures (Wang et al. 2015; Ng et al. 2017; Finelli et al. 2021; Fadanelli et al. 2021; Jain et al. 2022) or by means of fully-kinetic models (Pritchett 2001a,b; Divin et al. 2007; Haggerty et al. 2015) as in this work.

Magnetic reconnection drives electron acceleration and heating, thus feeding the global magnetosphere circulation pattern with suprathermal electrons. We focus on such a strong impact of magnetic reconnection on the electron dynamics in the next section.

4. Electron heating and circulation in the magnetosphere: Global feedback of magnetic reconnection

As outlined in Sect. 1, the role of the electrons in the interaction between the solar wind and the Hermean magnetosphere is still a matter of debate. In this section, we show that electrons are strongly energized and partially trapped in the Hermean magnetosphere under southward IMF conditions. We focus on the results of RunS since electron heating and injection in the magnetosphere are much more efficient for southward IMF conditions, as shown in Fig. 3 by comparing the two runs. In the case of northward IMF – although electrons are heated efficiently at the magnetopause boundary, their flux across the magnetopause is negligible; in turn, virtually no electrons interact directly with the planetary dipole. A more detailed comparison between the two runs is presented in Sect. 5.

Electron temperature RunN

Electron temperature RunS
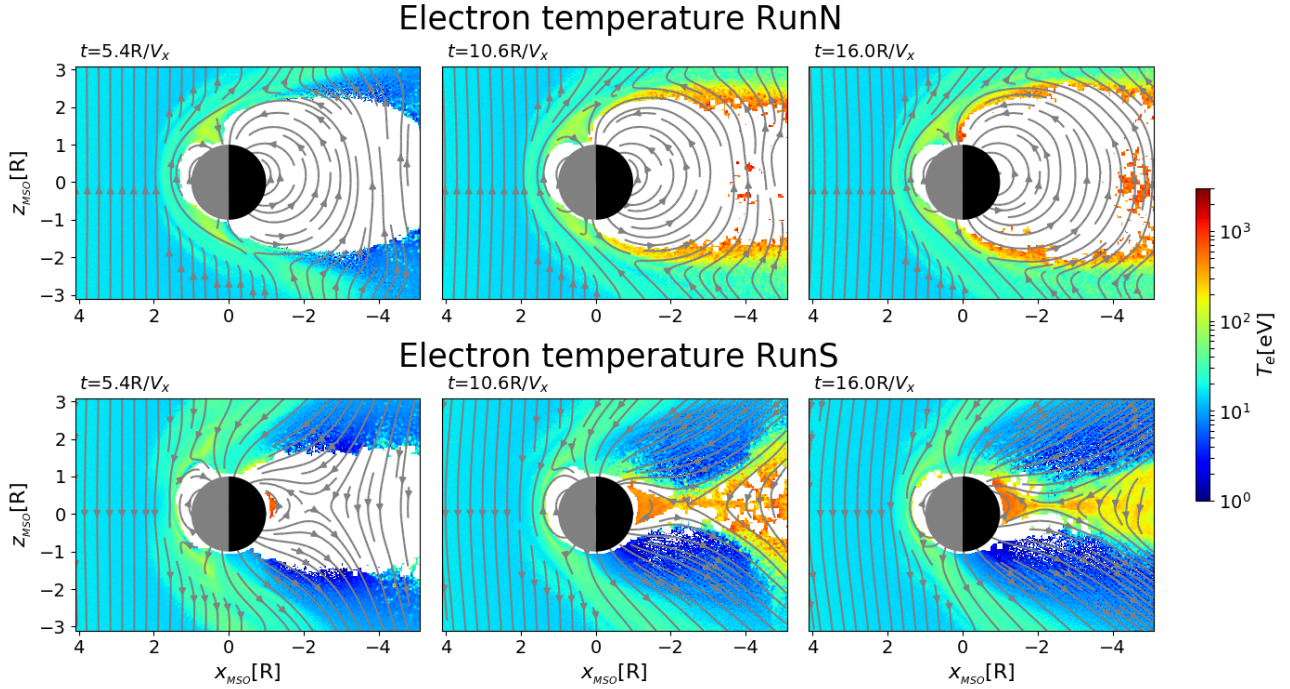
Fig. 3. Time evolution of electron temperature in nose and tail reconnection regions. Dipolar $Y_{\mathrm{MSO}} = 0$ cut of simulations RunN (*top panels*) and RunS (*bottom panels*) at different times (time advancing *from left to right*). We show the color map of the electron temperature $T_{\mathrm{e}} = (2T_{\perp,\mathrm{e}} + T_{\parallel,\mathrm{e}})/3$ in units of [eV] in logarithmic scale. On top of that, we superpose the in-plane magnetic field lines (gray solid lines). The white region around the planet corresponds to grid cells with a number of macro-particles too small to reliably compute the value of T_{e}.

The electron dynamics in RunS is mainly driven by (i) the occurrence of magnetic reconnection causing strong acceleration and heating and (ii) the planetary dipole magnetic field causing the trapping and drifting of electrons inside the magnetosphere. In the following, we discuss these two mechanisms separately.

First, magnetic reconnection affects plasma parcels flowing through the reconnection region by (i) accelerating the plasma (increase of the plasma bulk flow velocity) up to the Alfvén speed $V_{\mathrm{A,in}}$ computed from the inflow plasma parameters[1] and (ii) heating the plasma (increase of the thermal speed of the particles) by an amount proportional to the inflow magnetic energy $\Delta T \approx 0.1 m_{\mathrm{i}} V_{\mathrm{A,in}}^2$ (Phan et al. 2014; Shay et al. 2014; Haggerty et al. 2015). All in all, the magnetic field energy of the plasma in the inflow acts as an energy reservoir for the kinetic energy in the outflow.

In RunS, the two reconnection sites at the nose and tail of the magnetosphere present different electron temperatures in the outflows. In Fig. 3, by showing the evolution of the electron temperature $T_{\mathrm{e}} = (T_{\mathrm{e},\parallel} + 2T_{\mathrm{e},\perp})/3$ in the dipolar $Y_{\mathrm{MSO}} = 0$ plane (the reconnection plane), we highlight the circulation of solar-wind electrons from the nose of the magnetopause to the tail finally entering the magnetosphere cavity. The electron temperature increases with respect to its upstream value, $T_{\mathrm{e,SW}} \approx 20$ eV, up to 100–200 eV in the nose, reaching larger values on the order of few keVs in the tail. This asymmetry in electron heating between nose and tail reconnection regions is due to the different inflow plasma parameters; while in the nose the magnetic energy is $m_{\mathrm{i}} V_{\mathrm{A,in}}^2 \approx 1$ keV, in the tail it is $m_{\mathrm{i}} V_{\mathrm{A,in}}^2 \approx 10$ keV,

given the lower density and higher magnetic field amplitude in the lobes as compared to the magnetosheath. Thus, more magnetic energy is available for conversion into kinetic energy in the tail compared to the nose. This simple estimation explains why we observe electrons with higher energy in the tail (by around a factor of 10) with respect to the nose of the magnetosphere.

Magnetic reconnection allows for the injection of solar-wind electrons into the Hermean magnetosphere. As shown by the time evolution in Fig. 3, from the time $t \approx 10R/V_x$, the night-side part of the magnetosphere starts to be populated with high-energy electrons ejected from the reconnection site in the tail around $X_{\mathrm{MSO}} \approx -2R$ (such a planetward flow of plasma is also called a substorm, in analogy with Earth; Christon 1987). Once inside the Hermean magnetosphere, the motion of such an electron's substorm is driven by the dipolar structure of the magnetic field. Similarly to Earth, in this region electrons bounce back-and-forth along closed magnetic field lines with period τ_B. Electrons also move around the planet following a longitudinal drift motion with a period of τ_i due to curvature drift. These motions have very a different timescale, $\tau_{ce} \ll \tau_B \ll \tau_i$ (here, τ_{ce} is the electron gyro-period as defined in Sect. 2), thus allowing us to treat them separately using the adiabatic approximation (Northrop 1963).

Using the adiabatic approximation, the bouncing motion of electrons along a given magnetic field line is described by the conservation of energy:

$$E = \frac{1}{2} m_{\mathrm{e}} v_{\parallel}^2(s) + \mu B(s), \tag{1}$$

where $\mu = m \langle v_{\perp}^2 \rangle / 2B$ is the first adiabatic invariant. Here, brackets ($\langle \rangle$) indicate the average over the gyro-motion, and s is the curvilinear coordinate along magnetic field lines. Similarly to the problem of a harmonic oscillator, the inversion points s_{m} are defined as those where the kinetic energy goes to zero, and thus

---

[1] In the symmetric case, the inflow Alfvén speed is $V_{\mathrm{A,in}} = B_{\mathrm{r}}/\sqrt{4\pi m_{\mathrm{i}} n}$, where B_{r} is the reconnecting magnetic field. While, in the asymmetric case the generalization of this expression is $V_{\mathrm{A,in}} = \sqrt{B_1 B_2 / 4\pi m_{\mathrm{i}} (B_1 + B_2)/(n_1 B_1 + n_2 B_2)}$, as reported in Cassak & Shay (2007).
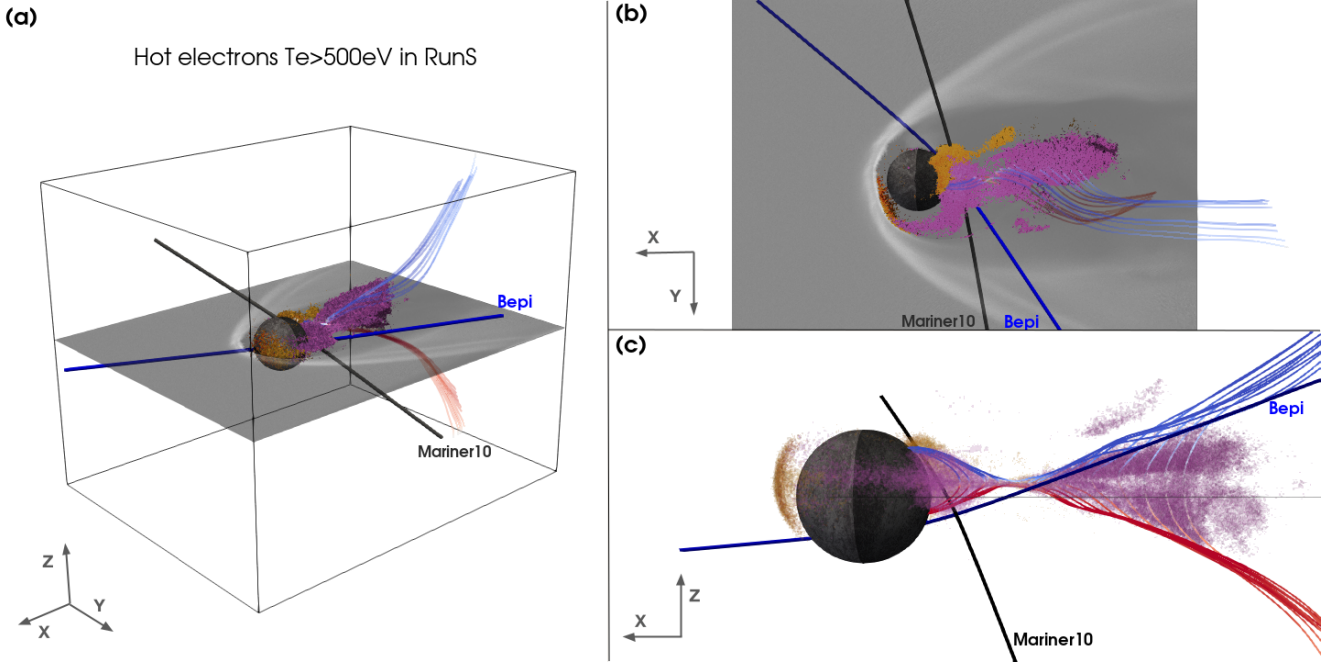
Fig. 4. Three-dimensional view of high-energy electron population in simulation RunS. The *three panels* show three different views of the same quantities. Grid cells with values of perpendicular (parallel) temperatures greater than 500 eV are shown in orange (purple). We show an equatorial cut of the electron density in grayscale. Magnetic field lines are shown around the neutral point in the tail, and these lines are colored according to the value of B_x (blue and red for sunward and antisunward directions, respectively). Both quantities are computed at a time of $15.9\,R/V_x$, which is the same as in Figs. 1 and 2. Mariner10 and BepiColombo first Mercury flyby trajectories are shown using gray and blue solid lines, respectively.

$$B(s_{\mathrm{m}}) = \frac{E}{\mu} = \frac{B(s_0)}{\sin^2\theta_0}, \qquad (2)$$

where θ_0 is the initial particle pitch angle, $\theta_0 \equiv \tan^{-1}(v_{0,\perp}/v_{0,\parallel})$, computed at s_0 (the point where the magnetic field line crosses the magnetic equator). From Eq. (2) and using the value of the magnetic field amplitude at Mercury's southern pole, B_{south} (on the order of 200 nT), we obtain the following loss-cone equation for electrons:

$$|\theta_0| < \sin^{-1}\sqrt{\frac{B(s_0)}{B_{\mathrm{south}}}}. \qquad (3)$$

This equation defines a family of loss cones associated with different magnetic field lines (parameterized by s_0) varying with radius and local time (hereafter LT). Thus, spatial variations of the magnetic field amplitude $B(s_0)$ in the equatorial plane induce variations in the electron pitch-angle distribution around the planet.

In RunS, we observe such a variation of electron distribution function around the planet as a function of local time. This is shown in Fig. 4 using three-dimensional spatial distributions of electrons with $T_{e,\perp} > 500\,$eV (orange) and $T_{e,\parallel} > 500\,$eV (purple). Fewer energetic electrons are observed in the dayside sector compared to the nightside one, and the few observed there have pitch angles close to 90°. This means that most of the electrons do not complete a full-drift orbit around the planet creating a stable continuous belt as on Earth, but rather bounce along magnetic field lines in the nightside before drifting dawnward and eventually falling on the planet surface. In the following, we refer to this partial circulation pattern as nightside-trapping.

To investigate such peculiar property of the Hermean environment, we look at the variation of the profiles $B(s)$ with local time (LT) and radial distance, as shown in Fig. 5. The compression of the dipole magnetic field by the solar wind stretches the field lines on the nightside (blue-black lines in Fig. 5) and compresses the field lines on the dayside (yellow-orange lines in Fig. 5). Such a dayside compression increases the magnetic field amplitude $B(s_0)$ at the subsolar equator, which in turn increases the loss-cone angle for electrons according to Eq. (3). The loss-cone angles resulting from Eq. (3) are reported in Figs. 5a–c for varying LT (0 corresponds to local midnight and 12 corresponds to local noon) and radial distance (from 1.1 to 1.5 R). For any radial distance close enough to the planet, the loss-cone angle steadily increases by moving from nightside (angle on the order of 45°) to dayside (angle on the order of 70°). This explains the nature of the electron nightside trapping observed in RunS. On top of that, the values of the loss-cone angles reported in Fig. 5 point out the higher probability of having trapped particles in the outer shells ($\approx 1.5\,R$) rather than very close to the planet ($\approx 1.1\,R$). This interpretation of adiabatic nightside trapping is consistent with the spatial distribution of high-energy electrons around the planet shown in Fig. 4.

The loss-cone mechanism creates an inhomogenous distribution of high-energy electrons inside the Hermean magnetosphere (in the range $R \approx 1.1{-}1.5$) with anisotropic energy distribution function ($T_{e,\perp} > T_{e,\parallel}$). Such an electron population is expected to be the target of observation by satellites, able to measure in situ electron energy distribution functions (hereafter eEDFs). In the next section, we address this point by showing synthetic eEDFs sampled along Mariner10 and BepiColombo first Mercury flyby trajectories in our simulations.

5. Comparison between observations and simulations

The simulation results discussed so far are of particular interest for the interpretation of in situ electron observations at Mercury. To ease comparison with observations, we sampled the
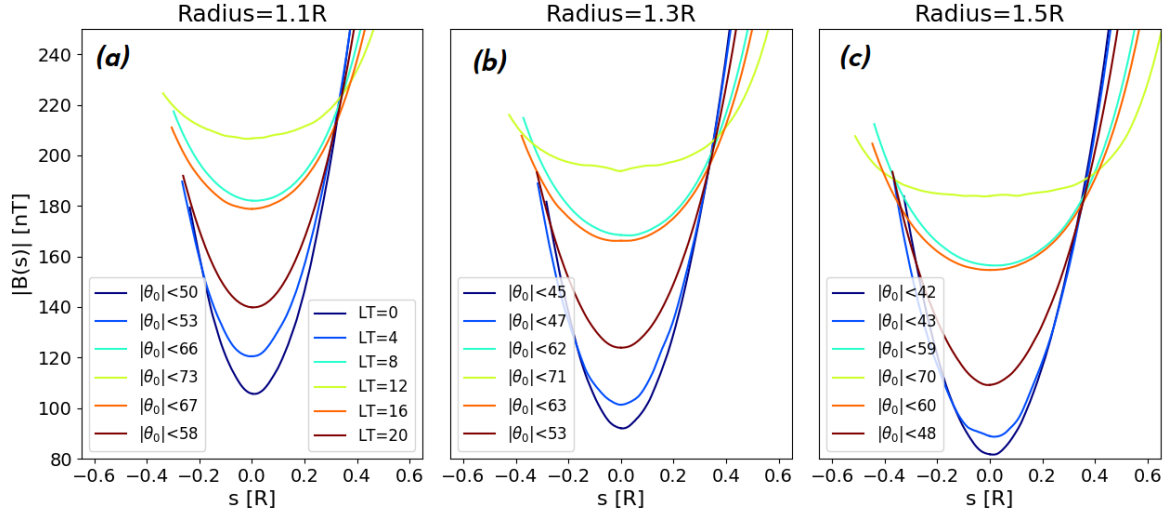
Fig. 5. Magnetic field amplitude along magnetic field lines $|B(s)|$ [nT] computed at different local times (LT). LT 12 corresponds to subsolar longitude (yellow) and LT 0 corresponds to local midnight (dark blue). *Panels (a)–(c)* correspond to different equatorial distances from the center of the planet: 1.1 R (a), 1.3 R (b), and 1.5 R (c). Resulting values for the loss-cone angle from Eq. (3) are also shown in each panel. Plots done at a time of 15.9 R/V_x, which is the same as in Figs. 1–4.

synthetic electron energy distribution functions (eEDFs) from our two simulations along Mariner10 and BepiColombo first-Mercury-flyby trajectories, as shown in Fig. 6.

To compute the energy spectra in Fig. 6 from our simulations, we select the macro-particles lying in the neighborhood of the spacecraft trajectory. In particular, we use a range of ± 4 cells (equal to $\approx \pm 0.06\,R$) in all directions in order to minimize the particle noise and mimic the effect of particle precipitation on the instruments in an acquisition time, δt. Moreover, we assume that the field of view of the instruments spans the whole 4π solid angle in an acquisition time of δt. Although this assumption is usually partially verified by the instruments, the main features of the spectra in Fig. 6 are also expected to hold in the case of limited field of view. To ease the comparison with in situ observations, the spectra in Figs. 6a,b have the same energy range and resolution of the Mariner10/PLS instrument (Ogilvie et al. 1974) and those in Figs. 6e,f of the BepiColombo/MEA1 (Saito et al. 2021) instrument operating in solar-wind mode during the flyby. Moreover, in Fig. 6 we report the bow shock and magnetopause crossing times obtained by the two spacecraft in situ at Mercury as discussed in Russell et al. (1988) (panels a–d) for Mariner10 and in André & Aizawa (priv. comm.) for BepiColombo (panels e–h). In the following, we discuss these two spacecraft's flybys modeling results separately.

Mariner10 synthetic eEDF and electron densities obtained from our simulations, shown in Figs. 6a–d, present clear signatures of (i) inbound bow shock crossing at a time of $t \approx [-20, -18]$, (ii) inbound magnetopause crossing at a time of $t \approx -7$, (iii) outbound magnetopause crossing at a time of $t \approx [6, 7]$, and (iv) outbound bow shock crossing at a time of $t \approx [12, 14]$ (times are given in minutes to closest approach). These crossing times are consistent with those observed by Mariner10 (Russell et al. 1988), and the latter are and shown in Fig. 6 using vertical black dashed lines and gray areas. A more precise comparison of the crossing times between observations and simulations would require an ad hoc simulation initialized with the upstream solar-wind parameters observed by Mariner10. A further step of this kind will be addressed in future works. Here, we mainly focus on the qualitative features of the eEDF in the Hermean magnetosphere. Inside the magnetosphere

$(t \approx [-7, +7])$ in both simulations the plasma density is strongly depleted, and we observe different signatures in the two runs.

In RunN, electrons with energies up to a few keV are observed around the magnetopause (the mechanism accelerating these electrons, however, remains unclear) and no electrons are observed inside the magnetosphere.

In RunS, electrons with energies up to tens of keV (well above the instrumental cutoff of 687 eV) are encountered around and after closest approach ($t \approx [0, +7]$). These high-energy electrons are produced by magnetic reconnection in the tail, as discussed in Sect. 4.

This result supports the interpretation of Mariner10/PLS observations outlined in past works (Ogilvie et al. 1974; Christon 1987), stating that Mariner10 observed substorm injected electrons around the closest approach with energies well above the instrumental cutoff. It can be further used to interpret the recent observations by BepiColombo on Mercury.

BepiColombo synthetic eEDF and electron densities obtained from our simulations, shown in Figs. 6e–h, present similar signatures to those of Mariner10. However, two main differences are observed. First, for BepiColombo the inbound bow shock crossing is less sharp than for Mariner10. This is due to the large distance from the planet of the spacecraft at the encounter of the inbound bow shock (see the trajectory in Fig. 4). BepiColombo's first flyby trajectory makes plasma observations more asymmetric between inbound and outbound as compared to Mariner10. Second, signatures of high-energy electrons around closest approach are fainter for BepiColombo than for Mariner10. This effect can be understood again in terms of trajectories. From Fig. 4, we note that BepiColombo passes beneath the high-energy region of the nightside, while Mariner10 passes right through such a region (shown in purple and orange in Fig. 4).

We stress that a more precise, quantitative comparison between observations and simulations would require a good knowledge of the upstream solar-wind parameters that define the precise values of, among others, the time of the bow shock and magnetopause crossings, the energy of the electrons inside the magnetosphere, and the density of electrons in the magnetosheath. Thus, the results of this section are limited to the
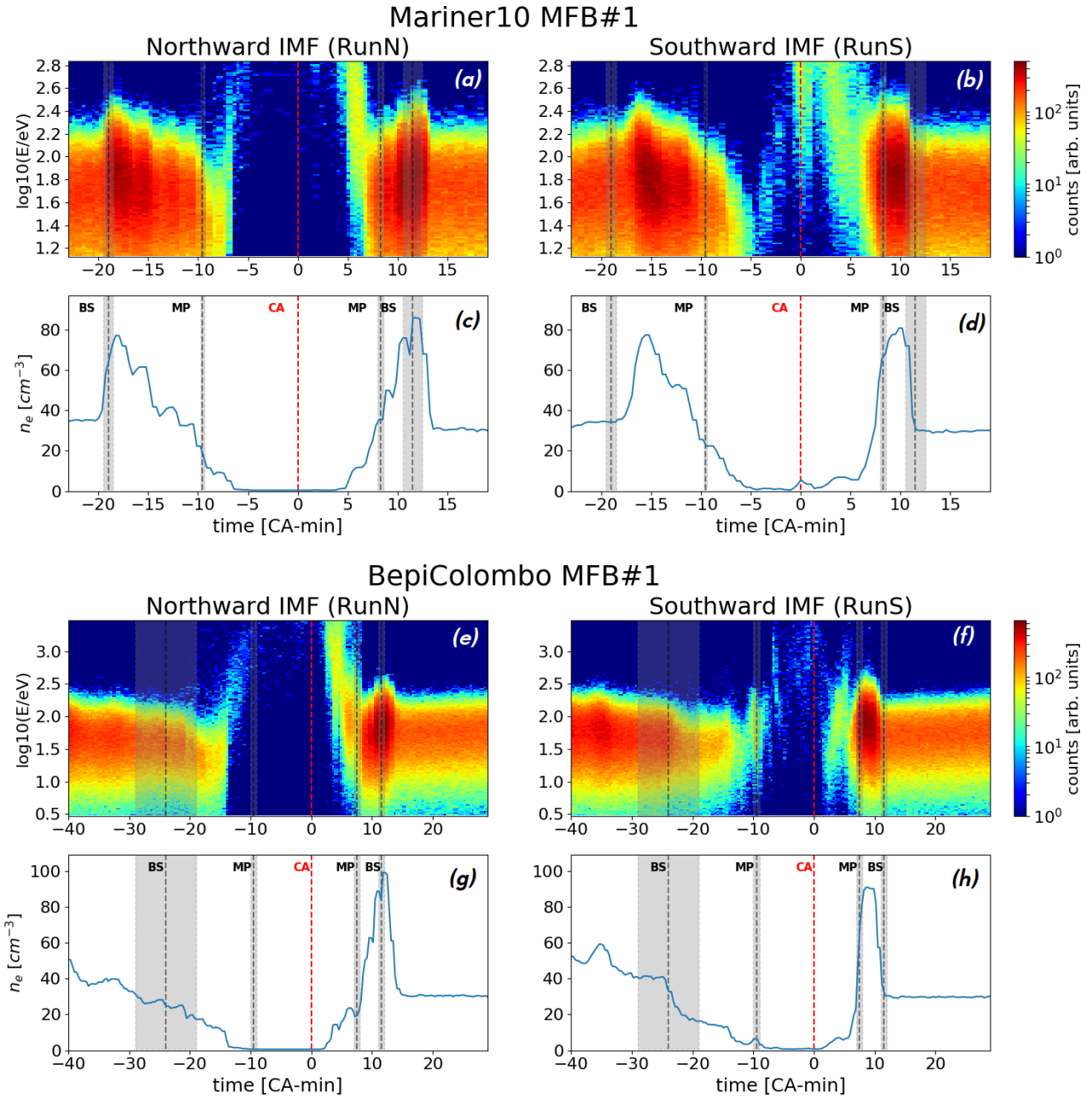
Fig. 6. Synthetic electron energy distribution functions (eEDFs) sampled along Mariner10 *(a)*–*(d)* and BepiColombo *(e)*–*(h)* first Mercury flybys in our simulation boxes using northward IMF (*left panels*) and southward IMF (*right panels*) conditions. The plots are done using simulation results at time = $14.7R/V_x$. The energy ranges and resolutions used to compute the eEDF are the same as those of the instruments PLS (onboard Mariner, *top*) and MEA1 (onboard BepiColombo, *bottom*). The horizontal axis shows the time from closest approach (CA) in minutes, and $t = 0$ is highlighted using vertical red dashed line. On the time axis, we highlight the bow shock and magnetopause crossings obtained by the two spacecraft in situ. These are highlighted using gray areas and vertical black dashed lines. The electron density was obtained by integrating the synthetic eEDF in energy at each given time.

qualitative main features observed by Mariner10 and Bepi-Colombo first Mercury flybys.

A comparison of the synthetic eEDF between RunN and RunS demonstrate that by changing only one parameter (the IMF direction), a sudden change in the energy and density of electrons inside the magnetosphere is induced, as shown in Fig. 6. We suggest that the Hermean environment responds to such changes in the solar wind by a corresponding reconfiguration as from RunN to RunS or viceversa. The characteristic timescale for such a reconfiguration is expected to be comparable to the Dungey cycle of $\tau \approx 10\,R/V_x \approx$ minutes. Thus, it is only in the

case of stable solar-wind conditions on timescale longer than a few minutes that observational signatures in the eEDF inside the magnetosphere can be linked to the upstream IMF direction.

6. Discussion and conclusions

This work represents a first step towards global, fully kinetic modeling of planetary magnetospheres in which the electron dynamics is included self-consistently from the global planetary scale down to the gyro-radius scale. The high computational needs of this model impose strong constraints on the

possible scale separation between planet, ion, and electron scale length, as discussed at the end of Sect. 2. Scaling down the ion-to-electron mass ratio and the plasma-to-cyclotron frequency ratio remains a classic procedure in fully-kinetic simulations, the effects of which have been extensively discussed in past works (Bret & Dieckmann 2010; Le et al. 2013; Lavorenti et al. 2021). On the other hand, using a smaller planet radius of ≈ 230 km instead of the realistic Mercury radius of ≈ 2400 km may have a significant impact on a simulation's results (in our work, the scale separation between planet radius and ion gyroradius remains of about a factor of 10).

First, scaling down the planet radius can have an impact on the global shape of the magnetosphere. To avoid this problem, the magnetic moment of the planet is scaled down proportionally to R^3 in order to preserve the shape of the magnetosphere. Therefore, the global shape of the interaction region is preserved, and in particular the bow shock d_{BS}/R and magnetopause d_{MP}/R stand-off distance in units of the planet radius are preserved, as discussed in Sect. 3. Moreover, adiabatic particle acceleration processes arising in the dipolar magnetic field of the planet (such as betatron and Fermi acceleration) are unaltered by the planet rescaling as well. This is particularly important for the discussion in Sect. 4 on the loss-cone angle around the planet.

Second, scaling down the planet radius can have an impact on magnetic reconnection in the tail in the case of southward IMF. Magnetic reconnection induces the formation of a region of drifting plasma close to the neutral point, the so-called diffusion region, where particles are no longer frozen in the magnetic field. Depending on the species, this region is called the ion (electron) diffusion region and it extends for about ten ion (electron) inertial lengths around the neutral point. By scaling down the planet radius, the ion (electron) diffusion region in the tail moves closer to the planet surface. In our case, given the scaled-down planet we are using ($R = 5.5\,d_i$, where $d_i \equiv c/\omega_{pi} \equiv c\sqrt{m_i/4\pi n_{SW}e^2}$ is the ion inertial length), the ion (electron) diffusion region is marginally (largely) separated from the planet. Thus, we expect ion dynamics in the outflow to be affected by the scaling down, at least partially, while this should not be the case for electrons. In particular, we expect the signatures of high-energy electrons observed in our simulations as a product of magnetic reconnection to hold true when using a real size planet.

Although we expect these two classes of plasma processes to be well-reproduced using the scaled-down parameters in our simulations, particular care must be taken when analyzing specific plasma quantities. Indeed, due to the rescaling of the plasma-to-cyclotron frequency ratio, electrons with energies above few tens of keV fall out of the range of validity of our model since their speed becomes ultra-relativistic (by reducing the ratio ω_{pe}/ω_{ce}, we are de facto reducing the value of the light speed c in our simulations). Moreover, by scaling down the ion-to-electron mass ratio, we reduce the ratio between the electron thermal speed and the flow speed (v_{the}/V_{SW}) from 5 to around 1.2. This means that the solar-wind electrons interacting with the planet in our simulations are injected with a slightly more anisotropic energy distribution function as compared to the real case. The relevance of these caveats to our simulation results remains unknown and should be further investigated in future works. We stress that global, fully kinetic simulations of planetary magnetospheres using realistic plasma parameters remain prohibitive using the present state-of-the-art HPC facilities.

Since this work represents a first step toward a fully kinetic global modeling of the Hermean environment, we chose to use a simple as possible realistic solar-wind configuration. Thus,

we chose a purely northward or southward IMF. This choice facilitates the analysis of the reconnection sites and outflows. A more realistic configuration would require a strong B_x component in the IMF. Such an in-plane component, typically found on Mercury, tends to create a foreshock region (absent from our simulations) and drives strong north-south asymmetries in the magnetosphere. A more realistic modeling of this kind will be addressed in future works.

To conclude, the results of this work show that high-energy electrons (up to tens of keV) are generated in the magnetotail of Mercury in the case of southward IMF. Such electrons form as a consequence of magnetic reconnection in the tail neutral line located at $X \approx -2R$ and move toward the planet drifting dawnward. When reaching the internal shells of the magnetosphere, the motion of these electrons (which can be treated as adiabatic) is strongly affected by loss-cone precipitation on the planet surface. We find that almost all drifting electrons are lost on the planet before completing a full longitudinal drift orbit. Therefore, the highest concentration of electrons in the range of hundreds of eV to some keV is on the nightside, especially in the post-midnight sector. This result supports electron observations by the Mariner10/PLS instrument, showing high-energy electrons around closest approach during its first Mercury flyby. Such in situ observations are in agreement with our simulation with the southward IMF. Moreover, we present synthetic electron data useful for the ongoing and future interpretation of BepiColombo/MEA first-Mercury-flyby observations. A detailed comparison between our simulations and MEA observations for this flyby will be done in the near future once the data have been fully calibrated. Finally, we envision a characterization of this energetic electron population by BepiColombo during its nominal science phase.

References

Aizawa, S., Griton, L., Fatemi, S., et al. 2021, Planet. Space Sci., 198, 105176
Baker, D. N., Dewey, R. M., Lawrence, D. J., et al. 2016, J. Geophys. Res. (Space Phys.), 121, 2171
Benkhoff, J., Murakami, G., Baumjohann, W., et al. 2021, Space Sci. Rev., 217, 90
Benna, M., Anderson, B. J., Baker, D. N., et al. 2010, Icarus, 209, 3
Berendeev, E., Dudnikova, G., Efimova, A., & Vshivkov, V. 2018, Math. Methods Appl. Sci., 41, 9276
Boardsen, S. A., Slavin, J. A., Anderson, B. J., et al. 2012, J. Geophys. Res. (Space Phys.), 117, A00M05
Brackbill, J. U., & Forslund, D. W. 1982, J. Comput. Phys., 46, 271
Bret, A., & Dieckmann, M. E. 2010, Phys. Plasmas, 17, 032109
Cassak, P. A., & Shay, M. A. 2007, Phys. Plasmas, 14, 102114
Chen, Y., Tóth, G., Jia, X., et al. 2019, J. Geophys. Res. (Space Phys.), 124, 8954
Christon, S. P. 1987, Icarus, 71, 448
Dewey, R. M., Raines, J. M., Sun, W., Slavin, J. A., & Poh, G. 2018, Geophys. Rev. Lett., 45, 110
Divin, A. V., Sitnov, M. I., Swisdak, M., & Drake, J. F. 2007, Geophys. Rev. Lett., 34, L09109
Dong, C., Wang, L., Hakim, A., et al. 2019, Geophys. Res. Lett., 46, 584
Exner, W., Heyner, D., Liuzzo, L., et al. 2018, Planet. Space Sci., 153, 89

Exner, W., Simon, S., Heyner, D., & Motschmann, U. 2020, J. Geophys. Res.: Space Phys., 125, e2019JA027691

Fadanelli, S., Lavraud, B., Califano, F., et al. 2021, J. Geophys. Res. (Space Phys.), 126, 1

Fatemi, S., Poirier, N., Holmström, M., et al. 2018, A&A, 614, A132

Fatemi, S., Poppe, A. R., & Barabash, S. 2020, J. Geophys. Res. (Space Phys.), 125, e27706

Finelli, F., Cerri, S. S., Califano, F., et al. 2021, A&A, 653, A156

Gershman, D. J., Slavin, J. A., Raines, J. M., et al. 2014, Geophys. Rev. Lett., 41, 5740

Gershman, D. J., Raines, J. M., Slavin, J. A., et al. 2015, J. Geophys. Res.: Space Phys., 120, 4354

Haggerty, C. C., Shay, M. A., Drake, J. F., Phan, T. D., & McHugh, C. T. 2015, Geophys. Res. Lett., 42, 9657

Herčík, D., Trávníček, P. M., Johnson, J. R., Kim, E.-H., & Hellinger, P. 2013, J. Geophys. Res. (Space Phys.), 118, 405

Herčík, D., Trávníček, P. M., & Å tverák, Å. t., & Hellinger, P., 2016, J. Geophys. Res. (Space Phys.), 121, 413

Ho, G. C., Krimigis, S. M., Gold, R. E., et al. 2012, J. Geophys. Res. (Space Phys.), 117, A00M04

Ho, G. C., Starr, R. D., Krimigis, S. M., et al. 2016, Geophys. Rev. Lett., 43, 550

Ip, W.-H., & Kopp, A. 2002, J. Geophys. Res. (Space Phys.), 107, 4

Jain, N., Muñoz, P., Farzalipour Tabriz, M., Rampp, M., & Büchner, J. 2022, Phys. Plasmas, 29, 053902

James, M. K., Imber, S. M., Bunce, E. J., et al. 2017, J. Geophys. Res. (Space Phys.), 122, 7907

Janhunen, P., & Kallio, E. 2004, Ann. Geophys., 22, 1829

Jia, X., Slavin, J. A., Gombosi, T. I., et al. 2015, J. Geophys. Res. (Space Phys.), 120, 4763

Jia, X., Slavin, J. A., Poh, G., et al. 2019, J. Geophys. Res. (Space Phys.), 124, 229

Kabin, K., Gombosi, T. I., DeZeeuw, D. L., & Powell, K. G. 2000, Icarus, 143, 397

Kallio, E., & Janhunen, P. 2003, Ann. Geophys., 21, 2133

Kidder, A., Winglee, R. M., & Harnett, E. M. 2008, J. Geophys. Res. (Space Phys.), 113, A9

Lapenta, G., Schriver, D., Walker, R. J., et al. 2022, J. Geophys. Res. (Space Phys.), 127, 4

Lavorenti, F., Henri, P., Califano, F., Aizawa, S., & André, N. 2021, A&A, 652, A20

Le, A., Egedal, J., Ohia, O., et al. 2013, Phys. Rev. Lett., 110, 135004

Markidis, S., Lapenta, G., & Rizwan-uddin., 2010, Math. Comput. Simul., 80, 1509

Markidis, S., Olshevsky, V., Tóth, G., et al. 2021, Kinetic Modeling in the Magnetosphere (American Geophysical Union (AGU)), 607

Milillo, A., Fujimoto, M., Murakami, G., et al. 2020, Space Sci. Revi., 216, 93

Müller, J., Simon, S., Wang, Y.-C., et al. 2012, Icarus, 218, 666

Ness, N. F., Behannon, K. W., Lepping, R. P., Whang, Y. C., & Schatten, K. H. 1974, Science, 185, 151

Ng, J., Hakim, A., Bhattacharjee, A., Stanier, A., & Daughton, W. 2017, Phys. Plasmas, 24, 082112

Northrop, T. G. 1963, Rev. Geophys. Space Phys., 1, 283

Ogilvie, K. W., Scudder, J. D., Hartle, R. E., et al. 1974, Science, 185, 145

Ogilvie, K. W., Scudder, J. D., Vasyliunas, V. M., Hartle, R. E., & Siscoe, G. L. 1977, J. Geophys. Res., 82, 1807

Pantellini, F., Griton, L., & Varela, J. 2015, Planet. Space Sci., 112, 1

Phan, T. D., Drake, J. F., Shay, M. A., et al. 2014, Geophys. Res. Lett., 41, 7002

Poh, G., Slavin, J. A., Jia, X., et al. 2017, Geophys. Res. Lett., 44, 678

Pritchett, P. L. 2001a, J. Geophys. Res. (Space Phys.), 106, 25961

Pritchett, P. L. 2001b, J. Geophys. Res., 106, 3783

Raines, J. M., Gershman, D. J., Slavin, J. A., et al. 2014, J. Geophys. Res. (Space Phys.), 119, 6587

Raines, J. M., DiBraccio, G. A., Cassidy, T. A., et al. 2015, Space Sci. Rev., 192, 91

Richer, E., Modolo, R., Chanteur, G. M., Hess, S., & Leblanc, F. 2012, J. Geophys. Res. (Space Phys.), 117, A10228

Russell, C. T., Baker, D. N., & Slavin, J. A. 1988, The Magnetosphere of Mercury (NTRS), 514

Saito, Y., Delcourt, D., Hirahara, M., et al. 2021, Space Sci. Rev., 217, 70

Sarantos, M., Killen, R. M., & Kim, D. 2007, Planet Space Sci., 55, 1584

Schmid, D., Narita, Y., Plaschke, F., et al. 2021, Geophys. Rev. Lett., 48, e92606

Shay, M. A., Haggerty, C. C., Phan, T. D., et al. 2014, Phys. Plasmas, 21, 122902

Shue, J. H., Chao, J. K., Fu, H. C., et al. 1997, J. Geophysi. Res., 102, 9497

Slavin, J. A., Anderson, B. J., Zurbuchen, T. H., et al. 2009, Geophys. Res. Lett., 36, 2

Solomon, S. C., & Anderson, B. J. 2018, in Mercury. The View after MESSENGER, eds. S. C. Solomon, L. R. Nittler, & B. J. Anderson, 1

Tóth, G., Chen, Y., Gombosi, T. I., et al. 2017, J. Geophys. Res. (Space Phys.), 122, 336

Trávníček, P., Hellinger, P., & Schriver, D. 2007, Geophy. Res. Lett., 34, L05104

Trávníček, P. M., Hellinger, P., Schriver, D., et al. 2009, Geophy. Res. Lett., 36, L07104

Trávníček, P. M., Schriver, D., Hellinger, P., et al. 2010, Icarus, 209, 11

Treumann, R. A., & Baumjohann, W. 2013, Front. Phys., 1, 31

Vasyliunas, V. M. 1975, Rev. Geophys. Space Phys., 13, 303

Walsh, B. M., Ryou, A. S., Sibeck, D. G., & Alexeev, I. I. 2013, J. Geophys. Res. (Space Phys.), 118, 1992

Wang, L., Hakim, A. H., Bhattacharjee, A., & Germaschewski, K. 2015, Phys. Plasmas, 22, 012108

Winslow, R. M., Anderson, B. J., Johnson, C. L., et al. 2013, J. Geophys. Res. (Space Phys.), 118, 2213

Yagi, M., Seki, K., Matsumoto, Y., Delcourt, D. C., & Leblanc, F. 2010, J. Geophys. Res. (Space Phys.), 115, A10

Yamada, M., Kulsrud, R., & Ji, H. 2010, Rev. Mod. Phys., 82, 603

5.4 Lavorenti et al. (2023a) *A&A*, 674, A153

Solar-wind electron precipitation on weakly magnetized bodies: The planet Mercury

Federico Lavorenti[1,2] , Pierre Henri[1,3], Francesco Califano[2], Jan Deca[4,5,6], Simon Lindsay[7],
Sae Aizawa[8,2,9], and Johannes Benkhoff[10]

[1] Laboratoire Lagrange, OCA, UCA, CNRS, 96 Bd de l'Observatoire, 06304 Nice, France
  e-mail: `federico.lavorenti@oca.eu`
[2] Dipartimento di Fisica "E. Fermi", Univ. di Pisa, L.go Bruno Pontecorvo 3, 56127 Pisa, Italy
[3] LPC2E, CNRS, Univ. d'Orléans, OSUC, CNES, 3 Av. de la Recherche Scientifique, 45071 Orléans, France
[4] LASP, Univ. of Colorado Boulder, 1234 Innovation Drive Boulder, CO 80303, USA
[5] IMPACT, NASA/SSERVI, 3400 Marine St., Boulder, CO 80303, USA
[6] LATMOS, UVSQ, 11 Bd D'Alembert, 78280 Guyancourt, France
[7] School of Physics & Astronomy, University of Leicester, University Rd LE1 7RH, Leicester, UK
[8] IRAP, UPS, CNRS, CNES, 9 Av. du Colonel Roche, 31028 Toulouse, France
[9] JAXA, 3-1-1 Yoshinodai, Chuo-ku, Sagamihara-shi, Kanagawa, Japan
[10] ESA/ESTEC, Keplerlaan 1, 2200 AG Noordwijk, The Netherlands

ABSTRACT

Rocky objects in the Solar System (such as planets, asteroids, moons, and comets) undergo a complex interaction with the flow of magnetized, supersonic plasma emitted from the Sun called solar wind. We address the interaction of such a flow with the planet Mercury, considered here as the archetype of a weakly magnetized, airless, telluric body immersed in the solar wind. Due to the lack of dense atmosphere, a considerable fraction of solar-wind particles precipitate on Mercury. The interaction processes between precipitating electrons and other nonionized parts of the system remain poorly understood. Shading light on such processes is the goal of this work. Using a 3D fully kinetic self-consistent plasma model, we show for the first time that solar-wind electron precipitation drives (i) efficient ionization of multiple neutral exosphere species and (ii) emission of X-rays from the surface of the planet. We conclude that, compared to photoionization, electron-impact ionization should not be considered a secondary process for the H, He, O, and Mn exosphere. Moreover, we provide the first, independent evidence of X-ray aurora-like emission on Mercury using a numerical approach.

Key words. planets and satellites: magnetic fields – plasmas – X-rays: general – planets and satellites: aurorae – solar wind – planet-star interactions

1. Introduction

The planet Mercury is a nearby example of a rocky, weakly magnetized body immersed in the solar-wind plasma. Mercury's environment presents an ideal scenario to better understand the physics governing the interaction between solid bodies (such as telluric planets, moons, asteroids, and comets) and the solar wind. Mercury's ionized environment is nonetheless intrinsically nonlinear and hard to understand. Such complexity is due (i) to the strong coupling between the plasma and the planet's magnetosphere, exosphere, and surface and (ii) to the strongly kinetic dynamics of the ions in such a small magnetosphere (5% the size of Earth's magnetosphere). At present, the physical processes controlling the electron interactions in the system are a scientific enigma, with underlying roots ranging from plasma to solid-state physics (Milillo et al. 2010). As an example, electron acceleration in the magnetosphere is thought to be at the origin of X-ray aurora-like emission from the surface of Mercury. However, on the one hand, this hypothesis remains to be confirmed, and on the other, the dependence of such a process on the upstream solar-wind conditions remains unknown.

The Sun acts as an external energy driver, sustaining the dynamics at Mercury. Solar radiation and particles are the source (via desorption and sputtering) and sink (via radiation pressure and ionization) of the neutral exosphere surrounding Mercury, respectively. Moreover, the solar-wind plasma considerably alters the shape of Mercury's magnetic field. The intrinsic magnetic field generates a scaled-down, Earth-like magnetosphere able to partially shield the planet's surface from the impinging solar wind. Part of the solar wind enters the magnetosphere, interacts with Mercury's magnetic field and, given the absence of an atmosphere, precipitates down to the planet surface. Studying this plasma precipitation is key to our understanding of the strong coupling between Mercury's magnetosphere, exosphere, and surface, and of coupling of this kind around weakly magnetized bodies in general.

To date, only two missions (Mariner 10 and MESSENGER) have been devoted to the exploration of Mercury's environment. Mariner 10 provided the first electron observations, showing electron fluxes in the range ~20–600 eV throughout the magnetosphere (Ogilvie et al. 1977). Sporadic bursts above tens of keV were also detected (Wurz & Blomberg 2001, and references

Table 1. Common numerical parameters of RunN and RunS with purely northward and southward IMF, respectively.

Box dimensions	(L_x, L_y, L_z)		$(-9{:}{+}6, \pm 6, \pm 6)\ R$
Number of cells	(N_x, N_y, N_z)		$(960, 768, 768)$
Spatial resolution	$(\mathrm{d}x, \mathrm{d}y, \mathrm{d}z)$		$0.015\ R$
Time resolution	$\mathrm{d}t$		$1.4\ \mathrm{ms}$
Macro-particles per cell [a]	PPC		128
Solar-wind number flux	$\mathcal{F}_\mathrm{sw}$	$n_\mathrm{sw} V_\mathrm{sw}$	$1.2 \times 10^9\ 1\,\mathrm{cm^{-2}\,s^{-1}}$
Solar-wind energy flux	$\mathcal{E}_\mathrm{sw}$	$T_{e,\mathrm{sw}} n_\mathrm{sw} V_\mathrm{sw}$	$2.4 \times 10^{10}\ \mathrm{eV\,cm^{-2}\,s^{-1}}$
Ion-to-electron mass ratio	$m_\mathrm{i}/m_\mathrm{e}$		100
Light-to-Alfvén speed ratio	$c/V_\mathrm{A,i}$	$c\sqrt{4\pi n_\mathrm{sw}}/B_\mathrm{sw}$	188
Planet-to-gyro radius ratio	R/ρ_i	$R \cdot B_\mathrm{sw} e/c \sqrt{m_\mathrm{i} T_\mathrm{i,sw}}$	10

Notes. [a]Total number of macro-particles, ions plus electrons.

therein). MESSENGER (Solomon et al. 2007) could not measure the core of the electron distribution function, but it provided direct observations of high-energy electrons above 35 keV (Ho et al. 2011, 2012) and indirect observations of suprathermal electrons in the range ~1–10 keV (Lawrence et al. 2015; Baker et al. 2016; Dewey et al. 2018; Ho et al. 2016). MESSENGER also reported the first evidence of electron-induced X-ray emissions from the surface (Lindsay et al. 2016, 2022). These missions provided a novel but still fragmented picture of the solar-wind electron interaction with Mercury and weakly magnetized bodies in general. In the near future, the joint ESA/JAXA space mission BepiColombo (Benkhoff et al. 2021) will revolutionize our understanding of Mercury's environment thanks to (i) its two-satellite composition and (ii) its instrumental payload with resolution down to electron kinetic scales (Milillo et al. 2020). BepiColombo will observe the whole electron (Saito et al. 2021; Huovelin et al. 2020) and X-ray (Bunce et al. 2020) spectrum with unprecedented resolution. This will allow better constraint of the current hypothesis on the electron motion in the system and exploration, for the first time, of the kinetic plasma dynamics at subion scales. However, the complexity of these measurements is such that only through global models, including the electron dynamics, can the true potential of these measurements be unveiled. Here, we present such a model, and use it to interpret the fragmented picture left by past MESSENGER observations, while paving the way for the future BepiColombo ones.

In the past, global numerical models of Mercury's interaction with the solar wind have focused on the ion dynamics (Kallio & Janhunen 2003; Trávníček et al. 2010; Richer et al. 2012; Fatemi et al. 2020). Such models included the ion kinetic physics self-consistently, but neglected the kinetic physics of electrons (treated as a massless neutralizing fluid). Those models neglect electron acceleration processes and therefore also their feedback on the magnetosphere and surface. Previous studies that did model electron trajectories prescribed constant electromagnetic fields (i.e., a test-particle approach; Schriver et al. 2011a; Walsh et al. 2013), but this completely neglects the feedback of electron physics on the large-scale global evolution. Nonetheless, Schriver et al. (2011a) provided a first estimate of electron precipitation maps at Mercury, but their results did not address the energy distribution of electrons at the surface (due to the small statistical sample of test electrons). To overcome these limitations, in this work we study the precipitation of electrons on Mercury-like bodies using a global, fully kinetic model. Our model includes the electron dynamics self-consistently from the large, planet scale down to the electron gyro-radius.

We assess electron precipitation at the surface of Mercury under purely northward and southward solar-wind conditions. Our numerical results are then used to compute (i) the electron impact ionization rates in Mercury's low-altitude exosphere, and (ii) the X-ray photon emission profiles from Mercury's surface. This novel, self-consistent approach provides (i) the first estimate of the efficiency of electron impact ionization – a process usually neglected in exosphere models – for multiple exospheric species, and (ii) the first estimate of the X-ray luminosity of a rocky, weakly magnetized body driven by solar-wind electron precipitation.

2. Methods

2.1. Three-dimensional fully-kinetic global plasma simulations

We use the semi-implicit particle-in-cell code iPIC3D, which solves the Vlasov–Maxwell system of equations in a three-dimensional Cartesian box by discretizing the ion and electron distribution function (Markidis et al. 2010). The simulation setup includes (i) a uniform solar-wind plasma composed of two oppositely charged species (ions and electrons with a normalized mass of $m_\mathrm{i} = 1$ and $m_\mathrm{e} = 1/100$, respectively) injected from the sunward side of the box and (ii) a scaled-down model of the planet Mercury with radius $R = 230$ km (radius reduced by around a factor 10 from its real value) and magnetic dipole moment $200\ nT/R^3$. The dipole field is shifted northward by $0.2\ R$ in agreement with the MESSENGER magnetic field observations (Anderson et al. 2012). A scaled-down planet enables us to run a global, fully kinetic simulation on present state-of-the-art computing facilities. Scaling-down the planet but keeping the good ordering of physical spatial and temporal scales preserves the global magnetosphere structure and dynamics (Lavorenti et al. 2022). Analogous planet-rescaling techniques have been used to run global simulations of Mercury using a hybrid code on past-decade computing facilities (Trávníček et al. 2007, 2009, 2010) in support to MESSENGER observations. On top of that, we adopt $m_\mathrm{i}/m_\mathrm{e}$ and $c/V_\mathrm{A,i}$ rescaling techniques (see Table 1), a procedure commonly used in fully kinetic simulations in order to target kinetic processes using manageable computational resources (Bret & Dieckmann 2010; Le et al. 2013; Lavorenti et al. 2021). The artificially increased electron mass adopted here is responsible for a reduced electron thermal speed in the solar wind (here 460 km s^{-1} instead of the realistic value 1970 km s^{-1}). However, this reduction does not alter the thermal energy of solar-wind electrons and preserves a value of the electron Mach number in the solar wind of smaller than one (here 0.87 instead

of 0.20). To reduce the ratio $c/V_{A,i}$ (equal to $\omega_{p,i}/\omega_{c,i}$), we artificially reduce the light speed c in the simulations. This reduction would severely affect the electromagnetic modes with $\omega/k \approx c$, but these are not included in our model. We further discuss the impact of these rescalings in Appendix A. At the box boundaries, the outermost cells are populated with solar-wind plasma and the electromagnetic fields are linearly smoothed to their solar-wind values. Inside the planet, macro-particles are removed using a charge-balanced scheme (Lavorenti et al. 2022). We initialize the simulations with a solar-wind density of $n_{sw} = 30\,cm^{-3}$, a speed of $V_{sw} = 400\,km\,s^{-1}$ in the Sun–planet direction, a magnetic field amplitude of $B_{sw} = 20\,nT$, and temperature of $T_{i,sw} = T_{e,sw} = 21.5\,eV$. Two different simulation setups are used, with purely northward (RunN) or southward (RunS) interplanetary magnetic field (IMF). These two IMF setups, not designed to be the most statistically significant at Mercury, are used to grasp the physics of interest in the system under a simplified geometry (see James et al. (2017) for a statistical analysis of the IMF at Mercury). This simulation setup was validated by Lavorenti et al. (2022), who compared the large-scale structure of Mercury's magnetosphere with the mean structure observed by MESSENGER. The numerical parameters employed in our two runs are reported in Table 1.

2.2. How to link plasma precipitation to exosphere and surface processes?

To compute electron impact ionization (EII) rates and X-ray fluorescence (XRF) emissions, we employ (i) the electron energy distribution at the surface $f_e(\phi, \theta, E)$ computed from our fully kinetic simulations and (ii) reference cross sections $\sigma_X(E)$ found in the literature. Hereafter, ϕ and θ are the geographical longitude and latitude, respectively, and E is the electron energy. To compute the EII rates of H, He, Na, Mg, Al, Si, K, and Mn, we use the analytical formula provided by Golyatina & Maiorov (2021); for O we use the NIST tool by Kim et al. (2005); and for Ca we use the curve in Zatsarinny et al. (2019, Fig. 8 therein). XRF cross sections are obtained using the NIST tool by Llovet et al. (2014). The rate of a given process (EII or XRF with a given atomic species) is:

$$\nu_X(\phi, \theta) = \int_0^\infty f_e(\phi, \theta, E)\sigma_X(E)\sqrt{\frac{2E}{m_e}}\,dE. \tag{1}$$

This quantity measures the typical interaction time $\tau_X = 1/\nu_X$ of the electron flux with one target atom at one point of the surface, and is independent of the number of target atoms. For this reason, the EII rates computed from Eq. (1) do not depend on the spatial distribution of exospheric neutral atoms. In Eq. (1), we use the physical electron mass m_e at the denominator to compute the rate in SI units.

To compute the X-ray flux emitted from the surface, information on surface density and composition are needed. Using Mercury's mean geochemical surface composition derived from MESSENGER observations (McCoy et al. 2018, Table 7.1 therein) and assuming a mean surface mass density of $3\,g\,cm^{-3}$, we obtain the number density n_s of the most abundant surface species (namely O, Na, Mg, Al, Si, S, Ca and Fe). We also assume an electron penetration depth $\delta = 1\,\mu m$. The total X-ray photon flux as a function of longitude, latitude is:

$$\mathcal{F}_{XRF}(\phi, \theta) = \sum_s F_{XRF,s}(\phi, \theta) = \delta \sum_s \nu_{XRF,s}(\phi, \theta)n_s, \tag{2}$$
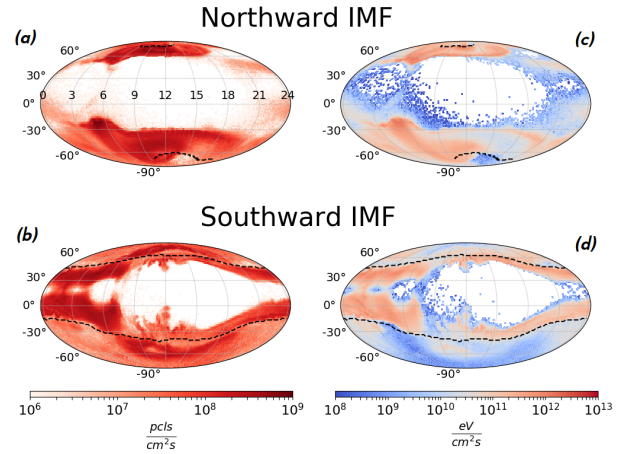
Fig. 1. Electron precipitation maps at the surface of Mercury using Mollweide projection. Panels a and b show the number fluxes in units of electrons cm^{-2} s. Panels c and d show the energy fluxes in units of eV cm^{-2} s. The vertical axis corresponds to geographical latitude and the horizontal axis corresponds to local time (as indicated in panel a, 12 is the subsolar longitude). Dashed black lines show the boundary between open and closed magnetic field lines (i.e., the cusps).

where $\nu_{XRF,s}$ is computed using Eq. (1). The emitted photon flux per species $F_{XRF,s}$ is proportional to both n_s and δ. Therefore, variations in the value of these two quantities, such as spatial variations on the surface between regions with different compositions, can be directly linked to variations in the emitted X-ray flux.

3. Results

3.1. Properties of electron precipitation on the planet's surface

In both simulations, the global system reaches a quasi-steady state after a time $T \approx 10$ s. This timescale T is comparable to the Dungey cycle period in our scaled-down Mercury. In our model, scaling down the magnetosphere size by a factor 10 corresponds to scaling down the Dungey cycle period from ≈ 2 min to ≈ 10 s. Starting from this time T, we integrate the plasma precipitation on the planet's surface for a time interval $\Delta t = 50$ ms, corresponding to about two electron gyro-periods ($\tau_{ce} = 2\pi/\omega_{ce} = 30$ ms in our simulations with the chosen electron mass rescaling). From the precipitated plasma, we compute the electron precipitation maps shown in Fig. 1. Moreover, solar-wind ion precipitation maps in the same format as Fig. 1 can be found in Appendix B. The precipitation maps are obtained using a total of $\sim 10^6$ macro-particles, enabling a good representation of the electron energy distribution function at the surface. Data concerning the macro-particles collected onto the surface are publicly available at this link[1].

The electron precipitation maps in Fig. 1 show significant spatial inhomogeneities for both explored IMF configurations. In the case of northward IMF (RunN), the solar-wind electrons are (i) energized up to energies of a few keV and (ii) concentrated onto the northern and southern cusps. In RunN, the northern cusp extends down to a latitude of $\sim +60°$ while the southern cusp extends to a latitude of $\sim -30°$. Such north–south asymmetry is due to the northward shift of the planetary magnetic dipole. Energy fluxes in the cusps reach values of $\sim 10^{12}$ eV cm^{-2} s, two

---

[1] https://doi.org/10.5281/zenodo.7589891
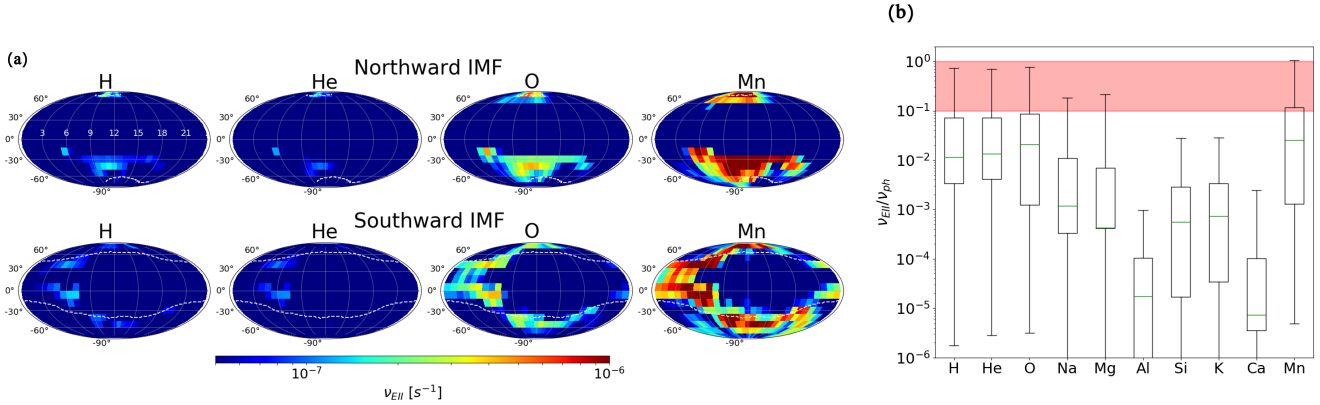
Fig. 2. Electron impact ionization rates in Mercury's exosphere. Panel a: maps in the same format as Fig. 1 of EII rates of exosphere H, He, O, and Mn. Panel b: box-plot of the distribution of EII-to-photoionization frequency ratios for multiple exosphere species (RunN and RunS are merged). The red box highlights the region of significant EII rates.

orders of magnitude higher than in the pristine solar wind (see Table 1). In the case of southward IMF (RunS), high-energy electrons (up to few keV) precipitate at low latitudes close to the magnetic equator (from $-50°$ to $+60°$) and mainly at the nightside. This energy flux is higher on the dawn side (LT 0–6 h) than on the dusk side (LT 18–24 h), in agreement with indirect electron observations by MESSENGER (Baker et al. 2016; Dewey et al. 2018; Lindsay et al. 2016). Possible drivers of such an electron enhancement at dawn are (i) the dawnward drift of electrons injected from the neutral line in the tail toward the planet (Christon 1987; Dong et al. 2019; Lavorenti et al. 2022) and (ii) the enhanced magnetic reconnection at dawn in the plasma sheet (Sun et al. 2022a, Chap. 4 therein). In RunS, low-energy electrons (around tens of eV) precipitate around the northern and southern poles. These electrons precipitate directly from the solar wind onto the surface without crossing the reconnection region.

We find that 1.5 times more electrons precipitate on the surface in RunS than in RunN. The rate of precipitating electrons is 1.7×10^{25} s^{-1} (2.6×10^{25} s^{-1}) in RunN (RunS), corresponding to an effective area of 2% (3%) of the total 4π planet surface area. The rates, fluxes, and energies reported here are in agreement with the findings of Schriver et al. (2011a). For unmagnetized bodies (such as Mars, Venus, comets, or the Moon), the effective area exposed to solar wind is 50% of the body's surface area given the absence of any magnetic field shielding. In those cases, precipitation is much higher as compared to Mercury, but the solar wind does not suffer acceleration in the magnetosphere (Kallio et al. 2008). A weak magnetic field, like that of Mercury, therefore (i) filters the solar-wind in precise regions of the surface and (ii) accelerates the incoming electrons by around a factor 100 in energy. Both effects (filtering and acceleration) are not possible around unmagnetized objects.

3.2. Interaction of precipitating electrons with the exosphere and surface

Before hitting the rocky surface of the planet, electrons interact with the exosphere. We address the efficiency of electron impact ionization (EII) of multiple exosphere species using the electron energy distribution from our simulations, because we want to assess the relevance of EII (usually considered a secondary, negligible effect) in comparison to photoionization (the primary ionization process). The distribution of EII rates computed from

Eq. (1) over the planet's surface is shown in Fig. 2a for hydrogen (H), helium (He), oxygen (O), and manganese (Mn) for both simulation runs. Moreover, maps of EII rates for all exosphere species considered in this work can be found in Appendix C in the same format as Fig. 2a. These four species have the highest EII-to-photoionization frequency ratio, as shown in Fig. 2b (photoionization rates ν_{ph} are taken from Huebner & Mukherjee (2015) for quiet sun conditions and rescaled to Mercury's aphelion). For H, He, O, and Mn, EII is relevant (i) in the dayside, where locally $\nu_{EII} \approx \nu_{ph}$ and (ii) in the nightside, where ionization of neutrals is dominated by EII with typical rates of $\sim 0.1 \, \nu_{ph}$. Differently from photoionization, EII is (i) localized on specific regions of the surface and (ii) strongly dependent on the upstream solar-wind parameters, as shown in Fig. 2a. Variations in the IMF direction, such as moving from northward to southward IMF, induce strong variations in EII rates locally at the surface. We also show that EII of sodium (Na), magnesium (Mg), aluminum (Al), silicon (Si), potassium (K), and calcium (Ca) are negligible under nominal solar-wind conditions, as shown in Fig. 2b. This result supports the common assumption of negligible EII for the Na exosphere (Sun et al. 2022b; Jasinski et al. 2021). Nevertheless, compared to photoionization, EII should not be considered a secondary process for the H, He, O, and Mn exosphere.

When hitting the surface, electrons induce the emission of photons from the surface atoms via X-ray fluorescence (XRF). This latter is driven by electrons with energies above a few hundred eV (Bunce et al. 2020, Table 5 therein). From the electron energy distribution at the surface obtained from our simulations, we compute the flux of emitted X-rays $\mathcal{F}_{XRF}$ from Eq. (2), as shown in Fig. 3a. We include XRF emission from the most abundant species on Mercury's surface, namely O, Na, Mg, Al, Si, S, Ca, and Fe. Figure 3b shows the relative intensity of each of the X-ray emission lines from these different elements. We find that electron-induced X-ray emissions from the surface of Mercury present strong spatial inhomogeneities dependent upon the upstream IMF conditions. Regions of strongest X-ray emission correspond to regions of high-energy electron precipitation, namely the poles (in the case of northward IMF) and the low-latitude, dawn–midnight sector (in the case of southward IMF). In these regions, the emitted X-ray flux reaches values of the order of 10^7 photons cm^{-2} s^{-1} (mostly coming from the O-Kα line). The MESSENGER/XRS instrument was able to measure X-rays from Si- and Ca-group ions at Mercury's
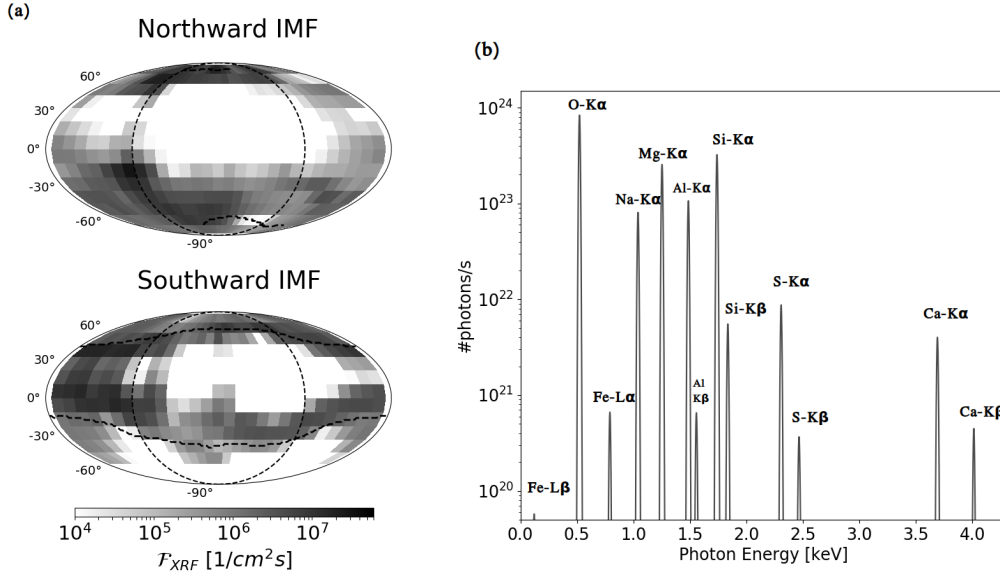
Fig. 3. X-ray emissions from the surface of Mercury induced from high-energy electron precipitation. Panel a: maps (same format as Fig. 1) showing the total X-ray photon flux emitted from the surface in our two runs, as computed in Eq. (2). Panel b: INTENSITY of the different X-ray emission lines considered in this study. The intensity of these lines corresponds to the surface integral of the X-ray photon flux $F_{XRF,s}$ in Eq. (2). To better visualize the lines, a Gaussian profile with a width of 5 eV is used.

nightside (Lindsay et al. 2016), and partially at the dayside (Lindsay et al. 2022) during periods of low solar activity. Due to limited energy range and energy resolution, XRS was not able to measure the rich variety of emission lines obtained from our simulations shown in Fig. 3b. Our results corroborate the idea – built upon MESSENGER observations – that Mercury's X-ray aurora-like emission is due to high-energy electron precipitation at the surface. Moreover, our modeled X-ray flux provides a new means to interpret and plan future in situ observations by the BepiColombo/MIXS instrument (Bunce et al. 2020). The integrated X-ray luminosity of Mercury from electron-induced XRF is $\mathcal{L} \approx 10^{24}$ photons s^{-1}. Such luminosity is comparable to that of other Solar System bodies shining in X-rays (Bhardwaj et al. 2007), such as comets, Jupiter, and Saturn. Nonetheless, remote observations from Earth of Mercury's X-ray aurora remain challenging due to the strong background of X-ray photons coming from the Sun.

4. Conclusions

To conclude, using a novel, fully kinetic 3D approach, we investigated the properties of solar-wind electron precipitation on the surface of Mercury-like bodies. The magnetosphere of those bodies acts (i) as a shield, allowing only a few percent of the solar wind to precipitate onto the surface and (ii) as an accelerator, increasing electron energies by a factor ~ 100. Using the self-consistently modeled electron precipitation fluxes as the input to exosphere and surface impact processes, we find two main results.

First, electron impact ionization of exospheric H, He, O, and Mn at Mercury is shown to be an efficient process. On the dayside, electron impact ionization is locally as efficient as photoionization. On the nightside, it is the dominant source of ionization of neutrals because photoionization is inhibited. The ionization rates provided here are crucial to complement fluid and hybrid models of Mercury's environment, which cannot model electron acceleration processes.

Second, electrons accelerated in the magnetosphere induce X-ray emission from the surface with fluxes of the order

of 10^7 photons cm^{-2} s^{-1}, mostly from surface oxygen. This result corroborates and provides the physical origin of the X-ray aurora-like emissions observed by the MESSENGER/XRS instrument; it also paves the way for the future planning of BepiColombo/MIXS observations.

References

Aizawa, S., Delcourt, D., Terada, N., & André, N. 2020, Planet. Space Sci., 193, 105079
Anderson, B. J., Johnson, C. L., Korth, H., et al. 2012, J. Geophys. Res. (Planets), 117, E00L12
Arró, G., Califano, F., & Lapenta, G. 2022, A&A, 668, A33
Bacchini, F., Pucci, F., Malara, F., & Lapenta, G. 2022, Phys. Rev. Lett., 128, 025101
Baker, D. N., Dewey, R. M., Lawrence, D. J., et al. 2016, J. Geophys. Res. (Space Phys.), 121, 2171
Benkhoff, J., Murakami, G., Baumjohann, W., et al. 2021, Space Sci. Rev., 217, 90
Bhardwaj, A., Elsner, R. F., Randall Gladstone, G., et al. 2007, Planet. Space Sci., 55, 1135
Bret, A., & Dieckmann, M. E. 2010, Phys. Plasmas, 17, 032109
Bunce, E. J., Martindale, A., Lindsay, S., et al. 2020, Space Sci. Rev., 216, 126
Christon, S. P. 1987, Icarus, 71, 448
Deca, J., Divin, A., Henri, P., et al. 2017, Phys. Rev. Lett., 118, 205101
Deca, J., Divin, A., Lue, C., Ahmadi, T., & Horányi, M. 2018, Commun. Phys., 1, 12

Deca, J., Henri, P., Divin, A., et al. 2019, Phys. Rev. Lett., 123, 055101

Dewey, R. M., Raines, J. M., Sun, W., Slavin, J. A., & Poh, G. 2018, Geophys. Res. Lett., 45, 10,110

Dibraccio, G. A., Slavin, J. A., Boardsen, S. A., et al. 2013, J. Geophys. Res. (Space Phys.), 118, 997

Dong, C., Wang, L., Hakim, A., et al. 2019, Geophys. Res. Lett., 46, 11,584

Dungey, J. W. 1961, Phys. Rev. Lett., 6, 47

Exner, W., Heyner, D., Liuzzo, L., et al. 2018, Planet. Space Sci., 153, 89

Fatemi, S., Poirier, N., Holmström, M., et al. 2018, A&A, 614, A132

Fatemi, S., Poppe, A. R., & Barabash, S. 2020, J. Geophys. Res. (Space Phys.), 125, e27706

Golyatina, R. I., & Maiorov, S. A. 2021, Atoms, 9, 90

Grošelj, D., Mallet, A., Loureiro, N. F., & Jenko, F. 2018, Phys. Rev. Lett., 120, 105101

Haggerty, C. C., Shay, M. A., Drake, J. F., Phan, T. D., & McHugh, C. T. 2015, Geophys. Res. Lett., 42, 9657

Herčík, D., Trávníček, P. M., Johnson, J. R., Kim, E.-H., & Hellinger, P. 2013, J. Geophys. Res. (Space Phys.), 118, 405

Herčík, D., Trávníček, P. M., Å tverák, Å. t., & Hellinger, P. 2016, J. Geophys. Res. (Space Phys.), 121, 413

Hesse, M., Schindler, K., Birn, J., & Kuznetsova, M. 1999, Phys. Plasmas, 6, 1781

Ho, G. C., Krimigis, S. M., Gold, R. E., et al. 2011, Science, 333, 1865

Ho, G. C., Krimigis, S. M., Gold, R. E., et al. 2012, J. Geophys. Res.: Space Phys., 117

Ho, G. C., Starr, R. D., Krimigis, S. M., et al. 2016, Geophys. Res. Lett., 43, 550

Huebner, W., & Mukherjee, J. 2015, Planet. Space Sci., 106, 11

Huovelin, J., Vainio, R., Kilpua, E., et al. 2020, Space Sci. Rev., 216, 94

James, M. K., Imber, S. M., Bunce, E. J., et al. 2017, J. Geophys. Res.: Space Phys., 122, 7907

Jasinski, J. M., Cassidy, T. A., Raines, J. M., et al. 2021, Geophys. Res. Lett., 48, e92980

Kallio, E., & Janhunen, P. 2003, Ann. Geophys., 21, 2133

Kallio, E., Wurz, P., Killen, R., et al. 2008, Planet. Space Sci., 56, 1506

Karimabadi, H., Roytershteyn, V., Wan, M., et al. 2013, Phys. Plasmas, 20, 012303

Kim, Y.-K., Irikura, K. K., Rudd, M. E., et al. 2005, Electron-Impact Ionization Cross Section for Ionization and Excitation Database, Version 3.0 (National Institute of Standards and Technology, Gaithersburg, Maryland)

Lapenta, G., Pucci, F., Goldman, M. V., & Newman, D. L. 2020, ApJ, 888, 104

Lavorenti, F., Henri, P., Califano, F., Aizawa, S., & André, N. 2021, A&A, 652, A20

Lavorenti, F., Henri, P., Califano, F., et al. 2022, A&A, 664, A133

Lawrence, D. J., Anderson, B. J., Baker, D. N., et al. 2015, J. Geophys. Res. (Space Phys.), 120, 2851

Le, A., Egedal, J., Ohia, O., et al. 2013, Phys. Rev. Lett., 110, 135004

Lindsay, S. T., James, M. K., Bunce, E. J., et al. 2016, Planet. Space Sci., 125, 72

Lindsay, S. T., Bunce, E. J., Imber, S. M., et al. 2022, J. Geophys. Res. (Space Phys.), 127, e29675

Llovet, X., Salvat, F., Bote, D., et al. 2014, NIST Database of Cross Sections for Inner-Shell Ionization by Electron or Positron Impact, Version 1.0 (Gaithersburg, Maryland: National Institute of Standards and Technology)

Markidis, S., Lapenta, G., & Rizwan-uddin 2010, Math. Comput. Simul., 80, 1509

McCoy, T. J., Peplowski, P. N., McCubbin, F. M., & Weider, S. Z. 2018, The Geochemical and Mineralogical Diversity of Mercury, eds. S. C. Solomon, L. R. Nittler, & B. J. Anderson, Cambridge Planetary Science (Cambridge University Press), 176

Milillo, A., Fujimoto, M., Kallio, E., et al. 2010, Planet. Space Sci., 58, 40

Milillo, A., Fujimoto, M., Murakami, G., et al. 2020, Space Sci. Rev., 216, 93

Ogilvie, K. W., Scudder, J. D., Vasyliunas, V. M., Hartle, R. E., & Siscoe, G. L. 1977, J. Geophys. Res., 82, 1807

Olshevsky, V., Servidio, S., Pucci, F., Primavera, L., & Lapenta, G. 2018, ApJ, 860, 11

Omidi, N., Blanco-Cano, X., Russell, C. T., & Karimabadi, H. 2004, Adv. Space Res., 33, 1996

Parashar, T. N., & Gary, S. P. 2019, ApJ, 882, 29

Parashar, T. N., Matthaeus, W. H., Shay, M. A., & Wan, M. 2015a, ApJ, 811, 112

Parashar, T. N., Salem, C., Wicks, R. T., et al. 2015b, J. Plasma Phys., 81, 905810513

Parashar, T. N., Matthaeus, W. H., & Shay, M. A. 2018, ApJ, 864, L21

Pezzi, O., Liang, H., Juno, J. L., et al. 2021, MNRAS, 505, 4857

Pucci, F., Matthaeus, W. H., Chasapis, A., et al. 2018, ApJ, 867, 10

Richer, E., Modolo, R., Chanteur, G. M., Hess, S., & Leblanc, F. 2012, J. Geophys. Res. (Space Phys.), 117, A10228

Roytershteyn, V., Boldyrev, S., Delzanno, G. L., et al. 2019, ApJ, 870, 103

Saito, S., & Nariyuki, Y. 2014, Phys. Plasmas, 21, 042303

Saito, Y., Delcourt, D., Hirahara, M., et al. 2021, Space Sci. Rev., 217, 70

Schriver, D., Trávníček, P., Ashour-Abdalla, M., et al. 2011a, Planet. Space Sci., 59, 2026

Schriver, D., Trávníček, P. M., Anderson, B. J., et al. 2011b, Geophys. Res. Lett., 38

Shay, M. A., & Drake, J. F. 1998, Geophys. Res. Lett., 25, 3759

Slavin, J. A., Lepping, R. P., Wu, C.-C., et al. 2010, Geophys. Res. Lett., 37, L02105

Solomon, S. C., McNutt, R. L., Gold, R. E., & Domingue, D. L. 2007, Space Sci. Rev., 131, 3

Sun, W., Dewey, R. M., Aizawa, S., et al. 2022a, Sci. China Earth Sci., 65, 25

Sun, W., Slavin, J. A., Milillo, A., et al. 2022b, J. Geophys. Res. (Space Phys.), 127, e30280

Tóth, G., Chen, Y., Gombosi, T. I., et al. 2017, J. Geophys. Res.: Space Phys., 122, 10,336

Trávníček, P., Hellinger, P., & Schriver, D. 2007, Geophys. Res. Lett., 34, L05104

Trávníček, P. M., Hellinger, P., Schriver, D., et al. 2009, Geophys. Res. Lett., 36, L07104

Trávníček, P. M., Schriver, D., Hellinger, P., et al. 2010, Icarus, 209, 11

Vega, C., Roytershteyn, V., Delzanno, G. L., & Boldyrev, S. 2020, ApJ, 893, L10

Verscharen, D., Parashar, T. N., Gary, S. P., & Klein, K. G. 2020, MNRAS, 494, 2905

Walsh, B. M., Ryou, A. S., Sibeck, D. G., & Alexeev, I. I. 2013, J. Geophys. Res. (Space Phys.), 118, 1992

Wurz, P., & Blomberg, L. 2001, Planet. Space Sci., 49, 1643

Zatsarinny, O., Parker, H., & Bartschat, K. 2019, Phys. Rev. A, 99, 012706

Appendix A: Fully kinetic simulations: Impact of rescaling

In our fully-kinetic simulations, we rescale the ion-to-electron mass ratio m_i/m_e, the plasma-to-cyclotron frequency ratio ω_{pi}/ω_{ci}, and the normalized planet radius R in order to be able to run the simulations on state-of-the-art HPC facilities while maintaining a good scale separation between electron, ion, and planetary scales. We are confident that the use of such rescaled parameters does not qualitatively alter the physical processes at play in our simulations.

On state-of-the-art HPC facilities, computational constraints impose the use of rescaled parameters to run fully kinetic simulations of large systems, such as Mercury's magnetosphere. If such rescalings are done "carefully", the modeled environment is still representative of the real one to a good degree of approximation, as demonstrated by the large number of publications for similar systems using reduced parameters. The exact meaning of "carefully" strongly depends on the plasma process under consideration. In the following, we address the impact of each of the rescaled parameters on the simulation results. In Sect. A.1, we show how the rescalings of m_i/m_e and ω_{pi}/ω_{ci} affect the microphysics in fully kinetic simulations while leaving the large-scale structure unchanged. In Sect. A.2, we discuss the role of a reduced planet radius on the results of global plasma simulations of planetary systems.

A.1. Effects of m_i/m_e and ω_{pi}/ω_{ci} on the microphysics

Fully kinetic simulations of space plasmas are commonly performed using (i) a reduced mass ratio m_i/m_e of the order of $25 - 400$ (Karimabadi et al. 2013; Deca et al. 2017, 2018; Pucci et al. 2018; Parashar et al. 2018; Olshevsky et al. 2018; Deca et al. 2019; Lapenta et al. 2020; Vega et al. 2020; Pezzi et al. 2021; Bacchini et al. 2022; Arró et al. 2022; Lavorenti et al. 2022) instead of the real hydrogen proton-to-electrom mass ratio of 1836, and (ii) a reduced ω_{pi}/ω_{ci} ratio of the order of 10–500 (Karimabadi et al. 2013; Saito & Nariyuki 2014; Parashar et al. 2015b,a; Grošelj et al. 2018; Parashar & Gary 2019; Royter-shteyn et al. 2019) instead of more realistic values of the order of 10^3–10^4 found typically in the solar wind. These two choices allow one to reduce the computational time needed to simulate a system of a given size. Indeed, the computational time of a fully kinetic simulation with fixed system size, grid resolution $dx \sim d_e$, time step $dt \sim \omega_{pe}^{-1}$, and time $T \sim \omega_{ci}^{-1}$ scales as:

$$T_{comp} \sim \left(\frac{\omega_{pi}}{\omega_{ci}}\right)\left(\frac{m_i}{m_e}\right)^{\frac{D+1}{2}}, \tag{A.1}$$

where D is the number of spatial dimensions of the system. Therefore, the rescalings typically operated on m_i/m_e and ω_{pi}/ω_{ci} reduce the computational time by several orders of magnitude.

Magnetic reconnection is a fundamental plasma process that regulates the energization and circulation of plasma in the magnetosphere of the Earth (Dungey 1961) and, to a similar extent, in that of Mercury (Slavin et al. 2010; Dibraccio et al. 2013). The impact of rescaled parameters on magnetic reconnection has been extensively investigated in past numerical works (Shay & Drake 1998; Hesse et al. 1999) that only had access to limited computational resources. There, the authors showed that rescaled parameters only affect the microphysics of the system while leaving the large-scale quantities, such as the reconnection rate, unchanged. Indeed, an increased electron mass impacts the electron distribution function in the electron diffusion region

very locally around the X-point, but leaves the plasma parameters of the outflow unchanged. In particular, electron acceleration by magnetic reconnection is weakly affected by the mass ratio m_i/m_e far from the X-point (Hesse et al. 1999; Haggerty et al. 2015). Magnetic reconnection with guide field is more strongly affected by a reduced ion-to-electron mass ratio (Le et al. 2013), but this is not the case in our simulations, where there is no guide field since the IMF is purely northward or southward. Based on the results of these past works, we expect a negligible impact of the rescaled parameters m_i/m_e and ω_{pi}/ω_{ci} on magnetic reconnection in our simulations of Mercury's magnetosphere.

In the interaction between the solar wind and Mercury's magnetosphere, multiple plasma waves are also excited. In principle, these waves can be affected by the rescalings of m_i/m_e and ω_{pi}/ω_{ci} both in their linear phase and in their corresponding nonlinear dynamics. A comprehensive study of the impact of these rescalings on the nonlinear dynamics of plasma waves is extremely challenging. On the other hand, Verscharen et al. (2020) studied the linear dependence of multiple plasma waves on the parameters m_i/m_e and ω_{pi}/ω_{ci}. There, the authors showed that plasma models with $m_i/m_e \gtrsim 100$ and $\omega_{pi}/\omega_{ci} \gtrsim 10$ (as it is in our case) successfully represents the physics at scales above $\gtrsim 0.2\, d_i$ (which corresponds to $2dx$ in our simulations). Analogous results were obtained by Bret & Dieckmann (2010) studying the impact of m_i/m_e on beam-plasma instabilities. There, the authors concluded that simulations with $m_i/m_e \gtrsim 100$ preserve the hierarchy of the linearly unstable modes and are therefore a good representation of the system.

A.2. Effect of a reduced planet radius

Global fully kinetic simulations of a large system, such as a planetary magnetosphere, are extremely challenging. The large scale separation between the magnetosphere size (at Mercury the magnetopause standoff distance is $d_{MP} \approx 1.5\, R \approx 4 \cdot 10^3$ km) and the ion scale (in the solar wind at Mercury $d_i \approx 50$ km) makes simulations of a real-sized planetary magnetosphere computationally very expensive. The computational time of a simulation with fixed grid resolution, fixed time step, system size $L \sim d_{MP}$, and time $T \sim L/V_{sw}$ scales as:

$$T_{comp} \sim \left(\frac{R}{d_i}\right)^{D+1}, \tag{A.2}$$

where D is the number of spatial dimensions of the system. Therefore, a reduction of the normalized planet radius $R \to \varepsilon R$ reduces the computational time by several orders of magnitude. This rescaling preserves the ratio d_{MP}/R because the magnetic moment of the planet is also reduced by a factor ε^3. In our simulations, we use $\varepsilon = 0.1$ to obtain a reduction in computational time of four orders of magnitude while keeping a good separation between ion kinetic scales (in the solar wind the ion gyroradius is $\rho_i \approx 23$ km) and planetary scales (the reduced planet radius is $R \approx 230$ km).

This rescaling technique was first introduced by Trávníček et al. (2007) for the study of Mercury using global 3D hybrid simulations. There, the authors showed that global simulations using a reduced planet radius (in their case $\varepsilon \approx 0.2$) enable a good representation of the real system and provide useful insight into the global kinetic ion dynamics in the magnetosphere. Further works by those authors using a reduced planet radius have led to important results on the magnetosphere of Mercury in support of MESSENGER observations; see for instance

Trávníček et al. (2009, 2010); Herčík et al. (2013, 2016); Schriver et al. (2011b).

On the one hand, the increased computational power of present HPC facilities (compared to those of 10-15 years ago) has enabled researchers to run global 3D hybrid simulations of Mercury using a real-sized planet (Fatemi et al. 2018; Exner et al. 2018; Aizawa et al. 2020). On the other hand, present state-of-the-art HPC facilities still do not allow global fully-kinetic simulations to be run using a real-sized planet (a computational gap that might be filled in 10-15 years as happened with hybrid simulations). Nonetheless, at present, fully kinetic simulations of the magnetosphere of Mercury are key to planning and interpreting in situ observations by BepiColombo, which is the first mission to address electron scale dynamics at Mercury.

Some authors tried to assess the impact of this planet rescaling on global magnetospheres. Omidi et al. (2004) identified different magnetosphere structures for different values of the normalized magnetopause standoff distance $D_p = d_{MP}/d_i$ using 2D global hybrid simulations. At Mercury, this parameter is of the order of $D_p \sim 1.5\ R/d_i \sim 100$. There, the authors found that values $D_p \sim 20$ or greater correspond to an Earth-like magnetosphere structure. Tóth et al. (2017) characterized the minimal rescaling factor ε to run global 3D simulations representative of Earth's magnetosphere using MHD simulations with embedded PIC regions. There, the authors found that, for Earth, a reduction factor of $\varepsilon \gtrsim 1/32$ yields comparable magnetosphere structures and dynamics.

We expect a negligible impact of the planet rescaling on electron adiabatic energization processes. Electrons in the magnetosphere undergo adiabatic betatron and Fermi acceleration while streaming towards the planet and along magnetic field lines, respectively. These processes are well modeled for electrons in our simulations given the large separation between planetary and electron scales (see also the discussion in Lavorenti et al. (2022)). On the contrary, for ions, adiabatic processes can only be poorly modeled in our simulations given the marginal separation between planetary and ion scales in some regions of the scaled-down magnetosphere.

Appendix B: Ion precipitation maps on the surface
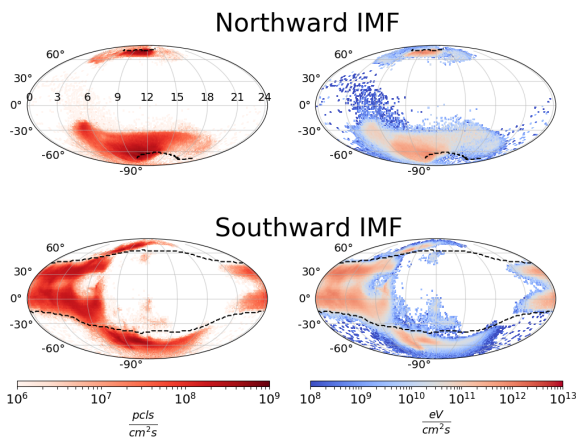
Fig. B.1. Ion precipitation maps (same format as Fig. 1) obtained from our fully kinetic simulations. These maps can be used for comparison with other works addressing proton precipitation at Mercury with hybrid models.

Appendix C: Complete set of EII rate surface maps

Fig. C.1. Full set of EII rates maps (same format as Fig. 2a) for all neutral species considered in this work. These maps are used to build the boxplot in Fig. 2b.

5.5 Lavorenti et al. (2023b) Planet. Sci. J., 4, 163

Maps of Solar Wind Plasma Precipitation onto Mercury's Surface: A Geographical Perspective

Federico Lavorenti[1,2] , Elizabeth A. Jensen[3] , Sae Aizawa[2,4], Francesco Califano[2] , Mario D'Amore[5], Deborah Domingue[3] ,
Pierre Henri[1,6], Simon Lindsay[7] , Jim M. Raines[8], and Daniel Wolf Savin[9]

[1] Laboratoire Lagrange, Observatoire de la Côte d'Azur, Université Côte d'Azur, CNRS, Nice, France
[2] Dipartimento di Fisica "E. Fermi", Università di Pisa, Pisa, Italy
[3] Planetary Science Institute, Tucson, AZ, USA
[4] Japan Aerospace Exploration Agency, Sagamihara, Kanagawa, Japan
[5] Institut für Planetenforschung, Deutsches Zentrum für Luft- und Raumfahrt (DLR), Rutherfordstr. 2, D-12489 Berlin, Germany
[6] LPC2E, CNRS, Univ. d'Orléans, CNES, Orléans, France
[7] School of Physics and Astronomy, The University of Leicester, Leicester, UK
[8] Department of Climate and Space Sciences and Engineering, University of Michigan, Ann Arbor, Michigan USA
[9] Columbia Astrophysics Laboratory, Columbia University, MC 5247, 550 West 120th Street, New York, NY 10027, USA
Received 2023 May 16; revised 2023 August 9; accepted 2023 August 9; published 2023 September 12

Abstract

Mercury is the closest planet to the Sun, possesses a weak intrinsic magnetic field, and has only a very tenuous atmosphere (exosphere). These three conditions result in a direct coupling between the plasma emitted from the Sun (namely, the solar wind) and Mercury's surface. The planet's magnetic field leads to a nontrivial pattern of plasma precipitation onto the surface that is expected to contribute to the alteration of the regolith over geological timescales. The goal of this work is to study the solar wind plasma precipitation onto the surface of Mercury from a geographical perspective, as opposed to the local time-of-day approach of previous precipitation modeling studies. We employ solar wind precipitation maps for protons and electrons from two fully kinetic numerical simulations of Mercury's plasma environment. These maps are then integrated over two full Mercury orbits (176 Earth days). We found that the plasma precipitation pattern at the surface is most strongly affected by the upstream solar wind conditions, particularly the interplanetary magnetic field direction, and less by Mercury's 3:2 spin–orbit resonance. We also found that Mercury's magnetic field is able to shield the surface from roughly 90% of the incoming solar wind flux. At the surface, protons have a broad energy distribution from below 500 eV to more than 1.5 keV, while electrons are mostly found in the range 0.1–10 keV. These results will help to better constrain space weathering and exosphere source processes at Mercury, as well as interpret observations by the ongoing ESA/JAXA BepiColombo mission.

Unified Astronomy Thesaurus concepts: Mercury (planet) (1024); Space weather (2037); Space plasmas (1544); Regolith (2294); Planetary science (1255); Planetary surfaces (2113); Solar wind (1534); Planetary geology (2288); Interplanetary magnetic fields (824); Magnetic fields (994)

1. Introduction

Mercury is the only telluric solar system planet other than Earth with an intrinsic magnetic field (Ogilvie et al. 1974). Mercury's magnetic field shapes the interaction between the planet's surface and the surrounding solar wind, a turbulent, supersonic, and magnetized plasma flowing outward from the Sun (Meyer-Vernet 2007). The interaction between Mercury's magnetic field and the solar wind is a crucial part of the global Hermean environment, both in shape and evolution. This is a result of the planet's proximity to the Sun (0.31 au at perihelion and 0.47 au at aphelion) and its relatively weak magnetic field (around 200 nT at the surface; Anderson et al. 2012).

The interaction between the solar wind and Mercury's magnetic field determines the precipitation of solar wind protons and electrons onto the planet's surface through a complex series of coupled local processes (Slavin 2004; Slavin et al. 2007). On the dayside, the presence of a bow shock in front of the planet along with magnetic reconnection in the magnetopause determines the pattern and energy of the precipitating plasma, while on the nightside, the precipitating plasma is mostly affected by magnetic reconnection and the magnetic field configuration in the tail. On the dayside, downstream of the bow shock (in the so-called magnetosheath), the plasma density, temperature, and magnetic field increase, while the plasma bulk velocity decreases. This slowdown leads to an order-of-magnitude reduction in the proton kinetic energy, which still dominates over the thermal energy component in the total energy of the protons. This differs with respect to the slowdown in the electron velocity, which does not significantly alter the electron total energy, as the thermal energy component dominates over the kinetic component in the total energy of the electrons. This proton and electron energy partition has been observed in situ at Earth's bow shock (Schwartz et al. 2022) and at interplanetary shocks (David et al. 2022); nonetheless, such in situ observations at Mercury are still lacking. Downstream of the magnetosheath, at the magnetopause, a part of the magnetic field carried by the solar wind connects with Mercury's magnetic field through magnetic reconnection (Dibraccio et al. 2013; Gershman et al. 2013). This process allows a fraction of shocked solar wind plasma to precipitate onto the surface, spiraling along newly opened magnetic field lines (Raines et al. 2022, and references therein). On the nightside, particles are accelerated and ejected
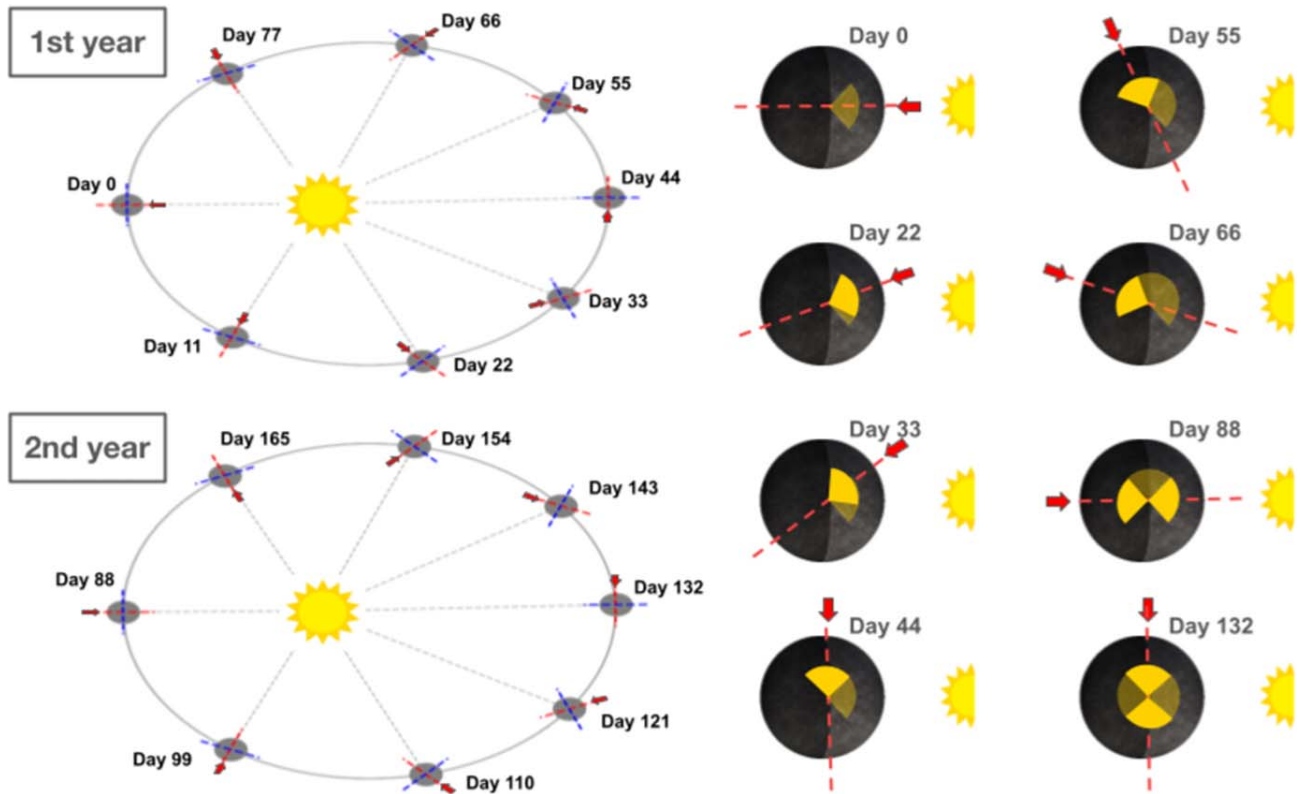
Figure 1. Sketch of plasma precipitation onto Mercury's surface over orbital time. The 3:2 spin–orbit resonance is responsible for increasing the cusp precipitation at the hot poles (red dashed lines) compared to the warm poles (blue dashed lines). The yellow sectors in the right panel approximately indicate the accumulation of plasma at the cusp over time.

planetward as magnetic field lines reconnect in the tail of the magnetosphere (Poh et al. 2017; Sun et al. 2017; Dewey et al. 2020). This high-energy plasma is accelerated through the plasma sheet horns (i.e., regions connecting the plasma sheet to the surface at midlatitudes, analogous to auroral ovals at Earth) and precipitates onto the surface, spiraling along magnetic field lines (Glass et al. 2022). The magnetic topology of the planet plus solar wind determines, to a large extent, the geographical distribution of plasma precipitation on both sides of the planet.

Plasma precipitation onto the surface of Mercury is further affected by the 3:2 spin–orbit resonance of the planet, as shown in Figure 1. As a consequence of this resonance, an observer standing at longitude $0°$ (or $180°$) faces the Sun for a longer time and at a closer distance compared to longitude $90°$ (or $-90°$). Therefore, Mercury's surface at longitudes $0°$ and $180°$ (called the hot poles) experiences a higher mean photon flux than at longitudes $90°$ and $-90°$ (called the warm poles). This was confirmed by the NASA MESSENGER mission (Solomon et al. 2007), which found a bimodal longitudinal pattern characterized by hot (warm) poles with maximal temperatures of 700 K (570 K; Bauch et al. 2021). A similar longitudinal pattern is expected to arise in the plasma fluxes at the surface when integrating over two full Mercury orbits. Past numerical works have addressed this problem in terms of "time of day" (local time) on the surface (Massetti et al. 2003, 2007; Mura et al. 2005; Kidder et al. 2008; Benna et al. 2010; Schriver et al. 2011; Fatemi et al. 2020; Lavorenti et al. 2023), but plasma precipitation has yet to be examined with regard to geographic location.

Looking at plasma precipitation from a geographic perspective will enable a correlation of plasma fluxes with spectral and compositional properties of the surface and thus an exploration of potential causal relationships with space weathering driven by the solar wind. Precipitation of solar wind particles onto the surface of Mercury drives space-weathering processes such as ion sputtering, ion implantation, electron-stimulated desorption (ESD), and X-ray fluorescence (XRF; Domingue et al. 2014; Wurz et al. 2022). Ion irradiation affects the surface at an atomic level and the exosphere at a global level. Ion sputtering is thought to be one of the main source processes for high-altitude sodium in the Hermean exosphere (Mangano et al. 2015; Exner et al. 2020; Killen et al. 2022). The maps presented in this work will allow researchers to better quantify ion sputtering at the surface of Mercury by relating the geographical distributions of ion fluxes with the surface distribution of sputtered species. ESD is another poorly understood source process of Mercury's exosphere (Madey et al. 1998; McLain et al. 2011; Domingue et al. 2014). The electron maps computed in this work, coupled with maps of surface temperature and composition, will enable a precise description of ESD for exosphere models. Driven by ~keV electrons, XRF converts precipitating electrons to X-ray photons at the surface of Mercury (Lindsay et al. 2016, 2022; Lavorenti et al. 2023). Future X-ray observations at Mercury by the joint ESA/JAXA BepiColombo mission (Benkhoff et al. 2021) will benefit from the electron precipitation maps computed in this work. The BepiColombo/MIXS instrument (Bunce et al. 2020) will be able to constrain the surface
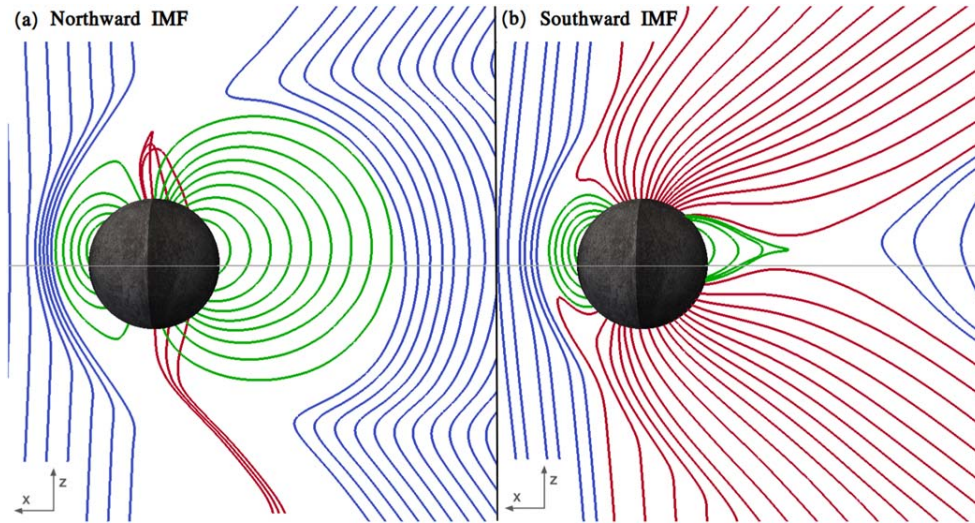
Figure 2. Magnetic field lines in the meridian plane (the X–Z plane in the Mercury-centered solar orbital coordinate system) for our two simulations. The left (right) panel corresponds to a simulation with a northward (southward) IMF. Blue lines correspond to magnetic field lines not connected to the planet (i.e., solar wind field lines). Red lines correspond to magnetic field lines with one end connected to the planet (i.e., magnetospheric open field lines). Green lines correspond to magnetic field lines with both ends connected to the planet (i.e., magnetospheric closed field lines). The horizontal gray lines indicate the geographic equator of the planet.

composition and mineralogy in part by using solar wind electrons to "probe" the Hermean surface via XRF.

Here we present the first plasma precipitation maps at Mercury integrated over two full Mercury orbits (176 Earth days) to account for the spin–orbit resonance. We use the proton and electron precipitation maps published in Lavorenti et al. (2023) as a function of "time of day" as inputs to our computations over Mercury's orbit. In this work, we neglect heavy solar wind ions (with atomic number $Z \geqslant 2$), micrometeoroid impacts, and thermal processes acting at the surface. The rest of the paper is organized as follows. Section 2 describes the methods used in this work. Section 3 presents the results with a focus on the spatial and energy distribution of particles at the surface of Mercury. In Section 4, we discuss the implications of our results for Mercury science and, more broadly, for space weathering of weakly magnetized bodies. Section 5 summarizes the conclusions of the paper.

2. Methods

We utilize the proton and electron precipitation maps published in Lavorenti et al. (2023), which were computed using a fully kinetic, global, three-dimensional plasma model of Mercury's magnetosphere. This numerical model solves the Vlasov–Maxwell system of equations using an implicit particle-in-cell (PIC) algorithm (Markidis et al. 2010). The model solves the plasma dynamics of the interaction between the solar wind and Mercury's magnetic field, self-consistently including the kinetic physics of both protons and electrons. Kinetic models differ from other fluid plasma models (e.g., magnetohydrodynamic models) that do not take into account the velocity distribution functions of the particles but use only averaged quantities such as density, bulk velocity, pressure, etc. In our simulations, the normalized planetary radius, the proton-to-electron mass ratio, and the light-to-Alfvén speed ratio are artificially reduced in order to be able to run on state-of-the-art high-performance computing facilities while maintaining a good —although compressed—separation of scales between the planetary radius, proton gyroradius, and electron gyroradius. This approach was validated in Lavorenti et al. (2022) by

comparing the bow shock and magnetopause positions from our model with the ones observed in situ by MESSENGER and averaged over the mission time period (Winslow et al. 2013). The artificially reduced scales used in our model induce a nonnegligible increase of proton nonadiabatic effects, as compared to the real system. This effect is important, for instance, in the ion diffusion region in the tail (extending $\sim$10 ion skin depths from the reconnection line) that reaches the planet surface in our simulations. However, rescaling techniques analogous to the ones used in this work were used in past hybrid models for Mercury (Trávníček et al. 2007, 2009, 2010; Schriver et al. 2011) and global models of Earth's magnetosphere (Tóth et al. 2017) to compensate for the lack of sufficient computational resources. A detailed discussion of this rescaling technique can be found in Lavorenti et al. (2023, Appendix A).

The solution of our numerical model depends upon the upstream solar wind parameters. We use solar wind parameters corresponding to typical mean values at Mercury's aphelion (Sarantos et al. 2007; James et al. 2017) with plasma density $n_{\rm sw} = 30$ cm^{-3}, speed $V_{\rm sw} = 400$ km s^{-1}, magnetic field amplitude $B_{\rm sw} = 20$ nT, and proton and electron temperatures $T_{\rm i,sw} = T_{\rm e,sw} = 21.5$ eV. These parameters are kept fixed in our two numerical simulations, while we vary the direction of the interplanetary magnetic field (IMF) in our two runs from purely northward to purely southward. Different directions of the IMF correspond to different magnetic configurations at the surface of Mercury, as shown in Figure 2. These configurations, in turn, affect plasma precipitation at the surface. In this work, we address two extreme IMF configurations (with $B_x = B_y = 0$) rarely found in the real system, but which are useful to grasp the role of the magnetic field in shaping the plasma precipitation at the surface. Our IMF configurations show the range of variability of the system by providing conditions for minimal (maximal) magnetic coupling between the solar wind and the planet when the IMF is northward (southward), i.e., when the IMF is antiparallel (parallel) to the planetary magnetic dipole moment.

Plasma precipitation maps as a function of local time were integrated along two full Mercury orbits, from 2022 January 23
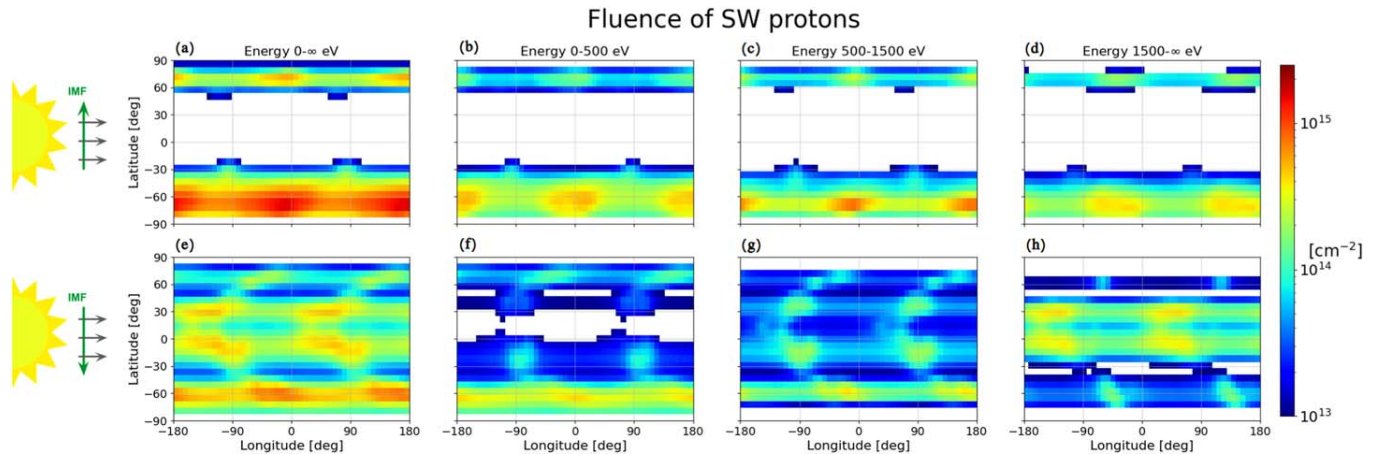
Fluence of SW protons

Figure 3. Proton precipitation maps integrated over two full Mercury orbits. Panels (a)–(d) are obtained from a simulation with a purely northward IMF and panels (e)–(h) with a purely southward IMF, shown by the green vectors on the left. The different columns correspond to different energy bins, given at the top of each column. At perihelion, when longitude 0° is subsolar, longitudes −90° and +90° correspond to local dawn and dusk, respectively. The white bins in the maps correspond to negligible fluences below 10^{13} cm^{-2}.
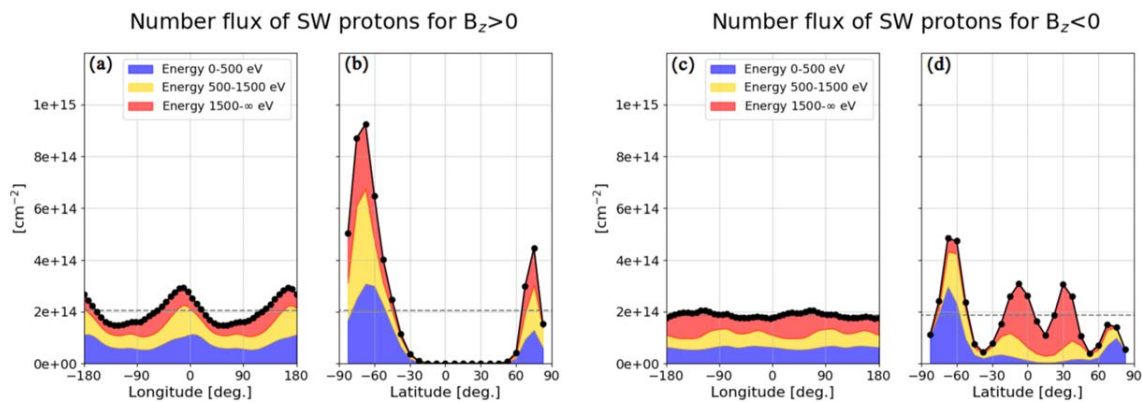
Figure 4. Proton precipitation maps integrated over two full Mercury orbits and averaged over latitude and longitude. The curves in panels (a) and (c) are obtained from the maps in Figures 3(a)–(d) and (e)–(h), respectively, by averaging in latitude. The curves in panels (b) and (d) are obtained, respectively, from the same maps by averaging in longitude. The black dots and line show the averages summed over all energies, and the colored areas show the contributions for the labeled energy bins. The horizontal dashed black lines show the mean value of the fluence (averaged in both latitude and longitude).

at 18:44:32 UTC to 2022 July 18 at 05:48:44 UTC; this corresponds to the time interval shown in Figure 1. We do not consider variations in the solar wind parameters along the orbit, which will be included in a future work that also includes a more realistic IMF configuration. We subdivide the orbit into 515 steps of equal time $dt = 8.21$ hr. At each time step, we rotate the planet and map the local time to surface longitude using the Jet Propulsion Laboratory's Navigation and Ancillary Information Facility (NAIF) SPICE files and routines. The NAIF/SPICE files enable a precise determination of the location of the Sun with respect to Mercury at each time of the orbit and consist of ephemeris files for the orbit of Mercury and planetary body information for its rotation. The geographical registration of local time to longitude through this time period is provided with the ancillary files to this publication (Lavorenti et al. 2023).

3. Results

3.1. Spatial Distribution of Particle Fluxes at the Surface

The spatial distribution of particle fluxes at the surface is organized into latitudinal bands with enhancements in longitude driven by the 3:2 resonance. For protons, this pattern is

shown by the maps in Figure 3, along with the latitudinal and longitudinal averages in Figure 4. The proton data are shown for energy bins of 0–500, 500–1500, and 1500–∞ eV, which we refer to as low, moderate, and high energies. For electrons, Figures 5 and 6 show the corresponding data. The electron data are shown for energy bins of 0–100, 100–1000, and 1000–∞ eV, which we refer to as low, moderate, and high energies. The results from these maps are summarized in Table 1 using a coarse spatial grid and averaging between the two IMF conditions under study. In these maps, longitudinal variations are controlled by Mercury's rotation, while latitudinal variations are controlled by the IMF. In the following, we discuss these two effects separately.

Mercury's rotation is responsible for the differential accumulation of particles versus longitude. Due to the 3:2 spin–orbit resonance of Mercury, subsolar (local time 12 hr) high-latitude proton precipitation is enhanced at the hot poles (longitude 0° and 180°), as shown in Figure 3. This effect is more prominent in the simulation with a northward IMF, as shown in Figures 3(a)–(d) and 4(a). Under a northward IMF, the topology of the magnetosphere (i.e., the "closed" topology shown in Figure 2(a)) channels plasma precipitation to the high-latitude cusps at local time 12 hr. This hot pole
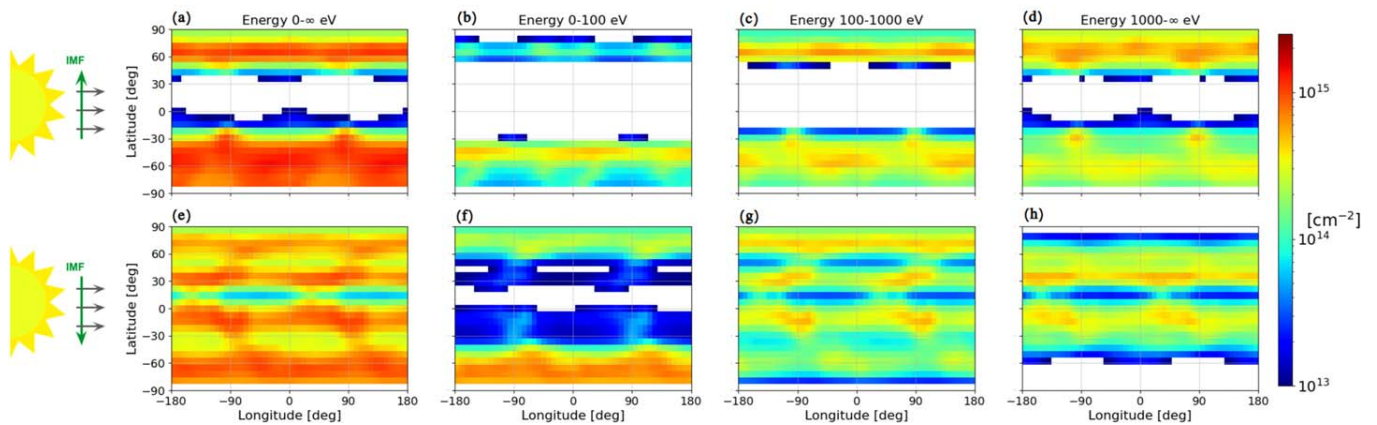
Figure 5. Same as Figure 3, but for electron precipitation.
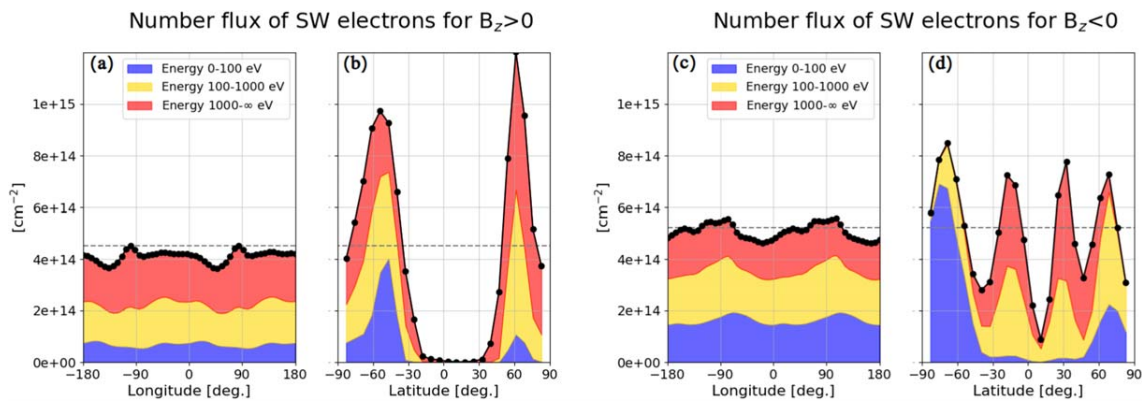
Figure 6. Same as Figure 4, but for electron precipitation.

enhancement shifts dawnward (by roughly −20° longitude, as shown in Figure 4(a)) with increasing proton energy. This energy-dependent shift is consistent with a grad-B drift of protons when approaching Mercury's surface and its higher magnetic field, as shown by Mura et al. (2005) using a test particle model. Under a southward IMF and the resulting "open" magnetic field topology of the magnetosphere shown in Figure 2(b), plasma precipitation occurs both at the cusps and at low latitudes. Cusp precipitation is enhanced at the hot poles due to the same mechanism at play with the northward IMF, as shown in Figures 3(e)–(g). This contrasts with the low-latitude proton precipitation, as shown in Figures 3(g) and (h). These low-latitude protons are ejected from the reconnection site in the tail and precipitate between roughly midnight and dawn in local time (Lavorenti et al. 2022, 2023). This is due to the combined action of the **ExB** (grad-B) drift that pushes protons dawnward (duskward) in the magnetotail that results, in the end, in a proton enhancement at dawn. This is in agreement with MESSENGER observations showing a more prominent proton population at dawn, as compared to dusk (Korth et al. 2011). Proton precipitation around dawn in local time translates to precipitation around the warm poles in geographical coordinates.

Electrons precipitate onto the surface of Mercury with a pattern somewhat similar to that of the protons, as both are driven by the magnetic field topology. Longitudinal enhancements for electrons are weaker than for protons due to their

higher thermal energy component (that accounts for random motion) as compared to their kinetic energy component (that accounts for ordered motion). This means that, although electrons are more magnetized, they have a higher random velocity parallel to the magnetic field, as compared to protons, and this drives a "background" precipitation of thermal electrons from the solar wind directly onto the surface along open magnetic field lines. Under a northward IMF, electron precipitation in the cusps is enhanced around the hot poles at high latitude, as shown in Figures 5(a)–(c). In this case, the "closed" magnetosphere topology channels electrons at high latitudes and inhibits electron precipitation at low latitudes. Under a southward IMF, the electron precipitation presents two distinct regions of precipitation, the high-latitude low-energy electrons in Figure 5(f) and the low-latitude moderate- and high-energy electrons in Figures 5(g) and (h). Both tend to be enhanced around the warm poles, as shown in Figure 6(c), although these enhancements are quite weak. These enhancements at the warm poles are a direct consequence of electron precipitation toward dawn in local time (Lindsay et al. 2022; Lavorenti et al. 2023).

Variations in the IMF drive strongly different latitudinal particle distributions at the surface. Under a northward IMF, Mercury's magnetic dipole is able to shield a large fraction of the planet from the impinging solar wind. In this case, protons and electrons precipitate mostly onto the cusps at high latitudes. Protons precipitate between latitudes 70°–80°N and

Table 1
Particle Fluences in Units of 10^{14} cm^{-2} for Different Regions at the Surface of Mercury, Averaged over the Two IMF Simulations

	Energy [eV]	North Pole	Equatorial Region	South Pole
Proton fluence [10^{14} cm^{-2}]	0–500	0.9	Small	1.8
	500–1500	0.8	Small	1.2
	1500–∞	0.5	0.7	0.9
Electron fluence [10^{14} cm^{-2}]	0–100	1.8	Small	2.8
	100–1000	3.0	2.0	2.0
	1000–∞	4.1	2.5	2.4

Note. North pole corresponds to latitudes from $+90°$ to $+60°$. Equatorial region corresponds to latitudes from $+60°$ to $-30°$. South pole corresponds to latitudes below $-30°$. The entries "small" in the table indicate negligible fluence values that are below 0.5×10^{14} cm^{-2}.

$-45°$S to $-90°$S, as shown in Figure 4(b). Electrons precipitate between latitudes $60°–80°$N and $-30°$S to $-70°$S, as shown in Figure 6(b). The north–south asymmetry in the size of the cusp precipitation region is a consequence of the northward shift of Mercury's magnetic dipole. The position of the northern cusp is in agreement with recent estimates by Raines et al. (2022) using MESSENGER/FIPS data. Under a northward IMF, particle precipitation is negligible in the equatorial region at latitudes spanning from $+60°$ to $-30°$. Conversely, under a southward IMF, the topology of the magnetosphere results in stronger precipitation at low latitudes, as shown in Figures 4(d) for protons and 6(d) for electrons. This low-latitude precipitating plasma is composed of high-energy protons and moderate- and high-energy electrons ejected planetward from the reconnection site in the tail. Respectively, comparing Figures 4(b) and (d) with Figures 4(a) and (c) for protons or, equivalently, Figures 6(b) and (d) with Figures 6(a) and (c) for electrons, we observe that latitudinal variations driven by the IMF are about 1 order of magnitude more important than longitudinal variations driven by Mercury's rotation.

The dependence of proton precipitation on the IMF was investigated by Massetti et al. (2003, 2007), Mura et al. (2005), and Sarantos et al. (2007) using test-particles models and by Kallio & Janhunen (2003) and Fatemi et al. (2020) using global hybrid models. Overall, they found that (i) magnetic reconnection can increase the proton energy up to some keV with fluxes of the order of 10^8–10^9 cm^{-2} s^{-1}, and (ii) the precipitation pattern is strongly dependent on the IMF direction, in particular that a (planetward) sunward component of the IMF increases the proton precipitation onto the (northern) southern hemisphere and that a larger B_z component increases the area of open magnetic field lines—and thus of precipitation—onto the surface. Our results build upon the findings of these past works and extend our current view of plasma precipitation onto the surface of Mercury by (i) including electrons self-consistently in the model and (ii) computing the precipitation in geographical coordinates instead of the commonly used "time-of-day" coordinates.

A coarse energy sampling of the precipitation maps in three energy bins, shown in Figures (3)–(6), enables one to identify the importance of various particle distributions in driving different processes at the surface. The fluences of the particles in each of the three energy bins are summarized in Table 1 using a coarse spatial grid and averaging over the two IMF

configurations under study. In this table, we show the mean fluence of protons and electrons in each energy bin in three regions at the surface of Mercury, namely, the north pole (above $60°$ latitude), the equatorial region (from $60°$ to $-30°$ latitude) and the south pole (below $-30°$ latitude). These fluence values can be used for a first-order estimate of space weathering due to plasma–surface interaction processes at Mercury. This point is further discussed in Section 4.

3.2. Energy Distribution of Particles at the Surface

For protons, the net effect of Mercury's magnetic field is to broaden their energy distribution. In our simulations, solar wind protons are initialized with a narrow Maxwellian energy distribution centered around $m_i V_{sw}^2/2 = 826$ eV, corresponding to a solar wind speed of $V_{sw} = 400$ km s^{-1} (shown by the red vertical solid lines in Figures 7(a) and (b)). The distribution width is of the order of $T_{i,sw} = 21.5$ eV, as shown by the orange curves in Figure 7(a) and (b). At the surface, the energy distribution of protons spreads out to a few keV, with a considerable population centered around $\sim$200 eV, as shown by the blue curves in Figure 7(a) and (b). Two competing processes are at play to slow down some of the solar wind protons and accelerate others. The slowdown of solar wind protons is due to the presence of a bow shock in front of the planet. Upon passing through the bow shock, protons are decelerated from the (upstream) solar wind speed of $V_{sw} = 400$ km s^{-1} to the (downstream) fast magnetosonic speed $V_f = (V_{A,i}^2 + V_{s,i}^2)^{1/2}$ (Belmont et al. 2019). The fast magnetosonic speed in the solar wind is $V_f = 120$ km s^{-1}, corresponding to a kinetic energy of 76 eV (shown by the green vertical dashed lines in Figures 7(a) and (b)). In principle, V_f should be computed using the density, temperature, and magnetic field values in the magnetosheath, but given the uncertainty associated with these values, here we use as a lower limit the fast magnetosonic speed in the solar wind, where $V_{A,i} = B_{sw}/\sqrt{4\pi m_i n_{sw}}$ is the Alfvén speed, $V_{s,i} = \sqrt{\gamma T_{i,sw}/m_i}$ is the ion sound speed, and $\gamma = 2$ is the adiabatic index of the plasma. The acceleration of solar wind protons is due to magnetic reconnection in the magnetosphere. For a northward IMF, magnetic reconnection is weakly driven at the lobes at high latitudes. For a southward IMF, magnetic reconnection is more strongly driven both at the nose and in the tail of the magnetosphere. Magnetic reconnection converts part of the magnetic energy stored in the planetary magnetic field configuration, corresponding to roughly 10 keV (shown by the green vertical solid lines in Figures 7(a) and (b)), to the kinetic energy of the particles. The efficiency of this conversion is on the order of 10% (Phan et al. 2014; Shay et al. 2014; Haggerty et al. 2015), meaning that roughly 1 keV of magnetic field energy is converted to the kinetic energy of the particles. These two competing processes (bow shock slowdown and acceleration by magnetic reconnection) are responsible for the proton fluences versus energy at the surface reported in Table 1. Substantial proton fluences below 500 eV—mostly at high latitudes—are a consequence of the plasma slowdown downstream of the bow shock, while proton fluences above 1.5 keV—mostly at high latitudes under a northward IMF or low latitudes under a southward IMF—are a consequence of magnetic reconnection and proton heating in the magnetosheath. This result has implications for current estimates of ion sputtering at Mercury that consider ions with a fixed energy of 1 keV amu^{-1} to approximate the solar wind proton energy
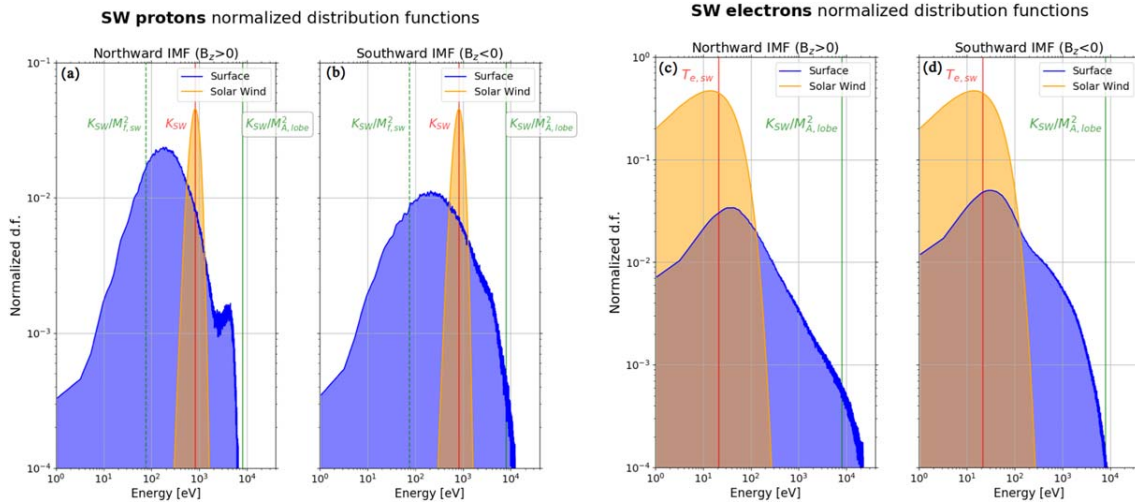
Figure 7. Normalized energy distribution of the particles in the solar wind (orange) and at the surface (blue). Panels (a) and (b) show the proton distribution functions. Panels (c) and (d) show the electron distribution functions. The red vertical solid lines show the mean energy of the solar wind plasma, which is equal to $K_{SW} = m_i V_{SW}^2/2 = 826$ eV for protons and $T_{e,SW} = 21.5$ eV for electrons. The green vertical dashed lines in panels (a) and (b) show an estimate of the proton energy downstream of the bow shock equal to $K_{SW}/M_{f,SW}^2$, where $M_{f,SW} = 3.3$ is the fast magnetosonic Mach number in the solar wind upstream of the bow shock. The green vertical solid lines show an estimate of the maximum magnetic energy available for magnetic reconnection equal to $K_{SW}/M_{A,lobe}^2$, where $M_{A,lobe} = 0.32$ is the Alfvén Mach number in the lobes computed using a magnetic field of 100 nT and density of 3 cm^{-3}.

upstream of the bow shock, i.e., Killen et al. (2022) and Morrissey et al. (2022). A broader discussion of the impact of proton energy distributions on sputtering yield can be found in Section 4.2.

For electrons, the net effect of Mercury's magnetic field is energization by magnetic reconnection. Solar wind electrons have a Maxwellian energy distribution with temperature $T_{e,SW} = 21.5$ eV, as shown by the orange curves in Figure 7(c) and (d). For electrons, the flow energy component $m_e V_{SW}^2/2 = 8.26$ eV (in the solar wind) is negligible with respect to the thermal energy component both outside and inside Mercury's magnetosphere. At the surface, the electron energy distribution displays a high-energy tail extending up to $\sim$10 keV, as shown by the blue curves in Figures 7(c) and (d). Magnetic reconnection energizes a substantial fraction of solar wind electrons up to the maximum magnetic energy available, shown by the green vertical solid lines in Figures 7(c) and (d). As a consequence, precipitating electrons are mostly found in the moderate- and high-energy bins with energies above hundreds of eV, as summarized by the fluences in Table 1.

4. Discussion and Implications

The study of solar wind particle precipitation on weakly magnetized bodies (such as Mercury) is more complex than that on unmagnetized bodies (such as the Moon). The presence of an intrinsic magnetic field—although weak—has a considerable effect on both where particles precipitate onto the surface and what energy these particles have. In the following, we discuss these two effects separately and their implications for plasma–surface interaction processes. Particular relevance is given to the comparison between weakly magnetized and unmagnetized bodies.

4.1. Magnetosphere as a Filter: The Effect of a Magnetic Field on the Spatial Distribution of Particles at the Surface

We consider here the interaction between a homogeneous, constant flow of plasma (i.e., an ideal solar wind) and a

spherical body (i.e., an ideal rocky body such as Mercury or the Moon). The body rotates with angular velocity ω and a spin axis perpendicular to the plasma flow. If the body is unmagnetized, the flux of particles reaching the surface integrated over a time $\Delta T \gg 2\pi/\omega$ corresponds to the solar wind fluence multiplied by the cross-sectional area πR^2 and divided by the total surface body area $4\pi R^2$:

$$\frac{n_{SW} V_{SW}}{4} \Delta T. \tag{1}$$

If the body is weakly magnetized, the fluence of particles at the surface is further reduced by a factor $\alpha > 1$ as follows:

$$\frac{n_{SW} V_{SW}}{4\alpha} \Delta T. \tag{2}$$

The effective shielding parameter α accounts for the average reduction of plasma flux from the solar wind onto the surface due to the magnetic field. From the averaged fluences reported in Figure 4 for protons and Figure 6 for electrons, we derive the effective shielding parameters for solar wind protons and electrons:

$$\alpha_p \approx 20, \tag{3}$$

$$\alpha_e \approx 10. \tag{4}$$

Our results indicate that the magnetic field effectively shields about 90% of the incoming solar wind particles, reducing the fluence at the surface by 1 order of magnitude as compared to the unmagnetized case. Similar shielding values were reported by Massetti et al. (2003) and Mura et al. (2005), focusing on proton precipitation at the cusps. The shielding values do not vary appreciably between our two runs using a purely northward or southward IMF, suggesting that the IMF direction weakly affects the total number of particles precipitating onto the surface. Raines et al. (2022) found a similar weak dependence in their estimates of cusp precipitation (their Figure 8(c)). A future study using a more realistic IMF

direction for Mercury (including B_x and B_y components) will address this point specifically.

The IMF direction controls where solar wind particles precipitate onto the surface. Although the total number of precipitating particles weakly depends on the IMF direction, at least for the configurations under study, the regions of strongest precipitation significantly differ between the simulations with a purely northward and southward IMF, as shown in Section 3.1. Therefore, time variations in the IMF direction—not included in our computation—would modify the location of the regions of strongest particle precipitation. Since the IMF direction changes on timescales of the order of tens of minutes due to the turbulence in the solar wind (James et al. 2017), we expect a continuously changing pattern of precipitation. The natural variability of the solar wind density and velocity at Mercury is also responsible for variations in the incoming plasma flux of roughly 1–2 orders of magnitude (Sarantos et al. 2007). Therefore, taking into account variations in both the IMF and the solar wind plasma flux, it is likely that the longitudinal accumulation of plasma driven by the 3:2 resonance would be hidden by such natural variability. The use of the effective shielding parameter α in Equation (2) remains, however, of deep interest, since it represents a first-order measure of a nonhomogeneous and time-varying process.

As recently highlighted by MESSENGER/FIPS observations of proton precipitation at the northern cusp (Raines et al. 2022), one pervasive characteristic of Mercury's interaction with the solar wind is high variability. Our study, however, focuses on representative cases with fixed solar wind conditions; we then computed the effect of these fixed cases over two full Mercury orbits. In doing so, several types of events that may provide substantial contributions to space weathering (such as coronal mass ejections, CMEs; interplanetary shocks; and solar energetic particle, SEP, events) have been omitted. These extreme events profoundly alter the ability of the planetary magnetic field to shield the surface. From MESSENGER observations, Winslow et al. (2015) identified a total of 61 CMEs from 2011 March to 2014 September, corresponding to an occurring frequency of roughly one CME every 20 days. The increase in ram pressure associated with these events compresses the dayside magnetopause, increases the surface exposed to solar wind flux, and, in few abnormally strong and rare cases, completely rips off the dayside magnetosphere (Slavin et al. 2014, 2019; Winslow et al. 2017; Exner et al. 2018; Jia et al. 2019). Concerning SEP events, Gershman et al. (2015) inferred the high-latitude precipitation of solar energetic electrons onto the surface of Mercury for 11 SEP events. As SEP events include protons over 15 MeV and electrons up to 3 MeV in energy at substantial fluxes, they can make substantial contributions to space weathering over periods of hours to days (Lario et al. 2013). However, the details concerning the probability of all of these events occurring, as well as their full impact on space-weathering processes, remain poorly known at present.

Ion precipitation onto the surface of Mercury is one of the drivers of space weathering via ion sputtering and implantation. Space weathering alters the spectral properties of the regolith by darkening the surface, decreasing absorption band depths, and changing the spectral slope (reddening from the visible to near-infrared, blueing from the ultraviolet to the visible; Noble et al. 2007; Blewett et al. 2021). The infrared spectrometer MERTIS on board BepiColombo will be able to measure those spectral variations at Mercury (Maturilli et al. 2014; Hiesinger et al. 2020).

The geographical distributions of proton fluxes at the surface of Mercury shown in Figure 3 when compared to spectral surface properties can provide key information to infer the role of solar wind ion irradiation in the spectral processing of the surface. However, given the strong dependence of these maps on the time-variable IMF direction, we introduced the proton effective shielding parameter $\alpha_p \approx 20$ in Equation (2). The use of this parameter will enable researchers to compare the partially shielded surface of Mercury with the unshielded surfaces of the Moon and unmagnetized asteroids such as Ryugu (Sawada et al. 2017) and Bennu (Lauretta et al. 2017), paving the way to comparative space-weathering studies.

Space-weathering studies of the Hermean regolith rely on comparisons with the Moon and asteroids (Domingue et al. 2014). Understanding how the magnetic field of Mercury shields the planetary surface compared to that of other unmagnetized bodies is a key point to comparatively study the effects of space weathering on solar system bodies. At Mercury, in this work, we showed that the surface is exposed, on average, to $\sim 2 \times 10^{14}$ protons cm^{-2} integrating over two full Mercury orbits. At the Moon, using Equation (1) and considering a solar wind flux of 3×10^8 protons cm^{-2} s^{-1}, we find a fluence of $\sim 10^{15}$ protons cm^{-2} for the same time period (this value would be reduced to $\sim 7 \times 10^{14}$ protons cm^{-2} if considering zero proton flux when the Moon crosses Earth's magnetosphere; Poppe et al. 2018). For main-belt asteroids, this fluence is further reduced by a factor of ~ 5–10 due to the increased distance from the Sun. Therefore, Mercury is bombarded by roughly three to five times fewer protons as compared to the Moon and roughly the same amount of protons as compared to a main-belt asteroid. At Mercury, the magnetic field screening compensates for the increase in solar wind flux as compared to the Moon. In this work, we neglected the interplay between ion irradiation and micrometeoroid processes such as impact gardening and comminution. Given that the micrometeoroid impactor flux at Mercury is about a factor of 40 higher than at the Moon (Pokorný et al. 2018, 2019; value obtained by comparing Figures 24 and 7 in these papers, respectively), this interplay might be important and should be addressed in future works.

Space weathering of Mercury's surface has consequences for the remotely sensed properties of the regolith, namely, the determination of composition via color and spectral properties. Composition, the identification of both specific minerals and their abundances, is based on the detection and strength of absorption features. Space weathering by both solar wind irradiation and micrometeoroid impacts reduces the strength of absorption features. For example, the 1 μm band diagnostic of the mineral olivine can be completely masked by the formation of a small amount of nanophase iron ($\sim 1\%$ in weight of np-Fe^0) via solar wind irradiation and micrometeoroid impact–generated vapor (Kohout et al. 2014). At Mercury, the MESSENGER infrared spectrometer MASCS/VNIR (McClintock & Lankton 2007) showed no distinct spectral features throughout the visible to near-infrared except for the possible indication of sulfide mineralogy within the hollows (Vilas et al. 2016). Given the reduced proton fluence onto Mercury's surface compared to the Moon (by roughly a factor of 3–5), we suggest that ion irradiation is not the main process at play in reducing spectral band signatures at Mercury.

4.2. Magnetosphere as an Accelerator and Decelerator: The Effect of a Magnetic Field on the Energy Distribution of Particles at the Surface

Our numerical simulations show that the energy distributions of both protons and electrons are affected differently by the Hermean magnetosphere. On the one hand, the protons impacting the surface are composed of one low-energy population (around $\sim$200 eV) and one moderate-to-high-energy population (around $\sim$1 keV). On the other hand, the electrons impacting the surface have a moderate energy of the order of $\sim$0.1–1 keV. The fluences of these different populations at the surface are summarized in Table 1.

Our results on the proton energy distribution at the surface are key to reliably modeling the exosphere of Mercury. Solar wind protons contribute to the exosphere of Mercury via ion sputtering. Ion sputtering is usually included in exosphere models assuming a monochromatic energy of 1 keV amu^{-1} (e.g., Killen et al. 2022; Morrissey et al. 2022). This is a good approximation for protons in the solar wind, as shown by the orange curves in Figures 7(a) and (b). However, this is not a good approximation at the Hermean surface, where the proton distribution (in blue in Figures 7(a) and (b)) shows a large population at lower energies coming from the interaction with the bow shock. Protons below $\sim$500 eV weakly contribute to ion sputtering (Eckstein 2007). Our modeling suggests that only $\sim$60% of the total number of precipitating protons will have significant sputtering yields. From the fluences in Table 1, we see that this value changes with latitude. Around the poles, $\sim$50% of the protons are efficient for sputtering (fluence of $\sim$1.7 × 10^{14} protons cm^{-2}), whereas around the equator, this value goes to 100% with a fluence of $\sim$0.7 × 10^{14} protons cm^{-2}. This mixture of spatial and energy dependence of the precipitating proton flux is a key ingredient that should be accounted for in the modeling of the Hermean magnetosphere and exosphere in the future.

Another major release mechanism for volatiles into Mercury's exosphere is photon-stimulated desorption (PSD; McGrath et al. 1986; Killen et al. 1990; Madey et al. 1998; Leblanc et al. 2022), a process that is enhanced by ion bombardment (McGrath et al. 1986; Mura et al. 2009; Leblanc et al. 2022). The coupling of these two processes is thought to produce a sodium exosphere in regions typical of ion sputtering but with the high efficiency and lower energy distribution of PSD. Estimates and patterns of volatile release via PSD will be modulated by the actual flux and energies of ions to the surface.

Solar wind electrons contribute to the exosphere of Mercury via ESD. This process is usually neglected in state-of-the-art exosphere models due to the lack of quantitative information on the flux and energy of precipitating electrons. Past works (McLain et al. 2011; Schriver et al. 2011) estimated that ESD can generate as many neutrals as ion sputtering at Mercury; however, such estimates come with large uncertainties. In our work, we provide quantitative estimates of the electron fluence and energy distribution at the surface of Mercury that will help to better evaluate the relevance of ESD as a source process for the exosphere of Mercury. The high-resolution maps in Figure 5 and the coarse grid values in Table 1, as well as the energy distribution in Figures 7(c) and (d), can be used to advance the exosphere modeling at Mercury including ESD.

Electrons accelerated within Mercury's magnetosphere in the range of 0.5–10 keV drive X-ray emissions from the surface via XRF. While this process does not affect the chemistry of the surface, it allows the detection and mapping of regions of electron precipitation. Such emission has been observed by the XRS instrument on board MESSENGER for lines of Si Kα (around 2 keV) and Ca Kα (around 4 keV; Lindsay et al. 2016, 2022). This emission is driven by keV electrons accelerated in the magnetosphere by magnetic reconnection, as shown by Lavorenti et al. (2023) and discussed in Section 3.2. However, the XRS observations had a limited energy resolution, and the surface coverage was constrained by MESSENGER's orbit. The MIXS instrument on board BepiColombo (Bunce et al. 2020) will extend the XRS observations by providing (i) more coverage in the southern hemisphere of Mercury; (ii) a higher energy resolution, allowing the separation of the Mg, Al, and Si lines; (iii) a larger energy range, enabling the observations of lines from Na, Fe, and O; and (iv) an improved spatial resolution of $\lesssim$10 km under optimal conditions that will allow better spatial characterization of regions of electron precipitation. The novel capabilities of MIXS to detect more and lower-energy fluorescence lines, coupled with electron observations from the Mio/MEA instrument (Saito et al. 2021), will help to constrain the energy spectrum and source process of precipitating $\sim$keV electrons at Mercury. The electron precipitation maps in Figure 5 coupled with surface composition models will help to interpret the future MIXS observations of electron-induced XRF at Mercury. From the maps in Figure 5, indirect information on the IMF direction can also be derived from the distribution of XRF onto the surface.

Surface charging at Mercury remains an open question at present. From the precipitating fluxes of protons and electrons computed in Section 3, we note a clear tendency of the surface to be negatively charged (the electron mean fluence is around a factor of 2 higher than that of protons, as shown in Table 1), at least on the nightside of the planet or within shadow in the dayside. This is somewhat expected given the higher mobility of electrons as compared to protons. Nonetheless, at this stage, it is hard to make any definitive conclusions about surface charging from our simulations given the lack of (i) sub-Debye-length kinetic physics in our implicit PIC code and (ii) photoelectron emission from the surface of Mercury in our model that is essential to constraining surface charging in illuminated regions of the Hermean surface. Future works could address this question using explicit PIC codes resolving the sub-Debye-length plasma–surface interactions, as well as including photoelectron emission from the illuminated surface. Proton and electron fluxes from the maps in this work (Figures (3)–(6)) could then be used as boundary conditions for such smaller-scale simulations.

5. Conclusion

From numerical simulations of the interaction of Mercury's magnetic field with solar wind plasma (protons and electrons), we have computed particle precipitation maps onto the planetary surface integrated over two full Mercury orbits (176 Earth days). Our results are as follows.

1. Mercury's 3:2 spin–orbit resonance has a weak effect on the time-integrated plasma precipitation pattern onto the surface. The surface pattern of precipitating plasma more strongly depends on the upstream magnetic field direction.

2. Mercury's weak magnetic field is able to shield, on average, 90% of the impinging solar wind protons and electrons.

3. Mercury's bow shock and magnetosphere tend to broaden the proton energy distribution going from the solar wind to the surface. A considerable number of protons at the surface have energies below 500 eV (mostly at high latitudes) and above 1.5 keV (mostly at low latitudes).

4. Mercury's magnetosphere tends to extend the electron energy distribution to high energies, with most of the electrons at the surface found in the range 0.1–10 keV.

Our results demonstrate the complexity of Mercury's geographical plasma precipitation and paves the way for future quantitative studies addressing the (i) space weathering of Mercury's regolith; (ii) plasma-driven source processes for Mercury's exosphere, such as ion sputtering and ESD; and (iii) electron-induced XRF emission from Mercury's regolith. The data used throughout the paper are publicly available at Lavorenti et al. (2023).

ORCID iDs

Federico Lavorenti ⓘ https://orcid.org/0000-0002-2893-3588
Elizabeth A. Jensen ⓘ https://orcid.org/0000-0003-0216-6621
Francesco Califano ⓘ https://orcid.org/0000-0002-9626-4371
Deborah Domingue ⓘ https://orcid.org/0000-0002-7594-4634
Simon Lindsay ⓘ https://orcid.org/0000-0002-2655-2589
Daniel Wolf Savin ⓘ https://orcid.org/0000-0002-1111-6610

References

Anderson, B. J., Johnson, C. L., Korth, H., et al. 2012, JGRE, 117, E00L12
Bauch, K. E., Hiesinger, H., Greenhagen, B. T., & Helbert, J. 2021, Icar, 354, 114083
Belmont, G., Rezeau, L., Riconda, C., & Zaslavsky, A. 2019, in Introduction to Plasma Physics, ed. G. Belmont et al. (Amsterdam: Elsevier), 195
Benkhoff, J., Murakami, G., Baumjohann, W., et al. 2021, SSRv, 217, 90
Benna, M., Anderson, B. J., Baker, D. N., et al. 2010, Icar, 209, 3
Blewett, D. T., Denevi, B. W., Cahill, J. T. S., & Klima, R. L. 2021, Icar, 364, 114472
Bunce, E. J., Martindale, A., Lindsay, S., et al. 2020, SSRv, 216, 126
David, L., Fraschetti, F., Giacalone, J., et al. 2022, ApJ, 928, 66
Dewey, R. M., Slavin, J. A., Raines, J. M., Azari, A. R., & Sun, W. 2020, JGRA, 125, e28112
Dibraccio, G. A., Slavin, J. A., Boardsen, S. A., et al. 2013, JGRA, 118, 997
Domingue, D. L., Chapman, C. R., Killen, R. M., et al. 2014, SSRv, 181, 121
Eckstein, W. 2007, Sputtering Yields (Berlin: Springer), 33
Exner, W., Heyner, D., Liuzzo, L., et al. 2018, P&SS, 153, 89
Exner, W., Simon, S., Heyner, D., & Motschmann, U. 2020, JGRA, 125, e2019JA027691
Fatemi, S., Poppe, A. R., & Barabash, S. 2020, JGRA, 125, e27706
Gershman, D. J., Raines, J. M., Slavin, J. A., et al. 2015, JGRA, 120, 8559
Gershman, D. J., Slavin, J. A., Raines, J. M., et al. 2013, JGRA, 118, 7181
Glass, A. N., Raines, J. M., Jia, X., et al. 2022, JGRA, 127, e2022JA030969
Haggerty, C. C., Shay, M. A., Drake, J. F., Phan, T. D., & McHugh, C. T. 2015, GeoRL, 42, 9657
Hiesinger, H., Helbert, J., Alemanno, G., et al. 2020, SSRv, 216, 110
James, M. K., Imber, S. M., Bunce, E. J., et al. 2017, JGRA, 122, 7907
Jia, X., Slavin, J. A., Poh, G., et al. 2019, JGRA, 124, 229
Kallio, E., & Janhunen, P. 2003, AnGeo, 21, 2133
Kidder, A., Winglee, R. M., & Harnett, E. M. 2008, JGRA, 113, A09223
Killen, R. M., Morrissey, L. S., Burger, M. H., et al. 2022, PSJ, 3, 139
Killen, R. M., Potter, A. E., & Morgan, T. H. 1990, Icar, 85, 145
Kohout, T., Čuda, J., Filip, J., et al. 2014, Icar, 237, 75
Korth, H., Anderson, B. J., Raines, J. M., et al. 2011, GeoRL, 38, L22201
Lario, D., Aran, A., Gómez-Herrero, R., et al. 2013, ApJ, 767, 41
Lauretta, D. S., Balram-Knutson, S. S., Beshore, E., et al. 2017, SSRv, 212, 925
Lavorenti, F., Henri, P., Califano, F., et al. 2022, A&A, 664, A133
Lavorenti, F., Henri, P., Califano, F., et al. 2023, A&A, 674, A153
Lavorenti, F., Jensen, E., Aizawa, S., et al. 2023, Maps of solar wind plasma precipitation onto Mercury's surface: a geographical perspective [Data set], Zenodo, doi:10.5281/zenodo.7927373
Leblanc, F., Schmidt, C., Mangano, V., et al. 2022, SSRv, 218, 2
Lindsay, S. T., Bunce, E. J., Imber, S. M., et al. 2022, JGRA, 127, e29675
Lindsay, S. T., James, M. K., Bunce, E. J., et al. 2016, P&SS, 125, 72
Madey, T. E., Yakshinskiy, B. V., Ageev, V. N., & Johnson, R. E. 1998, JGR, 103, 5873
Mangano, V., Massetti, S., Milillo, A., et al. 2015, P&SS, 115, 102
Markidis, S., Lapenta, G., & Rizwan-uddin 2010, Mathematics and Computers in Simulation, 80, 1509
Massetti, S., Orsini, S., Milillo, A., et al. 2003, Icar, 166, 229
Massetti, S., Orsini, S., Milillo, A., & Mura, A. 2007, P&SS, 55, 1557
Maturilli, A., Helbert, J., John, J. M., St, et al. 2014, E&PSL, 398, 58
McClintock, W. E., & Lankton, M. R. 2007, SSRv, 131, 481
McGrath, M. A., Johnson, R. E., & Lanzerotti, L. J. 1986, Natur, 323, 694
McLain, J. L., Sprague, A. L., Grieves, G. A., et al. 2011, JGRE, 116, E03007
Meyer-Vernet, N. 2007, Basics of the Solar Wind (Cambridge: Cambridge Univ. Press)
Morrissey, L. S., Tucker, O. J., Killen, R. M., Nakhla, S., & Savin, D. W. 2022, ApJL, 925, L6
Mura, A., Orsini, S., Milillo, A., et al. 2005, Icar, 175, 305
Mura, A., Wurz, P., Lichtenegger, H. I. M., et al. 2009, Icar, 200, 1
Noble, S. K., Pieters, C. M., & Keller, L. P. 2007, Icar, 192, 629
Ogilvie, K. W., Scudder, J. D., Hartle, R. E., et al. 1974, Sci, 185, 145
Phan, T. D., Drake, J. F., Shay, M. A., et al. 2014, GeoRL, 41, 7002
Poh, G., Slavin, J. A., Jia, X., et al. 2017, GeoRL, 44, 678
Pokorný, P., Janches, D., Sarantos, M., et al. 2019, JGRE, 124, 752
Pokorný, P., Sarantos, M., & Janches, D. 2018, ApJ, 863, 31
Poppe, A. R., Farrell, W. M., & Halekas, J. S. 2018, JGRE, 123, 37
Raines, J. M., Dewey, R. M., Staudacher, N. M., et al. 2022, JGRA, 127, e2022JA030397
Saito, Y., Delcourt, D., Hirahara, M., et al. 2021, SSRv, 217, 70
Sarantos, M., Killen, R. M., & Kim, D. 2007, P&SS, 55, 1584
Sawada, H., Okazaki, R., Tachibana, S., et al. 2017, SSRv, 208, 81
Schriver, D., Trávníček, P., Ashour-Abdalla, M., et al. 2011, P&SS, 59, 2026
Schriver, D., Trávníček, P. M., Anderson, B. J., et al. 2011, GeoRL, 38, L23103
Schwartz, S. J., Goodrich, K. A., Wilson, L. B., et al. 2022, JGRA, 127, e2022JA030637
Shay, M. A., Haggerty, C. C., Phan, T. D., et al. 2014, PhPl, 21, 122902
Slavin, J. A. 2004, AdSpR, 33, 1859
Slavin, J. A., DiBraccio, G. A., Gershman, D. J., et al. 2014, JGRA, 119, 8087
Slavin, J. A., Krimigis, S. M., Acuña, M. H., et al. 2007, SSRv, 131, 133
Slavin, J. A., Middleton, H. R., Raines, J. M., et al. 2019, JGRA, 124, 6613
Solomon, S. C., McNutt, R. L., Gold, R. E., & Domingue, D. L. 2007, SSRv, 131, 3
Sun, W. J., Raines, J. M., Fu, S. Y., et al. 2017, GeoRL, 44, 8149
Tóth, G., Chen, Y., Gombosi, T. I., et al. 2017, JGRA, 122, 10,336
Trávníček, P., Hellinger, P., & Schriver, D. 2007, GeoRL, 34, L05104
Trávníček, P. M., Hellinger, P., Schriver, D., et al. 2009, GeoRL, 36, L07104
Trávníček, P. M., Schriver, D., Hellinger, P., et al. 2010, Icar, 209, 11
Vilas, F., Domingue, D. L., Helbert, J., et al. 2016, GeoRL, 43, 1450
Winslow, R. M., Anderson, B. J., Johnson, C. L., et al. 2013, JGRA, 118, 2213
Winslow, R. M., Lugaz, N., Philpott, L. C., et al. 2015, JGRA, 120, 6101
Winslow, R. M., Philpott, L., Paty, C. S., et al. 2017, JGRA, 122, 4960
Wurz, P., Fatemi, S., Galli, A., et al. 2022, SSRv, 218, 10

5.6 OTHER RESULTS

In this section, I present new unpublished results addressing three main points. First, a more detailed comparison between MEA data during BepiColombo first Mercury flyby and the results of global fully-kinetic simulations (Sect. 5.6.1). Second, a further validation of the global numerical simulations using a semi-analytical magnetic field model for Mercury (Sect. 5.6.2). Third, a brief overview of the results of the recently-performed simulation with oblique IMF (Sect. 5.6.3). In the end, I also discuss my contributions to other published works not directly related to the topic of this PhD (Sect. 5.6.4).

5.6.1 COMPARISON BETWEEN MEA DATA AND GLOBAL SIMULATIONS

The results of the global fully-kinetic simulations discussed in Sect. 5.3 and summarized in Sect. 5.1 are of particular interest to interpret in situ electron observations at Mercury. The 1st of October 2021, BepiColombo performed its first Mercury flyby (MFB1) and performed electron observations at Mercury with the sensor MPPE/MEA (see Sect. 3.2.2). Albeit constrained by the "stacked" satellite configuration (see Fig. 3.1), these MEA observations are of great importance to test the predictive capabilities of our newly-developed fully-kinetic model for Mercury. Synthetic electron spectra along MFB1 trajectory have already been shown in Sect. 5.3 (Sect. 5 therein), using the two fully-kinetic simulations RunN and RunS. Here, I extend the discussion from that paper by (i) comparing the simulated spectra to MEA in situ data, and (ii) including the results of the simulation RunO with oblique IMF (unpublished).

In Fig. 5.1, I present a one-to-one comparison between MEA data (panels a-c) and fully-kinetic global simulations (panels d-g). The MEA instrument is composed of two sensors (MEA1 and MEA2), operating during the MFB1 in two different modes. MEA1 (resp. MEA2) observes in the so-called "solar wind mode" (resp. "magnetosphere mode") that has an energy range from few eV to 3 keV (resp. 26 keV) with 16 logarithmically spaced bins. Substantial data gaps were observed in MEA data during this flyby due to a telemetry issue, as shown by the blank spaces in Fig. 5.1a-b. In Fig. 5.1c, I show the MEA2 counts (in arbitrary units) for the energy bins centered around $\sim$ a few keV. These counts present a strong peak inside the magnetosphere, between closest approach (CA) and the outbound magnetopause crossing (MP), in agreement with the discussion in Sect. 3.2.2. From the synthetic spectra computed from global fully-kinetic simulations (Fig. 5.1d-g), I find that energetic electrons (above roughly 500 eV) are observed during MFB1 inside the magnetosphere. The intensity of this high-energy electron flux, as well as its position along the trajectory changes depending on the IMF conditions. The greatest electron peak is observed in RunN after closest approach (in agreement with MEA2 observations), while RunS and RunO present a weaker peak around and before CA, see Fig. 5.1g. This seminal comparison between BepiColombo data and fully-kinetic sim-

ulations aims at showing the capabilities of this model, in light of more refined and complete BepiColombo observations starting from 2026.
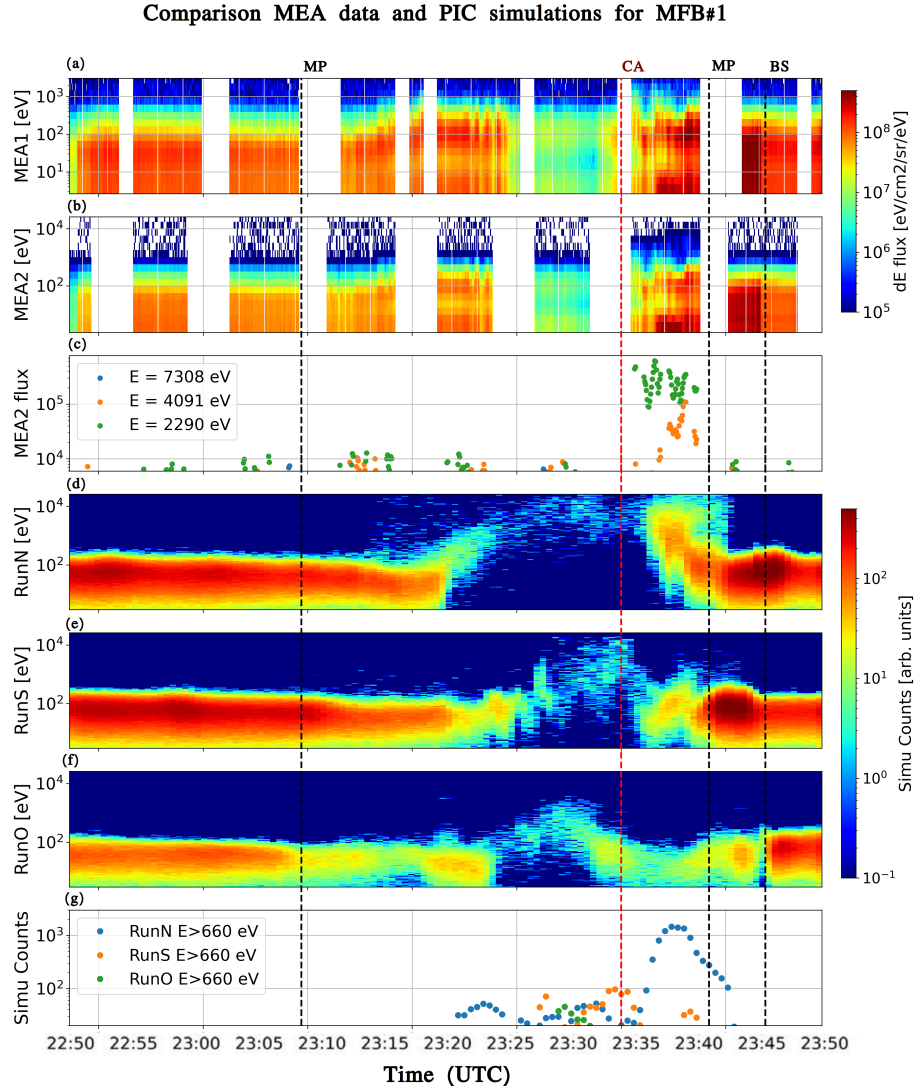
Figure 5.1: Comparison MEA data with synthetic electron spectra obtained from three fully-kinetic global simulations (RunN, RunS, and RunO). Panel (a): MEA1 observations in solar wind mode (3-3000 eV). Panel (b): MEA2 observations in magnetospheric mode (3-26000 eV). Panel (c): MEA2 electron flux in three energy bins centered around 2 keV, 4 keV, and 7 keV. Panel (d-f): simulation spectra (counts in arbitrary units) with the same energy range of MEA2, for the three different runs. Panel (g): integrated counts above 660 eV from the synthetic spetcra of the simulations. Vertical dashed lines show the magnetopause (MP) and bow shock (BS) crossings in black as published in Aizawa et al., 2023, and the closest approach (CA) in red.

5.6.2 Validation of global simulations using KT17 magnetic field model

In this section, I validate the results of my global simulations for Mercury's magnetosphere using the steady-state magnetic field model KT17 (Korth et al., 2017). The free parameters of this semi-analytical model are fitted against MESSENGER magnetic field observations. Therefore, a satisfactory matching between the magnetic field in my fully-kinetic simulations (using rescaled parameters) and the KT17 model provides an extra validation of my global simulation setup. The KT17 model remains however limited to the magnetic field inside the magnetopause. The magnetic field in the magnetosheath and further out of the bow shock can not be tested with this model.

In Fig. 5.2, I compare the magnetic fields of the different models along BepiColombo first Mercury flyby (MFB1) trajectory. The blue line indicates the KT17 model, initialized with the Sun-Mercury distance at the time of the flyby ($R_{sun} = 0.4$ AU) and a disturbance index of 100 (index defined in Korth et al. (2017) and value obtained by Aizawa et al. (2023) for MFB1). The orange, green and red lines show the results of the fully-kinetic simulations using different IMF directions: purely northward (RunN), purely southward (RunS) and oblique (RunO). More details on the simulations setup can be found in Sect. 4.3.2. The comparison shown in Fig. 5.2 validates the result of my fully-kinetic global model showing a quasi-perfect agreement in the components B_x (panel a), B_y (panel b) and in the magnitude of $\mathbf{B}$ (panel d). The largest discrepancies are observed in the component B_z of the magnetic field, as expected. This component is the most affected by the coupling IMF-planet since the dipole is parallel to the z-axis. Indeed, in RunN (RunS) one observes the least (maximum) coupling between the planet and the IMF, as shown by the orange (green) line in Fig. 5.2(c). An intermediate coupling IMF-planet is observed when the IMF is oblique, as shown by the red line in Fig. 5.2(c). This intermediate case is the one that agrees the most with the KT17 model. This is expected since the parameters in the KT17 model are averaged over a large ensemble of solar wind conditions, observed by MESSENGER, spanning a large range of IMF directions.

5.6.3 Results from a simulation run with oblique IMF

A simulation with oblique IMF (RunO) is performed to study IMF conditions more representative of those found at Mercury. The typical IMF at Mercury presents a strong B_x component (either sunward or anti-sunward), as discussed in Sect. 3.1.1. The parameters for RunO are presented in Sect. 4.3.2. Here, I only focus on the large-scale structure of the magnetosphere, showing seminal results from this newly-performed RunO.
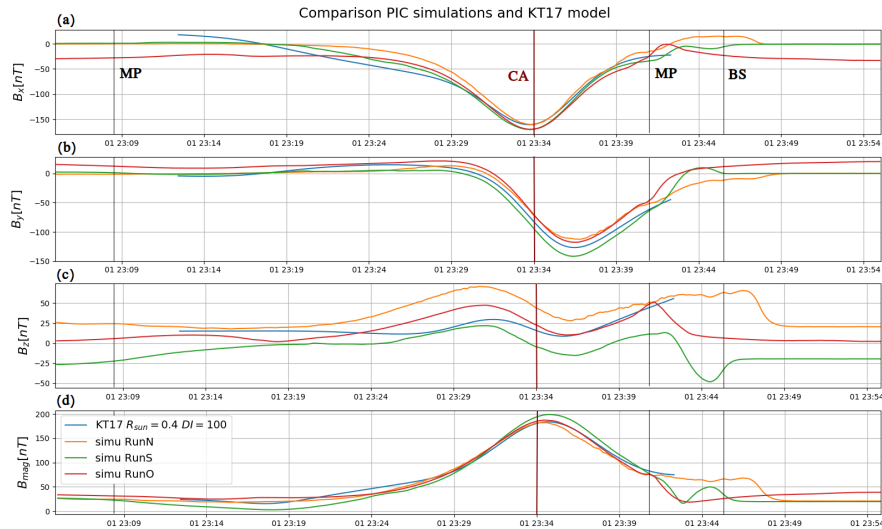
Figure 5.2: Validation of the fully-kinetic simulations by comparison with the KT17 magnetic field model along BepiColombo first Mercury flyby trajectory. The panels a-d show the B_x, B_y, B_z components in MSO coordinates, and the magnitude of **B**, respectively. Vertical dashed lines show the magnetopause (MP) and bow shock (BS) crossings in black as published in Aizawa et al., 2023, and the closest approach (CA) in red.

First, the large-scale magnetosphere structure is shown in Fig. 5.3 using the plasma density (left column), the magnetic field (central colomn), and the current density component J_y (right coloumn). The bow shock and magnetopause profiles obtained by Winslow et al. (2013) using MESSENGER observations are also shown in Fig. 5.3, using dashed and solid black lines, respectively. The bow shock and magnetopause found in the simulation match the ones observed by MESSENGER, in an average sense. Overall, the magnetosphere structure looks similar to the ones obtained in RunN and RunS (Sect. 5.3). The main difference is observed in the position of the plasma sheet. In RunO, the oblique IMF drives a north-south asymmetry in the nightside that "pushes" northward the plasma sheet in the tail. This effect has already been observed by past works using global hybrid simulations (Trávníček et al., 2007; Trávníček et al., 2010; Exner, 2021), and it has a relevant impact on the global topology of the magnetosphere and on the distribution of electrons inside it.

Second, the evolution of the electron temperature in the magnetosphere for RunO is shown in Fig. 5.4. The simulation evolves in time from left to right, reaching a quasi-steady state at $T \sim 14R/V_x$, this time corresponds roughly to one box ballistic time $T \sim L_x/V_x$ (panels e-f). The electrons in the magnetosphere tend to be energized around the nose of the magnetopause (panel a) and in the plasma sheet in the tail (panel c and e-f). Both regions create an energetic electron population with energies of the order of ~ 100 eV, but while at the nose, electrons are ejected northward/southward and therefore escape from the system, in the

plasma sheet, electrons are ejected planetward, and they form a quasi-permanent structure in the nightside close to the surface. This structure, expected to be the partial-ring-current, is shown in Fig. 5.4d-f. The results presented here address briefly a few important aspects of RunO to be deepened in future works. It will be particularly important to study the fully 3D structure of the magnetosphere, and not only 2D cuts as done in Fig. 5.3-5.4, to reliably assess the role of an oblique IMF on the magnetosphere structure and dynamics. Future works will address this point in more details.
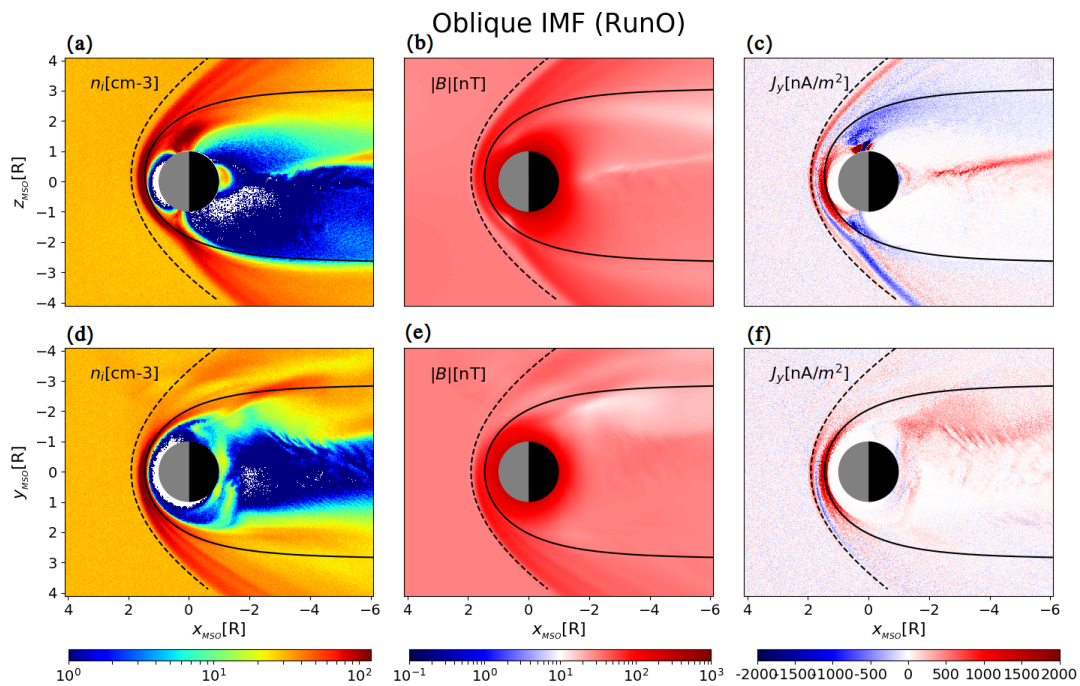
Figure 5.3: Same as Fig.1 in Sect. 5.3 but for the run with oblique IMF (RunO). The caption is copied here below:

Overview of large-scale structure and magnetosphere boundaries in our simulation. Panels (a)-(f) show the results of RunO. Panels (a)-(c) show dipolar $Y_{MSO} = 0$ cuts of the ion density n_i (a), magnetic field amplitude $|\mathbf{B}|$ (b), and plasma current density along the y-axis J_y (c). Panels (d)-(f) show equatorial $Z_{MSO} = 0$ cuts of the same quantities for RunO. All plots represent a time of $t = 14.7$ R/V_x. The average bow shock (dashed black line) and magnetopause (solid black line) profiles found by Winslow et al. (2013) using MESSENGER observations are added. The white region around the planet corresponds to grid cells with zero macro-particles.

Electron temperature RunO
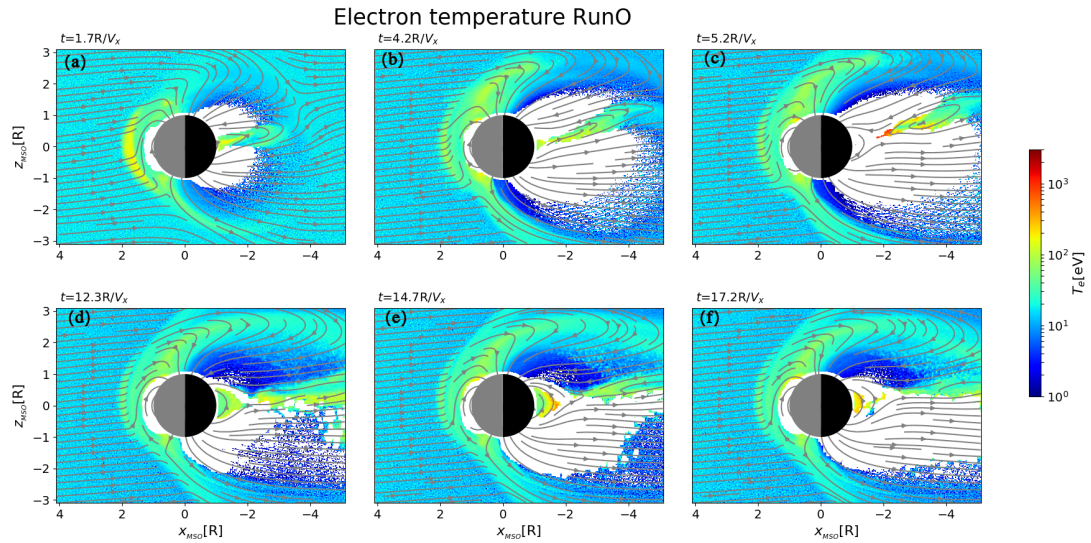
Figure 5.4: Same as Fig.3 in Sect. 5.3 but for the run with oblique IMF (RunO). The caption is copied here below:

Time evolution of electron temperature in nose and tail reconnection regions. Dipolar $Y_{MSO} = 0$ cut of simulations RunO at different times (time advancing from left to right). We show the color map of the electron temperature $T_e = (2T_{\perp,e} + T_{\|,e})/3$ in units of [eV] in logarithmic scale. On top of that, we superpose the in-plane magnetic field lines (gray solid lines). The white region around the planet corresponds to grid cells with a number of macro-particles too small to reliably compute the value of T_e.

5.6.4 A FULLY-KINETIC APPROACH TO INSTRUMENTAL MODELLING

In my PhD, I also contributed to the development and analysis of a fully-kinetic model for instrumental applications. In the works Bucciantini et al. (2023a) and Bucciantini et al. (2023b), as a co-author, I contributed to the development of a 1D-1V Vlasov-Poisson numerical model used for simulating the electric perturbations triggered in an unmagnetized plasma by localized emitting electric antennas. Such numerical model has been employed to investigate the instrumental response of a mutual impedance (MI) probe. This probe is an in situ plasma diagnostic instrument for the determination of the electron density and temperature. MI probes are typically composed of two dipolar antennas: one emitting antenna, that perturbs the plasma by emitting sinusoidal electric signals at specific amplitude and frequencies, and one receiving antenna, that measures the electric oscillations triggered in the plasma by the emission. The signals retrieved by the receiving dipole are used to compute the MI spectra, that represent the plasma response to the emitted excitation signals. From the analysis of the

resonances found in the MI spectra [1], one determines the electron density from the frequency corresponding to the resonance (i.e. the plasma frequency, see Sect. 2.1.1) and the electron temperature from the shape of the resonant curve. The numerical setup (to which I contributed) enabled a better understanding of the impact that specific parameters have on the instrumental response of MI probes. Part of these studies will have a direct application in the analysis and interpretation of future observations from the AM2P mutual impedance experiment onboard the Mio spacecraft on the BepiColombo mission, which is scheduled to perform its scientific operations around Mercury in 2026-2027 (Kasaba et al., 2020; Murakami et al., 2020).

In Bucciantini et al. (2023a), one dimensional Vlasov-Poisson simulations are employed in conjunction to plasma chamber experiments to assess the efficiency of novel instrumental modes for the optimization of MI measurements. Such new instrumental modes allow for a lower power consumption onboard the satellite and for a greater time resolution, two goals of great importance in light of future space missions. In particular, the newly defined MI modes facilitate the integration of MI instruments onboard future cube- and nano- satellite platforms: very small satellites that enable multi-point missions with limited costs. In Bucciantini et al. (2023b), the effect of small scale plasma inhomogeneities (e.g. plasma sheath) on the instrumental response of MI probes is studied numerically. In that work, we find that the electron density (resp. temperature) diagnostic of MI experiments is weakly (resp. severely) affected by the plasma sheath associated with spacecraft-plasma interactions. Therefore, while the presence of the plasma sheath can be neglected for the identification of the electron density, it is mandatory to take it into account for the identification of the electron temperature.

---

[1]In the case of an unmagnetized plasma, MI spectra have only one resonance, in correspondence to the plasma frequency. In the case of multiple electron populations (Gilet et al., 2019) or magnetized plasmas (Dazzi, 2021), multiple resonances are observed.

6 Conclusions and perspectives

This work contributes to the global understanding of the interaction between the Sun and the bodies in the Solar System, by applying plasma physics to the study of planetary environments. I particular, in this work I focus on the interaction between the solar wind and the planet Mercury to answer two main questions:

(Q1) What is the most relevant mechanism for electron acceleration in the magnetosphere of Mercury?

(Q2) What is the role of electrons in the coupling between the solar wind, magnetosphere, exosphere and surface at Mercury?

These two questions are addressed in this work using a fully-kinetic approach. Fully-kinetic simulations include the electron kinetic physics self-consistently, being therefore the most complete approach to study electron kinetic acceleration processes in the "small" magnetosphere of Mercury. I ran both (i) local simulations to study wave-particle interaction at a plasma boundary, i.e. a portion of the magnetopause, with high spatial and temporal resolution, and (ii) global simulations of the magnetosphere to study the acceleration and circulation of electrons in the whole system. For this purpose, I implemented a new initialization based on the equilibrium of Alpers (1969) in the code SMILEI (see Sect. 4.3.1), and I implemented a new set of both inner ant outer boundary conditions in the code iPIC3D (see Sect. 4.3.2-4.3.3). To my knowledge, the global simulations presented here (Sect. 5.3-5.6) are the first ab initio, fully-kinetic simulations representative of Mercury's magnetosphere.

My first main conclusion is that magnetic reconnection (MR) in the magnetotail is the most relevant process for electron acceleration in the magnetosphere of Mercury (Q1). In particular, I showed that electrons are accelerated to few keV in the tail (Lavorenti et al., 2022), and they are mostly found in the midnight-dawn sector of the magnetosphere (local times 0-6) in agreement with observations by Mariner10, MESSENGER, and BepiColombo (see Sect. 3.2.2 and Sect. 5.6.1). On the other hand, acceleration of electrons by the lower-hybrid-drift instability (LHDI) eventually increases the parallel temperature up to a factor x2 (roughly up to 100 eV) (Lavorenti et al., 2021). Although significant locally, this is however found not to be a substantial process in the global energy budget of the magnetosphere. Nonetheless, it

still plays a relevant role at the magnetopause where, for example, it can lead to secondary anisotropy-driven instabilities with $T_{\parallel,e} > T_{\perp,e}$. The most energetic electrons found in the magnetosphere are those ejected by MR from the magnetotail to the inner layers of the magnetosphere (Lavorenti et al., 2022). These electrons are preferentially found in the midnight-dawn sector, as a consequence of the curvature drift (Sect. 2.2.3). In that sector, substantial precipitation onto the surface occurs, thus coupling the high-energy electrons to the exosphere and surface of Mercury (Q2, see next paragraph).

In the low-altitude exosphere, where the density of neutrals is greatest, precipitating electrons ionize the atoms via electron-impact ionization (see Sect. 2.2.4 and Sec. 3.3). I showed that this process efficiently[1] ionize the exospheric species H, He, O, and Mn, while it is negligible for other exospheric species (Na, Mg, Al, Si, K, and Ca) (Lavorenti et al., 2023a). To my knowledge, this is the first quantitative estimate of electron-impact ionization (EII) rates at Mercury. This is a key quantitative information to be included in future exosphere models for Mercury. At the surface, electrons interact with the regolith to generate X-ray emissions, a process observed by MESSENGER for the first time (Lindsay et al., 2016; Lindsay et al., 2022). From the simulated flux of precipitating electrons, I found that X-ray emissions are driven by the high-energy electron population found in the midnight-dawn sector (Lavorenti et al., 2023a). The dawn-dusk asymmetry in X-ray emissions observed by MESSENGER is now explained as a consequence of the curvature drift of electrons ejected planetward from the reconnection line in the tail. Nonetheless, the simulations performed in this work suggest that the regions of strongest precipitation (and therefore of EII and X-ray emissions) strongly depend on the upstream direction of the IMF. The IMF direction affects the magnetosphere topology (see discussion in Sect. 3.1.2), that in turn determines the pattern of electron precipitation onto the surface. Furthermore, maps of electron (and ion) precipitation in geographical coordinates (latitude-longitude) were computed in this work from the output of the fully-kinetic simulations (Lavorenti et al., 2023b). These maps will help to correlate plasma precipitation at Mercury with space weathering of the surface and source processes for the exosphere (such as ion sputtering and ESD, see Sect. 3.3). However, I found that the geographical distribution (latitude-longitude) of precipitating plasma at Mercury strongly depends on the IMF direction, a point that limits the conclusiveness of this study simulating only a handful of IMF conditions.

The global model for the magnetosphere of Mercury developed in this PhD work successfully represents the kinetic electron physics in the system. This model has been built to support ongoing and future observations by BepiColombo, a goal of great importance to fully unveil the properties of the Hermean environment. The results of this model will be used to interpret electric field observations by the Mio-PWI consortium, electron observations by the Mio-MPPE instrument, and the origin of X-ray observations by the MPO-MIXS and MPO-SIXS

---

[1]Here, the term "efficiently" means that locally at the surface electron-impact ionization is as efficient as photoionization, that is the main ionization process in the system.

instruments (instruments described in Sect. 3.2.1). Moreover, observations of X-ray emission from the surface targeted by the MPO-MIXS instrument will provide a key opportunity to correlate electron observations in situ from Mio, with remote observations of X-rays from MPO, and with global information from the numerical model developed here. Observational opportunities for BepiColombo of interest to probe to electron environment at Mercury are discussed in Appendix B. However, to increase the predictive capabilities of the numerical model developed here, in light of future orbital observations by BepiColombo, it is important to fully assess the limitations of this numerical model. These limitations are extensively discussed in Sect. 4.2, and in the next part of this chapter I present some future perspectives for this numerical work aiming at, on the one hand, extending the existing numerical model, and on the other hand, overcoming the intrinsic limitations of fully-kinetic models by using other complementary modeling approaches.

The future perspectives for this work focus on increasing the predictive capabilities of the fully-kinetic global model developed here, in light of the ongoing exploration of Mercury by the BepiColombo mission. Fully-kinetic numerical plasma models have been historically used mainly for local simulations, just recently they are starting to be used for global simulations thanks to the increasing power of computational machines. This means that global fully-kinetic models have a large spectrum of scientific answers to address. On the one hand, with the existing version of the model, one can address many scientific questions of interest for Mercury exploration. One the other hand, the existing model is intrinsically limited by its huge computational costs, and for this reason, reduced parameters are commonly used (see Sec. 4.2.2). These reduced parameters hinder a quantitative investigation of the plasma around Mercury. A limitation of great relevance, that can only be overcame using more powerful machines (a goal unattainable in the coming years, as discussed in Sec. 4.2.2) or using other type of models.

On the one hand, with the existing version of the model one can address three important scientific questions of great relevance for Mercury and BepiColombo. A first question should address the variability of Mercury's environment with changing solar wind parameters. In this thesis, I have shown few solar wind initializations with fixed, nominal solar wind parameters and changing IMF direction. I argue that this is the most important parameter governing the shape and dynamics in the magnetosphere of Mercury, and thus the coupling plasma-exosphere-surface as well. This educated guess should be further tested in future works, aiming for a more complete set of simulations that span a wider range of solar wind parameter space. A second question should address the presence of waves around the electron cyclotron frequency $\omega_{c,e}$ in the magnetosphere of Mercury. In this thesis, I mainly focused on the properties of electrons and on the electron precipitation onto the surface, without investigating

the wave activity that is expected to come with such high-energy electron beams. This topic is especially relevant in light of the recently published Mio-PWI observations of whistler-mode waves at Mercury during the first and second BepiColombo flybys (Ozaki et al., 2023). A third question should address the importance of exospheric ions and exo-electrons in the global dynamics of the magnetosphere. During this thesis, I implemented and partially tested a new source term in the code iPIC3D that simulate the generation of ions and electrons by photoionization of exospheric neutrals. This newly developed module will be used in the future to include an ionized exosphere (or exo-ionosphere) in the global fully-kinetic simulations of Mercury.

On the other hand, since the existing fully-kinetic global model for Mercury is complex and expensive, one can develop simplified, reduced models for Mercury to be tested against the results of fully-kinetic global simulations. This strategy is analogous to the one adopted to study wave-particle interaction between the LHDI and electrons in Lavorenti et al. (2021). There, I used *first* fully-kinetic simulations with reduced plasma parameters to study the process, *then* I developed a reduced model (there called an extended quasilinear, or eQL, model) and validated it against the fully-kinetic results, and *finally* I used the reduced model to study the process using realistic plasma parameters. To apply this strategy to the study of electron acceleration and circulation in the global magnetosphere of Mercury, one has to develop a reduced model able to reproduce the physics observed in fully-kinetic simulations. For example, one such model could use test particles in the static electromagnetic fields of the fully-kinetic simulation –at a fixed timestep. Or going even to more reduced formulations, one could use analytical semi-empirical formulas to describe the particle flow from the solar wind down to the inner layers of the magnetosphere. In more details, one could use Rankine-Hugoniot-like conditions for the bow-shock crossing, describe the magnetosheath flow with the semi-analytical model of Schmid et al. (2022), model the magnetopause as a permeable boundary with effective diffusion and energization parameters, describe the outflow from MR in the tail using asymptotic relations such as the ones in Haggerty et al. (2015), and finally model the motion in the inner layers of the magnetosphere using adiabatic theory (see Sect. 2.2.3). Such a reduced model would leverage the limitations of fully-kinetic simulations –thus allowing to use a realistic electron mass, planet radius, and plasma-to-cyclotron frequency ratio– while being as good as the fully-kinetic model in the reduced-parameters regime.

In the end, numerical models such as the ones used and developed in this work, are of paramount importance to support the planning and operations of exploratory space missions in the Solar System. Fully-kinetic models can be used for this purpose, leveraging the computational power of nowadays HPC machines[2] to run global simulations of a "small" system, such as

---

[2]The fully-kinetic global model developed here for Mercury (Sect. 4.3.2) runs on $\sim$ 30 thousands CPU cores for $\sim$ 30 hours to obtain one complete simulation of Mercury's magnetosphere, with fixed solar wind and IMF conditions. The simulations were performed on the French supercomputer TGCC-Irene through yearly allocations of computational time.

the magnetosphere of Mercury. Other examples are the magnetosphere of Ganymede (one of Jupiter's moons), the induced ionosphere of Mars, Earth's Moon, comets (such as comet 67P explored by ESA Rosetta mission), and asteroids (especially magnetized asteroids, such as Psyche). All these objects are the target of one or multiple space missions, as a consequence, they provide the most fertile ground for future applications of the fully-kinetic 3D global model developed for Mercury in this work.

Appendices

A DETAILED DESCRIPTION OF THE NUMERICAL SCHEMES

In this appendix, I describe in more details the numerical schemes implemented in the PIC codes SMILEI (Derouillat et al., 2018) and iPIC3D (Markidis et al., 2010) (both briefly explained in Sect. 4.1). In the following, I indicate with the apex $^{(n)}$ the n-th timestep of the computation, with the subscript $_p$ the p-th particle of the simulation, with the subscript $_{(i,j,k)}$ the grid position $(i\Delta x, j\Delta y, k\Delta z)$ in Cartesian coordinates, and with Δt the timestep of the simulation. Equations are normalized using $4\pi = c = 1$.

Firstly, it is useful to write down the continuity and the wave equation from Maxwell equations. Taking the time derivative of Eq. 2.8 and substituting in the divergence of Eq. 2.9, the continuity equation reads:

$$\frac{\partial \rho}{\partial t} + \nabla \cdot \mathbf{J} = 0 \tag{A.1}$$

This equation is used in the following discussion of the explicit PIC code SMILEI (Sect. A.1). Moreover, it is useful to note that Eqs. (2.8)-(2.10) can be merged to obtain a single inhomogeneous wave equation for the electric field:

$$\frac{\partial^2 \mathbf{E}}{\partial t^2} - \nabla^2 \mathbf{E} = -\nabla \rho - \frac{\partial \mathbf{J}}{\partial t} \tag{A.2}$$

This equation is used in the following discussion of the implicit PIC code iPIC3D (Sect. A.2).

A.1 THE EXPLICIT PIC CODE SMILEI

The implementation of the four steps of the PIC loop (shown in Fig. 4.1) are extensively discussed in this section for the code SMILEI.

A Detailed description of the numerical schemes

Step (1): projection of the field at the macro-particle positions. This is readily done by computing the integral in Eqs. (4.4)-(4.5) numerically:

$$\mathbf{E}_p^{(n)} = \int \left[\sum_{i,j,k} \mathbf{E}_{(i,j,k)}^{(n)} b_0 \left(\frac{\mathbf{x} - \mathbf{x}_{(i,j,k)}}{\mathbf{\Delta x}} \right) \right] S(\mathbf{x} - \mathbf{x}_p) d\mathbf{x} \tag{A.3}$$

$$\mathbf{B}_p^{(n)} = \int \left[\sum_{i,j,k} \mathbf{B}_{(i,j,k)}^{(n)} b_0 \left(\frac{\mathbf{x} - \mathbf{x}_{(i,j,k)}}{\mathbf{\Delta x}} \right) \right] S(\mathbf{x} - \mathbf{x}_p) d\mathbf{x} \tag{A.4}$$

Where $b_0(\mathbf{x})$ is the b-spline function of order zero; it corresponds to a flat function inside the cell (i, j, k), with unitary integral. In SMILEI, the shape function $S(\mathbf{x})$ is a b-spline function of order 2:

$$S(\mathbf{x} - \mathbf{x}_p) = b_2 \left(\frac{\mathbf{x} - \mathbf{x}_p}{\mathbf{\Delta x}} \right) = b_2 \left(\frac{x - x_p}{\Delta x} \right) b_2 \left(\frac{y - y_p}{\Delta y} \right) b_2 \left(\frac{z - z_p}{\Delta z} \right) \tag{A.5}$$

Therefore, using the recursive property of b-splines, the equations for the fields read:

$$\mathbf{E}_p^{(n)} = \sum_{i,j,k} \mathbf{E}_{(i,j,k)}^{(n)} b_3 \left(\frac{\mathbf{x}_p - \mathbf{x}_{(i,j,k)}}{\mathbf{\Delta x}} \right) \Delta x \Delta y \Delta z \tag{A.6}$$

$$\mathbf{B}_p^{(n)} = \sum_{i,j,k} \mathbf{B}_{(i,j,k)}^{(n)} b_3 \left(\frac{\mathbf{x}_p - \mathbf{x}_{(i,j,k)}}{\mathbf{\Delta x}} \right) \Delta x \Delta y \Delta z \tag{A.7}$$

Step (2): particle pushing. The particles are pushed using a second order leap-frog integrator (the so-called Boris pusher; Boris 1970). After discretization in time, the equations of motion of the particles (Eqs. 4.2-4.3) become:

$$\frac{\mathbf{x}_p^{(n+1)} - \mathbf{x}_p^{(n)}}{\Delta t} = \frac{\mathbf{v}_p^{(n+\frac{1}{2})}}{\gamma_p} \approx \mathbf{v}_p^{(n+\frac{1}{2})} \tag{A.8}$$

$$\frac{\mathbf{v}_p^{(n+\frac{1}{2})} - \mathbf{v}_p^{(n-\frac{1}{2})}}{\Delta t} = \frac{q_s}{m_s} \left(\mathbf{E}_p^{(n)} + \frac{\mathbf{v}_p^{(n+\frac{1}{2})} + \mathbf{v}_p^{(n-\frac{1}{2})}}{2} \times \mathbf{B}_p^{(n)} \right) \tag{A.9}$$

Where $\gamma_p = \left(1 - |\mathbf{v}_p|^2 / c^2 \right)^{-1/2} \approx 1$ is the relativistic Lorentz factor. This is an explicit algorithm for the particles since the "new" values at timestep $(n+1)$ and $(n+\frac{1}{2})$ are computed explicitly from the "old" values at timestep (n) and $(n - \frac{1}{2})$. In particular, the solution of Eq. (A.9) for the velocity is expressed as follows:

$$\frac{\mathbf{v}^+ - \mathbf{v}^-}{\Delta t} = \frac{q_s}{2m_s} \left(\mathbf{v}^+ + \mathbf{v}^- \right) \times \mathbf{B}_p^{(n)} \tag{A.10}$$

Where, the velocities $\mathbf{v}^-$ and $\mathbf{v}^+$ represent respectively the old and new velocity, and they are defined as:

$$\mathbf{v}^- = \mathbf{v}_p^{(n-\frac{1}{2})} + \frac{q_s \Delta t}{2 m_s} \mathbf{E}_p^{(n)} \tag{A.11}$$

$$\mathbf{v}^+ = \mathbf{v}_p^{(n+\frac{1}{2})} - \frac{q_s \Delta t}{2 m_s} \mathbf{E}_p^{(n)} \tag{A.12}$$

Introducing the rescaled magnetic field $\boldsymbol{\mathcal{B}}_s^{(n)} = q_s \mathbf{B}_p^{(n)} \Delta t / 2 m_s$, the solution for the new speed $\mathbf{v}^+$ is obtained as follows:

$$\mathbf{v}^+ = \mathbf{v}^- + \frac{2}{1 + \left(\boldsymbol{\mathcal{B}}_s^{(n)}\right)^2} \left[\left(\mathbf{v}^- + \mathbf{v}^- \times \boldsymbol{\mathcal{B}}_s^{(n)}\right) \times \boldsymbol{\mathcal{B}}_s^{(n)} \right] \tag{A.13}$$

The solution for $\mathbf{v}^+$ from this equation yields the new velocity $\mathbf{v}_p^{(n+\frac{1}{2})}$ from Eq. (A.12), and in the end, the new position of the particle $\mathbf{x}_p^{(n+1)}$ is obtained from Eq. (A.8).

Step (3): computation of the particle moments on the grid. In SMILEI, the current density $\mathbf{J}$ is computed at timestep $(n + \frac{1}{2})$ from the particle velocities and positions, using the charge-conserving algorithm of Esirkepov (2001). This algorithm computes the current density $\boldsymbol{\mathcal{J}} = \mathbf{J}_{p,s}$ deposited by each particle of each species onto a grid cell using the conservation of charge flux trough the cell boundaries. As a consequence, this algorithm ensures the conservation of charge. From the continuity equation (A.1) for one particle $_p$ of species $_s$, it follows that:

$$\frac{\partial \mathcal{J}_x}{\partial x} + \frac{\partial \mathcal{J}_y}{\partial y} + \frac{\partial \mathcal{J}_z}{\partial z} = \frac{\partial \rho_{p,s}}{\partial t} \equiv -\frac{q_s w_p}{\Delta t} (W_x + W_y + W_z) \tag{A.14}$$

Where the auxiliary array $\mathbf{W} = (W_x, W_y, W_z)$ is introduced. This array, defined in Esirkepov (2001, Eq. 23 therein), decomposes the time derivative of the charge density in three terms that are used to equate the LHS terms (e.g. $\partial \mathcal{J}_x / \partial x$) with the RHS terms (e.g. $-q_s w_p W_x / \Delta t$). The functions in $\mathbf{W}$ are formed by linear combinations of the shape function $S(\mathbf{x})$ computed in eights different points around the positions $\mathbf{l_0} = \mathbf{x}_{(i,j,k)} - \mathbf{x}_p^{(n)}$ and $\mathbf{l_1} = \mathbf{x}_{(i,j,k)} - \mathbf{x}_p^{(n+1)}$. In the end, the solution for the current $\boldsymbol{\mathcal{J}}^{(n+\frac{1}{2})}$ reads:

$$\mathcal{J}_{x,(i+\frac{1}{2},j,k)} = \mathcal{J}_{x,(i-\frac{1}{2},j,k)} + \left(\Delta x \frac{q_s w_p}{\Delta t}\right) W_{x,(i+\frac{1}{2},j,k)} \tag{A.15}$$

$$\mathcal{J}_{y,(i,j+\frac{1}{2},k)} = \mathcal{J}_{y,(i,j-\frac{1}{2},k)} + \left(\Delta y \frac{q_s w_p}{\Delta t}\right) W_{y,(i,j+\frac{1}{2},k)} \tag{A.16}$$

$$\mathcal{J}_{z,(i,j,k+\frac{1}{2})} = \mathcal{J}_{z,(i,j,k-\frac{1}{2})} + \left(\Delta z \frac{q_s w_p}{\Delta t}\right) W_{z,(i,j,k+\frac{1}{2})} \tag{A.17}$$

and the total current density is computed as follows:

$$\mathbf{J}^{(n+\frac{1}{2})} = \sum_s \sum_{p=1}^{N_s} \boldsymbol{\mathcal{J}}^{(n+\frac{1}{2})} \tag{A.18}$$

Step (4): time evolution of the fields on the grid. First, the Ampère equation (2.9) is solved explicitly to compute the electric field at timestep $(n+1)$:

$$\frac{\mathbf{E}^{(n+1)} - \mathbf{E}^{(n)}}{\Delta t} = \nabla \times \mathbf{B}^{(n+\frac{1}{2})} - \mathbf{J}^{(n+\frac{1}{2})} \tag{A.19}$$

Then, using the new value of the electric field at timestep $(n+1)$, the magnetic field is computed from Faraday equation (2.10) as follows:

$$\frac{\mathbf{B}^{(n+\frac{3}{2})} - \mathbf{B}^{(n+\frac{1}{2})}}{\Delta t} = -\nabla \times \mathbf{E}^{(n+1)} \tag{A.20}$$

In the end, the time-centered magnetic field at step $(n+1)$ is computed as follows:

$$\mathbf{B}^{(n+1)} = \frac{\mathbf{B}^{(n+\frac{3}{2})} + \mathbf{B}^{(n+\frac{1}{2})}}{2} \tag{A.21}$$

This formulation of the field solver in Eqs. (A.19)-(A.21) preserves $\nabla \cdot \mathbf{B} = 0$ at any timestep as long as it is satisfied at $t = 0$. This solver also preserves Gauss equation (2.8) thanks to the use of the charge-conserving algorithm for the current discussed in Step (3).

A.2 THE IMPLICIT PIC CODE IPIC3D

The implementation of the four steps of the PIC loop (shown in Fig. 4.1) are extensively discussed in this section for the code iPIC3D.

Step (1): projection of the field at the macro-particle positions. This step is very similar between iPIC3D and SMILEI, just note that in iPIC3D the shape function $S(\mathbf{x})$ is a b-spline function of order zero (this choice leads to the so-called "cloud-in-cell" scheme; Hockney and Eastwood 1988):

$$S(\mathbf{x} - \mathbf{x}_p) = b_0\left(\frac{\mathbf{x} - \mathbf{x}_p}{\boldsymbol{\Delta}\mathbf{x}}\right)\frac{1}{\boldsymbol{\Delta}\mathbf{x}} = b_0\left(\frac{x - x_p}{\Delta x}\right)b_0\left(\frac{y - y_p}{\Delta y}\right)b_0\left(\frac{z - z_p}{\Delta z}\right)\frac{1}{\Delta x \Delta y \Delta z} \tag{A.22}$$

Therefore, the fields are computed as follows:

$$\mathbf{E}_p^{(n)} = \sum_{i,j,k} \mathbf{E}_{(i,j,k)}^{(n)} b_1 \left(\frac{\mathbf{x}_p - \mathbf{x}_{(i,j,k)}}{\mathbf{\Delta x}} \right) \tag{A.23}$$

$$\mathbf{B}_p^{(n)} = \sum_{i,j,k} \mathbf{B}_{(i,j,k)}^{(n)} b_1 \left(\frac{\mathbf{x}_p - \mathbf{x}_{(i,j,k)}}{\mathbf{\Delta x}} \right) \tag{A.24}$$

Step (2): particle pushing. The particles are pushed from the old timestep $(n-1)$ to the new timestep (n) using the implicit solver developed by Vu and Brackbill (1992) and Vu and Brackbill (1995). According to this algorithm, the equations of motion for the particle (Eqs. 4.2-4.3) are discretized in time as follows:

$$\frac{\mathbf{x}_p^{(n)} - \mathbf{x}_p^{(n-1)}}{\Delta t} = \mathbf{v}_p^{(n-\frac{1}{2})} \tag{A.25}$$

$$\frac{\mathbf{v}_p^{(n)} - \mathbf{v}_p^{(n-1)}}{\Delta t} = \frac{q_s}{m_s} \left(\mathbf{E}_{1/2}^{(n)} + \mathbf{v}_p^{(n-\frac{1}{2})} \times \mathbf{B}_{1/2}^{(n)} \right) \tag{A.26}$$

Where the electromagnetic fields $\mathbf{E}_{1/2}$ and $\mathbf{B}_{1/2}$ are computed at the intermediate position of the particle $\mathbf{x}_p^{(n-\frac{1}{2})} = (\mathbf{x}_p^{(n-1)} + \mathbf{x}_p^{(n)})/2$, and not in the position $\mathbf{x}_p^{(n-1)}$ as it is done in SMILEI. The solution for the velocity at timestep $(n - \frac{1}{2})$ is obtained from Eq. (A.26), using again the rescaled magnetic field $\boldsymbol{\mathcal{B}}_s^{(n)} = q_s \mathbf{B}_{1/2}^{(n)} \Delta t / 2 m_s$, as follows:

$$\mathbf{v}_p^{(n-\frac{1}{2})} = \frac{1}{1 + \left(\boldsymbol{\mathcal{B}}_s^{(n)} \right)^2} \left[\mathbf{v}^- + \mathbf{v}^- \times \boldsymbol{\mathcal{B}}_s^{(n)} + \left(\mathbf{v}^- \cdot \boldsymbol{\mathcal{B}}_s^{(n)} \right) \boldsymbol{\mathcal{B}}_s^{(n)} \right] \tag{A.27}$$

where the velocity $\mathbf{v}^-$ is defined in a similar way as the one for the Boris pusher in Eq. (A.11), in this case it reads:

$$\mathbf{v}^- = \mathbf{v}^{(n-1)} + \frac{q_s \Delta t}{m_s} \mathbf{E}_{1/2}^{(n-1)} \tag{A.28}$$

The equations (A.25)-(A.28) form a coupled system of nonlinear equations, where the new position $\mathbf{x}_p^{(n)}$ enters both in Eq. (A.25) and in the definition of the fields $\mathbf{E}_{1/2}^{(n)}$ and $\mathbf{B}_{1/2}^{(n)}$. Therefore, an iterative procedure is needed to find the solution. The code employs a Predictor-Corrector (PC) method (Riley et al., 2006). This stops either when the maximum amount of iterations N_{max} is reached, or when the difference between the new and old solution for the particle velocity $\mathbf{v}_p$ is below a given threshold. In my simulations, I use $N_{max} = 8$ and a threshold equal to $10^{-6} |\mathbf{v}_p^{old}|$.

Step (3): computation of the particle moments on the grid. The moments are computed from the particle positions and velocities via the following equations:

$$\rho_{(i,j,k)}^{(n)} = \sum_s q_s \sum_{p=1}^{N_s} \frac{1}{\boldsymbol{\Delta x}} b_1\left(\mathbf{x}_{(i,j,k)} - \mathbf{x}_p^{(n)}\right) \tag{A.29}$$

$$\mathbf{J}_{(i,j,k)}^{(n)} = \sum_s q_s \sum_{p=1}^{N_s} \mathbf{v}_p^{(n)} \frac{1}{\boldsymbol{\Delta x}} b_1\left(\mathbf{x}_{(i,j,k)} - \mathbf{x}_p^{(n)}\right) \tag{A.30}$$

Step (4): time evolution of the fields on the grid. The solution of Maxwell equations from timestep (n) to $(n + 1)$ is found using an implicit, approximated scheme that constitutes the core of the whole code (Mason, 1981; Brackbill and Forslund, 1982; Lapenta et al., 2006; Markidis et al., 2010). By discretizing Eq. (A.2), I obtain the following equation for the electric field:

$$\frac{\mathbf{E}^{(n+1)} - \mathbf{E}^{(n)}}{\Delta t^2} - \nabla^2 \mathbf{E}^{(n+1)} = -\left(\nabla \rho^{(n+1)} + \frac{\mathbf{J}^{(n+\frac{1}{2})} - \nabla \times \mathbf{B}^{(n)}}{\Delta t}\right) \tag{A.31}$$

In this form, this equation is very hard to solve since the electric field at the next timestep $(n + 1)$ is coupled to the moments (and therefore, to the particle positions and velocities) at $(n+1)$ as well. Instead, the "approximated" implicit scheme used in iPIC3D does not include the moments at the future step $(n+1)$ but just at the past step (n). This approximated scheme is obtained by Taylor-expanding to second order the charge and current densities on the RHS of Eq. (A.31). In this way, the charge and current densities are expressed in terms of their past values at timestep (n) and of the (unknown) future electric field at timestep $(n + 1)$. The resulting equation for the electric field reads:

$$\mathbf{A}^{(n)}\left[\mathbf{E}^{(n+1)}\right] = \boldsymbol{S}^{(n)} \tag{A.32}$$

where the linear differential operator $\mathbf{A}^{(n)}$ and the source term $\boldsymbol{S}^{(n)}$ are defined as follows:

$$\mathbf{A}^{(n)}[\mathbf{f}] = \left(\mathbf{I} + \chi^{(n)}\right) \cdot \mathbf{f} - \Delta t^2 \nabla^2 \mathbf{f} + \Delta t^2 \nabla\left(\nabla \cdot \chi^{(n)} \cdot \mathbf{f}\right) \tag{A.33}$$

$$\boldsymbol{S}^{(n)} = \mathbf{E}^{(n)} - \Delta t^2 \nabla \hat{\rho}^{(n)} - \Delta t\left(\hat{\mathbf{J}}^{(n)} - \nabla \times \mathbf{B}^{(n)}\right) \tag{A.34}$$

where $\mathbf{I}$ is the identity matrix, χ is the implicit susceptibility matrix (computed from the magnetic field $\mathbf{B}^{(n)}$), and $\hat{\rho}^{(n)}$, $\hat{\mathbf{J}}^{(n)}$ are the generalized moments (computed from $\rho^{(n)}$, $\mathbf{J}_s^{(n)}$ and the pressure tensor $\boldsymbol{\Pi}_s^{(n)}$); see Markidis et al. (2010, Eqs. 15-17 therein) for details. All in all, Eq. (A.32) is a linear equation and it can be solved using well-known numerical methods for the inversion of the matrix $\mathbf{A}^{(n)}$. In the code, Eq. (A.32) is solved using the Generalized Minimal Residual method (Kelley, 1995; Saad, 2003), that typically converges in 4 to 10 iterations

using a threshold value of 10^{-3}. In the end, the electric field obtained from Eq. (A.32) is corrected using the Conjugate Gradient method (Saad, 2003), using again a threshold value of 10^{-3}, to ensure that the continuity equation (A.1) is satisfied:

$$
\begin{aligned}
\mathbf{E}^{(n+1)}_{fin} &= \mathbf{E}^{(n+1)} - \nabla\Phi & \text{(A.35)} \\
\nabla^2\Phi &= \nabla \cdot \mathbf{E}^{(n+1)} - \rho^{(n)} & \text{(A.36)}
\end{aligned}
$$

and the magnetic field at timestep $(n+1)$ is computed from the final electric field using Faraday equation (2.10) as follows:

$$
\frac{\mathbf{B}^{(n+1)} - \mathbf{B}^{(n)}}{\Delta t} = -\nabla \times \mathbf{E}^{(n+1)}_{fin} \tag{A.37}
$$

In the code, a filter is applied to the electric field $\mathbf{E}$ and to the moments ρ, $\mathbf{J}$ to dissipate the energy accumulated by the numerical noise on the grid scale. The filter is a 7-points stencil that is applied two times for each field with a parameter $\alpha = 0.5$. The filter scheme applied to a general field V is as follows:

$$
\mathcal{F}_\alpha[V] = \alpha V_{i,j,k} + \frac{1-\alpha}{6}(V_{i-1,j,k} + V_{i+1,j,k} + V_{i,j-1,k} + V_{i,j+1,k} + V_{i,j,k-1} + V_{i,j,k+1}) \tag{A.38}
$$

B Observational opportunities for BepiColombo

In this Appendix, I outline a few observational opportunities for BepiColombo of great interest to test the conclusions of this work (see Chap. 6). BepiColombo will start its science phase in early 2026 (roughly 2.5 years from the time of the writing), while cruising to Mercury, discussions concerning the planning of the science phase is ongoing at ESA and JAXA (the leading space agencies for the mission). A solid planning of the BepiColombo science operations is of paramount importance to fulfill the scientific objectives of the mission. Therefore, the observational opportunities proposed here below should be considered in such a planning to fully address the role of electrons in the Hermean magnetosphere and their impact on the plasma-exosphere-surface coupling. This topic is of great relevance for Mercury's science and could not have been addressed by previous missions at Mercury, as discussed in Chap. 3.

The observational opportunities proposed below do not account for telemetry, thermal, and power constraints. These constraints further limit the observational opportunities for Bepi-Colombo. We assume that a precise planning of the proposed observations will account for these limiting effects.

B.1 Mio as a solar wind monitor

Around perihelion, Mio is found in the solar wind (roughly up to $5\ R_M$ upstream of the planet) while MPO remains close to the surface (between 0.2 and $0.62\ R_M$ altitude). In this configuration shown schematically in Fig. B.1, Mio can be used as an upstream monitor to measure the solar wind conditions for several hours, while MPO inside the magnetosphere can be used to measure the response of the Hermean system. This configuration requires Mio plasma instruments to operate in the standard solar wind mode, while MPO instruments should address the state of the plasma-exosphere-surface using a large suite of complementary observations. For instance, Mio characterizes the solar wind with the MPPE instrumental suite (for both low and high energy particles), with the MGF magnetometer, and with the PWI wave instruments. Simultaneously, MPO observes the Hermean response using the

MIXS instrument to observe electron-induced X-ray emissions from the surface, the SIXS-P instrument for the high-energy electron population in situ and SIXS-X to characterize the solar X-ray spectrum, and the magnetometer MAG to measure the magnetic coupling planet-IMF. With these instruments, one can extensively characterize the response of the Hermean system to solar wind perturbations. Additional information can be obtained using the MPO-SERENA instrument to detect the ions driving (and the neutrals originating from) plasma-surface interaction processes (e.g. ion sputtering), and also the MPO-PHEBUS instrument to probe the state of the exosphere. An extensive discussion of the Mio and MPO instruments is given in Sect. 3.2.1 and particularly in Tab. 3.2.
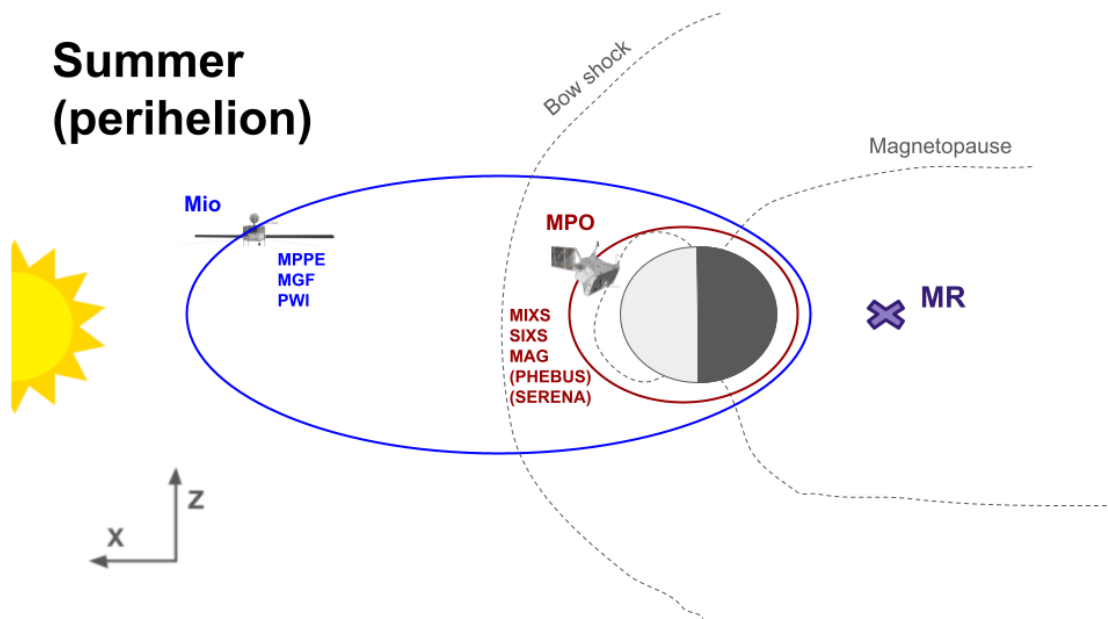
Figure B.1: Sketch of the observational opportunity named: *Mio as a solar wind monitor*. View from dusk at perihelion, where both Mio (blue) and MPO (red) spacecraft are shown. Magnetic reconnection (MR) in the tail is shown using a purple cross.

B.2 Mio-MPO electron observations in the nightside

Around perihelion, Mio passess very close to MPO in the nightside of Mercury, as shown in Fig. B.2. This interesting configuration allows for coordinated observations between Mio and MPO in the nightside, in particular focusing on electrons. On the one hand, Mio measures electrons with the MPPE/MEA and MPPE/HEP sensors, while also measuring the magnetic

field with MGF. On the other hand, MPO measures electron-induced X-rays with MIXS, high-energy electrons in situ wth SIXS-P, and the local magnetic field with MAG. If (i) Mio and MPO are on the same magnetic field line, or (ii) the MIXS footprint onto the surface corresponds to the footpoint of the magnetic field line crossing Mio, then coordinated observations of electrons can be performed using the two spacecraft payloads complementary. In the first case, MGF and MAG are used to determine when the magnetic field line connection between Mio and MPO occurs, and then MPPE/MEA and MPPE/HEP observations can be coupled to SIXS-P observations to obtain two simultaneous measurement points for electrons. In the second case, MGF is used to determine the magnetic connection between Mio and MIXS footprint onto the surface, and then MIXS observations of XRF in the nightside can be linked to MPPE/MEA and MPPE/HEP observations, using Mio as a monitor for the electron population precipitating onto the surface and driving the X-ray emissions observed by MIXS. Such interesting configurations will help to shade light on the role of high-energy electrons in the Hermean system, and particularly on the coupling electron-surface in the nightside of Mercury.
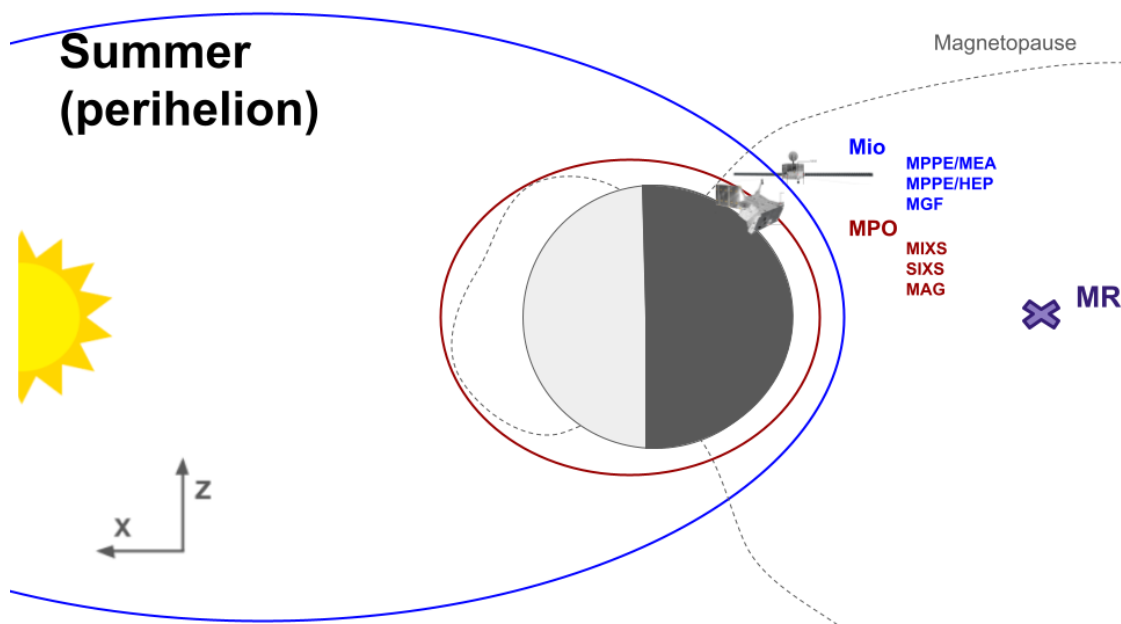
Figure B.2: Sketch of the observational opportunity named: *Mio-MPO electron observations in the nightside*. View from dusk at perihelion, where both Mio (blue) and MPO (red) spacecraft are shown. Magnetic reconnection (MR) in the tail is shown using a purple cross.

B.3 Mɪo-MPO ɪɴ sɪᴛᴜ ᴏʙsᴇʀᴠᴀᴛɪᴏɴs ᴀᴛ ᴅᴀᴡɴ

Around Mercury's spring (i.e. between aphelion and perihelion), Mio and MPO cross the dawnside of the magnetosphere at every orbit, as shown in Fig. B.3. The dawnside of the magnetosphere (local time around 6 h) is known to be a region of active plasma dynamics (Aizawa et al., 2023; Ozaki et al., 2023), and strong coupling between the magnetospheric plasma, the exosphere, and the surface (Lindsay et al., 2022; Lavorenti et al., 2023a). For this reason, in situ coordinated observations between Mio and MPO are of paramount importance to understand the complex dynamics at play there. At dawn, MPO can measure in situ high-energy electrons using SIXS-P, the magnetic field using MAG, as well as electron-induced and photon-induced X-rays using MIXS and SIXS-X complementary. On top of that, Mio can measure in situ plasma particles using MPPE, plasma waves using PWI, and the magnetic field using MGF. These two sets of complementary observations by MPO and Mio should be used in synergy to explore the dawnside of the magnetosphere. Therefore, the science planning of BepiColombo should focus on observational opportunities at dawn with (i) Mio-MPO magnetic connections, as discussed in the previous section B.2, and (ii) a short inter-spacecraft distance between Mio and MPO. These two conditions will allow to couple the plasma observations performed onboard Mio with the plasma and X-ray observations performed onboard MPO.
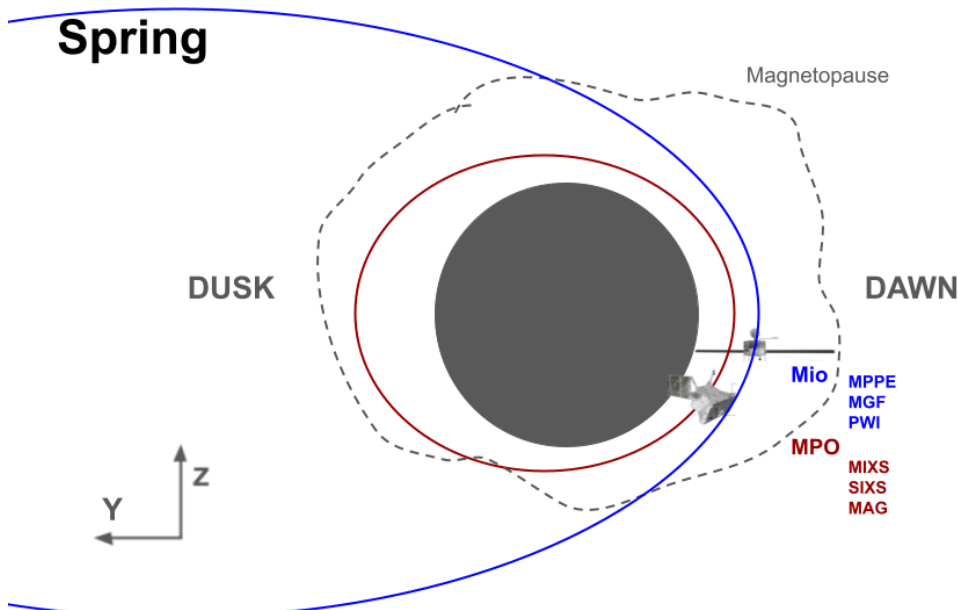
Figure B.3: Sketch of the observational opportunity named: *Mio-MPO in situ observations at dawn*. View from the nightside at the Hermean spring (meaning between aphelion and perihelion), where both Mio (blue) and MPO (red) spacecraft are shown.

C LIST OF PUBLICATIONS

First-authored papers:

- **Federico Lavorenti**, Pierre Henri, Francesco Califano, Sae Aizawa and Nicolas André, "Electron acceleration driven by the lower-hybrid-drift instability: An extended quasilinear model", Astronomy and Astrophysics, 652, A20, August, 2021

- **Federico Lavorenti**, Pierre Henri, Francesco Califano, Jan Deca, Sae Aizawa, Nicolas André and Johannes Benkhoff, "Electron dynamics in small magnetospheres: Insights from global, fully kinetic plasma simulations of the planet Mercury", Astronomy and Astrophysics, 664, A133, August, 2022

- **Federico Lavorenti**, Pierre Henri, Francesco Califano, Jan Deca, Simon Lindsay, Sae Aizawa and Johannes Benkhoff, "Solar-wind electron precipitation on weakly magnetized bodies: the planet Mercury", Astronomy and Astrophysics, 674, A153, June, 2023

- **Federico Lavorenti**, Elizabeth A. Jensen, Sae Aizawa, Francesco Califano, Mario D'Amore, Deborah Domingue, Pierre Henri, Simon Lindsay, Jim M. Raines, Daniel Wolf Savin, "Maps of solar wind plasma precipitation onto Mercury's surface: a geographical perspective", Planetary Science Journal, 4, 163, September, 2023

Co-authored papers:

- Luca Bucciantini, Pierre Henri, Pietro Dazzi, Gaëtan Wattieaux, **Federico Lavorenti**, Xavier Vallières, Jean-Yves Brochot, Fabrice Colin, Maria Chloi Katrougkalou, Germain Vengeons, Thomas Lecas, and Olivier Le Duff, "Instrumentation for ionized space environments: New high time resolution instrumental modes of mutual impedance experiments", Journal of Geophysical Research: Space Physics, 128, e2022JA031055, February, 2023

- Luca Bucciantini, Pierre Henri, Gaëtan Wattieaux, **Federico Lavorenti**, Pietro Dazzi and Xavier Vallières, "Space Plasma Diagnostics and Spacecraft Charging. The Impact of Plasma Inhomogeneities on Mutual Impedance Experiments.", Journal of Geophysical Research: Space Physics, 128, e2023JA031534, August, 2023

Acronyms

AU	Astronomical Unit
BC	Boundary Conditions
CIR	Co-rotating Interaction Region
CME	Coronal Mass Ejection
DDM	Disappearing Dayside Magnetopause
EDR	Electron diffusion region
EII	Electron-Impact Ionization
eQL	extended QuasiLinear
ESA	European Space Agency
ESD	Electron-Stimulated Desorption
HPC	High-Performance-Computing
IDR	Ion diffusion region
IMF	Interplanetary Magnetic Field
JAXA	Japan Aerospace Exploration Agency
LHDI	Lower-Hybrid-Drift Instability
LHS	Left-Hand-Side
LSAL	Linear Simple Absorption Layer
MESSENGER	MErcury Surface, Space EnviroNment, GeochEmistry and Ranging
MFB	Mercury FlyBy
MHD	Magneto-Hydro-Dynamics
MI	Mutual Impedance
MMO	Mercury Magnetospheric Orbiter
MMS	Magnetospheric Multiscale mission
MPO	Mercury Planetary Orbiter
MR	Magnetic Reconnection
MSO	Mercury-centered Solar Orbital
NASA	National Aeronautics and Space Administration
NMNL	Near Mercury Neutral Line
PIC	Particle-In-Cell
QL	QuasiLinear
RHS	Right-Hand-Side
SEP	Solar Energetic Particle
VM	Vlasov-Maxwell
XRF	X-Ray Fluorescence

Glossary

M_A	Alfvénic Mach number, ratio of Alfvén-to-flow speed in a plasma.
M_{th}	Thermal Mach number, ratio of thermal-to-flow speed in a plasma.
R_E	Earth radius, equal to 6370 km.
R_M	Mercury radius, equal to 2440 km.
T	Plasma temperature, mean quadratic speed of charged particles.
$T_\perp$	Temperature of the plasma perpendicular to the local magnetic field.
$T_\parallel$	Temperature of the plasma parallel to the local magnetic field.
V_A	Alfvén speed in a plasma.
$\int f d^3 v$	Density n, 0th order moment of the distribution function.
$\int f v_i d^3 v$	Momentum $n u_i$, 1st order moment of the distribution function.
$\int f v_i v_j d^3 v$	Pressure rank-2 tensor P_{ij}, 2nd order moment of the distribution function.
$\int f v_i v_j v_k d^3 v$	Heat flux rank-3 tensor Q_{ijk}, 3rd order moment of the distribution function.
λ_D	Debye length, the typical scale of electric shielding in a plasma.
ω	Pulsation of a given wave.
ω_c	Gyrofrequency, pulsation of a particle in magnetic field.
ω_p	Plasma frequency.
ρ	Charge density of a plasma.
σ	Cross section for a given interaction process plasma-atom.
ϱ	Gyroradius, radius of gyration of a particle in magnetic field.
c	Speed of light, equal to $3 \cdot 10^8$ m/s.
d	Skin depth.
e	Fundamental unit of charge, $1.6 \cdot 10^{19}$ C.
f	Distribution function in phase space of the plasma particles.
g	Plasma parameter, thermal-to-electrical energy ratio in a plasma.
k	Wavevector of a given wave.
m	Generic mass of a plasma particle.
m_e	Electron mass, equal to $9 \cdot 10^{-31}$ kg.
m_i/m_e	Ion-to-electron mass ratio, roughly 1836 for protons.
n	Plasma density.
q	Generic charge of a plasma particle.
u_D	Diamagnetic drift speed in a plasma.
v_{th}	Thermal speed, mean module of the particle's thermal speed.

Bibliography

Aizawa S., Delcourt D., Terada N., and André N. (2020). "Statistical study of non-adiabatic energization and transport in Kelvin-Helmholtz vortices at mercury". *Planetary and Space Science* 193, p. 105079. DOI: 10.1016/j.pss.2020.105079.

Aizawa S., Harada Y., André N., Saito Y., Barabash S., Delcourt D., Sauvaud J.-A., et al. (2023). "Direct evidence of substorm-related impulsive injections of electrons at Mercury". *Nature Communications* 14, p. 4019. DOI: 10.1038/s41467-023-39565-4.

Alexandrov A. F., Bogdankevich L. S., and Rukhadze A. A. (1984). *Principles of Plasma Electrodynamics*. Series in Electrophysics. Springer.

Alpers W. (1969). "Steady State Charge Neutral Models of the Magnetopause". *Astrophysics and Space Science* 5:4, pp. 425–437. DOI: 10.1007/BF00652391.

Anderson B. J., Johnson C. L., Korth H., Purucker M. E., Winslow R. M., Slavin J. A., Solomon S. C., et al. (2011). "The Global Magnetic Field of Mercury from MESSENGER Orbital Observations". *Science* 333:6051, p. 1859. DOI: 10.1126/science.1211001.

Anderson B. J., Johnson C. L., Korth H., Winslow R. M., Borovsky J. E., Purucker M. E., Slavin J. A., et al. (2012). "Low-degree structure in Mercury's planetary magnetic field". *Journal of Geophysical Research (Planets)* 117, E00L12. DOI: 10.1029/2012JE004159.

André M., Odelstad E., Graham D., Eriksson A., Karlsson T., Stenberg Wieser G., Vigren E., et al. (2017). "Lower Hybrid Waves at Comet 67P/Churyumov-Gerasimenko". *Monthly Notices of the Royal Astronomical Society* 469, S29–S38. DOI: 10.1093/mnras/stx868.

Andrews G. B., Zurbuchen T. H., Mauk B. H., Malcom H., Fisk L. A., Gloeckler G., Ho G. C., et al. (2007). "The Energetic Particle and Plasma Spectrometer Instrument on the MESSENGER Spacecraft". *Space Science Reviews* 131:1-4, pp. 523–556. DOI: 10.1007/s11214-007-9272-5.

Arró G., Califano F., and Lapenta G. (2022). "Spectral properties and energy transfer at kinetic scales in collisionless plasma turbulence". *Astronomy and Astrophysics* 668, A33. DOI: 10.1051/0004-6361/202243352.

Bibliography

Bacchini F., Pucci F., Malara F., and Lapenta G. (2022). "Kinetic Heating by Alfvén Waves in Magnetic Shears". *Physical Review Letters* 128:2, p. 025101. DOI: 10.1103/PhysRevLett.128.025101.

Barucq H. and Hanouzet B. (1997). "Asymptotic behavior of solutions to Maxwell's system in bounded domains with absorbing Silver–Müller's condition on the exterior boundary". *Asymptotic Analysis* 15, pp. 25–40. DOI: 10.3233/ASY-1997-15102.

Baumjohann W., Matsuoka A., Glassmeier K., Russell C. T., Nagai T., Hoshino M., Nakagawa T., et al. (2006). "The magnetosphere of Mercury and its solar wind environment: Open issues and scientific questions". *Advances in Space Research* 38:4, pp. 604–609. DOI: 10.1016/j.asr.2005.05.117.

Baumjohann W., Matsuoka A., Narita Y., Magnes W., Heyner D., Glassmeier K., Nakamura R., et al. (2020). "The BepiColombo-Mio Magnetometer en Route to Mercury". *Space Science Reviews* 216:8, p. 125. DOI: 10.1007/s11214-020-00754-y.

Belmont G., Grappin R., Mottez F., Pantellini F., and Pelletier G. (2013). *Collisionless Plasmas in Astrophysics*. Wiley-VCH.

Belmont G., Rezeau L., Riconda C., and Zaslavsky A. (2019). "7 - Shockwaves and Discontinuities". In: *Introduction to Plasma Physics*. Ed. by G. Belmont, L. Rezeau, C. Riconda, and A. Zaslavsky. Elsevier, pp. 195–218. ISBN: 978-1-78548-306-6. DOI: 10.1016/B978-1-78548-306-6.50007-X.

Benkhoff J., Murakami G., Baumjohann W., Besse S., Bunce E., Casale M., Cremosese G., et al. (2021). "BepiColombo - Mission Overview and Science Goals". *Space Science Reviews* 217:8, p. 90. DOI: 10.1007/s11214-021-00861-4.

Benna M., Anderson B. J., Baker D. N., Boardsen S. A., Gloeckler G., Gold R. E., Ho G. C., et al. (2010). "Modeling of the magnetosphere of Mercury at the time of the first MESSENGER flyby". *Icarus* 209:1, pp. 3–10. DOI: 10.1016/j.icarus.2009.11.036.

Berchem J. and Russell C. T. (1982). "The thickness of the magnetopause current layer: ISEE 1 and 2 observations". *Journal of Geophysical Research: Space Physics* 87:A4, pp. 2108–2114. DOI: 10.1029/JA087iA04p02108.

Berendeev E., Dudnikova G., Efimova A., and Vshivkov V. (2018). "A simple absorbing layer for EM-radiation from a beam-plasma interaction system". *Mathematical Methods in the Applied Sciences* 41:18, pp. 9276–9282. DOI: 10.1002/mma.5253.

Bida T. A. and Killen R. M. (2017). "Observations of the minor species Al and Fe in Mercury's exosphere". *Icarus* 289, pp. 227–238. DOI: 10.1016/j.icarus.2016.10.019.

Bida T. A., Killen R. M., and Morgan T. H. (2000). "Discovery of calcium in Mercury's atmosphere". *Nature* 404:6774, pp. 159–161. DOI: 10.1038/35004521.

Birdsall C. K. and Langdon A. B. (1991). *Plasma Physics via Computer Simulation*. Adam Hilger IOP Publishing.

Bonizzoni G. and Vassallo E. (2002). "Plasma physics and technology; industrial applications". *Vacuum* 64:3. The Fouth Iberian Vacuum Meeting, pp. 327–336. DOI: 10.1016/S0042-207X(01)00341-4.

Boris J. P. (1970). "Relativistic plasma simulation-optimization of a hybrid code". *Proceeding of Fourth Conference on Numerical Simulations of Plasmas*.

Boteler D. H. (2001). "Space weather effects on power systems". *Washington DC American Geophysical Union Geophysical Monograph Series* 125, pp. 347–352. DOI: 10.1029/GM125p0347.

Bougeret J., King J. H., and Schwenn R. (1984). "Solar Radio Burst and In-Situ Determination of Interplanetary Electron Density". *Solar Physics* 90:2, pp. 401–412. DOI: 10.1007/BF00173965.

Braams C. and Stott P. (2002). *Nuclear fusion: half a century of magnetic confinement fusion research*. IOP publishing.

Brackbill J. U. and Forslund D. W. (1982). "An Implicit Method for Electromagnetic Plasma Simulation in Two Dimensions". *Journal of Computational Physics* 46:2, pp. 271–308. DOI: 10.1016/0021-9991(82)90016-X.

Bret A. and Dieckmann M. E. (2010). "How large can the electron to proton mass ratio be in particle-in-cell simulations of unstable systems?" *Physics of Plasmas* 17:3, p. 032109. DOI: 10.1063/1.3357336.

Broadfoot A. L., Shemansky D. E., and Kumar S. (1976). "Mariner 10: Mercury atmosphere". *Geophysical Research Letters* 3:10, pp. 577–580. DOI: 10.1029/GL003i010p00577.

Bucciantini L., Henri P., Dazzi P., Wattieaux G., Lavorenti F., Vallières X., Brochot J. Y., et al. (2023a). "Instrumentation for Ionized Space Environments: New High Time Resolution Instrumental Modes of Mutual Impedance Experiments". *Journal of Geophysical Research (Space Physics)* 128:2, e2022JA031055. DOI: 10.1029/2022JA031055.

Bucciantini L., Henri P., Wattieaux G., Lavorenti F., Dazzi P., and Vallières X. (2023b). "Space Plasma Diagnostics and Spacecraft Charging. The Impact of Plasma Inhomogeneities on Mutual Impedance Experiments". *Journal of Geophysical Research (Space Physics)* 128:8, e2023JA031534. DOI: 10.1029/2023JA031534.

Bunce E. J., Martindale A., Lindsay S., Muinonen K., Rothery D. A., Pearson J., McDonnell I., et al. (2020). "The BepiColombo Mercury Imaging X-Ray Spectrometer: Science Goals, Instrument Performance and Operations". *Space Science Reviews* 216:8, p. 126. DOI: 10.1007/s11214-020-00750-2.

Burch J. L., Torbert R. B., Phan T. D., Chen L.-J., Moore T. E., Ergun R. E., Eastwood J. P., et al. (2016). "Electron-scale measurements of magnetic reconnection in space". *Science* 352, aaf2939. DOI: 10.1126/science.aaf2939.

Carter T. A., Yamada M., Ji H., Kulsrud R. M., and Trintchouk F. (2002). "Experimental study of lower-hybrid drift turbulence in a reconnecting current sheet". *Physics of Plasmas* 9:8, pp. 3272–3288. DOI: 10.1063/1.1494433.

Cassak P. A., Liu Y., and Shay M. A. (2017). "A review of the 0.1 reconnection rate problem". *Journal of Plasma Physics* 83:5, p. 715830501. DOI: 10.1017/S0022377817000666.

Chen Y., Tóth G., Jia X., Slavin J. A., Sun W., Markidis S., Gombosi T. I., and Raines J. M. (2019). "Studying Dawn-Dusk Asymmetries of Mercury's Magnetotail Using MHD-EPIC Simulations". *Journal of Geophysical Research (Space Physics)* 124:11, pp. 8954–8973. DOI: 10.1029/2019JA026840.

Chew G. F., Goldberger M. L., and Low F. E. (1956). "The Boltzmann Equation and the One-Fluid Hydromagnetic Equations in the Absence of Particle Collisions". *Proceedings of the Royal Society of London Series A* 236:1204, pp. 112–118. DOI: 10.1098/rspa.1956.0116.

Chien A., Gao L., Zhang S., Ji H., Blackman E. G., Daughton W., Stanier A., et al. (2023). "Non-thermal electron acceleration from magnetically driven reconnection in a laboratory plasma". *Nature Physics* 19:2, pp. 254–262. DOI: 10.1038/s41567-022-01839-x.

Christon S. P. (1987). "A comparison of the Mercury and Earth magnetospheres: Electron measurements and substorm time scales". *Icarus* 71:3, pp. 448–471. DOI: 10.1016/0019-1035(87)90040-6.

Chust T. and Belmont G. (2006). "Closure of fluid equations in collisionless magnetoplasmas". *Physics of Plasmas* 13:1, p. 012506. DOI: 10.1063/1.2138568.

Council N. R. (2007). *Plasma Science: Advancing Knowledge in the National Interest*. The National Academies Press, Washington, DC.

Cozzani G., Khotyaintsev Y. V., Graham D. B., Egedal J., André M., Vaivads A., Alexandrova A., et al. (2021). "Structure of a Perturbed Magnetic Reconnection Electron Diffusion Region in the Earth's Magnetotail". *Physical Review Letters* 127:21, p. 215101. DOI: 10.1103/PhysRevLett.127.215101.

Cuesta M. E., Chhiber R., Roy S., Goodwill J., Pecora F., Jarosik J., Matthaeus W. H., et al. (2022). "Isotropization and Evolution of Energy-containing Eddies in Solar Wind Turbulence: Parker Solar Probe, Helios 1, ACE, WIND, and Voyager 1". *The Astrophysical Journal* 932:1, p. L11. DOI: 10.3847/2041-8213/ac73fd.

Cuperman S., Salu Y., Bernstein W., and Williams D. J. (1973). "A computer simulation of cold plasma effects on the whistler instability for geostationary orbit plasma parameters". *Journal Geophysical Research* 78:31, pp. 7372–7387. DOI: 10.1029/JA078i031p07372.

Dargent J., Lavorenti F., Califano F., Henri P., Pucci F., and Cerri S. S. (2019). "Interplay between Kelvin–Helmholtz and lower-hybrid drift instabilities". *Journal of Plasma Physics* 85:6, p. 805850601. DOI: 10.1017/S0022377819000758.

Dazzi P. (2021). *Mutual impedance experiments in magnetized plasma*. Tesi di laurea magistrale. Università di Pisa.

de Boor C. (1978). *A practical guide to splines*. Springer.

Deca J., Divin A., Henri P., Eriksson A., Markidis S., Olshevsky V., and Horányi M. (2017). "Electron and Ion Dynamics of the Solar Wind Interaction with a Weakly Outgassing Comet". *Phys. Rev. Lett.* 118:20, p. 205101. DOI: 10.1103/PhysRevLett.118.205101.

Deca J., Divin A., Lue C., Ahmadi T., and Horányi M. (2018). "Reiner Gamma albedo features reproduced by modeling solar wind standoff". *Communications Physics* 1:1, p. 12. DOI: 10.1038/s42005-018-0012-9.

Deca J., Henri P., Divin A., Eriksson A., Galand M., Beth A., Ostaszewski K., and Horányi M. (2019). "Building a Weakly Outgassing Comet from a Generalized Ohm's Law". *Physical Review Letters* 123:5, p. 055101. DOI: 10.1103/PhysRevLett.123.055101.

Delcourt D. C., Grimald S., Leblanc F., Berthelier J.-J., Millilo A., Mura A., Orsini S., and Moore T. E. (2003). "A quantitative model of the planetary Na^+ contribution to Mercury's magnetosphere". *Annales Geophysicae* 21:8, pp. 1723–1736. DOI: 10.5194/angeo-21-1723-2003.

Delcourt D. C., Malova H. V., Zelenyi L. M., Sauvaud J. .-., Moore T. E., and Fok M. .-. (2005a). "Energetic particle injections into the outer cusp during compression events". *Earth, Planets and Space* 57, pp. 125–130. DOI: 10.1186/BF03352556.

Delcourt D. C., Seki K., Terada N., and Miyoshi Y. (2005b). "Electron dynamics during substorm dipolarization in Mercury's magnetosphere". *Annales Geophysicae* 23:10, pp. 3389–3398. DOI: 10.5194/angeo-23-3389-2005.

Derouillat J., Beck A., Pérez F., Vinci T., Chiaramello M., Grassi A., Flé M., et al. (2018). "Smilei : A collaborative, open-source, multi-purpose particle-in-cell code for plasma sim-

ulation". *Computer Physics Communications* 222, pp. 351–373. DOI: `10.1016/j.cpc.2017.09.024`.

Dewey R. M., Raines J. M., Sun W., Slavin J. A., and Poh G. (2018). "MESSENGER Observations of Fast Plasma Flows in Mercury's Magnetotail". *Geophysical Research Letters* 45:19, pp. 10, 110–10, 118. DOI: `10.1029/2018GL079056`.

Dibraccio G. A., Slavin J. A., Boardsen S. A., Anderson B. J., Korth H., Zurbuchen T. H., Raines J. M., et al. (2013). "MESSENGER observations of magnetopause structure and dynamics at Mercury". *Journal of Geophysical Research (Space Physics)* 118:3, pp. 997–1008. DOI: `10.1002/jgra.50123`.

Domingue D. L., Chapman C. R., Killen R. M., Zurbuchen T. H., Gilbert J. A., Sarantos M., Benna M., et al. (2014). "Mercury's Weather-Beaten Surface: Understanding Mercury in the Context of Lunar and Asteroidal Space Weathering Studies". *Space Science Reviews* 181, pp. 121–214. DOI: `10.1007/s11214-014-0039-5`.

Dong C., Wang L., Hakim A., Bhattacharjee A., Slavin J. A., DiBraccio G. A., and Germaschewski K. (2019). "Global Ten-Moment Multifluid Simulations of the Solar Wind Interaction with Mercury: From the Planetary Conducting Core to the Dynamic Magnetosphere". *Geophysical Research Letters* 46:21, pp. 11, 584–11, 596. DOI: `10.1029/2019GL083180`.

Dungey J. W. (1961). "Interplanetary Magnetic Field and the Auroral Zones". *Physical Review Letters* 6:2, pp. 47–48. DOI: `10.1103/PhysRevLett.6.47`.

Dunne J. A. (1974). "Mariner 10 Mercury Encounter". *Science* 185:4146, pp. 141–142. DOI: `10.1126/science.185.4146.141`.

Esirkepov T. Z. (2001). "Exact charge conservation scheme for Particle-in-Cell simulation with an arbitrary form-factor". *Computer Physics Communications* 135:2, pp. 144–153. DOI: `10.1016/S0010-4655(00)00228-9`.

Exner W. (2021). *Modeling of Mercury's Magnetosphere Under Different Solar Wind Conditions*. PhD thesis. Technische Universität Carolo-Wilhelmina zu Braunschweig.

Exner W., Heyner D., Liuzzo L., Motschmann U., Shiota D., Kusano K., and Shibayama T. (2018). "Coronal mass ejection hits mercury: A.I.K.E.F. hybrid-code results compared to MESSENGER data". *Planetary and Space Science* 153, pp. 89–99. DOI: `10.1016/j.pss.2017.12.016`.

Exner W., Simon S., Heyner D., and Motschmann U. (2020). "Influence of Mercury's Exosphere on the Structure of the Magnetosphere". *Journal of Geophysical Research: Space Physics* 125:7, e2019JA027691. DOI: `10.1029/2019JA027691`.

Fadanelli S., Lavraud B., Califano F., Cozzani G., Finelli F., and Sisti M. (2021). "Energy Conversions Associated With Magnetic Reconnection". *Journal of Geophysical Research (Space Physics)* 126:1, e28333. DOI: 10.1029/2020JA028333.

Fatemi S., Poirier N., Holmström M., Lindkvist J., Wieser M., and Barabash S. (2018). "A modelling approach to infer the solar wind dynamic pressure from magnetic field observations inside Mercury's magnetosphere". *Astronomy and Astrophysics* 614, A132. DOI: 10.1051/0004-6361/201832764.

Fatemi S., Poppe A. R., and Barabash S. (2020). "Hybrid Simulations of Solar Wind Proton Precipitation to the Surface of Mercury". *Journal of Geophysical Research (Space Physics)* 125:4, e27706. DOI: 10.1029/2019JA027706.

Finelli F. (2022). *Magnetic Reconnection In Space Plasmas: Advanced Numerical Models And Detection In Turbulence*. PhD thesis. Università di Pisa, Dottorato di Ricerca in Fisica.

Gaffey M. J. (2010). "Space weathering and the interpretation of asteroid reflectance spectra". *Icarus* 209:2, pp. 564–574. DOI: 10.1016/j.icarus.2010.05.006.

Gamborino D., Vorburger A., and Wurz P. (2019). "Mercury's subsolar sodium exosphere: an ab initio calculation to interpret MASCS/UVVS observations from MESSENGER". *Annales Geophysicae* 37:4, pp. 455–470. DOI: 10.5194/angeo-37-455-2019.

Gary S. P. (1993). *Theory of Space Plasma Microinstabilities*. Cambridge Atmospheric and Space Science Series. Cambridge University Press.

Gary S. P. and Sanderson J. J. (1978). "Density gradient drift instabilities: Oblique propagation at zero beta". *The Physics of Fluids* 21:7, pp. 1181–1187. DOI: 10.1063/1.862357.

Gazis P. R. and Lazarus A. J. (1982). "Voyager observations of solar wind proton temperature: 1-10AU". *Geophysical Research Letters* 9:4, pp. 431–434. DOI: 10.1029/GL009i004p00431.

Gershman D. J., Slavin J. A., Raines J. M., Zurbuchen T. H., Anderson B. J., Korth H., Baker D. N., and Solomon S. C. (2013). "Magnetic flux pileup and plasma depletion in Mercury's subsolar magnetosheath". *Journal of Geophysical Research (Space Physics)* 118:11, pp. 7181–7199. DOI: 10.1002/2013JA019244.

Gilet N., Henri P., Wattieaux G., Myllys M., Randriamboarison O., Béghin C., and Rauch J.-L. (2019). "Mutual Impedance Probe in Collisionless Unmagnetized Plasmas With Suprathermal Electrons-Application to BepiColombo". *Frontiers in Astronomy and Space Sciences* 6, p. 16. DOI: 10.3389/fspas.2019.00016.

github.com/flavorenti (n.d.). *flavorenti/iPIC3DxPEACE*. https://github.com/flavorenti/iPIC3DxPEACE. Accessed: 2023-10-21.

github.com/KTH-HPC (n.d.). *KTH-HPC/iPIC3D*. https://github.com/KTH-HPC/iPIC3D. Accessed: 2023-10-05.

Golyatina R. I. and Maiorov S. A. (2021). "Analytical Cross Section Approximation for Electron Impact Ionization of Alkali and Other Metals, Inert Gases and Hydrogen Atoms". *Atoms* 9:4, p. 90. DOI: 10.3390/atoms9040090.

Gombosi T. I., Dezeeuw D. L., Groth C. P. T., Hansen K. C., Kabin K., and Powell K. G. (2000). "MHD Simulations of Current Systems in Planetary Magnetospheres: Mercury and Saturn". *Washington DC American Geophysical Union Geophysical Monograph Series* 118, p. 363. DOI: 10.1029/GM118p0363.

Graham D. B., Khotyaintsev Y. V., Norgren C., Vaivads A., André M., Toledo-Redondo S., Lindqvist P.-A., et al. (2017). "Lower hybrid waves in the ion diffusion and magnetospheric inflow regions". *Journal of Geophysical Research: Space Physics* 122:1, pp. 517–533. DOI: 10.1002/2016JA023572.

Grošelj D., Mallet A., Loureiro N. F., and Jenko F. (2018). "Fully Kinetic Simulation of 3D Kinetic Alfvén Turbulence". *Physical Review Letters* 120:10, p. 105101. DOI: 10.1103/PhysRevLett.120.105101.

Grosser J., Glassmeier K., and Stadelmann A. (2004). "Induced magnetic field effects at planet Mercury". *Planetary and Space Science* 52:14, pp. 1251–1260. DOI: 10.1016/j.pss.2004.08.005.

Haggerty C. C., Shay M. A., Drake J. F., Phan T. D., and McHugh C. T. (2015). "The competition of electron and ion heating during magnetic reconnection". *Geophysics Research Letters* 42:22, pp. 9657–9665. DOI: 10.1002/2015GL065961.

Hammett G. W. and Perkins F. W. (1990). "Fluid moment models for Landau damping with application to the ion-temperature-gradient instability". *Physical Review Letters* 64:25, pp. 3019–3022. DOI: 10.1103/PhysRevLett.64.3019.

Hellinger P., Matteini L., Štverák Š., Trávníček P. M., and Marsch E. (2011). "Heating and cooling of protons in the fast solar wind between 0.3 and 1 AU: Helios revisited". *Journal of Geophysical Research (Space Physics)* 116:A9, A09105. DOI: 10.1029/2011JA016674.

Hellinger P., Trávníček P. M., Štverák Š., Matteini L., and Velli M. (2013). "Proton thermal energetics in the solar wind: Helios reloaded". *Journal of Geophysical Research (Space Physics)* 118:4, pp. 1351–1365. DOI: 10.1002/jgra.50107.

Herčík D., Trávníček P. M., Johnson J. R., Kim E.-H., and Hellinger P. (2013). "Mirror mode structures in the asymmetric Hermean magnetosheath: Hybrid simulations". *Journal of Geophysical Research (Space Physics)* 118:1, pp. 405–417. DOI: 10.1029/2012JA018083.

Herčík D., Trávníček P. M., Štverák Š., and Hellinger P. (2016). "Properties of Hermean plasma belt: Numerical simulations and comparison with MESSENGER data". *Journal of Geophysical Research (Space Physics)* 121:1, pp. 413–431. DOI: 10.1002/2015JA021938.

Hesse M., Schindler K., Birn J., and Kuznetsova M. (1999). "The diffusion region in collisionless magnetic reconnection". *Physics of Plasmas* 6:5, pp. 1781–1795. DOI: 10.1063/1.873436.

Heyner D., Auster H., Fornaçon K., Carr C., Richter I., Mieth J. Z. D., Kolhey P., et al. (2021). "The BepiColombo Planetary Magnetometer MPO-MAG: What Can We Learn from the Hermean Magnetic Field?" *Space Science Reviews* 217:4, p. 52. DOI: 10.1007/s11214-021-00822-x.

Hiesinger H., Helbert J., Alemanno G., Bauch K. E., D'Amore M., Maturilli A., Morlok A., et al. (2020). "Studying the Composition and Mineralogy of the Hermean Surface with the Mercury Radiometer and Thermal Infrared Spectrometer (MERTIS) for the BepiColombo Mission: An Update". *Space Science Reviews* 216:6, p. 110. DOI: 10.1007/s11214-020-00732-4.

Ho G. C., Krimigis S. M., Gold R. E., Baker D. N., Anderson B. J., Korth H., Slavin J. A., et al. (2012). "Spatial distribution and spectral characteristics of energetic electrons in Mercury's magnetosphere". *Journal of Geophysical Research: Space Physics* 117:A12. DOI: 10.1029/2012JA017983.

Ho G. C., Krimigis S. M., Gold R. E., Baker D. N., Slavin J. A., Anderson B. J., Korth H., et al. (2011). "MESSENGER Observations of Transient Bursts of Energetic Electrons in Mercury's Magnetosphere". *Science* 333:6051, p. 1865. DOI: 10.1126/science.1211141.

Ho G. C., Starr R. D., Krimigis S. M., Vandegriff J. D., Baker D. N., Gold R. E., Anderson B. J., et al. (2016). "MESSENGER observations of suprathermal electrons in Mercury's magnetosphere". *Geophysical Research Letters* 43:2, pp. 550–555. DOI: 10.1002/2015GL066850.

Hockney R. W. and Eastwood J. W. (1988). *Computer simulation using particles*. A. Hilger.

Hoshino M., Mukai T., Terasawa T., and Shinohara I. (2001). "Suprathermal electron acceleration in magnetic reconnection". *Journal of Geophysical Research* 106:A11, pp. 25979–25998. DOI: 10.1029/2001JA900052.

Huba J., Gladd T., and Papadopoulos K. (1978). "Lower-hybrid-drift wave turbulence in the distant magnetotail". *Journal of Geophysical Research* 83:A11, pp. 5217–5226. DOI: 10.1029/JA083iA11p05217.

Hubbard R. F. and Joyce G. (1979). "Simulation of auroral double layers". *Journal Geophysical Research* 84:A8, pp. 4297–4304. DOI: 10.1029/JA084iA08p04297.

Huovelin J., Vainio R., Kilpua E., Lehtolainen A., Korpela S., Esko E., Muinonen K., et al. (2020). "Solar Intensity X-Ray and Particle Spectrometer SIXS: Instrument Design and First Results". *Space Science Reviews* 216:5, p. 94. DOI: 10.1007/s11214-020-00717-3.

Ip W.-H. and Kopp A. (2002). "MHD simulations of the solar wind interaction with Mercury". *Journal of Geophysical Research: Space Physics* 107:A11, p. 1348. DOI: 10.1029/2001JA009171.

James M. K., Imber S. M., Bunce E. J., Yeoman T. K., Lockwood M., Owens M. J., and Slavin J. A. (2017). "Interplanetary magnetic field properties and variability near Mercury's orbit". *Journal of Geophysical Research: Space Physics* 122:8, pp. 7907–7924. DOI: 10.1002/2017JA024435.

Jia X., Slavin J. A., Gombosi T. I., Daldorff L. K. S., Toth G., and Holst B. (2015). "Global MHD simulations of Mercury's magnetosphere with coupled planetary interior: Induction effect of the planetary conducting core on the global interaction". *Journal of Geophysical Research (Space Physics)* 120:6, pp. 4763–4775. DOI: 10.1002/2015JA021143.

Jia X., Slavin J. A., Poh G., DiBraccio G. A., Toth G., Chen Y., Raines J. M., and Gombosi T. I. (2019). "MESSENGER Observations and Global Simulations of Highly Compressed Magnetosphere Events at Mercury". *Journal of Geophysical Research (Space Physics)* 124:1, pp. 229–247. DOI: 10.1029/2018JA026166.

Johnson C. L., Philpott L. C., Anderson B. J., Korth H., Hauck S. A., Heyner D., Phillips R. J., et al. (2016). "MESSENGER observations of induced magnetic fields in Mercury's core". *Geophysical Research Letters* 43:6, pp. 2436–2444. DOI: 10.1002/2015GL067370.

Johnson C. L., Purucker M. E., Korth H., Anderson B. J., Winslow R. M., Al Asad M. M. H., Slavin J. A., et al. (2012). "MESSENGER observations of Mercury's magnetic field structure". *Journal of Geophysical Research (Planets)* 117, E00L14. DOI: 10.1029/2012JE004217.

Kabin K., Gombosi T. I., DeZeeuw D. L., and Powell K. G. (2000). "Interaction of Mercury with the Solar Wind". *Icarus* 143:2, pp. 397–406. DOI: 10.1006/icar.1999.6252.

Kabin K., Heimpel M. H., Rankin R., Aurnou J. M., Gómez-Pérez N., Paral J., Gombosi T. I., et al. (2008). "Global MHD modeling of Mercury's magnetosphere with applications to the MESSENGER mission and dynamo theory". *Icarus* 195:1, pp. 1–15. DOI: 10.1016/j.icarus.2007.11.028.

Kallio E. and Janhunen P. (2003). "Modelling the solar wind interaction with Mercury by a quasi-neutral hybrid model". *Annales Geophysicae* 21:11, pp. 2133–2145. DOI: 10.5194/angeo-21-2133-2003.

Kallio E. and Janhunen P. (2004). "The response of the Hermean magnetosphere to the interplanetary magnetic field". *Advances in Space Research* 33:12, pp. 2176–2181. DOI: 10.1016/S0273-1177(03)00447-2.

Kasaba Y., Kojima H., Moncuquet M., Wahlund J.-E., Yagitani S., Sahraoui F., Henri P., et al. (2020). "Plasma Wave Investigation (PWI) Aboard BepiColombo Mio on the Trip to the First Measurement of Electric Fields, Electromagnetic Waves, and Radio Waves Around Mercury". *Space Science Reviews* 216:4, p. 65. DOI: 10.1007/s11214-020-00692-9.

Kelley C. T. (1995). *Iterative Methods for Linear and Nonlinear Equations*. Society for Industrial and Applied Mathematics.

Kidder A., Winglee R. M., and Harnett E. M. (2008). "Erosion of the dayside magnetosphere at Mercury in association with ion outflows and flux rope generation". *Journal of Geophysical Research: Space Physics* 113:A9, A09223. DOI: 10.1029/2008JA013038.

Killen R., Cremonese G., Lammer H., Orsini S., Potter A. E., Sprague A. L., Wurz P., et al. (2007). "Processes that Promote and Deplete the Exosphere of Mercury". *Space Science Reviews* 132:2-4, pp. 433–509. DOI: 10.1007/s11214-007-9232-0.

Killen R. M., Burger M. H., Vervack R. J., and Cassidy T. A. (2018). "Understanding Mercury's Exosphere: Models Derived from MESSENGER Observations". In: *Mercury. The View after MESSENGER*. Ed. by S. C. Solomon, L. R. Nittler, and B. J. Anderson. Cambridge University Press, pp. 407–429. DOI: 10.1017/9781316650684.016.

Kim, Y.-K., Irikura, K.K., Rudd, M.E., Ali, M.A., Stone, P.M., Chang, J., Coursey, J.S., et al. (2005). *Electron-Impact Ionization Cross Section for Ionization and Excitation Database*. Version 3.0. National Institute of Standards and Technology, Gaithersburg, Maryland. DOI: 10.6028/NIST.NSRDS.164.

King J. H. and Papitashvili N. E. (2005). "Solar wind spatial scales in and comparisons of hourly Wind and ACE plasma and magnetic field data". *Journal of Geophysical Research (Space Physics)* 110:A2, A02104. DOI: 10.1029/2004JA010649.

Kleij P. (2023). *Plasmonics in the Ultra Relativistic Regime*. PhD thesis. Institut Polytechnique de Paris.

Korth H., Anderson B. J., Acuña M. H., Slavin J. A., Tsyganenko N. A., Solomon S. C., and McNutt R. L. (2004). "Determination of the properties of Mercury's magnetic field by the MESSENGER mission". *Planetary and Space Science* 52:8, pp. 733–746. DOI: 10.1016/j.pss.2003.12.008.

Korth H., Anderson B. J., Johnson C. L., Slavin J. A., Raines J. M., and Zurbuchen T. H. (2018). "Structure and Configuration of Mercury's Magnetosphere". In: *Mercury. The View after MESSENGER*. Ed. by S. C. Solomon, L. R. Nittler, and B. J. Anderson. Cambridge University Press, pp. 430–460. DOI: 10.1017/9781316650684.017.

Korth H., Johnson C. L., Philpott L., Tsyganenko N. A., and Anderson B. J. (2017). "A Dynamic Model of Mercury's Magnetospheric Magnetic Field". *Geophysical Research Letters* 44:20, pp. 10, 147–10, 154. DOI: 10.1002/2017GL074699.

Korth H., Tsyganenko N. A., Johnson C. L., Philpott L. C., Anderson B. J., Al Asad M. M., Solomon S. C., and McNutt R. L. (2015). "Modular model for Mercury's magnetospheric magnetic field confined within the average observed magnetopause". *Journal of Geophysical Research (Space Physics)* 120:6, pp. 4503–4518. DOI: 10.1002/2015JA021022.

Koskinen H. E. J. and Kilpua E. K. J. (2022). *Physics of Earth's Radiation Belts; Theory and Observations*. Astronomy and Astrophysics Library. Springer.

Krall N. A. and Liewer P. C. (1971). "Low-Frequency Instabilities in Magnetic Pulses". *Phys. Rev. A* 4, 5, pp. 2094–2103. DOI: 10.1103/PhysRevA.4.2094.

Krall N. A. and Trivelpiece A. W. (1973). *Principles of plasma physics*. McGraw-Hill.

Lammer H., Lichtenegger H. I. M., Biernat H. K., Erkaev N. V., Arshukova I. L., Kolb C., Gunell H., et al. (2006). "Loss of hydrogen and oxygen from the upper atmosphere of Venus". *Planetary Science Journal* 54:13-14, pp. 1445–1456. DOI: 10.1016/j.pss.2006.04.022.

Lapenta G., Pucci F., Goldman M. V., and Newman D. L. (2020). "Local Regimes of Turbulence in 3D Magnetic Reconnection". *The Astrophysical Journal* 888:2, p. 104. DOI: 10.3847/1538-4357/ab5a86.

Lapenta G., Brackbill J. U., and Ricci P. (2006). "Kinetic approach to microscopic-macroscopic coupling in space and laboratory plasmasa)". *Physics of Plasmas* 13:5, p. 055904. DOI: 10.1063/1.2173623.

Lapenta G., Schriver D., Walker R. J., Berchem J., Echterling N. F., El Alaoui M., and Travnicek P. (2022). "Do We Need to Consider Electrons' Kinetic Effects to Properly Model a Planetary Magnetosphere: The Case of Mercury". *Journal of Geophysical Research (Space Physics)* 127:4, e30241. DOI: 10.1029/2021JA030241.

Lavorenti F., Henri P., Califano F., Aizawa S., and André N. (2021). "Electron acceleration driven by the lower-hybrid-drift instability. An extended quasilinear model". *Astronomy and Astrophysics* 652, A20. DOI: 10.1051/0004-6361/202141049.

Lavorenti F., Henri P., Califano F., Deca J., Aizawa S., André N., and Benkhoff J. (2022). "Electron dynamics in small magnetospheres. Insights from global, fully kinetic plasma simulations of the planet Mercury". *Astronomy and Astrophysics* 664, A133. DOI: 10.1051/0004-6361/202243911.

Lavorenti F., Henri P., Califano F., Deca J., Lindsay S., Aizawa S., and Benkhoff J. (2023a). "Solar-wind electron precipitation on weakly magnetized bodies: The planet Mercury". *Astronomy and Astrophysics* 674, A153. DOI: 10.1051/0004-6361/202245711.

Lavorenti F., Jensen E. A., Aizawa S., Califano F., D'Amore M., Domingue D., Henri P., et al. (2023b). "Maps of Solar Wind Plasma Precipitation onto Mercury's Surface: A Geographical Perspective". *Planetary Science Journal* 4:9, p. 163. DOI: 10.3847/PSJ/acef15.

Lawrence D. J., Anderson B. J., Baker D. N., Feldman W. C., Ho G. C., Korth H., McNutt R. L., et al. (2015). "Comprehensive survey of energetic electron events in Mercury's magnetosphere with data from the MESSENGER Gamma-Ray and Neutron Spectrometer". *Journal of Geophysical Research (Space Physics)* 120:4, pp. 2851–2876. DOI: 10.1002/2014JA020792.

Le A., Egedal J., Ohia O., Daughton W., Karimabadi H., and Lukin V. S. (2013). "Regimes of the Electron Diffusion Region in Magnetic Reconnection". *Physical Review Letters* 110:13, p. 135004. DOI: 10.1103/PhysRevLett.110.135004.

Leblanc F., Doressoundiram A., Schneider N., Mangano V., López Ariste A., Lemen C., Gelly B., et al. (2008). "High latitude peaks in Mercury's sodium exosphere: Spectral signature using THEMIS solar telescope". *Geophysical Research Letters* 35:18, p. L18204. DOI: 10.1029/2008GL035322.

Lepping R. P., Burlaga L. F., and Klein L. W. (1981). "Surface waves on Saturn's magnetopause". *Nature* 292:5825, pp. 750–753. DOI: 10.1038/292750a0.

Leyser R. P., Imber S. M., Milan S. E., and Slavin J. A. (2017). "The Influence of IMF Clock Angle on Dayside Flux Transfer Events at Mercury". *Geophysical Research Letters* 44:21, pp. 10, 829–10, 837. DOI: 10.1002/2017GL074858.

Lindsay S. T., Bunce E. J., Imber S. M., Martindale A., Nittler L. R., and Yeoman T. K. (2022). "MESSENGER X-Ray Observations of Electron Precipitation on the Dayside of Mercury". *Journal of Geophysical Research (Space Physics)* 127:1, e29675. DOI: 10.1029/2021JA029675.

Lindsay S. T., James M. K., Bunce E. J., Imber S. M., Korth H., Martindale A., and Yeoman T. K. (2016). "MESSENGER X-ray observations of magnetosphere-surface interaction on the nightside of Mercury". *Planetary and Space Science* 125, pp. 72–79. DOI: 10.1016/j.pss.2016.03.005.

Llovet X., Salvat F., Bote D., Salvat-Pujol F., A. J., and Powell C. (2014). *NIST Database of Cross Sections for Inner-Shell Ionization by Electron or Positron Impact*. Version 1.0. National Institute of Standards and Technology, Gaithersburg, Maryland. DOI: 10.6028/NIST.NSRDS.164.

Luhmann J. G., Russell C. T., and Tsyganenko N. A. (1998). "Disturbances in Mercury's magnetosphere: Are the Mariner 10 "substorms" simply driven?" *Journal of Geophysical Research* 103:A5, pp. 9113–9120. DOI: `10.1029/97JA03667`.

Maksimovic M., Zouganelis I., Chaufray J., Issautier K., Scime E. E., Littleton J. E., Marsch E., et al. (2005). "Radial evolution of the electron distribution functions in the fast solar wind between 0.3 and 1.5 AU". *Journal of Geophysical Research (Space Physics)* 110:A9, A09104. DOI: `10.1029/2005JA011119`.

Mangano V., Massetti S., Milillo A., Plainaki C., Orsini S., Rispoli R., and Leblanc F. (2015). "THEMIS Na exosphere observations of Mercury and their correlation with in-situ magnetic field measurements by MESSENGER". *Planetary and Space Science* 115, pp. 102–109. DOI: `10.1016/j.pss.2015.04.001`.

Mangeney A., Califano F., Cavazzoni C., and Travnicek P. (2002). "A Numerical Scheme for the Integration of the Vlasov-Maxwell System of Equations". *Journal of Computational Physics* 179:2, pp. 495–538. DOI: `10.1006/jcph.2002.7071`.

Mariani F., Ness N. F., Burlaga L. F., Bavassano B., and Villante U. (1978). "The large-scale structure of the interplanetary magnetic field between 1 and 0.3 AU during the primary mission of Helios 1". *Journal of Geophysical Research* 83:A11, pp. 5161–5166. DOI: `10.1029/JA083iA11p05161`.

Markidis S., Lapenta G., and Rizwan-uddin (2010). "Multi-scale simulations of plasma with IPIC3D". *Mathematics and Computers in Simulation* 80, pp. 1509–1519. DOI: `10.1016/j.matcom.2009.08.038`.

Marsch E., Pilipp W. G., Thieme K. M., and Rosenbauer H. (1989). "Cooling of solar wind electrons inside 0.3 AU". *Journal of Geophysical Research* 94:A6, pp. 6893–6898. DOI: `10.1029/JA094iA06p06893`.

Marsch E., Schwenn R., Rosenbauer H., Muehlhaeuser K., Pilipp W., and Neubauer F. M. (1982). "Solar wind protons: Three-dimensional velocity distributions and derived plasma parameters measured between 0.3 and 1 AU". *Journal of Geophysical Research* 87:A1, pp. 52–72. DOI: `10.1029/JA087iA01p00052`.

Mason R. J. (1981). "Implicit Moment Particle Simulation of Plasmas". *Journal of Computational Physics* 41:2, pp. 233–244. DOI: `10.1016/0021-9991(81)90094-2`.

Massetti S., Orsini S., Milillo A., Mura A., De Angelis E., Lammer H., and Wurz P. (2003). "Mapping of the cusp plasma precipitation on the surface of Mercury". *Icarus* 166:2, pp. 229–237. DOI: `10.1016/j.icarus.2003.08.005`.

McClintock W. E., Cassidy T. A., Merkel A. W., Killen R. M., Burger M. H., and Vervack R. J. (2018). "Observations of Mercury's Exosphere: Composition and Structure". In: *Mercury.*

The View after MESSENGER. Ed. by S. C. Solomon, L. R. Nittler, and B. J. Anderson. Cambridge University Press, pp. 371–406. DOI: 10.1017/9781316650684.015.

McClintock W. E. and Lankton M. R. (2007). "The Mercury Atmospheric and Surface Composition Spectrometer for the MESSENGER Mission". *Space Science Reviews* 131:1-4, pp. 481–521. DOI: 10.1007/s11214-007-9264-5.

McClintock W. E., Vervack R. J., Bradley E. T., Killen R. M., Mouawad N., Sprague A. L., Burger M. H., et al. (2009). "MESSENGER Observations of Mercury's Exosphere: Detection of Magnesium and Distribution of Constituents". *Science* 324:5927, p. 610. DOI: 10.1126/science.1172525.

McCoy T. J., Peplowski P. N., McCubbin F. M., and Weider S. Z. (2018). "The Geochemical and Mineralogical Diversity of Mercury". In: *Mercury. The View after MESSENGER*. Ed. by S. C. Solomon, L. R. Nittler, and B. J. Anderson. Cambridge University Press, pp. 176–190. DOI: 10.1017/9781316650684.008.

McMillan B. F. (2020). "Is it necessary to resolve the Debye length in standard or δf PIC codes?" *Physics of Plasmas* 27:5, p. 052106. DOI: 10.1063/1.5139957.

Milillo A., Fujimoto M., Murakami G., Benkhoff J., Zender J., Aizawa S., Dósa M., et al. (2020). "Investigating Mercury's Environment with the Two-Spacecraft BepiColombo Mission". *Space Science Reviews* 216:5, p. 93. DOI: 10.1007/s11214-020-00712-8.

Milillo A., Wurz P., Orsini S., Delcourt D., Kallio E., Killen R. M., Lammer H., et al. (2005). "Surface-Exosphere-Magnetosphere System Of Mercury". *Space Science Reviews* 117:3-4, pp. 397–443. DOI: 10.1007/s11214-005-3593-z.

Miteva R., Samwel S. W., and Tkatchova S. (2023). "Space Weather Effects on Satellites". *Astronomy* 2:3, pp. 165–179. DOI: 10.3390/astronomy2030012.

Müller J., Simon S., Wang Y.-C., Motschmann U., Heyner D., Schüle J., Ip W.-H., et al. (2012). "Origin of Mercury's double magnetopause: 3D hybrid simulation study with A.I.K.E.F." *Icarus* 218:1, pp. 666–687. DOI: 10.1016/j.icarus.2011.12.028.

Mura A., Orsini S., Milillo A., Delcourt D., Massetti S., and De Angelis E. (2005). "Dayside H$^+$ circulation at Mercury and neutral particle emission". *Icarus* 175:2, pp. 305–319. DOI: 10.1016/j.icarus.2004.12.010.

Murakami G., Hayakawa H., Ogawa H., Matsuda S., Seki T., Kasaba Y., Saito Y., et al. (2020). "Mio—First Comprehensive Exploration of Mercury's Space Environment: Mission Overview". *Space Science Reviews* 216:7, p. 113. DOI: 10.1007/s11214-020-00733-3.

Murchie S. L., Klima R. L., Izenberg N. R., Domingue D. L., Blewett D. T., and Helbert J. (2018). "Spectral Reflectance Constraints on the Composition and Evolution of Mercury's

Surface". In: *Mercury. The View after MESSENGER*. Ed. by S. C. Solomon, L. R. Nittler, and B. J. Anderson. Cambridge University Press, pp. 191–216. DOI: 10.1017/9781316650684.009.

Nakamura T. K. M., Hasegawa H., Daughton W., Eriksson S., Li W. Y., and Nakamura R. (2017). "Turbulent mass transfer caused by vortex induced reconnection in collisionless magnetospheric plasmas". *Nature Communications* 8, p. 1582. DOI: 10.1038/s41467-017-01579-0.

Nakazono J. and Miyake Y. (2023). "Unconventional Surface Charging Within Deep Cavities on Airless Planetary Bodies: Particle-In-Cell Plasma Simulations". *Journal of Geophysical Research (Planets)* 128:2, e2022JE007589. DOI: 10.1029/2022JE007589.

Ness N. F. (1967). "Direct measurements of interplanetary magnetic field and plasma". *NASA Technical Memorandum (TM)* NASA-TM-X-55830.

Ness N. F. (1970). "Magnetometers for Space Research". *Space Science Reviews* 11:4, pp. 459–554. DOI: 10.1007/BF00183028.

Ness N. F., Behannon K. W., Lepping R. P., and Whang Y. C. (1976). "Observations of Mercury's Magnetic Field". *Icarus* 28:4, pp. 479–488. DOI: 10.1016/0019-1035(76)90121-4.

Ness N. F., Behannon K. W., Lepping R. P., Whang Y. C., and Schatten K. H. (1974). "Magnetic Field Observations near Mercury: Preliminary Results from Mariner 10". *Science* 185:4146, pp. 151–160. DOI: 10.1126/science.185.4146.151.

Newbury J. A. (1996). "Electron temperature in the solar wind at 1 AU". *EOS Transactions* 77:47, pp. 471–471. DOI: 10.1029/96E000315.

Nittler L. R., Chabot N. L., Grove T. L., and Peplowski P. N. (2018). "The Chemical Composition of Mercury". In: *Mercury. The View after MESSENGER*. Ed. by S. C. Solomon, L. R. Nittler, and B. J. Anderson. Cambridge University Press, pp. 30–51. DOI: 10.1017/9781316650684.003.

Nittler L. R. and Weider S. Z. (2019). "The Surface Composition of Mercury". *Elements* 15:1, pp. 33–38. DOI: 10.2138/gselements.15.1.33.

Noble S. K. and Pieters C. M. (2003). "Space Weathering on Mercury: Implications for Remote Sensing". *Solar System Research* 37:1, pp. 31–35. DOI: 10.1023/A:1022395605024.

Olshevsky V., Servidio S., Pucci F., Primavera L., and Lapenta G. (2018). "Properties of Decaying Plasma Turbulence at Subproton Scales". *The Astrophysical Journal* 860:1, p. 11. DOI: 10.3847/1538-4357/aac1bd.

Orsini S., Livi S. A., Lichtenegger H., Barabash S., Milillo A., De Angelis E., Phillips M., et al. (2021). "SERENA: Particle Instrument Suite for Determining the Sun-Mercury Interaction from BepiColombo". *Space Science Reviews* 217:1, p. 11. DOI: `10.1007/s11214-020-00787-3`.

Orsini S., Mangano V., Milillo A., Plainaki C., Mura A., Raines J. M., De Angelis E., et al. (2018). "Mercury sodium exospheric emission as a proxy for solar perturbations transit". *Scientific Reports* 8, p. 928. DOI: `10.1038/s41598-018-19163-x`.

Ozaki M., Yagitani S., Kasaba Y., Kasahara Y., Matsuda S., Omura Y., Hikishima M., et al. (2023). "Whistler-mode waves in Mercury's magnetosphere observed by BepiColombo/Mio". *Nature Astronomy*. DOI: `10.1038/s41550-023-02055-0`.

Pantellini F., Griton L., and Varela J. (2015). "Rarefaction and compressional standing slow mode structures in Mercury's magnetosheath: 3D MHD simulations". *Planetary and Space Science* 112, pp. 1–9. DOI: `10.1016/j.pss.2015.04.007`.

Parashar T. N. and Gary S. P. (2019). "Dissipation of Kinetic Alfvénic Turbulence as a Function of Ion and Electron Temperature Ratios". *The Astrophysical Journal* 882:1, p. 29. DOI: `10.3847/1538-4357/ab2fc8`.

Parashar T. N., Matthaeus W. H., and Shay M. A. (2018). "Dependence of Kinetic Plasma Turbulence on Plasma β". *The Astrophysical Journal* 864:1, p. L21. DOI: `10.3847/2041-8213/aadb8b`.

Parashar T. N., Matthaeus W. H., Shay M. A., and Wan M. (2015a). "Transition from Kinetic to MHD Behavior in a Collisionless Plasma". *The Astrophysical Journal* 811:2, p. 112. DOI: `10.1088/0004-637X/811/2/112`.

Parashar T. N., Salem C., Wicks R. T., Karimabadi H., Gary S. P., and Matthaeus W. H. (2015b). "Turbulent dissipation challenge: a community-driven effort". *Journal of Plasma Physics* 81:5, p. 905810513. DOI: `10.1017/S0022377815000860`.

Pezzi O., Liang H., Juno J. L., Cassak P. A., Vásconez C. L., Sorriso-Valvo L., Perrone D., et al. (2021). "Dissipation measures in weakly collisional plasmas". *Monthly Notices of the Royal Astronomical Society* 505:4, pp. 4857–4873. DOI: `10.1093/mnras/stab1516`.

Pieters C. M. and Noble S. K. (2016). "Space weathering on airless bodies". *Journal of Geophysical Research (Planets)* 121:10, pp. 1865–1884. DOI: `10.1002/2016JE005128`.

Poh G., Slavin J. A., Jia X., Raines J. M., Imber S. M., Sun W.-J., Gershman D. J., et al. (2017). "Mercury's cross-tail current sheet: Structure, X-line location and stress balance". *Geophysical Research Letters* 44:2, pp. 678–686. DOI: `10.1002/2016GL071612`.

Bibliography

Potter A. and Morgan T. (1985). "Discovery of Sodium in the Atmosphere of Mercury". *Science* 229:4714, pp. 651–653. DOI: `10.1126/science.229.4714.651`.

Potter A. E. and Morgan T. H. (1986). "Potassium in the atmosphere of Mercury". *Icarus* 67:2, pp. 336–340. DOI: `10.1016/0019-1035(86)90113-2`.

Pu Z.-Y., Quest K. B., Kivelson M. G., and Tu C.-Y. (1981). "Lower-hybrid-drift instability and its associated anomalous resistivity in the neutral sheet of Earth's magnetotail". *Journal of Geophysical Research: Space Physics* 86:A11, pp. 8919–8928. DOI: `10.1029/JA086iA11p08919`.

Pucci F., Matthaeus W. H., Chasapis A., Servidio S., Sorriso-Valvo L., Olshevsky V., Newman D. L., et al. (2018). "Generation of Turbulence in Colliding Reconnection Jets". *The Astrophysical Journal* 867:1, p. 10. DOI: `10.3847/1538-4357/aadd0a`.

Quémerais E., Chaufray J.-Y., Koutroumpa D., Leblanc F., Reberac A., Lustrement B., Montaron C., et al. (2020). "PHEBUS on Bepi-Colombo: Post-launch Update and Instrument Performance". *Space Science Reviews* 216:4, p. 67. DOI: `10.1007/s11214-020-00695-6`.

Richer E., Modolo R., Chanteur G. M., Hess S., and Leblanc F. (2012). "A global hybrid model for Mercury's interaction with the solar wind: Case study of the dipole representation". *Journal of Geophysical Research (Space Physics)* 117:A10, A10228. DOI: `10.1029/2012JA017898`.

Riley K. F., Hobson M. P., and Bence S. J. (2006). *Mathematical methods for physics and engineering*. Cambridge University Press.

Roytershteyn V., Boldyrev S., Delzanno G. L., Chen C. H. K., Grošelj D., and Loureiro N. F. (2019). "Numerical Study of Inertial Kinetic-Alfvén Turbulence". *The Astrophysical Journal* 870:2, p. 103. DOI: `10.3847/1538-4357/aaf288`.

Saad Y. (2003). *Iterative Methods for Sparse Linear Systems*. Society for Industrial and Applied Mathematics.

Saito Y., Delcourt D., Hirahara M., Barabash S., André N., Takashima T., Asamura K., et al. (2021). "Pre-flight Calibration and Near-Earth Commissioning Results of the Mercury Plasma Particle Experiment (MPPE) Onboard MMO (Mio)". *Space Science Reviews* 217:5, p. 70. DOI: `10.1007/s11214-021-00839-2`.

Sarantos M., Killen R. M., and Kim D. (2007). "Predicting the long-term solar wind ion-sputtering source at Mercury". *Planetary and Space Science* 55:11, pp. 1584–1595. DOI: `10.1016/j.pss.2006.10.011`.

Schmid D., Narita Y., Plaschke F., Volwerk M., Nakamura R., Baumjohann W., Heyner D., et al. (2022). "Solar-wind-dependent streamline model for Mercury's magnetosheath. A

hydrodynamic magnetosheath model for Mercury". *Astronomy and Astrophysics* 668, A113. DOI: 10.1051/0004-6361/202245008.

Schriver D., Trávníček P., Ashour-Abdalla M., Richard R. L., Hellinger P., Slavin J. A., Anderson B. J., et al. (2011a). "Electron transport and precipitation at Mercury during the MESSENGER flybys: Implications for electron-stimulated desorption". *Planetary and Space Science* 59:15, pp. 2026–2036. DOI: 10.1016/j.pss.2011.03.008.

Schriver D., Trávníček P. M., Anderson B. J., Ashour-Abdalla M., Baker D. N., Benna M., Boardsen S. A., et al. (2011b). "Quasi-trapped ion and electron populations at Mercury". *Geophysical Research Letters* 38:23, p. L23103. DOI: 10.1029/2011GL049629.

Scurry L., Russell C. T., and Gosling J. T. (1994). "Geomagnetic activity and the beta dependence of the dayside reconnection rate". *Journal of Geophysical Research* 99:A8, pp. 14811–14814. DOI: 10.1029/94JA00794.

Shay M. A. and Drake J. F. (1998). "The role of electron dissipation on the rate of collisionless magnetic reconnection". *Geophysical Research Letters* 25:20, pp. 3759–3762. DOI: 10.1029/1998GL900036.

Shue J., Chao J. K., Fu H. C., Russell C. T., Song P., Khurana K. K., and Singer H. J. (1997). "A new functional form to study the solar wind control of the magnetopause size and shape". *Journal of Geophysical Research* 102:A5, pp. 9497–9512. DOI: 10.1029/97JA00196.

Siscoe G. L., Ness N. F., and Yeates C. M. (1975). "Substorms on Mercury?" *Journal of Geophysical Research* 80:31, p. 4359. DOI: 10.1029/JA080i031p04359.

Sittler E. C. J. and Scudder J. D. (1980). "An empirical polytrope law for solar wind thermal electrons between 0.45 and 4.76 AU: Voyager 2 and Mariner 10". *Journal of Geophysical Research* 85:A10, pp. 5131–5137. DOI: 10.1029/JA085iA10p05131.

Slavin J. A. (2004). "Mercury's magnetosphere". *Advances in Space Research* 33:11, pp. 1859–1874. DOI: 10.1016/j.asr.2003.02.019.

Slavin J. A., Middleton H. R., Raines J. M., Jia X., Zhong J., Sun W., Livi S., et al. (2019). "MESSENGER Observations of Disappearing Dayside Magnetosphere Events at Mercury". *Journal of Geophysical Research (Space Physics)* 124:8, pp. 6613–6635. DOI: 10.1029/2019JA026892.

Slavin J. A., Anderson B. J., Baker D. N., Benna M., Boardsen S. A., Gold R. E., Ho G. C., et al. (2012). "MESSENGER and Mariner 10 flyby observations of magnetotail structure and dynamics at Mercury". *Journal of Geophysical Research (Space Physics)* 117:A1, A01215. DOI: 10.1029/2011JA016900.

Bibliography

Slavin J. A., Anderson B. J., Zurbuchen T. H., Baker D. N., Krimigis S. M., Acuña M. H., Benna M., et al. (2009). "MESSENGER observations of Mercury's magnetosphere during northward IMF". *Geophysical Research Letters* 36:2. DOI: 10.1029/2008GL036158.

Slavin J. A., Baker D. N., Gershman D. J., Ho G. C., Imber S. M., Krimigis S. M., and Sundberg T. (2018). "Mercury's Dynamic Magnetosphere". In: *Mercury. The View after MESSENGER*. Ed. by S. C. Solomon, L. R. Nittler, and B. J. Anderson. Cambridge University Press, pp. 461–496. DOI: 10.1017/9781316650684.018.

Slavin J. A. and Holzer R. E. (1981). "Solar wind flow about the terrestrial planets 1. Modeling bow shock position and shape". *Journal of Geophysical Research: Space Physics* 86:A13, pp. 11401–11418. DOI: 10.1029/JA086iA13p11401.

Solomon S. C., McNutt R. L., Gold R. E., and Domingue D. L. (2007). "MESSENGER Mission Overview". *Space Science Reviews* 131:1-4, pp. 3–39. DOI: 10.1007/s11214-007-9247-6.

Sonnerup B. U. O., Smith E. J., Tsurutani B. T., and Wolfe J. H. (1981). "Structure of Jupiter's magnetopause: Pioneer 10 and 11 observations". *Journal of Geophysical Research* 86:A5, pp. 3321–3334. DOI: 10.1029/JA086iA05p03321.

Sulem P. L. and Passot T. (2008). "FLR Landau fluids for collisionless plasmas". *Communications in Nonlinear Science and Numerical Simulations* 13:1, pp. 189–196. DOI: 10.1016/j.cnsns.2007.05.002.

Szabo P. S., Poppe A. R., Mutzke A., Fatemi S., Vorburger A., and Wurz P. (2023). "Energetic Neutral Atom (ENA) Emission Characteristics at the Moon and Mercury From 3D Regolith Simulations of Solar Wind Reflection". *Journal of Geophysical Research (Planets)* 128:9, e2023JE007911. DOI: 10.1029/2023JE007911.

Torbert R. B., Burch J. L., Phan T. D., Hesse M., Argall M. R., Shuster J., Ergun R. E., et al. (2018). "Electron-scale dynamics of the diffusion region during symmetric magnetic reconnection in space". *Science* 362:6421, pp. 1391–1395. DOI: 10.1126/science.aat2998.

Trávníček P. M., Hellinger P., and Schriver D. (2007). "Structure of Mercury's magnetosphere for different pressure of the solar wind: Three dimensional hybrid simulations". *Geophysical Research Letters* 34:5, p. L05104. DOI: 10.1029/2006GL028518.

Trávníček P. M., Hellinger P., Schriver D., Herčík D., Slavin J. A., and Anderson B. J. (2009). "Kinetic instabilities in Mercury's magnetosphere: Three-dimensional simulation results". *Geophysical Research Letters* 36:7, p. L07104. DOI: 10.1029/2008GL036630.

Trávníček P. M., Schriver D., Hellinger P., Herčík D., Anderson B. J., Sarantos M., and Slavin J. A. (2010). "Mercury's magnetosphere-solar wind interaction for northward and southward interplanetary magnetic field: Hybrid simulation results". *Icarus* 209:1, pp. 11–22. DOI: 10.1016/j.icarus.2010.01.008.

unh.edu (n.d.). *University of New Hampshire experimental space plasma group*. http://www-ssg.sr.unh.edu/tof/Smart/Students/lees/periods.html. Accessed: 2023-10-04.

Usui H., Miyake Y., Nishino M. N., Matsubara T., and Wang J. (2017). "Electron dynamics in the minimagnetosphere above a lunar magnetic anomaly". *Journal of Geophysical Research (Space Physics)* 122:2, pp. 1555–1571. DOI: 10.1002/2016JA022927.

Varela J., Pantellini F., and Moncuquet M. (2016). "Slow modes in the Hermean magnetosphere: Effect of the solar wind hydrodynamic parameters and IMF orientation". *Planetary and Space Science* 125, pp. 80–86. DOI: 10.1016/j.pss.2016.02.015.

Vasyliunas V. M. (1975). "Theoretical models of magnetic field line merging, 1." *Reviews of Geophysics and Space Physics* 13, pp. 303–336. DOI: 10.1029/RG013i001p00303.

Vay J. (2008). "Simulation of beams or plasmas crossing at relativistic velocity". *Physics of Plasmas* 15:5, p. 056701. DOI: 10.1063/1.2837054.

Vega C., Roytershteyn V., Delzanno G. L., and Boldyrev S. (2020). "Electron-only Reconnection in Kinetic-Alfvén Turbulence". *The Astrophysical Journal* 893:1, p. L10. DOI: 10.3847/2041-8213/ab7eba.

Venzmer M. S. and Bothmer V. (2018). "Solar-wind predictions for the Parker Solar Probe orbit. Near-Sun extrapolations derived from an empirical solar-wind model based on Helios and OMNI observations". *Astronomy and Astrophysics* 611, A36. DOI: 10.1051/0004-6361/201731831.

Vernazza P., Binzel R. P., Rossi A., Fulchignoni M., and Birlan M. (2009). "Solar wind as the origin of rapid reddening of asteroid surfaces". *Nature* 458:7241, pp. 993–995. DOI: 10.1038/nature07956.

Verscharen D., Parashar T. N., Gary S. P., and Klein K. G. (2020). "Dependence of kinetic plasma waves on ion-to-electron mass ratio and light-to-Alfvén speed ratio". *Monthly Notices of the Royal Astronomical Society* 494:2, pp. 2905–2911. DOI: 10.1093/mnras/staa977.

Vervack R. J., Killen R. M., McClintock W. E., Merkel A. W., Burger M. H., Cassidy T. A., and Sarantos M. (2016). "New discoveries from MESSENGER and insights into Mercury's exosphere". *Geophysical Research Letters* 43:22, pp. 11, 545–11, 551. DOI: 10.1002/2016GL071284.

Vu H. X. and Brackbill J. U. (1992). "CELEST1D: an implicit, fully kinetic model for low-frequency, electromagnetic plasma simulation". *Computer Physics Communications* 69:2-3, pp. 253–276. DOI: 10.1016/0010-4655(92)90165-U.

Bibliography

Vu H. X. and Brackbill J. U. (1995). "Accurate Numerical Solution of Charged Particle Motion in a Magnetic Field". *Journal of Computational Physics* 116:2, pp. 384–387. DOI: 10.1006/jcph.1995.1037.

Walsh B. M., Ryou A. S., Sibeck D. G., and Alexeev I. I. (2013). "Energetic particle dynamics in Mercury's magnetosphere". *Journal of Geophysical Research (Space Physics)* 118:5, pp. 1992–1999. DOI: 10.1002/jgra.50266.

Winske D. and Hewett D. W. (1975). "Flute Instabilities in Two-Dimensional Simulations of Strongly Inhomogeneous Theta-Pinch Plasmas". *Phys. Rev. Lett.* 35, 14, pp. 937–940. DOI: 10.1103/PhysRevLett.35.937.

Winske D. and Liewer P. C. (1978). "Particle simulation studies of the lower hybrid drift instability". *Physics of Fluids* 21:6, pp. 1017–1025. DOI: 10.1063/1.862321.

Winslow R. M., Anderson B. J., Johnson C. L., Slavin J. A., Korth H., Purucker M. E., Baker D. N., and Solomon S. C. (2013). "Mercury's magnetopause and bow shock from MESSENGER Magnetometer observations". *Journal of Geophysical Research: Space Physics* 118:5, pp. 2213–2227. DOI: 10.1002/jgra.50237.

Wurz P. and Blomberg L. (2001). "Particle populations in Mercury's magnetosphere". *Planetary and Space Science* 49:14-15, pp. 1643–1653. DOI: 10.1016/S0032-0633(01)00102-7.

Yagi M., Seki K., Matsumoto Y., Delcourt D. C., and Leblanc F. (2010). "Formation of a sodium ring in Mercury's magnetosphere". *Journal of Geophysical Research: Space Physics* 115:A10. DOI: 10.1029/2009JA015226.

Yang Y., Matthaeus W. H., Parashar T. N., Wu P., Wan M., Shi Y., Chen S., et al. (2017). "Energy transfer channels and turbulence cascade in Vlasov-Maxwell turbulence". *Physical Review E* 95:6, p. 061201. DOI: 10.1103/PhysRevE.95.061201.

Yee K. (1966). "Numerical solution of initial boundary value problems involving maxwell's equations in isotropic media". *IEEE Transactions on Antennas and Propagation* 14:3, pp. 302–307. DOI: 10.1109/TAP.1966.1138693.

Yoshikawa I., Korablev O., Kameda S., Rees D., Nozawa H., Okano S., Gnedykh V., et al. (2010). "yThe Mercury sodium atmospheric spectral imager for the MMO spacecraft of Bepi-Colombo". *Planetary and Space Science* 58:1. Comprehensive Science Investigations of Mercury: The scientific goals of the joint ESA/JAXA mission BepiColombo, pp. 224–237. DOI: 10.1016/j.pss.2008.07.008.

Zatsarinny O., Parker H., and Bartschat K. (2019). "Electron-impact excitation and ionization of atomic calcium at intermediate energies". *Physical Review A* 99:1, p. 012706. DOI: 10.1103/PhysRevA.99.012706.

Zeller E. J. and Ronca L. B. (1967). "Space Weathering of Lunar and Asteroidal Surfaces". *Icarus* 7:1, pp. 372–379. DOI: 10.1016/0019-1035(67)90082-6.

Zhong J., Shue J., Wei Y., Slavin J. A., Zhang H., Rong Z. J., Chai L. H., and Wan W. X. (2020). "Effects of Orbital Eccentricity and IMF Cone Angle on the Dimensions of Mercury's Magnetosphere". *The Astrophysical Journal* 892:1, p. 2. DOI: 10.3847/1538-4357/ab7819.

Zhong J., Wan W. X., Slavin J. A., Wei Y., Lin R. L., Chai L. H., Raines J. M., et al. (2015a). "Mercury's three-dimensional asymmetric magnetopause". *Journal of Geophysical Research (Space Physics)* 120:9, pp. 7658–7671. DOI: 10.1002/2015JA021425.

Zhong J., Wan W. X., Wei Y., Slavin J. A., Raines J. M., Rong Z. J., Chai L. H., and Han X. H. (2015b). "Compressibility of Mercury's dayside magnetosphere". *Geophysical Research Letters* 42:23, pp. 10, 135–10, 139. DOI: 10.1002/2015GL067063.

Zhong J., Lee L.-C., Slavin J. A., Zhang H., and Wei Y. (2023). "MESSENGER Observations of Reconnection in Mercury's Magnetotail Under Strong IMF Forcing". *Journal of Geophysical Research (Space Physics)* 128:2, e2022JA031134. DOI: 10.1029/2022JA031134.